JAEA-Conf 2019-001
INDC(JPN)-205
DOI:10.11484/jaea-conf-2019-001

JAEA-Conf

Proceedings of the 2018 Symposium on Nuclear Data November 29-30, 2018, Tokyo Institute of Technology, Ookayama Campus, Tokyo, Japan

(Eds.) Satoshi CHIBA, Chikako ISHIZUKA, Kohsuke TSUBAKIHARA and Osamu IWAMOTO

Nuclear Science and Engineering Center
Sector of Nuclear Science Research

November 2019
Japan Atomic Energy Agency
日本原子力研究開発機構

本レポートは国立研究開発法人日本原子力研究開発機構が不定期に発行する成果報告書です。
本レポートの入手並びに著作権利用に関するお問い合わせは、下記あてにお問い合わせ下さい。
なお、本レポートの全文は日本原子力研究開発機構ホームページ（https://www.jaea.go.jp）
より発信されています。

国立研究開発法人日本原子力研究開発機構 研究連携成果展開部 研究成果管理課
〒319-1195 茨城県那珂郡東海村大字白方 2 番地4
電話 029-282-6387, Fax 029-282-5920, E-mail:ird-support@jaea.go.jp

This report is issued irregularly by Japan Atomic Energy Agency.
Inquiries about availability and/or copyright of this report should be addressed to
Institutional Repository Section,
Intellectual Resources Management and R&D Collaboration Department,
Japan Atomic Energy Agency.
2-4 Shirakata, Tokai-mura, Naka-gun, Ibaraki-ken 319-1195 Japan
Tel +81-29-282-6387, Fax +81-29-282-5920, E-mail:ird-support@jaea.go.jp

JAEA-Conf 2019-001
INDC(JPN)-205

Proceedings of the 2018 Symposium on Nuclear Data

November 29-30, 2018,

Tokyo Institute of Technology,

Ookayama Campus, Tokyo, Japan

(Eds.) Satoshi CHIBA*, Chikako ISHIZUKA*, Kohsuke TSUBAKIHARA*
and Osamu IWAMOTO

Nuclear Science and Engineering Center, Sector of Nuclear Science Research,
Japan Atomic Energy Agency
Tokai-mura, Naka-gun, Ibaraki-ken

（Received September 10, 2019）

The 2018 Symposium on Nuclear Data was held at Multi-Purpose Digital Hall and Collaboration Room of Tokyo Institute of Technology, on November 29 and 30, 2018. The symposium was organized by the Nuclear Data Division of the Atomic Energy Society of Japan (AESJ) in cooperation with Sigma Special Committee of AESJ, Nuclear Science and Engineering Center of Japan Atomic Energy Agency, and Laboratory for Advanced Nuclear Energy of Institute of Innovative Research, Tokyo Institute of Technology. In the symposium, there were one tutorial, “Development of nuclear data processing code FRENDY”, one special lecture “What the future holds for Nuclear Energy” and seven oral sessions, “Nuclear Data and Future Perspectives”, “Current Status and Future Perspectives of Reactor Physics”, “Topics”, “Nuclear Data Applications”, “International Session”, “Nuclear Data Measurements and New Technology for Nuclear Reactor Diagnosis”, and “Data Needs from New Fields”. In addition, recent research progress on experiments, evaluation, benchmark and application was presented in the poster session. Among 82 participants, all presentations and following discussions were very active and fruitful. This report consists of total 35 papers including 13 oral and 22 poster presentations.

Keywords: Nuclear Data Symposium 2018, Experiments, Nuclear Theory, Nuclear Data Evaluation, Benchmark Test, Nuclear Data Applications

---

* Tokyo Institute of Technology

Organizers: Satoshi Chiba (Chair, Tokyo Tech), Yukinobu Watanabe (Co-chair, Kyushu Univ.), Masaaki Kimura (Hokkaido Univ.), Koichi Kino (AIST), Toshiya Sanami (KEK), Tatsuya Katabuchi (Tokyo Tech), Ken Nakajima (Kyoto Univ.), Jun-ichi Hori (Kyoto Univ.), Isao Murata (Osaka Univ.), Nobuhiro Shigyo (Kyushu Univ.), Hideaki Otsu (RIKEN), Katsuhisa Nishio (JAEA), Taira Hazama (JAEA), Osamu Iwamoto (JAEA), Satoshi Kunieda (JAEA), Shoji Nakamura (JAEA), Hiroyuki Koura (JAEA), Yutaka Utsuno (JAEA)

JAEA-Conf 2019-001
INDC(JPN)-205

2018 年度核データ研究会報告集

2018 年 11 月 29 日～30 日

東京工業大学

大岡山キャンパス、東京都

日本原子力研究開発機構　原子力科学研究部門　原子力基礎工学研究センター

（編）千葉　敏*、石塚　知香子*、椿原　康介*、岩本　修

（2019 年 9 月 10 日受理）

2018 年度核データ研究会は、2018 年 11 月 29 日～30 日に、東京都目黒区東京工業大学大岡山キャンパス東工大デジタル多目的ホールおよびコラボレーションルームにて開催された。本研究会は、日本原子力学会核データ部会が主催、日本原子力学会核データ部会、日本原子力学会「シグマ」特別専門委員会、日本原子力研究開発機構原子力基礎工学研究センター、東京工業大学科学技術創成研究院先導原子力研究所が共催した。今回、チュートリアルとして「核データ処理システム　FRENDY」を、特別講演として「原子力発電のこれから」を実施した。また講演・議論のセッションとして「核データ研究の現状と展望」、「炉物理研究の現状と展望」、「話題」、「核データ応用分野」、「国際セッション」、「核データ測定及び原子炉診断の新技術」、「新分野からのデータニーズ」の 7 件を企画し実施した。さらに、ポスターセッションでは、実験、評価、ベンチマーク、応用など、幅広い研究内容について発表が行われた。参加者総数は 82 名で、それぞれの口頭発表及びポスター発表では活発な質疑応答が行われた。本報告集は、本研究会における口頭発表 13 件、ポスター発表 22 件の論文をまとめている。

キーワード: 2018 年度核データ研究会、実験、核理論、核データ評価、ベンチマークテスト、核データ応用

原子力科学研究所：〒319-1195 茨城県那珂郡東海村大字白方 2-4
*東京工業大学

Contents

Poster Session

目次

ポスター発表論文

1 Program of 2018 Symposium on Nuclear Data

Date: November 29 - 30, 2018
Venue: Multi-Purpose Digital Hall (Main Venue) & Collaboration Room (Poster Session)
(Ookayama Campus, Tokyo Institute of Technology, Meguro, Tokyo)
Co-Host:Nuclear Data Division, AESJ
Special Committee for Nuclear Data, AESJ
Nuclear Science and Engineering Center, Japan Atomic Energy Agency
Laboratory for Advanced Nuclear Energy, Institute of Innovative Research,
Tokyo Institute of Technology

November 29(Thur.)

9：30- Registration at the entrance of Multi-Purpose Digital Hall
Party fee: 6000 yen(General)/2000 yen(Student)
10:00-10:10 **Opening** Fukahori, Tokio (Director of Nuclear Data Division)
Announcement Chiba, Satoshi (Tokyo Tech)

Session 1 Nuclear Data and Future Perspectives(Chair: Shigyo, Nobuhiro(Kyushu Univ.))

10:10-10:40 Iwamoto, Osamu (JAEA)
Status and future plan of JENDL
10:40-11:10 Watanabe, Yukinobu (Kyushu Univ.)
Progress of Nuclear Data Research in the ImPACT Program on Reduction and Resource Recycling of High-level Radioactive Wastes through Nuclear Transmutation
11:10-11:40 Seung-Woo Hong (Sungkyunkwan University, Korea)
Status of RAON and nuclear data production system

11:40-12:40 Lunch

12：40-14:00 Poster Session at Collaboration Room

Session 2 Current Status and Future Perspectives of Reactor Physics
(Chair: Nakajima, Ken (Kyoto Univ.))

14:00-14:30 Chiba, Go (Hokkaido Univ.)
Needs and application of covariance data
14:30-15:00 Yamamoto, Akio (Nagoya Univ.)
Development of GENESIS, a three-dimensional transport code in heterogeneous geometry

15:00-15:10 Break

Tutorial (Chair: Chiba, Go (Hokkaido Univ.))

15:10-16:20 Tada, Kenichi (JAEA)
Development of nuclear data processing code FRENDY

16:20-16:40 Conference Photo, Break

Session 3 Topics (Chair: Utsuno, Yutaka (JAEA))

16:40-17:10 Sumiyoshi, Kohsuke (Numazu CT)
Neutrino transport by Sn method and supernovae

17:10-17:40 Fukahori, Tokio (JAEA)
Intermediate Energy Nuclear Data and Related International Collaboration
18:00- Convivial Gathering (Moving to the venue on foot)
1F of EEI building, Ookayama Campus, Tokyo Tech)

November 30(Fri.)

Session 4 Nuclear Data Applications (Chair: Katabuchi, Tatsuya (Tokyo Tech))
9:00- 9:30 Tanaka, Kenichi (IAE)
Requests from characterization for decomissioning to nuclear data
9:30-10:00 Nauchi, Yasushi (CRIEPI)
Nuclear data required for measurements of reactivity and nuclear material composition
10:00-10:30 Toh, Yosuke (JAEA) Development of Active Neutron NDA System

10:30-10:40 Break

Session 5 International Session (Chair: Fukahori, Tokio (JAEA))
10:40-11:10 Paraskevi (Vivian) Dimitriou (IAEA)
Nuclear Structure and Decay Data Libraries: current status and perspectives
11:10-11:40 Kawano, Toshihiko (LANL)
CoH_3:The Coupled-Channels and Hauser-Feshbach Code

11:40-13:00 Lunch

Session 6 Nuclear Data Measurements and New Technology for Nuclear Reactor Diagnosis (Chair: Hori, Junichi (Kyoto Univ.))
13:00-13:30 Nishio, Katsuhisa (JAEA)
Fission data from multi-nucleon transfer reactions
13:30-14:00 Okada, Kohichi (HITACHI)
Reactor power monitoring using neutron induced prompt gamma ray

14:00-14:10 Break

Special Lecture (Chair: Chiba, Satoshi (Tokyo Tech))
14:10-15:20 Omoto, Akira (Tokyo Tech/Former Member of JAEC)
What the future holds for Nuclear Energy

15:20-15:30 Break

Session 7 Data Needs from New Fields (Chair: Iwamoto, Osamu (JAEA))
15:30-16:00 Sagara, Hiroshi (Tokyo Tech)
Nuclear Security and Nuclear Data (tentative title) 16:00-16:30 Asano, Hidekazu (RWMC)
Geological disposal of high-level radioactive waste; long-term safety and reduction of environmental impact

16:30- **Poster Award Ceremony** Fukahori, Tokio
(Director of Nuclear Data Division)
Closing Watanabe, Yukinobu
(Chair of Executive Comittiee for Next Symposium)

Poster session list

PA: candidates for poster award,　PB: not candidates for poster award

PA1　ロビラ レベロニ ジェラルド　Rovira Leveroni, Gerard
Measurement of the Neutron Capture Cross Section of 237Np Using ANNRI at MLF/J-PARC

PA2　山口 雄司　Yuji Yamaguchi
180 度近傍における中エネルギー(p, p'x)反応の二重微分断面積
Double-Differential Cross Sections in the Vicinity of 180 Degrees for Medium-Energy (p, p'x) Reactions

PA3　今村 亮太　Ryota Imamura
70 MeV 陽子入射反応における 2 次陽子の低エネルギー下限スペクトル測定
Measurement of Low Threshold Energy Spectra of Secondary Protons for 70-MeV Proton-Induced Reactions

PA4　石井 葉子　Yoko Ishii
反対称化分子動力学を用いる重イオン多核子移行反応の研究
Study on heavy-induced multinucleon transfer reaction by antisymmetrized molecular dynamics

PA5　佐藤 俊輔　Shunsuke Sato
^{93}Zr、^{107}Pd 標的に対する陽子及び重陽子入射核破砕反応における準位密度の odd-even staggering への影響
Effect of the level density on the odd-even staggering in proton- and deuteron-induced spallation reactions on ^{93}Zr and ^{107}Pd

PA6　竹下 隼人　Hayato Takeshita
LiF, C, Si, Ni, Mo, Ta 標的に対する 13.4 MeV 重陽子入射中性子収量の測定
Measurement of thick target neutron yields from 13.4-MeV deuteron bombardment on LiF, C, Si, Ni, Mo and Ta

PA7　藤原 有規　Yuki Fujiwara
14 MeV 中性子による粉体ターゲットの後方散乱断面積ベンチマーク実験の検討
Examination of benchmark experiment for large angle scattering reaction cross section at 14 MeV for a flake target

PA8　山口 篤輝　Atsuki Yamaguchi
二つのシャドーバーを用いた鉄の 14MeV 中性子後方散乱断面積ベンチマーク実験
Benchmark experiment of large angle scattering reaction cross section of iron at 14MeV using two shadow bars

PA9 江幡 修一郎 Shuichiro Ebata
Microscopic calculations for the charge polarization of fission fragments

PA10 田中 翔也 Tanaka Shoya
マルチチャンス核分裂を採用した高励起エネルギー核分裂の理論研究 Theoretical study on fission process at high excitation energy with a concept of multi-chance fission

PA11 椿原 康介 Kohsuke Tsubakihara
殻補正効果を考慮した核分裂収率の評価法
The Evaluation Method for Independent Yield Including the Effect of the Shell Correction

PA12 牧永 あや乃（講演取消し） Ayano Makinaga(Cancelled)
ヘリウム・陽子線ハイブリッド型粒子線治療に必要な核データの検討
Nuclear data required for the helium-proton hybrid type particle therapy

PA13 ケアン クン ラタ Kean Kun Ratha
Fission Barrier Heights of Actinide Nuclei Obtained in Multi-Nucleon Transfer Reactions of $^{18}O+^{237}Np$

PA14 中尾 慎人 Makoto Nakao
中重核のアルファクラスター構造と双極子励起
Alpha cluster structures and dipole excitations in medium-heavy nuclei

PA: candidates for poster award, PB: not candidates for poster award

PB1 リー ジョンヨン Lee, Jeongyeon
Cl-35、Cl-36、および Cl-37 における中性子誘起反応の評価
Evaluations of neutron induced reactions on Cl-35, Cl-36, and Cl-37

PB2 西川 崇 Takashi Nishikawa
TDDFT + Langevin 模型で探るエネルギー散逸の起源
TDDFT + Langevin calculation for the origin of dissipation

PB3 小浦 寛之 Hiroyuki Koura
核図表 2018 のためのコンパイレーション; 包括的な崩壊データ
Compilation for Chart of the Nuclides 2018: a comprehensive decay data

PB4 西川 崇 Takashi Nishikawa
拘束ハートレーフォック計算に基づく、原子核媒質効果の核分裂障壁への影響
Nuclear medium effects on the fission barrier height based on the Constrained Hartree Fock calculatons

PB5 中野 正博 Masahiro Nakano
Total Reaction Cross Sections below 50MeV Based on the Intra-Nuclear Cascade Model

PB6 今野 力 Chikara Konno
TENDL-2015 公式 ACE ファイルの問題
Problems of TENDL-2015 official ACE files

PB7 湊 太志 Futoshi Minato
奇数個の中性子数を持つ Ni 同位体のガモフテラー遷移分布
Gamow-Teller Strength Distribution of Nickel Isotopes with Odd Neutrons

PB8 李 在洪 Lee Jaehong
固体減速材における温度依存熱中性子スペクトル測定のための予備実験
Preliminary Experiment for Temperature-dependent Thermal Neutron Spectrum in Solid Moderator

PB9 合川 正幸 Masayuki Aikawa
^{89}Y 標的への重陽子入射反応による ^{89}Zr 生成反応断面積
Production cross sections of ^{89}Zr by deuteron-induced reactions on ^{89}Y

PB10 石塚 知香子 Chikako Ishizuka
4 次元ランジュバン模型を用いた中性子欠損水銀同位体の核分裂
Nuclear fission of the neutron-deficient mercury isotopes using 4D-Langevin model

PB11 片渕竜也 Tatsuya Katabuchi
核変換システム開発のための長寿命マイナーアクチニドの中性子捕獲反応データ測定
Neutron capture data measurement of long-lived minor actinides for study on nuclear transmutation system

PB12 稲倉 恒法 Tsunenori Inakura
コンクリート深層透過問題に対する断面積誤差の影響評価
Propagation of uncertainties of 28Si cross section to neutron dose in deep concrete penetration

PB13 ウラディーミル リトネフスキー Vladimir Litnevsky
Description of the mass-asymmetric fission of the Pt isotopes, obtained in the reaction ^{36}Ar + ^{142}Nd, within the two-stage fusion-fission model

PB14 奥村 森 Shin Okumura
Hauser-Feshbach 統計崩壊とベータ崩壊による独立・累積核分裂収率の計算
Independent and Cumulative Fission Product Yield Calculations with Hauser-Feshbach Theory and Beta Decay

PB15　木村 真明　Masaaki Kimura

核応答で観るクラスター共鳴

Cluster resonances probed by nuclear responses

2 Status and future plan of JENDL

Osamu IWAMOTO
Nuclear Data Center, Japan Atomic Energy Agency
Tokai-mura, Naka-gun, Ibaraki-ken 319-1195 Japan
e-mail: iwamoto.osamu@jaea.go.jp

Status and future plan of JENDL special- and general-purpose files are briefly reported. Regarding the special purpose files, two files of JENDL/AD-2017 and JENDL/PD-2016 were released recently. Concerning the general-purpose file, the next version, JENDL-5, is under development. In addition to the revision over a wide range of the data of JENDL-4.0, new evaluations covering whole stable isotopes are planned. Charged particle induced reaction data will be included to meet the needs of various fields of applications.

1. Introduction

Since the release of JENDL-1 [1] in 1977, JENDL general-purpose files have been gradually updated. The latest version JENDL-4.0 [2] was made open to the public in 2010. In addition to the intensive update of the nuclear data of fission products and minor actinides, it is notable that covariance data were given over all actinides in JENDL-4.0. It was one of the most advanced evaluated nuclear data libraries in the world at that time. However, more than 8 years have already passed and a lot of new knowledge about the nuclear data have been accumulated. It was desired to integrate them and strengthen the completeness of the covariance data to meet the needs from various application fields such as nuclear reactor safety, reduction of high-level radioactive waste, decommissioning of nuclear facility, development of accelerator-related systems and so on. Nuclear Data Center of JAEA is planning to develop the next version of the general-purpose file, JENDL-5.

In addition to the general-purpose file, special purpose files for photonuclear reactions and activation cross sections were recently released as JENDL/PD-2016 [3] and JENDL/AD-2017 [4] to meet the needs of electron accelerator application and the decommissioning of nuclear facilities, respectively.

2. Special purpose file

2.1 JENDL/AD-2017

JENDL Activation Cross Section File for Nuclear Decommissioning 2017 (JENDL/AD-2017), has been developed [4]. The new activation file is focused on the needs of radioactive inventory evaluation on decommissioning of nuclear facilities. Based on the 221 RIs which are important for dose and clearance

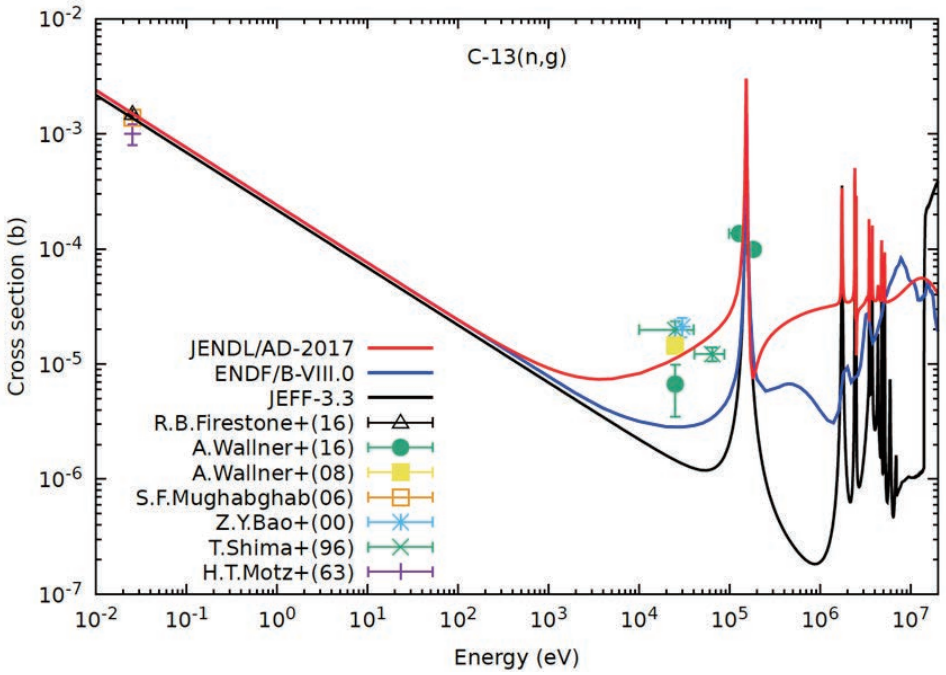

Fig. 1 Neutron capture cross section of ^{13}C

evaluations, 311 nuclides were selected for the target nuclei of the file by taking account of the possibility of production of the RIs through nuclear reactions in nuclear reactor facilities. It includes not only nuclides of structure materials and concrete shields but also nuclides contained in control rods and radiation shielding with heavy nuclei. The evaluations were performed by reflecting the up-to-date knowledges of the measurements and theories. Figure 1 shows the neutron capture cross section of ^{13}C. The data of JENDL/AD-2017 was evaluated by taking account direct capture contributions interfering with resonances.

2.2 JENDL/PD-2016

Previous version of JENDL Photonuclear Data File, JENDL/PD-2004 [5], contains the data for the isotopes of the wide range of the elements from Z=1 to 93. However, the number of isotopes is limitted to 68. A new version of JENDL/PD have been developed with increasing the number of nuclei as well as updating the data on the basis of the up-to-date experimental and theoretical knowledges. They were released as JENDL/PD-2016 providing the data for nuclides from Z=1 to Z=103 from photon energy range from 1 to 140 MeV [3]. JENDL/PD-2016 contains the data of various photon induced reaction cross sections such as absorption, fission, and particle and residual-nuclide productions. It also gives the data related to energy-angle distributions of particle emissions. JENDL/PD-2016 provides data in two versions, *i.e.* the standard version which contains the data for 181 nuclides along the beta-stability line, and the expanded version which includes the data mainly based on model calculations for 2681 nuclides covering a wide range of unstable ones in addition to the data of the standard version.

3. General purpose file

Development of next version of general-purpose file JENDL-5 is in progress. It is intended to improve reliability and completeness for various applications. Revision of the data will be performed over a wide range of nuclei covering light nuclei, structural materials, fission products and actinides. To meet the needs of various fields of applications, data of all stable isotopes will be prepared. Enhancement of covariance data is one of the main targets of JENDL-5. The general-purpose files until JENDL-4.0 have been developed with emphasizing on the applications related to neutron transportation in reactors or other facilities, and data for the other purposes were provided by various special purpose files. It means the general-purpose files still have some restriction in application, and it might cause confusion to users. In developing JENDL-5, we are stepping forward to merge the special purpose files to make it simple to use as possible. As the first step, isomer production cross sections will be added to the newly evaluated data in JENDL-5 for the backend application that needs to evaluate activation inventories. In addition to the neutron induced reaction, the data induced by other particles such as proton and deuteron will be included in JENDL-5 to broaden the applications of JENDL.

For the evaluation of light nuclei, a new R-matrix code, AMUR [6], has been developed and applied to the neutron induced reaction of ^{16}O, ^{15}N and ^{19}F. Their covariance data are also deduced by the R-matrix analysis. The neutron reaction data for structure materials such as Cu, Zr and Nb isotopes were evaluated [7, 8, 9]. The data of many nuclides of fission products were revised in JENDL-4.0. Remaining data of fission products have been updated to complete the revision of the data with applying the modern nuclear reaction codes such as CCONE [10, 11] and POD [12]. Intensive studies for the accuracy

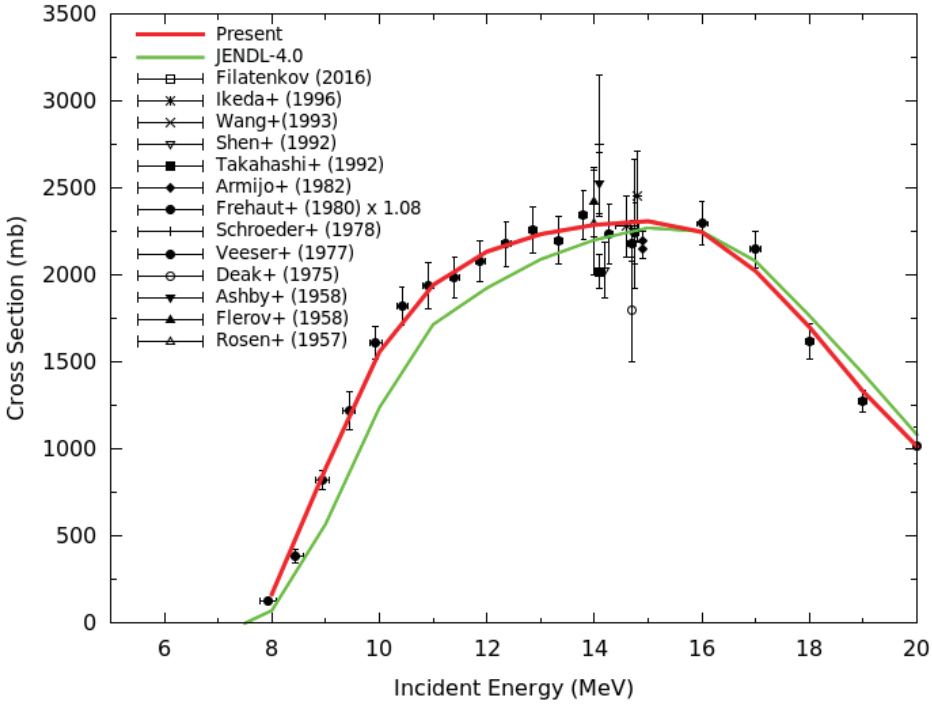

Fig. 2 Evaluated cross section of (n,2n) reaction on ^{209}Bi

improvements of minor actinide nuclear data were conducted under the framework of AIMAC projects [13]. New experimental data of $^{241, 243}$Am at resonance region were obtained by ANNRI at J-PARC and resonance analyses were performed with those data. Other new evaluation efforts are also in progress. Data of Bi are required for the nuclear transmutation of radioactive wastes by ADS. Neutron reaction cross sections are being evaluated by CCONE. Figure 2 shows the preliminary result of ^{209}Bi (n,2n) cross section. It improves the agreement with experimental data significantly.

The first test version, JENDL-5α1, was created in 2018. It includes the updated and newly-evaluated data for more than 90 isotopes of Ga, Zr, Nb, Tc, Ru, Sb, Te, I, Pr, Gd, Er, Ta, Re, Pt, Hg, Tl, U, Pu and Am. Regarding the major actinides, the results of the resonance parameters evaluated in the framework of the recent international collaboration CIELO [14] were taken for testing. A new evaluation of thermal scattering law data for light water done by Abe *et al.* [15] has been adopted. The benchmark testing of JENDL-5α1 for reactors and shielding is in progress.

4. Conclusion

Recent progress and future plan of JENDL are briefly reported. As the next version of general-purpose file, JENDL-5 is under development. It is planned to be released in FY 2021. It will include newly evaluated data for light nuclei and structure materials with covariance data. Data of the fission products and the actinides will be revised as well. Isomer productions and charged particle induced data will be contained to broaden the possible applications. Recently released two special purpose files JENDL/PD-2016 and JENDL/AD-2017 are also mentioned.

References

[1] S. Igarashi, T. Nakagawa, K. Kikuchi, T. Asami, T. Narita,“Japanese Evaliuated Nuclear Data Library, Version-1 – JENDL-1 –”, JAERI 1261 (1979).

[2] K. Shibata, O. Iwamoto, T. Nakagawa, N. Iwamoto, A. Ichihara, S. Kunieda, S. Chiba, K. Furutaka, N. Otuka, T. Ohsawa, T. Murata, H. Matsunobu, A. Zukeran, S. Kamada, and J. Katakura:“JENDL-4.0: A New Library for Nuclear Science and Engineering”, *J. Nucl. Sci. Technol.* **48**(1), 1-30 (2011).

[3] N. Iwamoto, K. Kosako, T. Murata“Photonuclear Data File”, JAEA-Conf 2016-004, 53-58 (2016).

[4] K. Shibata, N. Iwamoto, S. Kunieda, F. Minato, O. Iwamoto,“Activation Cross-section File for Decommissioning of LWRs”, JAEA-Conf 2016-004, 47-52 (2016).

[5] N. Kishida et al.,“JENDL Photonuclear Data File”, Proceedings of International Conference on Nuclear Data for Science and Technology, Santa Fe, New Mexico, USA, Sep. 26 - Oct. 1, 2004, **1**, 199 (2004).

[6] S. Kunieda, “Status of the R-matrix Code AMUR toward a consistent cross-section evaluation and covariance analysis for the light nuclei”, *EPJ Web of Conferences* **146**, 12029 (2017).

[7] N. Nakayama, “Calculation of neutron cross-sections on copper-63 and -65”, *J. Nucl. Sci. Technol*. **55**(6), 614-622 (2018).

[8] A. Ichihara, “Theoretical calculation of neutron cross sections for ^{90,91,92,94,96}Zr in the incident energy range between 200 keV and 20 MeV”, *J. Nucl. Sci. Technol*. **55**(9), 1087-1098 (2018).

[9] A. Ichihara, “Calculation of cross sections for metastable state production in the (n,γ), (n,n'), (n,2n) and (n,3n) reactions of ^{93}Nb”, *J. Nucl. Sci. Technol*. **53**(12), 2049-2055 (2016).

[10] O. Iwamoto, “Development of a Comprehensive Code for Nuclear Data Evaluation, CCONE, and Validation Using Neutron-Induced Cross Sections for Uranium Isotopes”, *J. Nucl. Sci. Technol.* **44**(5), 687-698 (2007).

[11] O. Iwamoto, N. Iwamoto, S. Kunieda, F. Minato, K. Shibata, “The CCONE Code System and its Application to Nuclear Data Evaluation for Fission and Other Reactions”, *Nucl. Data Sheets* **131**, 259-288 (2016).

[12] A. Ichihara, O. Iwamoto, S. Chiba, S. Kunieda, K. Shibata, “Program POD; A Computer code to calculate cross sections for neutron-induced nuclear reactions”, JAEA-Data/Code 2007-012 (2007).

[13] H. Harada, O. Iwamoto, N. Iwamoto, A. Kimura, K. Terada, T. Nakao, S. Nakamura, K. Mizuyama, M. Igashira, T. Katabuchi, T. Sano, Y. Shibahara, Y. Takahashi, K. Takamiya, C. H. Pyeon, S. Fukutani, T. Fujii, J. Hori, H. Yashima, “Research and development for accuracy improvement of neutron nuclear data on minor actinides”, *EPJ Web of Conferences* **146**, 11001 (2017).

[14] M.B. Chadwick *et al.*, “CIELO Collaboration Summary Results: International Evaluations of Neutron Reactions on Uranium, Plutonium, Iron, Oxygen and Hydrogen”, *Nucl. Data Sheets* **148**, 189-213 (2018).

[15] Y. Abe, “Evaluation of the neutron scattering cross-section for light water by molecular dynamics”, *Nucl. Instrum. methods Phys. Res. A* **735**, 568-573 (2014).

This is a blank page.

3 Progress of Nuclear Data Research in the ImPACT Program on Reduction and Resource Recycling of High-level Radioactive Wastes through Nuclear Transmutation

Yukinobu WATANABE

[1]*Faculty of Engineering Sciences, Kyushu University, 6-1 Kasuga, Fukuoka 816-8580, Japan*

E-mail: watanabe@aees.kyushu-u.ac.jp

The ImPACT Fujita Program (JFY2014-2018) has been conducted to propose a new option of reduction and resource recycling of high-level radioactive wastes through nuclear transmutation of long-lived fission products (LLFPs) without isotope separation. The progress of basic research and development on nuclear data in the ImPACT program is overviewed.

This work was funded by ImPACT Program of Council for Science, Technology and Innovation (Cabinet Office, Government of Japan).

1. Introduction

Nuclear waste disposal of high-level radioactive waste (HLW) produced when the spent nuclear fuel is reprocessed is a crucial issue in nuclear power generation. As HLW contains nuclides with a long half-life, public concern remains over the long-term storage of HLW. Research and development of the safe treatment methods to transform HLW into short-lived and/or low-toxic materials are strongly desired. Nuclear transmutation is expected to be one of the promising methods for reduction of HLW. Under the above situations, the ImPACT Fujita Program (JFY2014-2018) [1,2] started five years ago in order to explore a new transmutation path of long lived fission products (LLFPs) contained in HLW, for which disposal in the deep layer has been the only option. Here, ImPACT is an abbreviation of Impulsing PAradigm Change through disruptive Technology by Cabinet Office, Government of Japan, which is a program through which the Council for Science, Technology and Innovation will encourage high-risk, high-impact R&D, and aim to realize a sustainable and expandable innovation system [3].

The ImPACT Fujita Program is composed of the following five projects. Each project consists of multiple research topics:

- Project 1: Separation and Recovery Technologies
- Project 2: Nuclear Reaction Data Acquisition and Demonstration of Nuclear Transmutation
- Project 3: Reaction Theory Model and Simulation
- Project 4: Transmutation System and Elemental Technology
- Project 5: Scenario and Process Concept

In the present report, I will focus on Projects-2 and -3 and overview the progress of nuclear data research which has been conducted in close collaboration between researchers in nuclear physics and nuclear engineering communities.

2. Project-2

2.1 Overview

The aim of Project-2 is to acquire nuclear reaction data to propose an effective reaction path for reduction and resource recycling of LLFPs through nuclear transmutation with accelerator. New experimental data have been measured by using innovative measurement techniques at high performance accelerator facilities such as RIKEN RI Beam Facility and J-PARC. The role of Project-2 is of essential importance in the ImPACT program because the accuracy of nuclear data has an impact on the feasibility study of transmutation system.

The major subjects of this project are composed of the following research subjects: (a) Neutron knockout (RIKEN), (b) Fast neutron induced spallation (Kyushu U.), (c) Coulomb breakup (TIT), (d) Negative muon capture reaction (RIKEN), (e) Neutron capture (JAEA), and (f) Low-speed RI beam (U. of Tokyo, RIKEN). Fig. 1 illustrates a full picture of these measurement subjects.

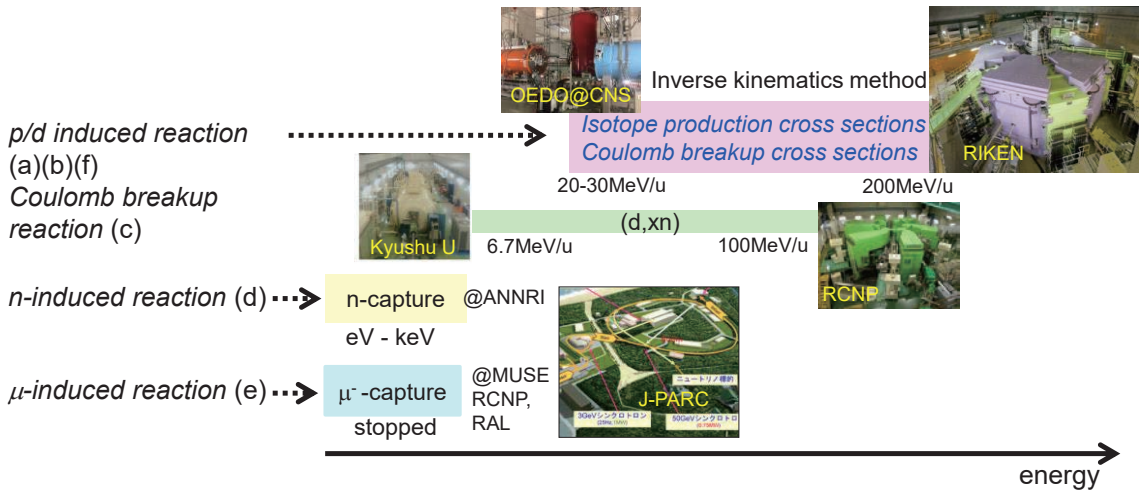

Fig. 1. Overview of nuclear data measurements conducted in the ImPACT Fujita program

In the research subjects (a), (b) and (c), a series of experiments have been conducted at the RIKEN RI Beam Facility (RIBF). The inverse kinematic technique has been applied to systematic measurements of isotopic production cross sections for proton and deuteron induced spallation reactions on LLFP nuclides (^{79}Se, ^{93}Zr, ^{107}Pd, ^{126}Sn, ^{135}Cs) at 50, 100, and 200 MeV/u [4,5,6] as well as Coulomb breakup reactions on ^{93,94}Zr at 200 MeV/u [7]. The mesaurement of isotopic production cross sections for ^{93}Zr will be described below.

In the subject (f), a new beam line with the Optimized Energy Degrating Optics for RI beams (OEDO) [8] has been developed at RIBF to obtain the LLFP beam of around 20-30 MeV/u. Two experiments were conducted for the proton and deuteron induced reactions on ^{93}Zr and ^{107}Pd at 20-30 MeV/u and the ^{77,79}Se(d,p) reactions as a surrogate for the ^{79}Se(n,γ)^{80}Se reaction. The preliminary results are reported in Ref.[9].

Fast neutron capture cross sections of ^{135}Cs were measured using ANNRI at J-PARC MLF in the subject

(e)[10], and themal neutron cross sections were also mesaured by an activation method at Kyoto Univeristy Research Reactor facility. Moreover, measurement of activation cross sections by negative muon capture reactions on ^{107}Pd was condcuted at J-PARC MUSE [11] and neutrons produced by muon capture reaction were measured at RCNP MuSIC facility in order to consider an innovative utilization of negative muons for nuclear transmutation in the research subject (d).

In the subject (b), deuteron-induced neutron production data were also measured at two accelerator facilities, CABAS (Kyushu U.) and RCNP (Osaka U.), for the desigh of accelerator neutron sources for nuclear transmutation. The results will be reported below.

The Project-2 also includes a demonstartion experiment of nuclear transmutaion. An enriched ^{107}Pd target was fabricated using an ion implantation apparatus, and it was irradiated by intense 24-MeV deuteron beams for a long period to demonstrate stable isotope production exerimentally. The irradaition test is still in progress.

2.2 Isotopic production cross section of proton- and deuteron-induced reactions on ^{93}Zr

Measurements of isotopic production cross sections for proton- and deuteron-induced reactions on ^{93}Zr at 50, 105, and 209 MeV/u were carried out using the inverse kinematics technique at RIBF. A secondary beam including ^{93}Zr was produced by in-flight fission of a ^{238}U beam at 345 MeV/u on a ^{9}Be production target and separated by using the BigRIPS in-flight separator. Then the secondary beam bombarded CH_2, CD_2, and pure C targets and the fragments produced through the spallation reaction were identified event-by-event by using the ZeroDegree spectrometer in the 105-MeV/u experiment [5]. A liquid hydrogen and deuterium target was employed in the 200-MeV/u experiment [6] and particle identification of reaction products was performed by using the SAMURAI spectrometer. In the lowest energy 50-MeV experiment, a hydrogen and deuterium gas target and the ZeroDegree spectrometer for particle identification were used. The measured isotopic production cross sections for the proton-induced reaction are shown and compared with the calculated ones with PHITS [12] in Fig. 2. The PHITS calculation is in overall agreement with the measured cross sections.

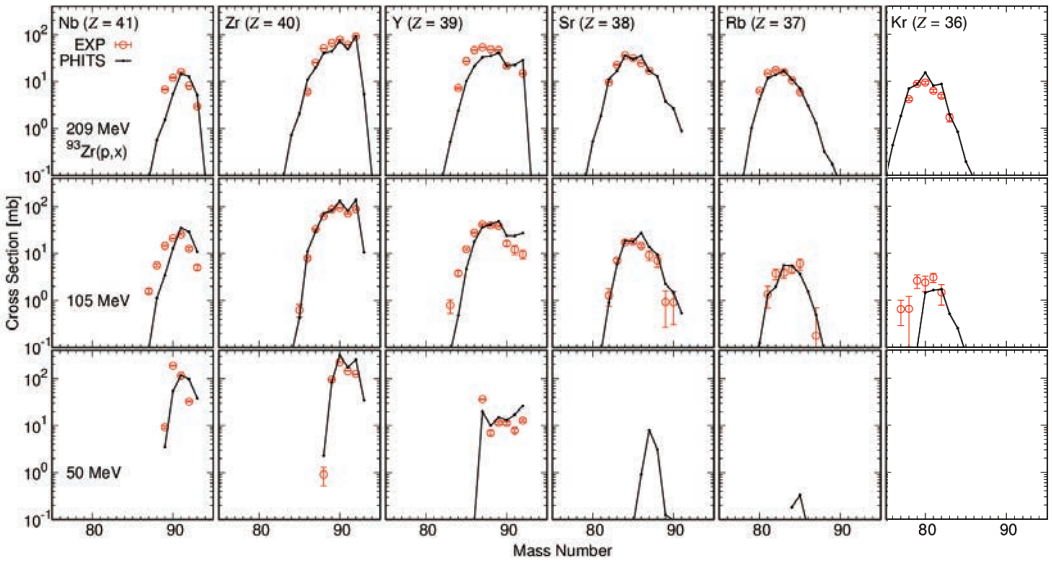

Fig. 2. Isotopic production cross sections of the proton- and deuteron-induced reactions on ^{93}Zr at 50, 105, and 209 MeV/u

2.3 Neutron production in deuteron-induced reactions

Two experiments were conducted to study neutron production in deuteron-induced reactions for the design of accelerator-based neutron sources. Double-differential neutron production cross sections (DDXs) for deuteron-induced reactions on Li, Be, C, Al, Cu, Nb, In, Ta, and Au at 200 MeV were measured at forward angles ≤ 25° by means of a time of flight (TOF) method with EJ301 liquid organic scintillators at RCNP, Osaka University [13]. The measured DDXs for Li are shown in the left panel of Fig. 3. A characteristic broad peak is clearly observed around half the incident energy, which is caused by deuteron breakup processes. Experimental data of thick target neutron yields (TTNYs) from 13.4-MeV deuteron bombardment on C, LiF, Si, Ni, Mo, and Ta were also taken using an EJ301 detector at CABAS, Kyushu University [14]. The TTNYs measured at 0 degree are plotted in the right panel of Fig.3. The incident energy and targets were chosen to compare the available triton-induced TTNY data [15] at the same incident energy per nucleon. The spectral shape and magnitude are found to depend strongly on the target atomic number. Theoretical model analyses for these experimental data were performed using DEURACS [16].

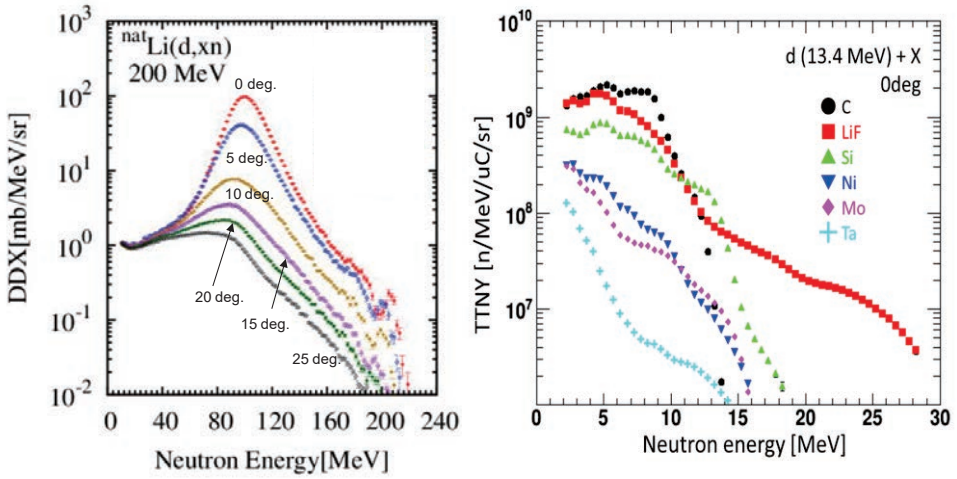

Fig. 3. Neutron production from deuteron-induced reactions. Double differential cross sections of the Li(d,xn) reaction at 200 MeV(left panel), and thick target neutron yields from 13.4-MeV deuteron bombardment on C, LiF, Si, Ni, Mo, and Ta (right panel).

3. Project-3

The aim of Project-3 is to explore optimal reaction paths based on engineering consideration in which transmutation rates, heat generation, radiation damage, and so on are estimated by simulation with PHITS. Various works on nuclear physics and nuclear data have so far been performed to improve the predictive power of PHITS. The project-3 consists of the following five research subjects: (a) Reaction theory (Osaka U.), (b) Structure theory (U. of Tsukuba), (c) Nuclear data evaluation (JAEA), (d) Nuclear reaction simulation (RIST), and (e) Nuclear data compilation (Hokkaido U.). A correlation chart of individual research subjects is shown in Fig.4. To use the measured isotopic production cross sections in PHITS, a new option with a data file "Ndata" and "FragData" in which the experimental data are stored was incorporated in the Yield tally of PHITS. As a result, we can discuss an impact of nuclear data on PHITS simulation for a macroscopic system by comparing the simulation with experimental data and that with implemented nuclear models.

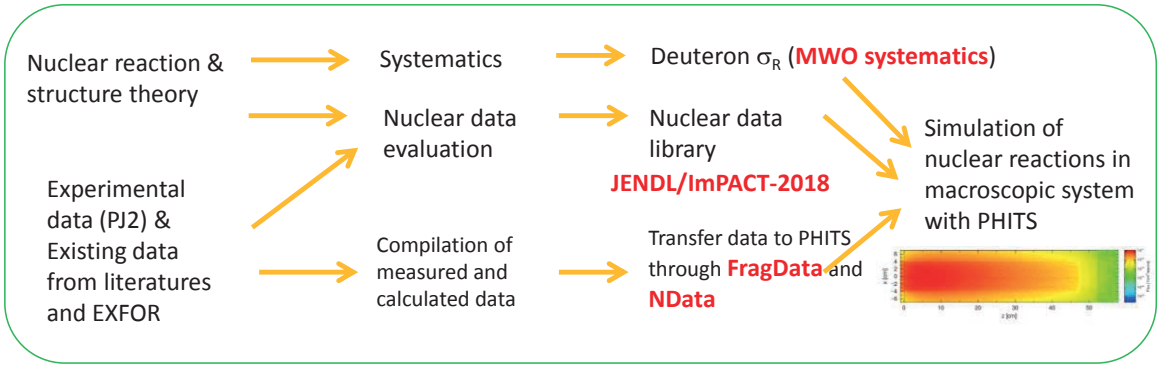

Fig. 4. Overview of Project-3

Cross section calculations based on microscopic effectve reaction theory were also applied to production of nuclear data. One of the examples is a new MWO systematics [17] of total reaction cross sections for deuteron, which was implemented in PHITS. Physical quantities related to nuclear structure such as level density and gamma strength function are improtant in statitcal model calculations. Although phenomelogical approach with optimized parameters based on stable nuclei were used in the past evaluation of JENDL, its application to unstable nuclei such as LLFPs is not necessarily validated. The results of microscopic approaches to nuclear strucuture and reactions were reflected in cross section calculations: for instance, the Finite-Temperature Hartree-Fock-Bogoliubov (FTHFB) calculation executed by the HFBTHO code [18] in estimation of the level density of deformed states [19] and the canonical-basis time-dependent Hartree-Fock-Bogoliubov (Cb-TDHFB) model [20] for calculation of γ- strength function.

Development of a new evaluated nuclear data library of LLFPs, called JENDL/ImPACT-2018 [21], is one of the noteworthy achievements in Project-3. The above-mentioned results were integrated into the CCONE code [22] that had been developed for nuclear data evaluation. Then isotopic production cross sections and energy-angular distributions of secondary particles in neutron and proton induced reactions up to 200 MeV were evaluated using the CCONE code. Finally, JENDL/ImPACT-2018 was produced for total 32 elements and 163 nuclides ranging from the atomic number Z= 25 to 56 including LLFPs (^{79}Se, ^{93}Zr, ^{107}Pd, and ^{135}Cs).

JENDL/ImPACT-2018 does not include deuteron induced reactions. The experimental data of Project-2 indicates some advantages of deuteron-induced reaction in nuclear transmutation with spallation reaction as well as fast neutron production. The DEUteron-induced Reaction Analysis Code System (DEURACS) was successfully applied to model calculations of deuteron-induced spallation reactions on ^{93}Zr (Fig.2) and ^{107}Pd [16] as well as the Li(d,xn) reaction (Fig. 3) [13].

4. Summary

This report focuses on the nuclear data research in the ImPACT Fujita program on reduction and resource recycling of high-level radioactive wastes through nuclear transmutation and the progress of Project 2 (Nuclear Reaction Data Acquisition and Demonstration of Nuclear Transmutation) and Project-3 (Reaction Theory Model and Simulation) is outlined. In the ImPACT program, application-oriented research on nuclear data has been conducted in collaboration between nuclear physics and nuclear engineering communities in Japan. Particularly, the first large-scale collaboration in cross section measurements was successfully carried

out. As a result, the cross section data for LLFPs were measured at leading-edge accelerator facilities (RIKEN RIBF, J-PARC MLF, etc.), particularly by using the inverse kinematics method in RIKEN RIBF. Moreover, the evaluated nuclear data file "JENDL/ImPACT-2018" was developed by using the experimental data and advanced reaction theories in close collaboration between experiment and theory. Finally, this program has contributed to human resource development of young researchers and students and to personal exchange between nuclear physics and engineering communities.

References

[1] R. Fujita, J. of the Atomic Energy Society of Japan, **58**(2), 28-30 (2016) (in Japanese).

[2] R. Fujita, JAEA-Conf 2017-001, 5-7 (2017).

[3] https://www.jst.go.jp/impact/program/08.html (September 16, 2019).

[4] H. Wang *et al*., Prog. Theor. Exp. Phys. 2017, 021D01 (10 pages) (2017).

[5] S. Kawase *et al*., Prog. Theor. Exp. Phys. 2017, 093D03(10 pages) (2017).

[6] S. Kawase *et al*., JAEA-Conf 2018-001, 111-114 (2018).

[7] S. Takeuchi *et al*., Prog. Theor. Exp. Phys. 2019, 013D02 (2019).

[8] S. Michimasa *et al*., Prog. Theor. Exp. Phys. (2019), in press.

[9] N. Imai *et al*., JAEA-Conf 2018-001, 39-44 (2018).

[10] S. Nakamura *et al*., JAEA-Conf 2018-001, 199-204 (2018).

[11] T. Matsuzaki *et al*., KEK Progress Report 2018-2, 31-32 (2018); ibid., 71-72 (2018).

[12] T. Sato *et al*., J. Nucl. Sci. Technol. **55**, 684-690 (2018).

[13] H. Sadamatsu *et al*., JAEA-Conf 2018-001, 131-136 (2018).

[14] H. Takeshita *et al*., presented at 2018 Symp. on Nuclear Data, Nov. 29-30, 2018, Tokyo Institute of Technology, Japan

[15] M. Drosg and D.M. Drake, Nucl. Sci. Eng. **182**, 256-260 (2016).

[16] S. Nakayama *et al*., Phys. Rev. C **98**, 044606 (2018).

[17] K. Minomo, K. Washiyama, and K. Ogata, J. Nucl. Sci. Technol. **54**, 127-130 (2017).

[18] M.V. Stoitsov *et al*., Comp Phys Communications **184**, 1592-1604 (2013).

[19] N. Furutachi *et al*., to be published in J. Nucl. Sci. Technol. (2019).

[20] S. Ebata *et al*., Physical Review C **82**, 034306 (2010).

[21] S. Kunieda *et al*., to be published in J. Nucl. Sci. Technol. (2019).

[22] O. Iwamoto *et al*., Nucl. Data Sheets **131**, 259-288 (2016).

4 Needs and Application of Covariance Data

Go CHIBA
Graduate School of Engineering, Hokkaido University
Sapporo, Hokkaido, 060-8628 Japan
e-mail: go_chiba@eng.hokudai.ac.jp

Although significant efforts have been devoted to evaluation and application of covariance data of nuclear data so far, there remain several issues which should be addressed by experts working in the field of nuclear data. In Japanese nuclear data community, a new working-group has been established in the JENDL committee to tackle this. This paper describes currently-discussed issues about the covariance data.

1. Introduction

In Japan, there have been strong needs to reduce nuclear data-induced uncertainties of reactor physics parameters of fast neutron reactors, and efficient uses of integral data have been attempted. This has been attained by the nuclear data adjustment procedure based on the Bayesian theorem, and covariance data of nuclear data have been required to do this. The initial version of the adjusted nuclear data for fast reactors application, ADJ91, was developed in 1991 [1][2] and updating of adjusted nuclear data [3][4] have been carried out so far. Covariance data of nuclear data have been also revised and improved in Japanese evaluated nuclear data library JENDL, and the latest version JENDL-4.0 released in 2010 includes covariance data for 95 nuclides. In the neutronics design works in other advanced nuclear systems, such as accelerator-driven system (ADS), similar approach has been adopted and the covariance data have been utilized [5]. In thermal neutron reactors, uncertainties induced by numerical modeling and methods had been considered dominant in the past, but owing to the significant advancement of computers, sophisticated numerical methods can be applied at present, so impact of nuclear data-induced uncertainties on reactor physics parameters predictions has become relatively larger than the past. Uncertainty quantification works on thermal neutron reactors have been recently carried out and relevant covariance data of nuclear data are utilized [6][7].

As mentioned above, applications of covariance data of nuclear data have been significantly grown in the field of nuclear engineering, but there have been discussions about application of the covariance data to actual problems in recent years [8][9]. Some important notes about covariance data application are presented in the paper of the latest version of the ENDF/B library, ENDF/B-VIII.0 (Please see page 60 in Ref. [10]).

To attempt to obtain answers to questions raised through these discussions, collaborative works among experts on various fields in nuclear data such as measurement, evaluation and application are essential. Under this circumstance, a new working group (WG), the covariance

data use promotion WG, has been established in April 2018 in the JENDL committee, and it has started their three-year activity. The purposes of this WG are as follows:

- To specify unquantified or difficult-to-quantify nuclear data uncertainty,
- To specify nuclear data uncertainty which has been quantified, but whose reliability is unsatisfactory,
- To consider methods to validate covariance data,
- To discuss which actions should be taken to promote covariance data use in application fields, and
- To discuss how covariance data should be generated in evaluated nuclear data libraries when information of integral data testing is taken into account in the evaluation process.

In this manuscript, some points discussed in this WG will be described.

2. Three unknowns

Nuclear data are physical quantities and there should be true values, but generally it is impossible for us to know them. Thus, evaluated nuclear data should include some uncertainties, and quantified uncertainties are defined as covariance data. In most cases, there should be many origins of uncertainties of evaluated nuclear data, so these uncertainties (or unknowns) should be taken into account in covariance data evaluation process as much as possible.

While there have been many discussions about unknowns [8], here those are categorized into the following three: (1) known and considered unknowns, (2) known but unconsidered unknowns, and (3) unknown unknowns.

The first unknowns are well known and recognized by experts, and these are properly considered in the covariance data evaluation process.

The second unknowns are recognized, but not considered in the evaluation process. Unknowns which are difficult to quantify correspond to them. It is not impossible to consider these unknowns in the evaluation process if experts take some actions, but experts' technical judgement would be required in some cases.

The third unknowns are not yet recognized by experts, and those would be problematic when we apply the covariance data to realistic problems such as licensing of nuclear facilities. In such cases, the following question would be raised; *Is this facility safe even though there should be some unrecognized uncertainties?* This question should be general and not be limited in the field of nuclear data. Reference [11] provides some insightful suggestions: improvement of the resilience against unknown risks is important; evidence of quantified uncertainties can be enhanced by sensitivity analyses; new knowledges obtained during experiences should be paid attentions. In other words, continuous efforts to reduce the unknown unknowns, by using currently available information as much as possible, are important. [12]

3. Feedback of integral data testing to nuclear data evaluation and resulting covariance data

How to validate covariance data provided in evaluated nuclear data files would be one of important questions in actual applications. It would be possible to test covariance data by

checking statistical consistency among Calculation-to-Experiment (C/E) values and nuclear data-induced uncertainties in a set of integral data. However, it is impossible to do this for recent evaluated nuclear data files since information on integral data testing are taken into consideration in evaluation process of nuclear data files. Figure 1 shows C/E values and nuclear data-induced uncertainties of neutron multiplication factors of several small-sized fast critical assemblies. A nuclear data file ENDF/B-VII.1 is used here. C/E values are extremely close to unity under relatively large nuclear data-induced uncertainties. This is because of tuning made at the final stage of nuclear data evaluation process, and this is common for other recent nuclear data files.

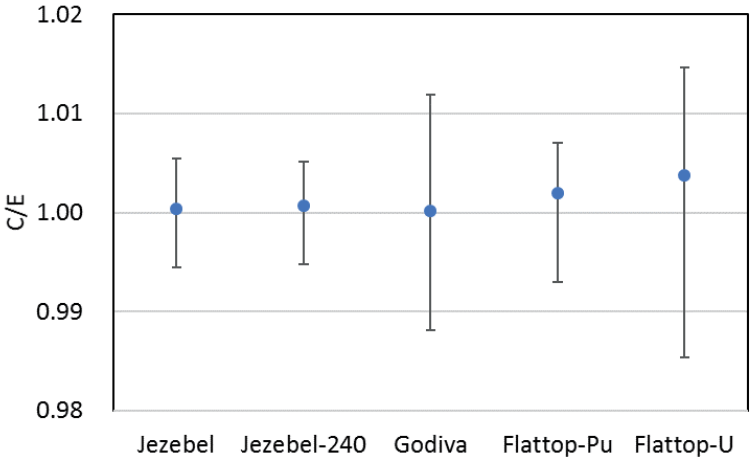

Fig.1 C/E values and nuclear data-induced uncertainties of fast critical assembly neutron multiplication factors

Systematic final tuning in nuclear data evaluation was initially adopted in the JENDL actinoid file-2008 development [13]. This was done with the maximum-likelihood method with the constraining covariance matrix. Tuning (or correction) of input parameters in nuclear data evaluation is quite small, but those can significantly improve performance in integral data testing of nuclear data as shown in Fig. 1. It was assumed that covariance data are unchanged through the tuning in the JENDL actinoid file-2008 case because the correction is slight, but this treatment is theoretically incorrect. Recent evaluated nuclear data files have adopted similar tuning, but this final tuning with integral data is not considered in the evaluation process of covariance data since the resulting covariance matrix becomes fully-correlated and huge-sized if it is done. This inconsistency between prediction accuracy and derived uncertainty is now discussed in the field of nuclear data.

4. Concluding remarks

In this paper, several issues have been presented to improve covariance data and to increase its reliability. It is hopefully expected that this can be addressed through activity of the JENDL covariance data use promotion WG established in the JENDL committee.

References

[1] M. Ishikawa, *et al.*: "Development of an adjusted group cross-section set for large LMFBR cores using the JUPITER analytical results", JAERI-M 93-046, p.36 (1993).

[2] M. Ishikawa, *et al.*: "Improvement of nuclear design method for large LMFBR cores using the cross-section adjustment", Proc. Int. Conf. Mathematical Methods and Supercomputing in Nuclear Application (M&C+SNA93), **1**, p.593 (1993).

[3] M. Ishikawa, *et al.*: "Development of a unified cross-section set ADJ2000 based on adjustment technique for fast reactor analysis", J. Nucl. Sci. Technol. Supplement **2**, p.1073 (2002).

[4] K. Sugino, *et al.*: "Development of a unified cross-section set ADJ2010 based on adjustment technique for fast reactor core design", J. Korean Phys. Soc., **59**, p.1357 (2011).

[5] H. Iwamoto, *et al.*: "Sensitivity and uncertainty analysis for a minor-actinoid transmuter with JENDL-4.0", Nucl. Data Sheets, **118**, p.519 (2014).

[6] A. Yamamoto, *et al.*: "Uncertainty quantification of LWR core characteristics using random sampling method", Nucl. Sci. Eng., **181**, p.160 (2015).

[7] G. Chiba, *et al.*: "Uncertainty quantification of neutron multiplication factors of light water reactor fuels during depletion", J. Nucl. Sci. Technol., **55**, p.1043 (2018).

[8] P. Talou: "Evaluating nuclear data and their uncertainties", EPJ Nucl. Sci. Technol., **4**, p.29 (2018).

[9] M. White, *et al.*: "By using lower limits, covariance are completely asinine", presented at Covariance Workshop 2017, CW2017, available at http://www.cw2017.com/Presentations.

[10] D.A. Brown, *et a*l.: "ENDF/B-VIII.0: The 8th major release of the nuclear reaction data library with CIELO-project cross sections, new standards and thermal scattering data", Nucl. Data Sheets, **148**, p.1 (2018).

[11] A. Yamaguchi: "Nuclear energy risk and scientific decision making: Is this facility safe even though there should be some unrecognized uncertainties?", available at http://www.canon-igs.org/event/report/161122_yamaguchi_document.pdf (in Japanese)

[12] A. Yamamoto: private communication.

[13] O. Iwamoto, *et al.*: "JENDL actinoid file 2008", J. Nucl. Sci. Technol., **46**, p.510 (2009).

5 **Development of GENESIS, a general Three-dimensional Transport Code based on the Legendre Polynomial Expansion of Angular Flux Method**

Akio YAMAMOTO, Akinori GIHO, Tomohiro ENDO
Graduate School of Engineering, Nagoya University
Furo-cho, Chikusa-ku, Nagoya, 464-8603 Japan
e-mail: a-yamamoto@energy.nagoya-u.ac.jp

Outline of the GENESIS code, which is a general three-dimensional transport code based on the Legendre polynomial Expansion of Angular Flux method, is described. The GENESIS code can handle various geometries appeared in core analysis and can perform stable numerical calculation including highly voided conditions that may appear under the design extension conditions.

1. INTRODUCTION

Accurate prediction of core characteristics is one of the fundamentals to quantify safety margin, which plays a very important role in nuclear safety. In order to achieve this goal, higher resolution of spatial, angular, and energetic behaviors of neutrons should be considered. The continuous energy Monte-Carlo method adopts less approximations on the simulation of neutron behavior thus its spatial, angular, and energetic resolutions are almost ideal. Therefore, the continuous energy Monte-Carlo method has been widely used in core analysis to provide a reference solution. The crucial drawbacks of the Monte-Carlo method are the statistical uncertainties in calculation results and longer computation time. Therefore, its applications to practical core analyses are still prohibitive even if a latest high-end computer is used.

In parallel to the development of Monte-Carlo method, deterministic calculation methods with higher spatial, angular, and energetic resolutions are being developed. The method of characteristics (MOC) is one of the most successful transport methods in the area of core analysis – two-dimensional MOC is used as the de facto standard method for lattice physics calculations [1]. For core analysis, the planar MOC method is winning its admiration and is adopted by the various cutting-edge core analysis codes [2]-[7]. The planar MOC method assumes that a three-dimensional core consists of a stack of two-dimensional planes of certain thickness. In current reactor designs, most geometrical heterogeneity appears for radial direction (e.g., pellet-clad-moderator) while a core is considerably homogeneous for axial direction. The planar MOC method well utilizes this feature – heterogeneity for radial direction is explicitly treated by MOC while that of axial direction is considered by a low-order transport method such as the simplified Pn theory. By combining two methods (MOC and the simplified Pn), computational efficiency is significantly improved.

The planar MOC method is adopted in recent core analysis codes and shows good accuracy on the prediction results. Though the planar MOC method is a very efficient method, it has drawbacks on the numerical stability and accuracy in a configuration with large neutron leakage for axial direction. Such case would appear in the design basis accidents or the design extension conditions (DECs) of light water reactors, *e.g.*, the loss of coolant accident (LOCA), the main steam line break (MSLB) with anticipated transient without scram (ATWS).

In order to address this issue and to eliminate the approximation adopted in the planar MOC method (*i.e.*, coupling of radial planes by low-order angular fluxes or neutron currents), the Legendre polynomial Expansion of Angular Flux (LEAF) method is developed in Nagoya University [8],[9],[10]. The present paper summarizes the outline and features of the GENESIS code.

2. MAJOR FEATURES OF GENESIS

2.1 Outline

The GENESIS code is a multi-group neutron/gamma transport code for two- and three-dimensional geometries developed in Nagoya University. Major features are summarized as follows:

•Multi-group transport calculation in 2D (MOC) or 3D (LEAF)

- Flexible geometry treatment using the factorial geometry [11] and the R-function methods [12].
- Geometric components (line, circle, rectangular, hexagonal, elliptic, polygon, and generalized quadratic shape in 2D) are combined to form an object and the defined objects can be also combined to form another object. Objects can be nested at any depth. Thus a very complicated geometry can be treated.
- Cyclic ray trace in rectangular and hexagonal geometry using the direct neutron path linking (DNPL) method [13].
- Angular flux distribution in a flux region can be expanded up to 2nd order for axial and radial directions.
- Neutron source distribution in a flux region can be expanded up to 2nd and 1st order for axial and radial directions, respectively.
- The two-level generalized coarse mesh rebalance (GCMR) method [14][15] or the CMFD method [16] is used for convergent acceleration both for fixed source and eigenvalue problems.
- Various stabilization techniques for acceleration calculations [10].
- Treatment of anisotropic scattering of any order using the rigorous spherical harmonics method or the simplified Pn method [10].
- Treatment of mirror or rotational symmetry.

In the following subsection, some of the features of the GENESIS code are described.

2.2 Geometry handling

The GENESIS code can handle any geometry that consists of line, circle, elliptic, and general quadratic formula in 2D. Since region assignment of complicated regions is a very cumbersome task, the GENESIS code utilizes the factorial geometry method to handle it. Examples are shown in Fig.1.

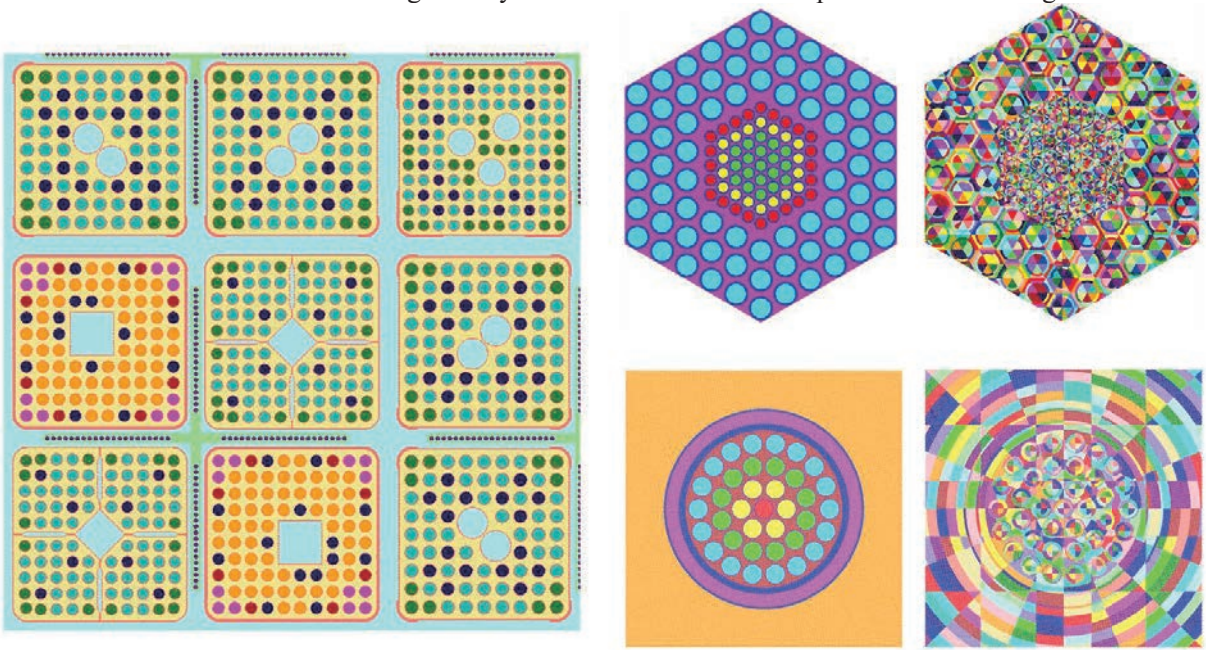

Fig.1 Examples of calculation geometry of the GENESIS code. The most right two figures show flux regions and the rest three figures show material regions.

2.3 LEAF method

The GENESIS code can perform two- or three-dimensional calculations. In the case of two-dimensional geometry, the GENESIS code utilizes the conventional MOC while it utilizes the LEAF method for three-dimensional geometry, which is an improved method of ASMOC3D [11]. The concept of the LEAF method is shown in Fig.2. In this method, calculation geometry is constructed by the stack of planes. By cutting a three-dimensional geometry with planes that are perpendicular to radial direction (parallel to axial direction), the geometry is covered by parallel planes.

Since extruded geometry for axial direction is assumed, each plane consists of rectangular regions as shown in Fig.2. Once the geometry is covered by the set of parallel planes, neutron or gamma transport calculations for a particular direction on these planes are carried out. The transmission probability method

that considers the angular dependence of particle flight direction is used for efficient computation. To reduce spatial discretization errors, incoming and outgoing angular fluxes and neutron source spatial distribution in a rectangular region are spatially expanded by up to the 2nd order Legendre polynomials. Once the average angular flux on a rectangular region is obtained, region wise angular and scalar fluxes are obtained by spatial and angular integrations.

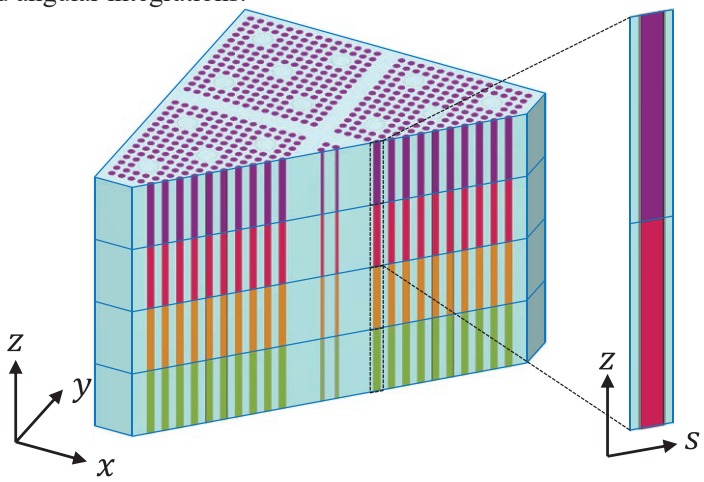

Fig.2 Concept of the LEAF method

2.4 Acceleration

An efficient and stable acceleration method is essential for a transport calculation in large geometry. Especially in large commercial reactors, convergence of the discrete ordinate method and MOC is very slow due to high scattering ratio and large dominance ratio of eigenvalues (both close to unity). The generalized coarse mesh rebalance (GCMR) or the coarse mesh finite difference (CMFD) acceleration method is implemented in the GENESIS code to address this issue. Even for large commercial LWRs or FBRs, typically less than 20 transport sweeps are necessary to obtain fully converged solution of eigenvalue problems. Without these acceleration methods, several thousands of iterations are necessary – the acceleration method improves execution efficiency by a factor of 100.

Though the GCMR and CMFD acceleration methods are very efficient, numerical instability (divergence) is sometimes observed especially for thick and diffusive meshes. The GENESIS code utilizes various stabilization techniques to improve numerical instability [10].

2.5 Parallelization

A three-dimensional transport calculation using the LEAF method requires considerable computational resources though it is much more efficient than the direct three-dimensional MOC method. To reduce computation time, parallel calculation capability is implemented in the GENESIS code using OpenMP. In a parallel calculation using OpenMP, conflicts in memory access can significantly degrade parallel efficiency. To avoid the conflicts in memory access, independent tally array for angular fluxes is prepared for each thread.

3. VERIFICATIONS

Verification calculations of the GENESIS code have been carried out for various problems as follows:
-KAIST benchmark problem (small LWR, 2D, 7g)
-C5G7 benchmark problem (small LWR, 3D, 7g)
-C5G7 hexagonal benchmark problem (small LWR, 3D, 7g)
-Takeda benchmark No.1 (small LWR, 3D, 4g, with large void region)
-Kobayashi 3D benchmark problem (bulk shielding with duct or large void, 1g)
-FBR benchmark problem (large FBR, 2D, 4g)

The comparisons with reference solution show excellent agreement, indicating the validity of the GENESIS code. As an example, error of pin-by-pin fission rate (axially integrated value) in the C5G7 3D benchmark problem with void region (Fig. 3)[9][18] is shown in Fig.4. Note that the benchmark problem

with void region is not included in the original one [18].

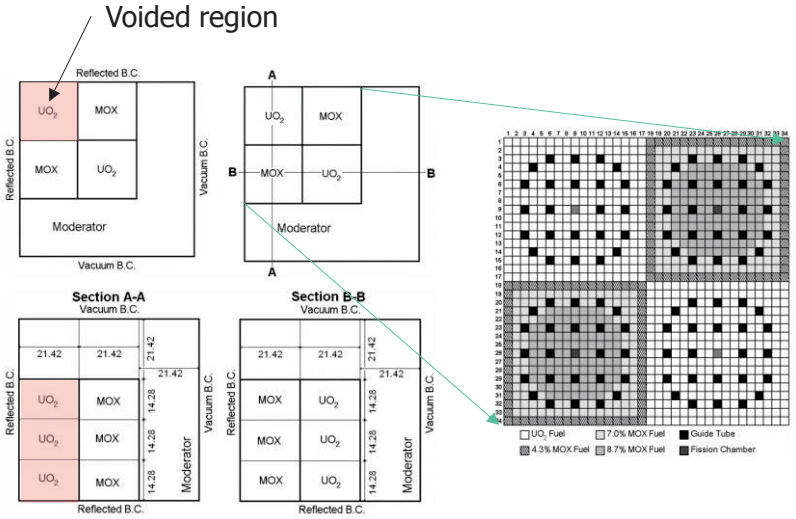

Fig.3 C5G7 3D void benchmark problem

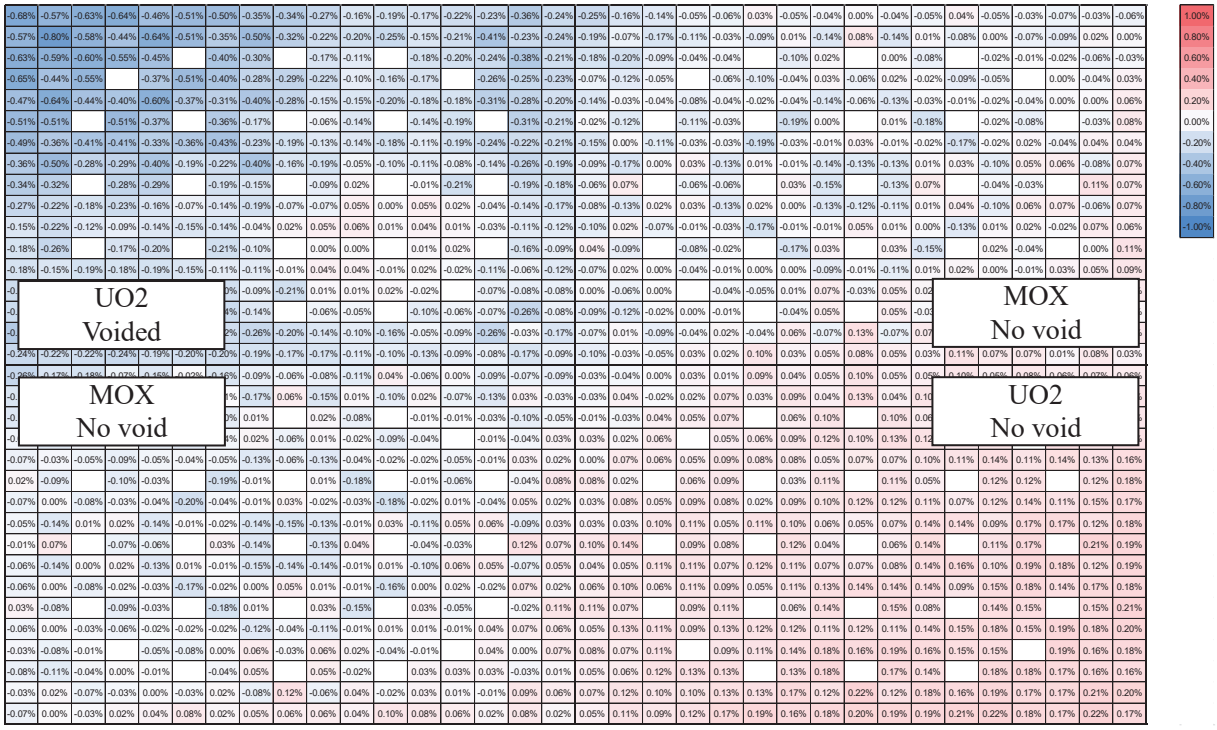

Fig.4 Error of pin-by-pin fission rate distribution for C5G7 3D void benchmark problem

4. SUMMARY

In the present paper, the current status of the GENESIS code, which is a neutron and gamma transport code for two- or three-dimensional geometry, is described. The GENESIS code can handle various geometries appeared in reactor core analysis. Calculations in large geometries (*e.g.*, commercial LWRs and large FBRs) can be carried out by the efficient acceleration methods (GCMR or CMFD). Validity of the GENESIS code has been confirmed through various benchmark calculations in two- and three-dimensional geometries including large void regions.

The GENESIS code has been released to Japanese users in June 2018 for academic and research purposes. The documents can be downloaded from the website [19]. The source code is distributed based on the request by users.

The following points are potential future tasks of the GENESIS code:

- Further improvement of execution efficiency, especially with parallel execution in two-dimensional geometry
- Treatment of various cross section types
- Development of effective multi-group cross section generation and coupling with this feature
- Efficient calculation algorithm to treat discontinuity factors

ACKNOWLEDGEMENTS

This work was supported in part by JSPS KAKENHI, Grant-in-Aid for Scientific Research (C) (16K06956).

REFERENCES

[1] Lattice Physics Computation, "Handbook of Nuclear Engineering", Vol. 2, Chap. 9, D. G. Cacuci, Ed., Springer (2010).
[2] J. Y. Cho *et al*., "Three-Dimensional Heterogeneous Whole Core Transport Calculation Employing Planar MOC Solutions", *Trans. Am. Nucl. Soc*., **87**, 234 (2002).
[3] S. Kosaka and T. Takeda, "Verification of 3D Heterogeneous Core Transport Calculation Utilizing Non-Linear Iteration Technique", *J. Nucl. Sci. Technol*., **41**, 645 (2004).
[4] H. G. Joo *et al*., "Methods and Performance of a Three-Dimensional Whole-Core Transport Code DeCART", *Proc.PHYSOR 2004*, Chicago, Illinois, April 25–29, 2004, American Nuclear Society (2004).
[5] B. Kochunas *et al*., "Overview of Development and Design of MPACT: Michigan Parallel Characteristics Transport Code", *Proc. M&C 2013*, Sun Valley, Idaho, May 5–9, 2013, American Nuclear Society (2013).
[6] Y. S. Jung *et al*., "Practical Numerical Reactor Employing Direct Whole Core Neutron Transport and Subchannel Thermal/Hydraulic Solvers," *Ann. Nucl. Energy*, **62**, 357 (2013).
[7] M. Ryu et al., "Solution of the BEAVRS Benchmark Using the nTRACER Direct Whole Core Calculation Code", *J. Nucl. Sci. Technol*., **52**, 961 (2015).
[8] Y. Kato, T. Endo, and A. Yamamoto, "Development of Legendre Expansion of Angular Flux Method for 3D MOC Calculation", *Proc. PHYSOR 2014*, Kyoto, Japan, September 28–October 3, 2014, Japan Atomic Energy Agency (2014).
[9] A. Yamamoto, A. Giho, Y. Kato, T. Endo, "GENESIS - a three-dimensional heterogeneous transport solver based on the Legendre polynomial expansion of angular flux method", *Nucl. Sci. Eng*., **186**, 1 (2017).
[10] A. Yamamoto, A. Giho, Y. Kato, T. Endo, "Recent developments in the GENESIS code based on the Legendre polynomial expansion of angular flux method", *Nucl. Eng. Technol*. **49**, 1143, (2017).
[11] Z. Weiss and G. Ball, "Ray-Tracing in Complicated Geometries", *Ann. Nucl. Energy*, **18**, 483 (1991).
[12] T. Jevremovic, J. Vujic, and K. Tsuda, "ANEMONA—A Neutron Transport Code for General Geometry Reactor Assemblies Based on the Method of Characteristics and R-Function Solid Modeler", *Ann. Nucl. Energy*, **28**, 125 (2001).
[13] S. Kosaka and E. Saji, "Transport Theory Calculation for a Heterogeneous Multi-Assembly Problem by Characteristics Method with Direct Neutron Path Linking Technique", *J. Nucl. Sci. Technol*., **37**, 1015 (2000).
[14] A. Yamamoto *et al*., "Convergence Improvement of Coarse Mesh Rebalance Method for Neutron Transport Calculations", *J. Nucl. Sci. Technol*., **41**, 781 (2004).
[15] A. Yamamoto, "Generalized Coarse-Mesh Rebalance Method for Acceleration of Neutron Transport Calculations", *Nucl. Sci. Eng*., **151**, 274 (2005).
[16] K. Smith and J. D. Rhodes, "Full-Core, 2-D, LWR Core Calculations with CASMO-4E," *Proc. PHYSOR 2002*, Seoul, Korea, October 7–10, 2002.
[17] A. Giho, K. Sakai, Y. Imamura, H. Sakurai, K. Miyawaki, "Development of axially simplified method of characteristics in three-dimensional geometry", *J. Nucl. Sci. Technol*., **45**, 985 (2003).
[18] "Benchmark on Deterministic Transport Calculations Without Spatial Homogenisation—MOX Fuel Assembly 3-D Extension Case", *NEA/NSC/DOC(2005)16*, Organisation for Economic Co-operation and Development/Nuclear Energy Agency (2005).
[19] GENESIS documents, https://nuss.nagoya-u.ac.jp/s/XP6Gl0NyZoymgaU (2018). [in Japanese]

This is a blank page.

6 Nuclear Data Processing Code FRENDY

Kenichi Tada

Nuclear Science and Engineering Center, Japan Atomic Energy Agency
Tokai-mura, Naka-gun, Ibaraki-ken 319-1195 Japan
e-mail: tada.kenichi@jaea.go.jp

A new nuclear data processing code FRENDY has been developed in order to process the evaluated nuclear data library JENDL. Development of FRENDY helps to disseminate JENDL and various nuclear calculation codes. This report describes an overview of FRENDY.

1. Introduction

The transport calculation codes are used to calculate k-effective, flux distribution, reaction rate, dose ratio, and so on. These codes cannot read the nuclear data file directly and a cross-section data library, which is generated by the nuclear data processing code, is required, as shown in Fig. 1. The nuclear data processing system is not just a converter but performs many processes, *e.g.*, reconstruction of the resonance region, linearization, Doppler broadening, and calculation of the probability table in the unresolved resonance region[1,2].

NJOY[3] of Los Alamos National Laboratory and PREPRO[4] of International Atomic Energy Agency have been widely used throughout the world including Japan for several decades. However, these are sometimes unable to process the newly released JENDL[5] correctly, and this problem cannot be resolved in a timely manner. Therefore, expertise on particle transport codes, as well as the nuclear data, has been desired in the domestic nuclear data processing system, since it serves as an indispensable interface between nuclear data files and particle transport codes.

JAEA has developed a new nuclear data processing code FRENDY (FRom Evaluated Nuclear Data librarY to any apprication) to generate a cross-section data library from the evaluated nuclear data library JENDL with simple input file[6,7].

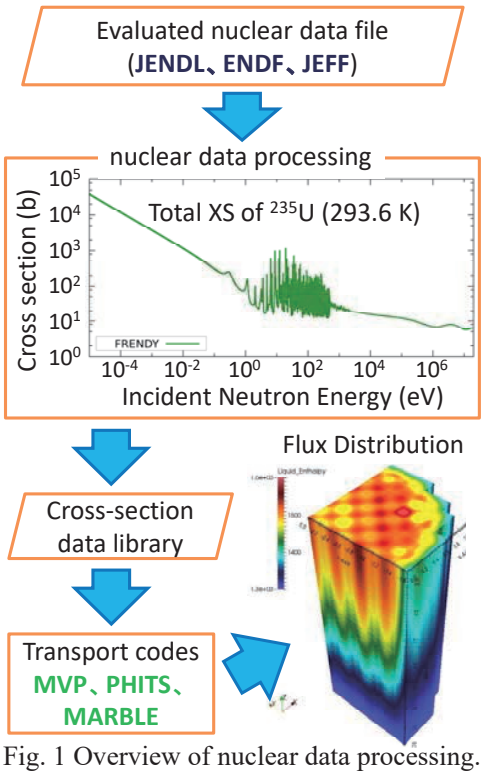

Fig. 1 Overview of nuclear data processing.

2. Overview of FRENDY

The processing method of FRENDY is similar to that of NJOY. The current version of FRENDY treats the ENDF-6

format for the nuclear data format and generates the ACE file which is used for the continuous energy Monte Carlo codes including PHITS[8] and MCNP[9]. FRENDY is developed not only to process the evaluated nuclear data file but also to implement the FRENDY functions to other calculation codes. Users can easily use many functions *e.g.*, read, write, and process the evaluated nuclear data file, in their own codes if they implement the classes of FRENDY to their codes.

The system structure of FRENDY is shown in Fig. 2. The modules with solid-lined shapes have been already implemented, while the ones with dashed-lined shapes have not been developed yet. Recently, the introduction of the Generalized Nuclear Data Structure (GNDS) has been considered as a new nuclear data format[10]. FRENDY can treat not only the ENDF-6 format but also other nuclear data format. FRENDY converts the nuclear data from each nuclear data format to NuclearDataObject. FRENDY can treat the GNDS format if parser, writer, and converter modules are implemented. FRENDY has parser and writer modules to handle the ACE file. These modules are useful not only for the ACE file generation but also for the ACE file modification. Users can modify the ACE file if users write a main (control) program with the ACE data parser and writer modules in FRENDY.

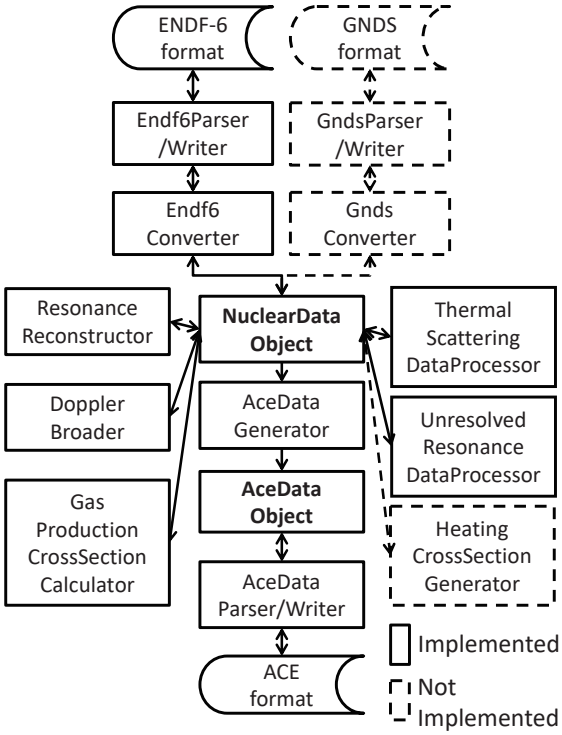

Fig. 2 The system structure of FRENDY.

FRENDY can treat two types of input format. One is the FRENDY original input format and another is NJOY99 compatible format. The original input format requires only the processing mode name and evaluated nuclear data file name at minimum. FRENDY has default values in the source code for the processing. Users can give the parameters in the input file if they want to change the parameters. The original input format is

```
ace_fast_mode  // Processing mode
 nucl_file_name   U235.dat
 ace_file_name    U235.ace
 temp  /* [eV] */  296.0
```

Fig. 3 Sample input file of FRENDY original input format.

```
reconr                          / command
 20  21                         / input(tape20), output(tape21)
'pendf tape for JENDL-4 U235'   / identifier for PENDF
 9228                           / mat
 1.00e-03  0.00                 / err, temp
 0                              /
broadr                          / command
 20  21  22                     / endf, pendf(in), pendf(out)
 9228  1                       / mat, temp no
 1.00e-03  -5.0E+2              / err, thnmax
 296.0                          / temp
 0                              /
gaspr                           / command
 20  22  23                     / endf, pendf(in), pendf(out)
purr                            / command
 20  23  25                     / endf, pendf(in), pendf(out)
 9228  1  10  20  200           / mat, temp no, sig no, bin no, lad no
 296.0                          / temp
 1E10  1E6  1E5  1E4 1E3 100  35  10  1  0.1  / sig zero
 0                              /
acer                            / command
 20  25   0  30  31             / nendf, npend, ngend, nace, ndir
 1   1   1  0.30                / iopt(fast), iprint(max), itype, suffix
 'ACE file for JENDL-4 U235'    / descriptive character
 9228  296.0                    / mat, temp
 1  1                           / newfor(yes), iopp(yes)
 1  1  1                        / thin(1), thin(2), thin(3)
stop                            /
```

Fig. 4 Sample input file of NJOY 99 compatible format.

simple and it does not require the expertise of the nuclear data processing.

FRENDY can also treat the NJOY99 input files and the PENDF file which is the intermediate file used in NJOY. NJOY is widely used in many laboratories and companies to generate the cross-section data library for their nuclear calculation codes. The NJOY users can easily use FRENDY without modification of their processing environment, *e.g.*, running shell scripts, input files, and post processing programs. They can easily use FRENDY without changing the input files for NJOY. They can therefore replace NJOY modules with FRENDY ones as they need. In addition, the modules of FRENDY and NJOY can be used in combination. For example, users can generate the multi-group cross-section data library using the GROUPR module of NJOY with the PENDF file generated by FRENDY.

Figures 3 and 4 show sample input files of FRENDY original input format and NJOY99 compatible format, respectively. FRENDY original input format accepts comment lines. The C++ style comments are available, *i.e.*, "//" for a single line comment and "/* … */" for multi-line comments. Comparing both sample input files, the FRENDY original input format is easy to understand for beginners.

3. Comparison of the processing results

The processing results of FRENDY are compared with those of NJOY99 to verify FRENDY. All nuclei and materials prepared in JENDL-4.0 and JENDL-3.3 are used for the verification.

Figure 5 shows the comparison of the Doppler broadened cross-section at 300 K and the relative difference. As shown in Fig. 5, the small difference is observed in the elastic scattering cross-section. The cause of this difference is the calculation method of the cross section at 0 eV. The cross section at 0 eV is required to calculate the Doppler broadened cross-sections at the low energy region. NJOY99 assumes that the cross section obeys the 1/v law. This approximation is appropriate for many reactions. However, the elastic scattering cross-sections does not obey the 1/v law since the elastic scattering cross-section is constant due to the potential scattering cross-section at the low energy region. In such a case, this approximation is inappropriate. FRENDY determines the cross sections at 0 eV by the linear extrapolation with the cross sections at the lowest and next-to-the-lowest energy grid points. As shown in Fig. 5, the difference of the cross sections of the linear extrapolation is so small, even if the fission cross-section, which obeys the 1/v law, is concerned. Therefore, the linear extrapolation is appropriate for the treatment of the cross section at 0 eV.

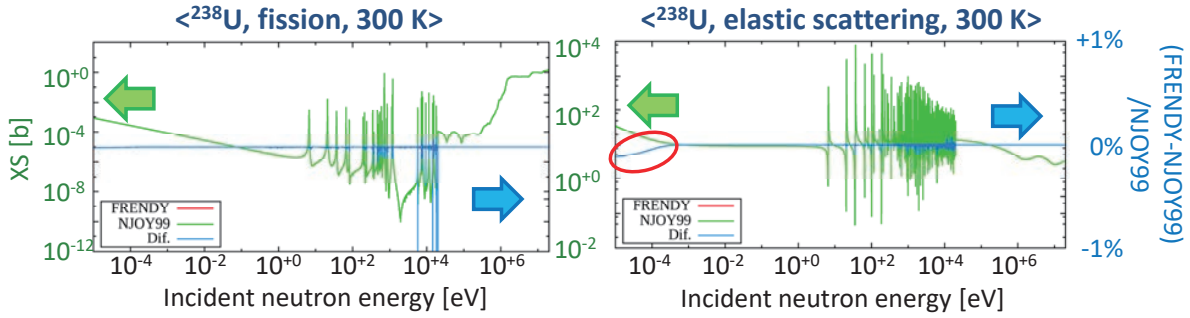

Fig. 5 Comparison of the fission and elastic scatter cross sections for ^{238}U from JENDL-4.0.

Figures 6 and 7 show the comparison of the incoherent inelastic scattering cross-sections for H in H_2O at 300 K and H in ZrH at 400 K and the relative differences. As shown in Fig. 7, the large difference is observed in H in ZrH. The cause of this difference is the adoption of the fixed incident neutron energy grid to calculate the incoherent inelastic scattering cross-section. The THERMR module of NJOY99 uses the fixed incident neutron energy grid,

which consists of 117 energy grid points from 10^{-5} to 10 eV to calculate the incoherent inelastic scattering cross-section and secondary energy and angular distributions. The incoherent inelastic scattering cross-section at the other energy grid points are interpolated using the fifth order Lagrange interpolation and secondary energy and angular distributions are not calculated to reduce calculation time and data size. As shown in Fig. 6, the incoherent inelastic scattering cross-section for many materials can be represented with a slowly varying function. In such a case, the fixed incident neutron energy grid is appropriate. However, the fixed incident neutron energy grid is inappropriate for some materials, *e.g.*, H in ZrH for which the incoherent inelastic scattering cross-section is oscillated as shown in Fig. 7. The adoption of the finer energy grid is required to adequately reproduce the incoherent inelastic scattering cross-section distribution in such materials[11]. FRENDY calculates the incoherent inelastic scattering cross-section in all energy grid points of the total cross-section to appropriately treat such materials when the thermal scattering law data is given.

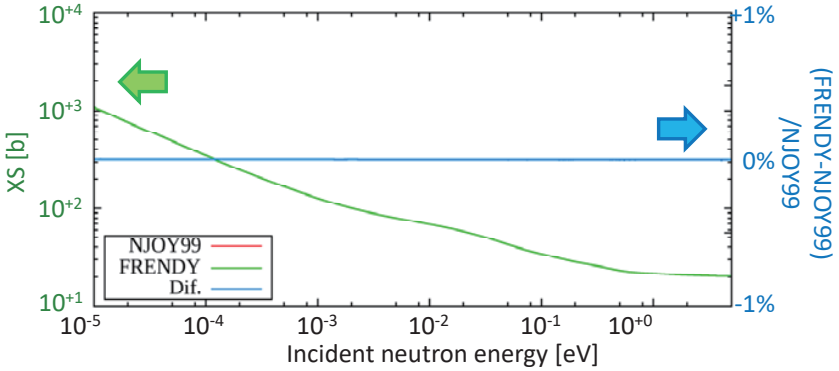

Fig. 6 Comparison of the incoherent inelastic scatter cross sections for H in ZrH from JENDL-4.0.

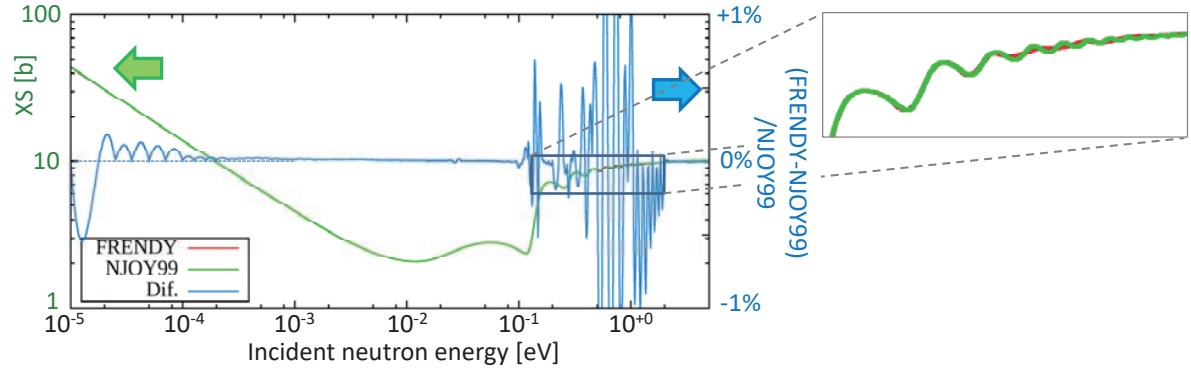

Fig. 7 Comparison of the incoherent inelastic scatter cross sections for H in ZrH from JENDL-4.0.

Development of FRENDY also contributes to verify the conventional nuclear data processing codes, *e.g.*, NJOY and PREPRO. The verification of the conventional nuclear data processing codes is so difficult because the available nuclear data processing codes are limited. The comparison of the processing results of FRENDY and those of the conventional processing codes is not only to verify FRENDY but also to verify the conventional processing codes and the conventional processing method. The other problems of NJOY are listed in Refs. 12 and 13.

4. Comparison of k-effective values using ACE file processed by FRENDY and NJOY

The k-effective values of MCNP5[9] using the ACE file generated by FRENDY are compared those by NJOY99 to verify the ACE file generation function. The MCNP sample input files in the ICSBEP handbook[14] were used for the comparison of the k-effective values. Many of them were not intended to be used for the strict validation of the

evaluated nuclear data file and neutronics calculation codes by the comparison of calculation results with experimental results. In this verification, these sample input files are only used to compare the k-effective values using the ACE files processed by FRENDY with those by NJOY99. The processing conditions are as follows:

Nuclear data library	JENDL-4.0
Temperature	296.0 K
Tolerance (error)	0.1%

Figure 8 shows the comparison of k-effective values for benchmark experiments using the ACE files processed by FRENDY and NJOY99. The benchmark name in Fig. 8 indicates fissile material, physical form of the fissile material, neutron energy range, and experimental number. The relative difference is small and it is not so varied with the fissile material, neutron energy range. The comparison results indicate that the cross section differences caused by the problems of NJOY which are described in Sec. 3 do not affect the k-effective values and FRENDY properly generates ACE files.

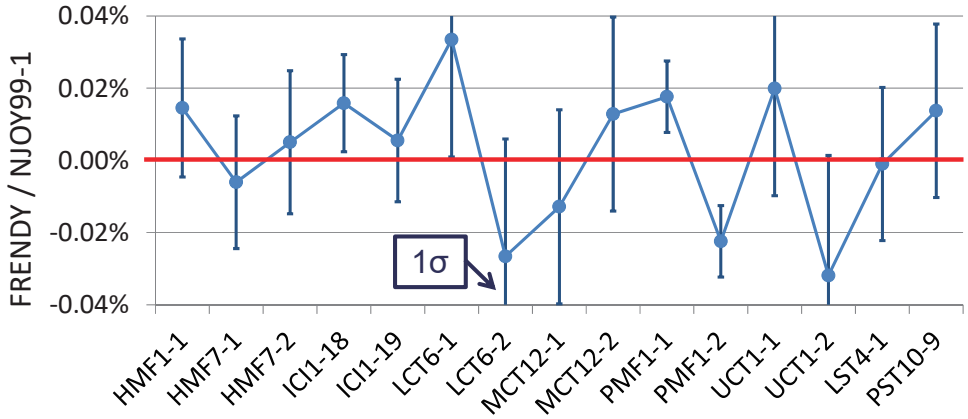

Fig. 8 Comparison of k-effective results for benchmark experiments using ACE files processed by FRENDY and NJOY99.

5. Conclusions

JAEA has provided the evaluated nuclear data library JENDL and the nuclear calculation codes. JENDL and these domestic codes have been widely used in many universities and industrial companies in Japan. However, we sometimes find problems in imported processing systems and need to revise them when the new JENDL is released. To overcome such problems and immediately process the nuclear data when it is released, JAEA started developing a new nuclear data processing code, FRENDY.

The process results of FRENDY are compared to those of NJOY99 for the verification of FRENDY. The development of FRENDY found problems of NJOY99. In this paper, the author showed the calculation method of the cross section at 0 eV and the adoption of the fixed incident neutron energy grid to calculate the incoherent inelastic scattering cross-section.

The k-effective values of MCNP5 using the ACE file generated by FRENDY are compared with those by NJOY99 to verify the ACE file generation function. The MCNP sample input files of the integral experiments in the ISCSBEP handbook are used for comparison. The k-effective values of FRENDY are similar to those of NJOY99. These results

indicate that FRENDY properly generates the ACE files.

References

[1] K. Tada, K. Kosako, K. Yokoyama, C. Konno, “Cutting-edge studies on Nuclear Data for Continuousand Emerging Need (7); Processing and Validation on Nuclear Data,” *Journal of Atomic Energy Society of Japan*, **60**, pp.168-172 (2018).

[2] D. E. Cullen, “Nuclear Data Preparation”, Handbook of Nuclear Engineering, 1, pp.282-425, Springer, Berlin (2010).

[3] A. C. Kahler, Ed., “The NJOY Nuclear Data Processing System, Version 2016,” LA-UR-17-20093, Los Alamos National Laboratory (2016).

[4] D. E. Cullen, “PREPRO 2017, 2017 ENDF/B Pre-processing Codes (ENDF/B-VII of proposed VIII Tested)”, IAEA-NDS-39, Rev.17, International Atomic Energy Agency (2017).

[5] K. Shibata, O. Iwamoto, T. Nakagawa, et al., “JENDL-4.0: A New Library for Nuclear Science and Engineering”, *J. Nucl. Sci. Technol.*, **48**, pp.1-30 (2011).

[6] K. Tada, Y. Nagaya, S. Kunieda, et al., "Development and verification of a new nuclear data processing system FRENDY," *J. Nucl. Sci. Technol.*, **54**, pp.806-817 (2017).

[7] K. Tada, Y. Nagaya, S. Kunieda, et al., “FRENDY: A new nuclear data processing system being developed at JAEA,” *EPJ Web of Conferences*, **146**, 02828 (2017).

[8] T. Sato, Y. Iwamoto, S. Hashimoto, et al., “Features of Particle and Heavy Ion Transport code System (PHITS) version 3.02”, *J. Nucl. Sci. Technol.*, **55**, pp.684-690 (2018).

[9] X-5 Monte Carlo Team, “MCNP – A General Monte Carlo N-Particle Transport Code, Version 5,” *LA-UR-03-1987*, Los Alamos National Laboratory (2003).

[10] C. M. Mattoon, B. R. Beck, N. R. Patel, et al., “Generalized Nuclear Data: A New Structure (with Supporting Infrastructure) for Handling Nuclear Data”, *Nucl. Data Sheets*, **113**, pp.3145-1371 (2012).

[11] A. Yamamoto, N. Sugimura, “Improvement on multi-group scattering matrix in thermal energy range generated by NJOY”, *Ann. Nucl. Energy*, **33**, pp.555-559 (2006).

[12] K. Tada, S. Kunieda, Y. Nagaya, “Nuclear Data Processing Code FRENDY Version 1,” JAEA-Data/Code 2018-014, Japan Atomic Energy Agency (2019).

[13] K. Tada, “Comparison of the processing results between FRENDY and NJOY,” Technical Meeting on Nuclear Data Processing, Dec. 4-7, 2017, Vienna, Austria (2017).

[14] OECD/NEA, “International Handbook of Evaluated Criticality Safety Benchmark Experiments,” NEA/NSC/DOC(95)03 (2014).

7 Neutrino Transport by S_n Method and Supernovae

Kohsuke SUMIYOSHI
National Institute of Technology, Numazu College
Ooka 3600, Numazu, Shizuoka 410-8501, Japan
sumi@numazu-ct.ac.jp

In astrophysical phenomena of core-collapse supernovae, neutrino transport plays the essential role in the mechanism of supernova explosion. Recent computational technology enables us to perform numerical simulations of the first-principle-type calculation of the neutrino-radiation hydrodynamics of supernova explosions from gravitational collapse of massive stars. The description by the Boltzmann equation for neutrino transport in supernovae is also important in the neutron transport of nuclear engineering. The recent progress of the neutrino transport in supernova explosions is described with discussion on possible connections with computing technology of neutron transport.

1. Introduction

Supernovae are astrophysical phenomena, which suddenly appear as very bright displays and fade out afterward. They are stellar explosions and the dynamical outcome of stars at the end of their lives. Among many supernovae frequently observed, core-collapse supernovae are the explosions originated from massive stars. They are the birth place of neutron stars and a site for the nucleosynthesis of heavy elements. Despite the importance of core-collapse supernovae in astrophysics and nuclear physics, the mechanism of supernova explosion has been elusive even after extensive studies for decades [1]. Difficulty of the problem resides in the extreme condition of hot and dense matter in nuclear physics and in the treatment of neutrino transport through reactions and propagation.

Neutrinos play an essential role of core-collapse supernovae as an agent of energy transport for explosion. The so-called neutrino heating mechanism is the key for the explosion together with hydrodynamical instabilities [1, 2]. Precise treatment of neutrino transport is crucial to evaluate the amount of neutrino heating for successful explosions. The phenomena of neutrino transport streaming from diffusion regime resemble those of neutron transport in nuclear reactors. The neutrino transport also relies on the nuclear data for dense matter and neutrino reaction rates. In this report, I describe recent issues in physics of supernova explosion and demonstrate the latest progress by the neutrino transport using the S_n method for the Boltzmann equation [3,4]. Exchanging the knowledge of computing technology of particle transport between astrophysics and atomic energy science would be valuable through its close similarity.

2. Supernova mechanism through neutrinos

The scenario of supernova starts from the central Fe core of a massive star with a mass of more than 10 times the solar mass (Fig 1 left). Gravitational collapse of the Fe core is triggered by electron capture on nuclei and photo-dissociation of Fe nuclei. The collapse leads to very high densities beyond the nuclear matter density (0.16 fm^{-3} or $3x10^{14}$ gcm^{-3}) and the shock wave is launched due to the repulsive hard core of nuclear force. If the shock wave propagates to the Fe core surface, it leads to the explosion of entire star. However, the shock wave stalls due to the photo-dissociation of nuclei and the accretion of matter from outer layers and it is difficult to have successful explosions for typical models of massive stars. It is believed that a combination of hydrodynamical instabilities, such as convection, and the effect of neutrino heating is necessary to obtain a healthy explosion which matches observational facts.

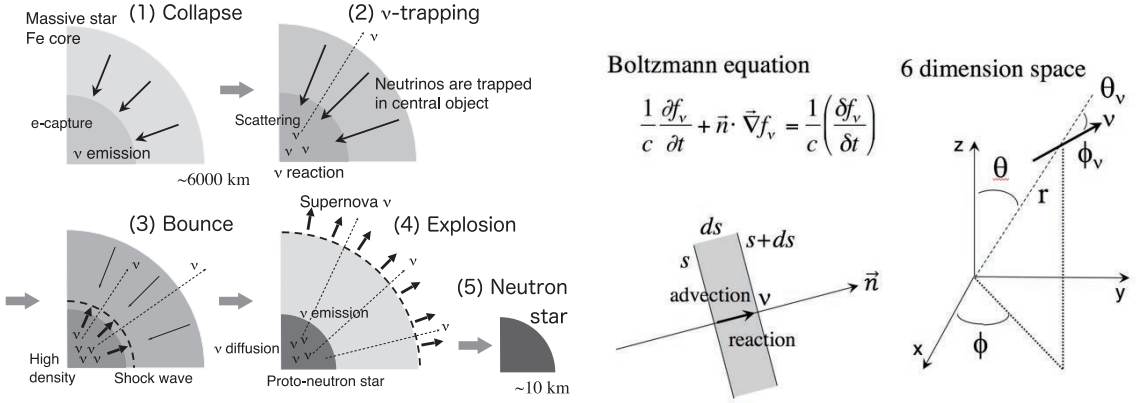

Figure 1: (left) Schematic diagram of core-collapse supernovae from collapse, bounce and explosion. (right) Boltzmann equation handles neutrino distributions in 6 dimensions of space and momentum.

Neutrinos play an essential role to drive the explosion mechanism through the neutrino heating. The neutrinos are created by electron captures at the beginning and they are trapped inside the central core due to high densities (>10^{11} gcm^{-3}). Thermal processes additionally produce a bunch of neutrinos and anti-neutrinos at high temperature due to compression. Neutrino are emitted from the surface of a nascent compact object just born at center after the core bounce. A part of these neutrinos is absorbed by nucleons in accreting matter and contributes to the heating behind the shock wave.

This energy transfer of energy from neutrinos to matter assists the revival of stalled shock wave and ensuing explosion if it is enough. Whether it leads to a successful explosion depends on the efficiency of neutrino heating. Although a huge energy of 10^{53} erg is provided by the gravitational energy release of the collapse from Fe core to neutron star, most of the energy is carried away by freely streaming neutrinos. In fact, the total energy of supernova neutrinos (~10^{53} erg) is derived by the detection of supernova neutrinos from the supernova explosion observed in 1987. The explosion energy of supernovae is typically ~ 10^{51} erg, therefore, one needs to extract a tiny fraction (~1%) of energy through absorption during neutrino propagation. Delicate extraction of energy requires a precise evaluation of neutrino transport with emission, scattering and absorption.

3. Importance of neutrino transport

Description of neutrino transport in the supernova core is one of remaining issues in the unsolved supernova mechanism. It is a challenging problem due to difficulties of the treatment of neutrino transport in extreme and variable conditions. One has to describe the entire transport from diffusive to free-streaming regimes due to the wide range of conditions: density, temperature and composition. Note that the important part of neutrino transport resides in the intermediate regime between diffusion and free-stream regarding the heating region behind the shock wave. Hence, it is not appropriate to make simple approximations of transport in principle. It is further difficult to handle the neutrino transport since neutrino reactions strongly depend on energy, angle, neutrino species and target particles (leptons, nucleons and nuclei). One has to perform calculations with multi-angle and multi-energy group scheme.

It has been common to make a certain level of approximations in neutrino transport due to the limitation of computing resources for many decades. The diffusion approximation, which is also used in nuclear engineering, is one of popular ways to reduce the computing cost. As the computing power grows, the shift from approximate methods to the exact method is desirable since the neutrino heating is known to be sensitive to the approximation of neutrino transport [3, 5]. Under the spherical symmetry (1D), the first-principle calculation (general relativistic neutrino-radiation hydrodynamics) has become possible in the last decade. It has been shown in this sophisticated level that no explosion occurs in 1D for typical massive stars [6]. It is then recognized that hydrodynamical instabilities in 2D/3D are crucial by breaking the spherical symmetry. The time for heating is prolonged by non-spherical motion of accreting material, hovering behind the stalled shock wave due to convection, for example, instead of rapidly falling radial motion [1]. Most of the-state-of-art simulations in 2D/3D often adopt approximations in neutrino transport even with the current resources of high-performance computing [2]. Therefore, there has been some uncertain factors left in 2D/3D simulations, in which successful explosions are routinely demonstrated, due to the adopted approximations of neutrino transport such as diffusion approximations and/or ray-by-ray-type schemes. More elaborated schemes using the moment formalism adopt the analytic formulae of closure relations.

4. Simulations of core-collapse supernovae by Boltzmann equation

Recently the computation of neutrino transport in 3D space by the direct solution of Boltzmann equation has become possible [3]. The numerical code handles the neutrino distribution in 6 dimensions: 3 dimensions for space (r, θ, ϕ) and 3 dimensions for momentum space (neutrino energy and two angles to designate the neutrino direction) (Fig. 2 right). The Boltzmann equation is solved by the discretized form in space and neutrino angles (S_n method) with an implicit time-advancing. The collision term contains complicated contributions due to energy and angle dependence for incoming and/or outgoing neutrinos, frame dependence and non-linearity due to pair processes (coupling between neutrinos and anti-neutrinos). The 6D Boltzmann equation solver has been applied to explore the features of neutrino transfer in 3D supernova cores and to examine the validity of

approximations [7].

More recently, the numerical code of the neutrino-radiation hydrodynamics has been developed and applied for 2D/3D supernova simulations [8]. The 6D Boltzmann equation solver is coupled with hydrodynamics and gravity under the axial symmetry (2D). The code describes the neutrino transport in dynamical situations such as neutrino emissions from convective regions of a compact object. It properly handles the neutrino distributions in fluid flow in a seamless way from diffusion to free-streaming regimes by treating the relativistic effects such as Doppler-shift and aberration.

Figure 2 (left) shows the first outcome of the numerical results of the neutrino-radiation hydrodynamics in 2D using the 6D Boltzmann solver [4]. We follow the time evolution of the hydrodynamical variables and neutrino distributions in the 2D stellar model starting from the gravitational collapse of a massive star to core-bounce and propagating shock wave. It is necessary to perform long-term numerical simulations to find out whether the propagation of shock wave results in an explosion or not. It is to be noted that the high-performance computing resources such as K-computer have been used to solve the large-scale computations of neutrino transport via sparse matrix solver for implicit time-advancing.

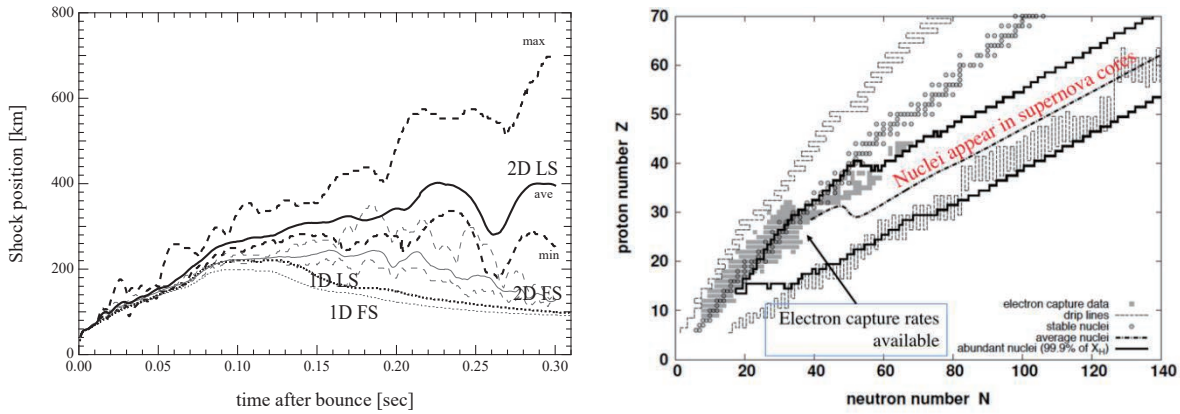

Figure 2: (left) Time evolution of the position of shock wave in 1D and 2D calculations with two EOSs. [4] (right) Nuclear species in supernova core in the nuclear chart and available area of electron capture rates. [9, 10, courtesy by Furusawa]

In Fig. 2 (left), the time evolution of position of shock wave in numerical results for a $11M_{sun}$ star in 1D and 2D is shown. The two sets of data table of equation of state (EOS) are adopted to examine the dependence on the properties of hot and dense matter. The behavior of the shock wave is different in 2D calculations depending on the adopted EOS. In the case with the Lattimer-Swesty EOS [11], which is softer than the Furusawa EOS [9] (extended version of Shen EOS [12]) as noted below, the shock wave expands in an asymmetric way showing the sign of explosion. The shock wave does not revive, on the other hand, with the Furusawa EOS, and does not lead to the explosion. In spherical calculations, there is no explosion for the two EOS cases and the difference is small between them. This comparison is the first step to investigate the dependence on nuclear physics in the first-principle-type calculations using the 6D Boltzmann solver. We are extending our studies to

explore the systematic behavior of core-collapse supernovae in 2D for other models of massive stars with and without rotations and to examine the dependence on nuclear data. The full 3D calculations are prepared under the Post-K computer project and planned at the next generation supercomputer of Exa-flops scale in Japan.

5. Data of neutrino and nuclear physics

Physics processes inside the supernova core are important ingredients for the reliable numerical simulations of hydrodynamics and neutrino transport. The equation of state of hot and dense matter is essential to calculate the structure and dynamics of supernova core. Consistent sets of thermodynamic quantities with the wide coverage of extreme conditions of density, temperature and composition, are necessary to perform numerical simulations in various situations. There has been a progress of the sets of equation of state since 1990 [9,11,12] and the updated data tables of EOS have become available with constraints from neutron star observations and nuclear experiments [13]. One of the popular sets are Lattimer-Swesty EOS [11] and Shen EOS [12] which are based on the different frameworks of nuclear mean field models. The former, having weak repulsion at high densities, tends to have more compression of the central core and is called soft as compared with the latter. The soft EOS holds compact neutron stars with small radii and may have advantageous to release a large gravitational energy. This dependence must be clarified in the 2D/3D supernova simulations with 6D Boltzmann solver.

The reaction rates of neutrinos are also essential in the neutrino transport as ingredients in the collision term of Boltzmann equation. It is to be noted that the composition (nucleons and mixture of nuclei) in the EOS is important to evaluate the reaction rates of neutrinos. Nuclear data such as masses and shell effects in a wide area of the nuclear chart are utilized to determine the composition. Electron captures on nuclei are important to determine the amount of neutrino trapping during the gravitational collapse. Figure 2 (right) displays the range of nuclei appearing in the supernova simulations. Various nuclei in neutron-rich side in the nuclear chart are important in supernovae and the coverage of neutrino reaction rates with those nuclei is mandatory. At the moment, the limited evaluation of electron capture rates on nuclei is available, though. In this sense, providing the nuclear data in supernovae shares the importance with nuclear engineering.

6. Relation to neutron transport

The neutrino transport in supernovae has close similarity to neutron transport in nuclear engineering. Extraction of neutron from the diffusion regime and the usage of neutron fluxes to reactions in a precise manner require the reliable treatment of particle transport. The basic equation comes from Boltzmann equation and the diffusion approximation is commonly used for practical problems. The treatment of multi-energy group is inevitable since the energy spectrum is crucial for nuclear reactions as in the supernova problems. The diffusion approximation poorly describes the neutron fluxes in the intermediate regime and requires suitable formulae to connect

with free-streaming limit. Although there is a significant difference of conditions between supernova and nuclear reactors, there are a number of common problems to tackle from the point of view of transport phenomena and computing technology.

7. Summary

Neutrino transport is one of the keys to clarify the mechanism of core-collapse supernovae, which are gigantic astrophysical phenomena. Puzzles to solve the explosion mechanism relies on the transfer of energy from neutrinos to matter via neutrino reactions in neutrino fluxes emitted from the central object. Recent computing technology enables us to perform the first-principle-type calculations of neutrino transport for supernova dynamics. Extraction of particles from the diffusive environment in supernovae is strikingly similar to the one in nuclear engineering. Since the basic equation is exactly the same and challenging issues in computing technology are common in both fields, it would be fruitful to exchange the information, expertise and new ideas between astrophysics and nuclear engineering.

Acknowledgements

This article is based on the collaboration with the research members in Waseda University, Kyoto University, RIKEN, KEK, and Princeton University. This work is supported by Grant-in-Aid for Scientific Research (26104006, 15K05093, 17H06357, 17H06365), Japan. The usage of high-performance computing resources at KEK, RCNP, YITP, Nagoya U. and U. Tokyo are acknowledged. This work was partly supported by research programs at K-computer, HPCI and Post-K project.

References

[1] H.-T. Janka *et al.*, Ann. Rev. Nucl. Part. Sci. **62** (2012) 407.
[2] K. Kotake *et al.*, Prog. Theor. Exp. Phys. 2012 (2012) 01A301.
[3] K. Sumiyoshi and S. Yamada, Astrophys. J. Suppl. **199** (2012) 17.
[4] H. Nagakura *et al.*, Astrophys. J. **854** (2018) 136.
[5] S. Yamada *et al.*, Astron. Astrophys. **344** (1999) 533.
[6] K. Sumiyoshi *et al.* Astrophys. J **629** (2005) 922.
[7] K. Sumiyoshi *et al.*, Astrophys. J. Suppl. **216** (2015) 5.
[8] H. Nagakura *et al.*, Astrophys. J. Suppl. **214** (2014) 16, Astrophys. J. Suppl. **229** (2017) 42.
[9] S. Furusawa *et al.*, Astrophys. J. **738** (2011) 178, Astrophys. J. **772** (2013) 95.
[10] S. Furusawa *et al.*, Phys. Rev. C**95** (2017) 025809.
[11] J. Lattimer and D. Swesty, Nucl. Phys. A**535** (1991) 331.
[12] H. Shen *et al.*, Nucl. Phys. A**637** (1998) 435, Prog. Theor. Phys. **100** (1998) 1013.
[13] M. Hempel *et al.*, Astrophys. J. **748** (2012) 70.

8 Nuclear Data Required for Measurements of Reactivity and Nuclear Material Composition

Yasushi Nauchi
Nuclear Technology Research Laboratory, Central Research Institute of Electric Power Industry
2-6-1 Nagasaka, Yokosuka-shi, Kanagawa 240-0196 JAPAN
e-mail: nauchi@criepi.denken.or.jp

Nuclear data significant for reactivity measurements of a system are discussed. Near critical states, reactivities are measured based on the point kinetics. For the measurements, delayed neutron fractions and decay constants of precursors of the second and the first groups are significant. In subcritical states far from the criticality where the point kinetics is not available, gamma ray spectra measurement associated with neutron interaction is focused on since it gives information on material composition included in the target system and its negative reactivity.

1. Introduction

Management of neutron multiplication is essential in a system where uranium and plutonium exist. The multiplication is denoted by k_{eff} which is the expected number ratio of fission neutron emission between successive generations. The reactivity ρ defined as $1 - 1/k_{eff}$ is also used to see how the system departs from the critical. In a reactor, k_{eff} is controlled to unity by adjusting positions of control rods, concentration of soluble boron in coolant, or flow rate of the coolant. Without such control mechanisms, a system must be kept sub-critical.

k_{eff} and ρ are determined by spatial distribution of materials and their isotopic compositions. Thanks to developments of computer technology and evaluations of nuclear data, accurate calculations of k_{eff} and ρ are currently available [1]. However, except for the critical state, k_{eff} or ρ are indirectly measured quantities with help of data base or calculations with evaluated nuclear data files. Thus, the measurement accuracies of k_{eff} and ρ depend on those of nuclear data. In this work, relevant nuclear data required for some reactivity measurements are discussed.

2. Point kinetics

Near critical states, neuron population N and precursor density vary exponentially with time t. Reciprocal of $(\mathrm{d}N/\mathrm{d}t)/N$ is called the reactor period T. T is related to ρ with the effective delayed neutron fraction repartition per precursor group, $\beta_{eff,ij}$, and its decay constant λ_{ij} in accordance with eq. (1) [2].

$$\rho = \frac{\Lambda}{T} + \sum_{ij} \frac{\beta_{eff,ij}}{1+\lambda_{ij}T} \approx \sum_{ij} \frac{\beta_{eff,ij}}{1+\lambda_{ij}T} \ , \quad (1)$$

Here i is fission nuclide and j is the precursor group. The neutron generation time Λ is small so that Λ/T term in the right hand side of eq. (1) is negligibly small in conventional reactivity measurements. λ_{ij} is directly listed in evaluated nuclear data files. Definitions of $\beta_{eff,ij}$ is as follows.

$$\beta_{eff,ij} = \frac{\langle \phi^* (\int dE' \int d\Omega' \chi_{d,ij} \nu_{d,ij} \sigma_{f,i} N_i \phi) \rangle}{\langle \phi^* (\int dE' \int d\Omega' \sum_i \chi_{t,i} \nu_{t,i} \sigma_{f,i} N_i \phi) \rangle} \ . \quad (2)$$

Meanings of each symbol are as the same as in reference [3]. $\beta_{eff,ij}$ is usually calculated with nuclear data. To validate the calculated $\beta_{eff,ij}$ and the evaluated λ_{ij}, the reactivity ρ based on eq. (1) is compared to differences of reciprocal of k_{eff} between the critical and perturbed systems [3, 4]. For CROCUS perturbed cores (H2, H3, H4, B-ejection, and Er-ejection) [5], the reactivities are calculated by $\Delta(1/k_{eff})$ as listed in Table 1. The variation of the reactivities for different nuclear data files are less than 5%. Also, $\beta_{eff,ij}$ are calculated for critical cores and the reactivities are deduced with the measured period T for the perturbed cores based on eq. (1). The ρ with ENDF/B-VII.0 are 16~18% less than those by JEFF=3.1.1 and JENDL-4.0 and they do not agree with the reactivity by $\Delta(1/k_{eff})$. In the left figure of Fig. 1, $\beta_{eff,ij}$ of ENDF/B-VII.0 and JENDL-4.0 are compared. Although the difference in the summation of $\beta_{eff,ij}$ is within 3.3%, each $\beta_{eff,ij}$ shows differences. The largest difference is shown in the 4th group of ^{235}U fission. In the deduction of reactivity, reactivity component $\beta_{eff,ij}/(1+\lambda_{ij}T)$ are obtained. Comparison of the components is shown in the right figure of Fig. 1. The difference of the component is the maximum for the 2nd group of ^{235}U fission. Although the 2nd component $\beta_{eff,i2}$ is not dominant in β_{eff}, it is enhanced by $(1+\lambda_{ij}T)^{-1}$ term. This results indicate the significance of accuracy of the group wised $\beta_{eff,ij}$. Looking at eq. (2), nuclear data of $\nu_{d,ij}$ and $\chi_{d,ij}$ are important as well as λ_{ij}. Such kinds of validation with JEFF-3.1.1 has also been performed for FUBILA MOX fueled cores mocked up in EOLE. The reactivities deduced with the calculated $\beta_{eff,ij}$, evaluated λ_{ij} and measured flux variation with time agrees with those by $\Delta(1/k_{eff})$ within 4.1% error [3].

Table 1 Reactivity by equation (1) and those by $\Delta(1/k_{eff})$ [4]

Geometry	JEFF-3.1.1		ENDF/B-VII.0		JENDL-4.0	
(perturbed)	ρ by eq. (1)	ρ by Δ(1/k)	ρ by eq. (1)	ρ by Δ(1/k)	ρ by eq. (1)	ρ by Δ(1/k)
H2	88.9	86.5	73.7	87.5	87.5	90.5
H3	110.6	106.4	92.0	109.3	108.8	109.4
H4	131.2	127.2	109.6	128.2	129.1	132.3
B-ejection	85.8	82.5	71.2	82.5	84.7	82.6
E-ejection	162.3	162.0	136.5	158.0	160.1	163.1

In ENDF/B-VII.0 and JENDL-4.0, the delayed neutron emission data are evaluated in 6 precursor groups varying λ_{ij} for different fission nuclides. Contrarily in JEFF-3.1.1, $\nu_{d,ij}$, $\chi_{d,ij}$, and λ_{ij} are evaluated in 8 precursor groups using a universal λ_{ij} for different fission nuclides. When a negative reactivity is inserted

into core, the reactivity component $\beta_{eff,ij}$ /(1+$\lambda_{ij}T$) of the smallest λ_{ij} (j=1) would be dominant and it determines how rapidly the core power decreases in a case of reactor scram. Considering the significance, careful evaluation of λ_{i1} is required for actinides even if their fission rates are low.

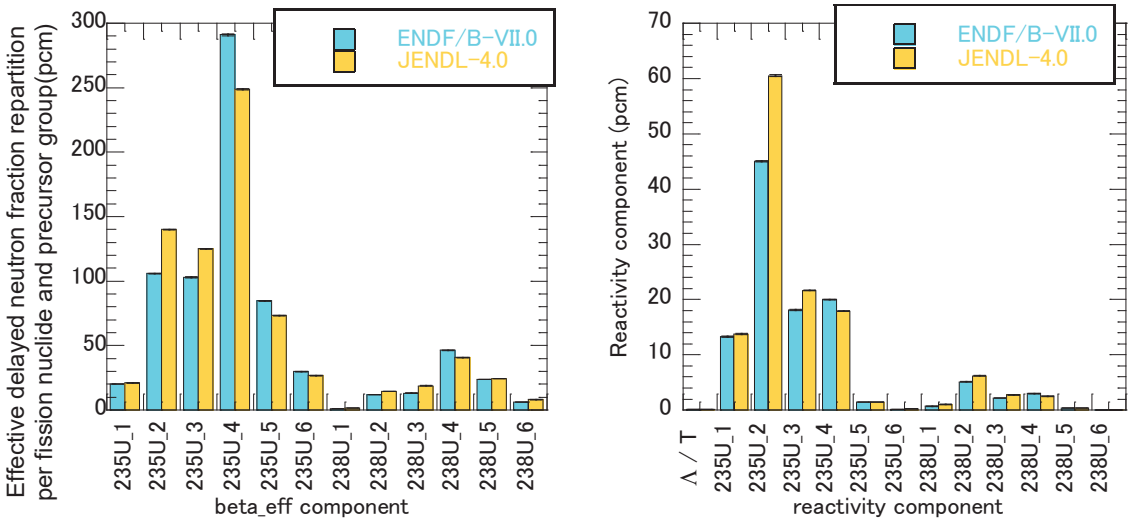

Fig. 1 Effective delayed neutron fraction (left) and reactivity (right) repartition per fission nuclide and precursor group [4].

3. Passive Measurement for Subcritical Multiplication Factor

In the deep subcritical systems where k_{eff} is less than 0.9, the direct measurement of k_{eff} is difficult since the neutron population decreases rapidly before the precursor density distribution converges to the fundamental mode. For the reason, other subcritical indices are measured such as the subcritical multiplication factor k_{sub} defined as follows.

$$k_{sub} = s_{2nd}/\left(s_{prim} + s_{2nd}\right) , \tag{3}$$

here, s_{prim} and s_{2nd} mean the number of neutron emission from an outer source and from induced fission reactions, respectively. Generally, neutron emission reactions are associated with γ ray emission. Then the total yield ratio of γ ray to neutron, (γ/ s) is related to k_{sub} as

$$(\gamma/s) = (\gamma/s)_{prim}(1 - k_{sub}) + (\gamma/s)_{2nd}k_{sub} \ . \tag{4}$$

(γ/ s)$_{\mathrm{prim}}$ is independent of system sub-criticality (1- k_{eff}). For a system where intact nuclear fuel assemblies (FAs) of the same material compositions are immersed in light water or borated water, (γ / s)$_{2\mathrm{nd}}$ is also independent of k_{sub} by measuring only higher energy γ rays (> 3 MeV) [6]. If (γ / s)$_{2\mathrm{nd}}$ separates from (γ / s)$_{\mathrm{prim}}$ enough, quantification of k_{sub} by measurement of (γ / s) is feasible. Neutron emissions from spontaneous fission and induced fission are considered to be well evaluated. Whereas, the γ ray emission above 3MeV in the system mainly consists of 1) prompt γ rays from spontaneous fission of ^{244}Cm and induced fission of ^{235}U, $^{239, 241}$Pu and 2) decay γ rays from short lived fission products (FPs). In the system, (γ / s)$_{2\mathrm{nd}}$ was estimated by MCNP-5 calculations [7] with the ENDF/B-VII.6 library for the 1) component and FPGS 90 calculations for the 2) component [8]. The ratio of (γ / s)$_{2\mathrm{nd}}$ to (γ / s)$_{\mathrm{prim}}$ based on the

ORIGEN original library [9] is 1.95~2.0 for assembly-burn up from 30 to 55 MWd/kgHM [10], i.e. $(\gamma / s)_{prim}$ and $(\gamma / s)_{2nd}$ are well separated. However, according to Verbeke, the number ratio (γ / s) of thermal fission of ^{235}U including whole energy region of γ ray is 2.79 ±0.31 and that of spontaneous fission of ^{244}Cm is 2.57 ±0.30 [11], i.e. $(\gamma / s)_{prim}$ and $(\gamma / s)_{2nd}$ are not separated well. To judge the feasibility to determine k_{sub} based on (γ / s), fission prompt γ ray emission data have to be reviewed referring resent measurements [12, 13]. Also, comprehensive validation of the γ ray emission data from short lived FP in latest libraries [14] should be performed.

4. Neutron Induced Gamma Ray Spectroscopy

Since necessary parameters such as $\beta_{eff,ij}$ or $(\gamma / s)_{prim,2nd}$ depend on material compositions and its distribution, measurements of absolute sub-criticality is difficult for a system where the material composition is unknown. In a prevention toward approach of criticality management, k_{eff} of a system is calculated with a conservative geometry and material composition model where fuel of the maximum enrichment distributes in the optimum condition with neutron moderator. If we apply such method for storage of fuel debris formed in unit 1~3 of Fukushima Daiichi nuclear power station, large area is required for its storage. To mitigate the situation, the author has proposed to measure γ ray spectra from fuel debris enclosed in a canister.

Generally, γ ray spectra measurement for spent fuel is suffered from high γ ray dose from long-lived FPs contained in spent fuel. The γ ray energy ranges up to 3.4 MeV (^{106}Rh). Thus we focused on neutron induced γ ray spectroscopy (NIGS). γ rays of NIGS consist of 1) fission prompt γ ray, 2) decay γ ray of short-lived FP, 3) capture γ ray, 4) de-excitation γ ray associated with nucleon emission reaction including inelastic scattering. Energy of those γ rays ranges greater than 3.4 MeV so that they can be distinguished from the γ rays from the long-lived FP.

One candidate to use NIGS for the fuel debris is to take capture Credit (CapC). In fuel debris, significant amount of stainless steel (SS) and other neutron absorbing materials are included. The number ratio of neutron absorption by some capture reaction l to fission is proportional to the negative reactivity brought by the capture reaction l [15]. The ratio can be measured by NIGS focusing on discrete energy γ ray emission from reaction l. In Kyoto university critical assembly facility (KUCA) uranium – aluminum alloy fuel (U) and stainless steel (SS) plates were loaded in light water and ^{252}Cf source was put. γ ray spectra were measured with a BGO scintillator. As shown in Fig. 2, fission prompt components from 3 MeV to 5 MeV decreases as the SS ratio increases and the capture γ ray of 5~10 MeV increases. The results have shown feasibility of CapC by NIGS. By a numerical simulation, the possibility to confirm negative reactivity of residual ^{157}Gd by counting 6.75 MeV γ ray was also indicated [16]. To know the negative reactivities brought by SS and ^{157}Gd ensures the sub-criticality margin and enables denser storage of fuel debris.

Another candidate to use NIGS is determination of some isotopic compositions of uranium and plutonium, those would be good clue to estimate the residual enrichment. In KUCA, a sub-critical uranium core of 5.4 wt% - average ^{235}U enrichment is mocked up and NIGS were performed with a Germanium

detector [17]. The measured spectra are shown in Fig. 3. Here, 4.06 MeV γ ray peak from ^{238}U(n,γ) reaction is found above continuum spectrum of the fission prompt γ ray. Also, γ rays from short lived FP such as ^{90,91}Rb and ^{97}Y are observed. The results indicate possibility of the delayed gamma ray analyses to give fission repartition per isotopes such as ^{235}U:^{238}U:^{239}Pu:^{241}Pu [18].

To quantify the reaction rate ratios enable denser storage of the fuel debris, yields and spectra of γ ray emission are essential. Capture γ ray data are evaluated for thermal neutron reaction [19], but the accuracy of ^{56}Fe(n,γ) γ ray emission is only 17% and γ ray emission per capture is not evaluated for ^{53}Cr(n,γ) data. In addition, γ ray emission per thermal neutron capture of ^{238}U may differ from that of the resonance capture reactions [20]. Therefore, more accurate and detailed evaluations for γ ray emissions are required.

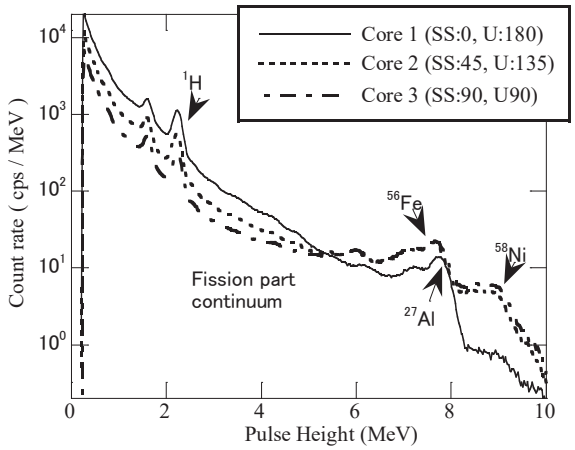

Fig. 2 γ ray pulse height spectra measured for simulated fuel debris which consists of U-Al alloy fuel (U) and SS plates [15].

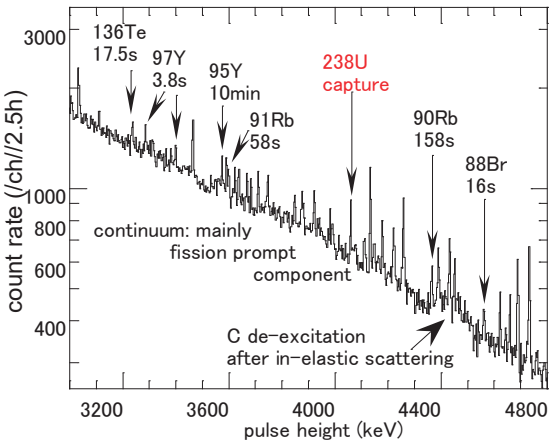

Fig. 3 γ ray pulse height spectra measured for polyethylene moderated core of uranium fuel equivalent to 5.4 wt% enrichment [17].

5. Summary

Nuclear data required for reactivity measurements were discussed. For measurements based on the point kinetics, $\nu_{d,ij}$, $\chi_{d,ij}$, λ_{ij} of j = 1 and 2 are important. For the determination of k_{sub} by (γ / s) ratio, fission prompt γ ray emission data should be well reviewed as well as γ ray emission data from short lived FP. Those data are also essential for estimation of material compositions and negative reactivities by NIGS. For NIGS, review of capture γ ray emission data for actinides and structural materials are required.

References

[1] Chiba G., Okumura K., Sugino K., *et a*l. JENDL-4.0 benchmarking for fission reactor applications, Journal of Nuclear Science and Technology. 2011; **48**(2):172-187.

[2] Keepin GR.Physics of Nuclear Kinetics. U.S.: Addison Wesley Publishing Company, Inc; 1965.

[3] Nauchi Y., Blaise P., Jouanne C., Zoia A., Monte carlo calculation of kinetic parameters to deduce pilot rod worth of FUBILA MOX cores, Proceedings of PHYSOR2018;2018 Apr 22-26; Cancun, Q.R., Mexico.

[4] Zoia A., Nauchi Y., Brun E., *et al*., Monte Carlo analysis of the CROCUS benchmark on kinetics

parameters calculation, Annals of Nuclear Energy. 2016; **96**:377-388.

[5] Paratte, J.M., Früh R., Kasemeyer U. *et al*., A benchmark on the calculation of kinetic parameters based on reactivity effect experiments in the CROCUS reactor, Annals of Nuclear Energy. 2006; **33**:739-748.

[6] Nauchi Y., Kameyama T., Matsumura T. *et al*., Measurement and Analysis of High Energy Gamma Ray and Neutron in MOX Fuel Lattices for Subcriticality Estimation, Proceedings of PHYSOR2002:2002 Oct7-10; Seoul Korea.

[7] X-5 Monte Carlo team, MCNP –a general Monte Carlo n-particle transport code version 5., Los Alamos, NM, US: Los Alamos national laboratory;2003 (LA-UR-03-1987).

[8] Ihara H., Katakura J., Nakagawa T., A Computer code for calculation of radioactive nuclide generation and depletion, decay heat and γ ray spectrum: FPGS90. Tokai, Ibaraki, Japan: Japan Atomic Energy Research Institute;1995 (JAERI-Data/Code 95-014).

[9] Croff A.G., ORIGEN2 – a revised and updated version of the Oak Ridge isotope generation and depletion code. Oakridge, TN, US: Oakridge National Laboratory;1980(ORNL-5621).

[10] Nauchi Y., Kameyama T., Sasahara A., Estimation of the effective multiplication factor for a spent - fuel storage pool -The method utilizing the yield ratio of high energy gamma rays to neutrons- . Tokyo, Japan: Central Research Institute of Electric Power Industry;2004.(CRIEPI Research Report T02024).

[11]Verbeke J.M., Hagmann C., Write D., Simulation of Neutron and Gamma Ray Emission from Fission and Photofission. LLNL Fission Library 2.0.2.CA, US: Lawrence Livermore National Laboratory, 2016 (UCRL-AR-228518-REV-1).

[12] Oberstedt S., Billnert R., Gatera A. *et al*., Prompt fission γ-ray spectra characteristics - a first summary, Physics Procedia. 2015;**64**: 83-90.

[13] Makii H., Nishio K., Hirose K. *et al*. Measurement of high-energy prompt gamma-rays from neutron induced fission of U-235, EPJ Web of Conferences. 2017;146:04036.

[14] Katakura J., JENDL FP Decay Data File 2011 and Fission Yields Data File 2011. Tokai, Ibarakai, Japan: Japan Atomic Energy Agency;2012 (JAEA-Data/Code 2011-025).

[15] Nauchi Y., Ohta H., Unesaki H. *et al.*, Concept of capture credit based on neutron induced gamma ray spectroscopy, Journal of Nuclear Science and Technology. 2015;**52**(7-8):1074-1083

[16] Nauchi Y., Characterization study of candidate technologies for nuclear material quantification in fuel debris at Fukushima Daiichi nuclear power station (5) Active γ Method. In: Proceedings of 2017 spring meeting of Atomic Energy Society of Japan: 2017 Mar 27-29; Tokai-Univ., Hiratsuka, Kanagawa, Japan.

[17] Nauchi Y., Sato S., Suzuki M. *et al*., Measurement of ^{238}U(n, γ) γ ray from sub critical system., Kumatori, Osaka, Japan: Kyoto University Reactor Research Institute: 2018 (KURRI progress report 2017).

[18] Koizumi M., Rossi F., Rodriguez D.C. *et al*., Delayed gamma-ray spectroscopy combined with active neutron interrogation for nuclear security and safeguards, EPJ Web Conf. 2017; **146**: 09018.

[19] Thermal Neutron Capture γs (CapGam). 2013 [cited 2019 Dec 26] Available from: https://www.nndc.bnl.gov/capgam/.

[20] Harada H., Goko S., Kimura A. *et al*., Study of neutron capture reactions using 4π Ge spectrometer, Journal of the Korean Physical Society. 2011; **59**(2):1547-1552.

9 Development of Active Neutron NDA System

Yosuke Toh
Japan Atomic Energy Agency (JAEA),Tokai-mura, Naka-gun, Ibaraki 319-1195, Japan
e-mail:toh.yosuke@jaea.go.jp

The Joint Research Centre (JRC) of the European Commission and the Japan Atomic Energy Agency (JAEA) Collaboration Action Sheet-7 started in 2015 to develop an active neutron NDA system for nuclear non-proliferation and nuclear security. In this project we have developed an innovative non-destructive analysis (NDA) system using a D-T pulsed neutron source. Four active neutron NDA techniques, namely Differential Die-Away Analysis (DDA), Prompt Gamma-ray Analysis (PGA), Neutron Resonance Transmission Analysis (NRTA) and Delayed Gamma-ray Analysis (DGA) have been studied and developed with Monte Carlo simulation codes. The different techniques can provide complementary information which is particularly useful for quantification of Special Nuclear Material (SNM) and Minor Actinide (MA) in highly radioactive nuclear materials. This project has two phases. In the first phase of the project, we developed a combined NDA system, which enables the simultaneous measurements of DDA and PGA, at NUclear fuel Cycle safety Engineering research Facility (NUCEF) in the JAEA Tokai-site. The second phase focuses on the development of the active neutron NDA system for highly radioactive materials, such as nuclear waste and spent nuclear fuel. In this phase, we continue to conduct additional research to improve the methodology and develop an integrated NDA system which can be used for NRTA as well as DDA and PGA. Monte Carlo simulation provides a powerful means to determine design of the active neutron NDA system. Nuclear data is necessary for accurate evaluation of the results of the Monte Carlo simulation in the developments of the NDA system. However, some of nuclear data is not accurate enough to obtain sufficient information.

1. Introduction

The Joint Research Centre (JRC) of the European Commission and the Japan Atomic Energy Agency (JAEA) collaboration Action Sheet-7 launched to develop an active neutron NDA system for highly radioactive nuclear materials in 2015[1,2]. Figure 1 shows main components of our project. The project aims at contributing to the establishment of an innovative non-destructive analysis (NDA) system using a D-T pulsed neutron source. Four active neutron NDA techniques, namely Differential Die-Away Analysis: DDA, Prompt Gamma-ray Analysis: PGA (and Neutron Resonance Capture Analysis: NRCA), Neutron Resonance Transmission Analysis: NRTA and Delayed Gamma-ray Analysis: DGA have been studied in the project. The basic principles of the techniques are shown in Table 1. Four techniques can provide complementary information which is necessary for quantification of Special Nuclear Material (SNM) and Minor Actinide (MA) in highly radioactive nuclear materials. In the first phase of the project, we developed a combined NDA system at NUclear fuel Cycle safety Engineering research Facility (NUCEF) in the JAEA Tokai-site. The developed NDA system enables the simultaneous measurements of DDA and PGA. The second phase focuses on the development of the active neutron NDA system for highly radioactive materials, such as nuclear waste and spent nuclear fuel. In this phase, we continue to conduct additional research to improve the methodology and develop an integrated NDA system which consists of NRTA as well as DDA and PGA (See Fig.2).

Monte Carlo simulation codes, such as PHITS [3] and MVP [4], which have been developed by JAEA, are indispensable tools for developments of an active neutron NDA system. The simulation codes have been widely used in the developments of an active neutron NDA system consisting of detector systems, neutron and gamma-ray shields, neutron moderators and neutron reflectors etc. A desired target accuracy of an NDA system is typically 5%, although it depends on the purpose of the measurements. Therefore, the simulation for the NDA system requires accurate nuclear data. In particular, nuclear data is necessary to evaluate the NRTA and NRCA system because these techniques have to utilize resonance parameters that can only be given from

nuclear data. Thus nuclear data plays an important role in Monte Carlo simulations for the active neutron NDA system.

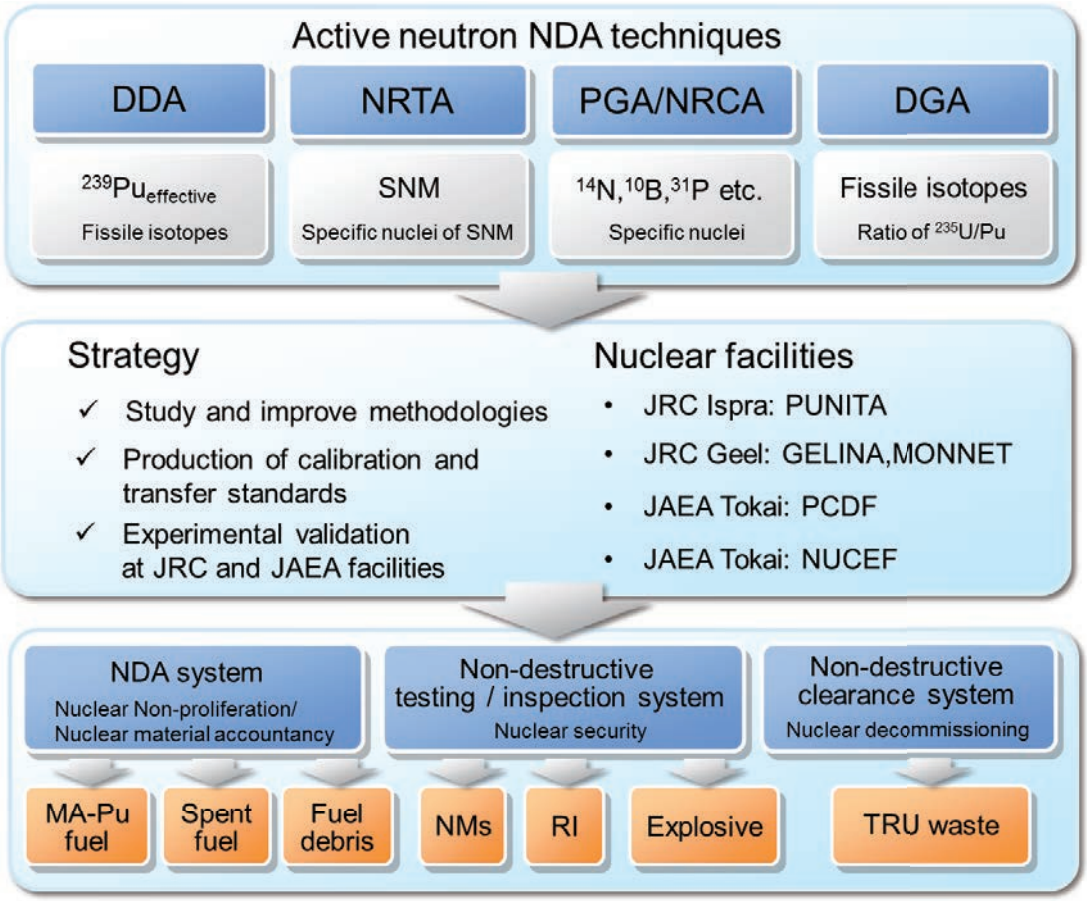

Figure 1. Schematic diagram of JRC – JAEA collaboration: Action Sheet -7.

Table 1: Principles of active neutron NDA techniques and quantities of interest.

NDA techniques	Principles	Quantities of interest
DDA	Interrogation by a pulsed neutron Detection of induced prompt fission neutrons Correction of matrix effect	Total fissile content
NRTA	Irradiation by a moderated pulsed neutron beam Detection of neutrons transmitted through a sample Analysis of neutron transmission spectrum	U and Pu contents
PGA NRCA	Irradiation by a (pulsed) neutron beam Detection of prompt γ rays from (n,γ) reactions Analysis of γ-rays/time-of-flight spectrum	Specific nuclides contents (explosives, chemical warfare agents, etc.)
DGA	Irradiation by a (moderated) neutron Detection of delayed γ rays from fission products Analysis of γ-rays spectrum	$^{235}U/^{239}Pu$ and/or $^{241}Pu/^{239}Pu$

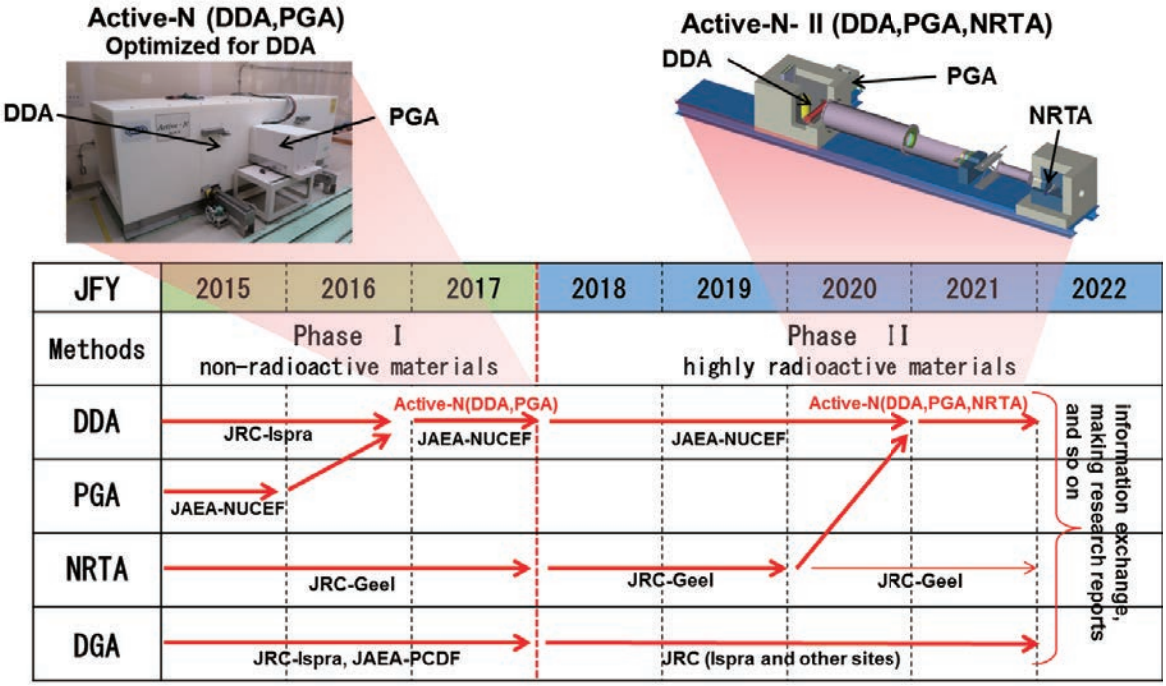

Figure 2. Research timeline of developments of Active-N system.

2. Simulation and experimental studies

Four active neutron methods DDA, NRTA, PGA/NRCA and DGA have been studied and improved with Monte Carlo simulation codes, such as PHITS [3], MVP [4]. Experimental measurements have been conducted at the JRC Geel site Linear Accelerator (GELINA), the PUNITA facility in the JRC Ispra site and the NUCEF in JAEA.

2.1 DDA

The DDA technique requires a pulsed neutron source which is used for sample interrogation. DDA measures fission neutrons and can detect very small amounts of the fissile materials, such as ^{235}U and ^{239}Pu. The prompt fission neutrons are detected in a neutron He-3 detector bank, and can be distinguished from the interrogation neutrons. The DDA technique has been investigated and developed for many years. Several different systems and methodologies have been proposed. The most common method of DDA uses a thermal neutron for sample interrogation because the fission probability remains constant during the interrogation period. On the other hand, JAEA-DDA utilizes fast and epi-thermal neutrons for interrogation. There are differences between conventional DDA and JAEA-DDA in many ways, such as methodology, hardware and software. The project involves the exchange of the results of scientific and technical research for the DDA technique, as well as the exchange of information arising from the collaboration. The Active-N system for DDA and PGA measurements was designed and developed by Monte Carlo simulation codes, and installed at the NUCEF in the JAEA Tokai-site at the end of 2017 (See Fig. 2). The optimal value (around 5-7cm) of the moderator thickness of a vial bottle (ϕ26 x 40mm) was determined from the simulation results. The neutron flux distributions in a sample, which are very important in the measurements of the samples having a non-uniform composition, are also investigated with simulations and experiments. Figure 3 shows calculation to experiment ratios (C/E) of the neutron flux distribution in a polyethylene sample [5]. There are rather large discrepancies (approximately 15%) at the positions C, D and E. On the other hand, the ratios of positions A and B, which are located near the neutron source, are small. Therefore, the discrepancies may be caused by an error of a neutron scattering law S(α,β). It appears that accuracy improvement of nuclear data S(α,β) is needed for the evaluation of the simulation results with regard to the active neutron NDA system.

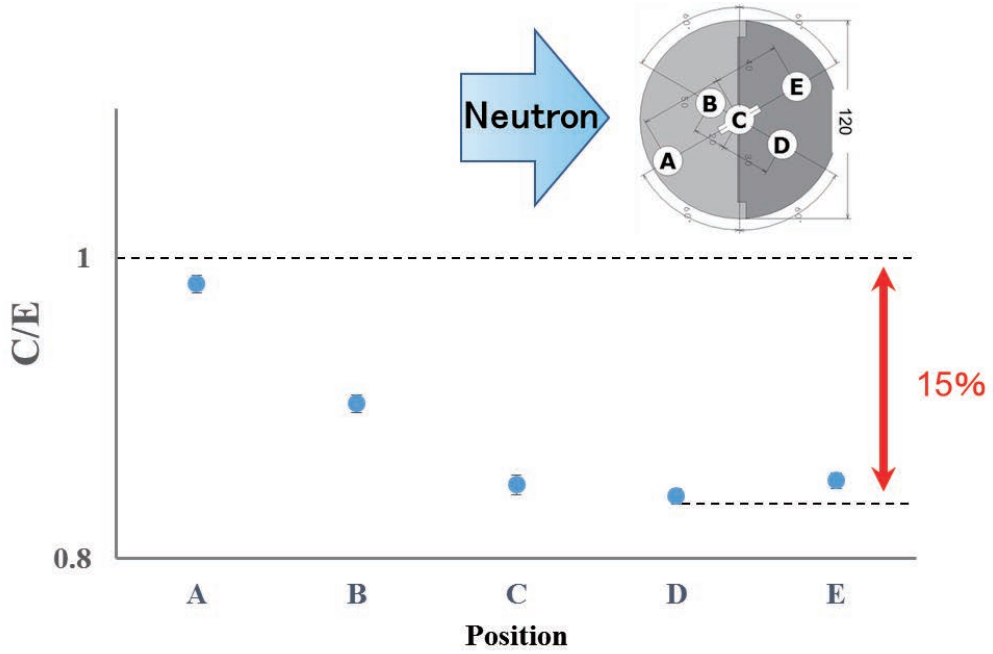

Figure 3. Calculation to experiment ratios (C/E) of neutron flux distribution in polyethylene.

2.2 NRTA

NRTA is an NDA technique which utilizes the energies of resonances to identify nuclides (elements) by the time-of-flight technique [6,7]. NRTA can quantify almost all medium and high-Z elements and is known as one of the most accurate NDA techniques to quantify the amount of SNM and MA. However, the quantification accuracy of NRTA is highly depended on the uncertainty of nuclear data because the resonance analysis program REFIT [8] use nuclear data in the analytical process. The experiments of metallic natural Cu samples were performed at the TOF-facility GELINA. Figure 4 shows the results of REFIT code analysis of the 579 eV resonance peak in the NRTA spectrum of the Cu sample which has a thickness of 20 mm [9,10]. The blue dotted line indicates the result from using Γ_n=0.59 [11]. On the other hand, the red solid line shows the

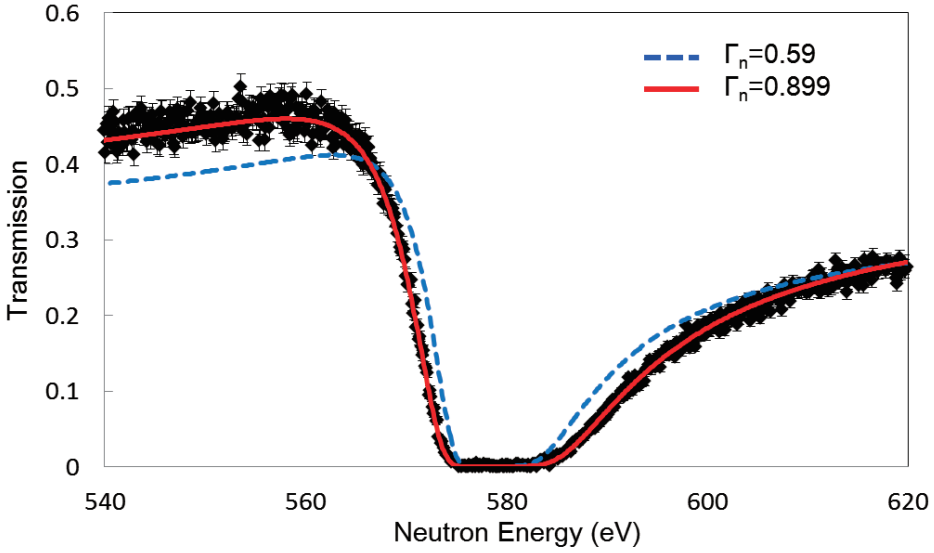

Figure 4. REFIT code analysis of NRTA spectrum of a Cu sample. The blue dotted line shows the fitting result from using Γ_n=0.59. The red solid line shows Γ_n=0.899.

result from using Γ_n=0.899 that is obtained from the fitting of the spectrum. Obviously, the accuracy of the resonance parameter of Cu is not enough to quantify the Cu sample. Note that this will not be an exceptional case. The resonance parameters of most nuclei should be improved for the accurate quantification of NRTA.

2.3 PGA / NRCA

PGA utilizes neutron capture γ rays, which are characteristic of each particular nuclide. These provide the means to identify and quantify the elemental constituents of a sample. Thus, PGA has been used as a rapid, non-destructive method for performing both qualitative and quantitative multi-elemental analysis and is well acknowledged to be especially valuable for the measurement of light elements such as H, B, N, Si, S, and Cl, as well as Cd, Gd, Sm, and Hg. Therefore, PGA is used for the quantification of neutron poison and particularly useful for the detection of explosives, since the most typical high explosive materials contain nitrogen. The principle of NRCA is essentially similar to that of NRTA [6,7]. It differs from NRTA in that it detects γ rays emitted in neutron resonance capture reactions. In general, NRCA has a better detection limit compared to NRTA for most elements. However, for high radioactive nuclear materials, NRCA may lose the advantage in the detection limit since the γ rays from radioactive materials increase the background in the γ-rays spectrum. The PGA detector system, which can install two detectors: a high energy resolution Ge detector and a fast response $LaBr_3$ detector, was designed with Monte Carlo simulation codes which require nuclear data. PGA and NRCA use many of nuclear data, such as intensities and energies of γ rays and resonance parameters. However, nuclear data is still lacking for PGA and NRTA.

2.4 DGA

DGA typically utilizes delayed (mainly β decay) γ rays emitted from the fission products. The mass distribution of the fission products is correlated with the mass of the fissile nuclei, such as ^{235}U, ^{239}Pu and ^{241}Pu. Therefore, the intensities of individual gamma-ray peaks in the DGA spectra allow us to determine the ^{235}U/^{239}Pu and/or ^{241}Pu/^{239}Pu ratio. DGA systems were designed and examined with Monte Carlo simulation codes[12]. Nuclear data especially with regard to high-energy delayed gamma rays is required to accurate evaluation of the results of DGA.

3. Summary

JRC – JAEA collaboration AS-7 aims at contributing to the establishment of an innovative non-destructive analysis (NDA) system for the quantification of SNM and MA in highly radioactive nuclear materials. Four active neutron NDA techniques, namely DDA, PGA/NRCA, NRTA and DGA have been studied and improved. The Monte Carlo simulation code was utilized to develop the NDA system, consisting of detector systems, neutron and gamma-ray shields, neutron moderators and neutron reflectors etc. Nuclear data plays an important role in Monte Carlo simulation of the NDA system. However, nuclear data is still lacking to accurate evaluation of the results of the calculation. Therefore, nuclear data should be improved, especially for the developments of the NDA system.

4. Acknowledgements

This research was implemented under the subsidiary for nuclear security promotion of MEXT.

5. References

[1] Kureta M. *et al.*; *JAEA − JRC Collaboration on the Development of Active Neutron NDA Techniques*, Proceedings of 37th ESARDA Symposium on Safeguards and Nuclear Non-Proliferation, Manchester, UK; 2015; pp.111-120.

[2] Toh Y. *et al.*,; *Development of Active Neutron NDA Techniques for Nuclear Non-proliferation and Nuclear Security,* Proceedings of 39th ESARDA Symposium on Safeguards and Nuclear Non-Proliferation, Meliá Düsseldorf, Düsseldorf, Germany; 2017;pp.684-693.

[3] Sato T. *et al*.; *Particle and Heavy Ion Transport code System, PHITS, version 2.52*; Journal of Nuclear Science and Technology; **50**[9]; 2013; pp. 913-923.

[4] Nagaya Y. et al.; *MVP/GMVP II: General Purpose Monte Carlo Codes for Neutron and Photon Transport Calculations based on Continues Energy and Multigroup Methods*; JAERI 1348; 2005.

[5] Maeda M. *et al*., *Comparison between simulation and experimental results for neutron flux in DDA systems*, ESARDA Symposium 2017 / 39th Annual Meeting, Düsseldorf Germany, pp.694-701; 2017.

[6] Postma H. and Schillebeeckx P.; *Neutron Resonance Capture and Transmission Analysis*; Encyclopedia of Analytical Chemistry (John Wiley & Sons Ltd); 2009; pp.1-22.

[7] Schillebeeckx P. *et al*.; *Neutron Resonance Spectroscopy for the Characterisation of Materials and Object*, Report EUR 26848 EN.

[8] Moxon M. and Brisland J.; *GEEL REFIT, A least squares fitting program for resonance analysis of neutron transmission and capture data computer code*; AEA-InTec-0630; AEA Technology; October 1991.

[9] Tsuchiya H. *et al*.; *Impact of systematic effects on results of neutron resonance transmission analysis*, Nucl. Instrum. Methods Phys. Res. A **767**; pp.364-371; 2014.

[10] Tsuchiya H. *et al*.; *Development of active neutron NDA techniques for nonproliferation and nuclear security (2) Study on a compact NRTA system*, Proceedings of INMM 57th Annual Meeting; Marriott Marquis, Atlanta, GA, USA; 24-28 July 2016.

[11] Mughabghab, S.F.; “Atlas of Neutron Resonances,5th Edition”, Elsevier Science, ISBN: 0-44-52035-X 2006.

[12] Koizumi, M. *et al*.; *Delayed gamma-ray spectroscopy combined with active neutron interrogation for nuclear security and safeguards*, EPJ Web of Conferences 146, 09018, 2017.

10 The Importance of Nuclear Structure and Decay Data for Nuclear Science and Applications

Paraskevi Dimitriou
Nuclear Data Section, Division of Physical and Chemical Sciences,
International Atomic Energy Agency,
Wagramerstrasse 5, A-1400 Austria
Email: P.Dimitriou@iaea.org

Nuclear structure and decay data are essential for many applications such as Nuclear power, Nuclear fusion, Medicine, Non-destructive testing, Environmental monitoring, Safety and Security, but also for basic nuclear sciences. The availability of reliable, up-to-date and well-structured nuclear structure and decay data libraries, with user-friendly visualization and retrieval tools, are indispensable not only for the nuclear specialists in the various applications fields, but also for the nuclear physics researchers who need the data to improve their knowledge from existing studies and to plan future activities that may lead to new discoveries.
In this paper we showcase the importance of evaluated nuclear structure and decay data and the role of the international network of nuclear structure and decay data evaluators.

1. Introduction

Reliable, up-to-date and well-structured nuclear structure and decay data libraries are indispensable not only for the nuclear specialists in the various applications fields, but also for the nuclear physics researchers, therefore, such credible and reliable data libraries have a profound societal impact as they connect science and technology with society.
The collection, evaluation and dissemination of nuclear structure and decay data is a laborious task that relies on contributions from experts in basic and applied science research communities. Efforts carried out on a national and international level benefit from the coordination provided by international organizations such as the International Atomic Energy Agency in Vienna (IAEA) and the Nuclear Energy Agency of the Organisation for Economic Co-operation and Development (NEA-OECD) in Paris. The development and maintenance of nuclear data libraries, and dissemination of nuclear data to various user communities is the main goal of the international networks associated with these agencies: the Nuclear Reaction Data Centres Network (NRDC/IAEA) [1], the Nuclear Structure and Decay Data evaluators (NSDD/IAEA) [2], and the Working Party on International Nuclear Data Evaluation Co-operation (WPEC/NEA) [3].
In the last decades, the support of national funding agencies for activities related to compilation, evaluation and dissemination of nuclear structure and decay data has decreased significantly. On the other hand, the research activity has increased through the development of new technologies and advent of radioactive beam facilities, leading to a rapid growth in the production of new experimental data. At the same time, the demand from applications for more reliable and precise data produced in these new facilities is also rising.

The challenge is to assure that the new data produced by the advances in nuclear science and technology, are reflected in the available databases. The key issue that needs to be addressed by the nuclear sciences community, is how to maintain a high level of expertise in the area of nuclear structure and decay data evaluation to meet the requirements of a continuously developing research and applied sciences landscape.

2. Evaluated Nuclear Structure Data File (ENSDF)

The Evaluated Nuclear Structure Data File (ENSDF) [1] is a collection of recommended data for nuclear properties including decay branches, level energies and lifetimes, transition multipolarities, strengths and conversion coefficients, and complete radiation properties, for all known nuclides. These data are evaluated and maintained by the international network of Nuclear Structure and Decay Data evaluators (NSDD) [2].

The NSDD network was established in 1974 under the auspices of the IAEA, and since 2017 includes 17 data centers and over 20 internationally-recognized experts from more than 10 countries including USA, Canada, China, Japan, Australia, India, Russia, Hungary, Romania, Bulgaria. The evaluations are published in the peer-reviewed journal Nuclear Data Sheets. In addition, they also compile the most recent experimental nuclear structure and decay published results in the experimental unevaluated nuclear data list (XUNDL) [3]. These databases contain the data in computerized format and are available both online and offline. They are both hosted and managed by the National Nuclear Data Center (NNDC) at Brookhaven National Laboratory.

The ENSDF database draws information on atomic masses (Q values) from the Atomic Mass Evaluation [4] provided by the Atomic Mass Data Centre (France and China), and on nuclear moments from the compilations of N. Stone [5] which are also available online at the IAEA Nuclear Moments Database [6].

ENSDF is a unique database, as it is comprehensive, continuously updated and serves as the source of data for several derivative, special-purposes databases and products as is illustrated in Figure 1. For example, the vast majority of decay data included in the general purpose evaluated data libraries such as ENDF/B, JEFF, JENDL, ROSFOND, CENDL in their decay data sub-libraries, are taken from ENSDF.

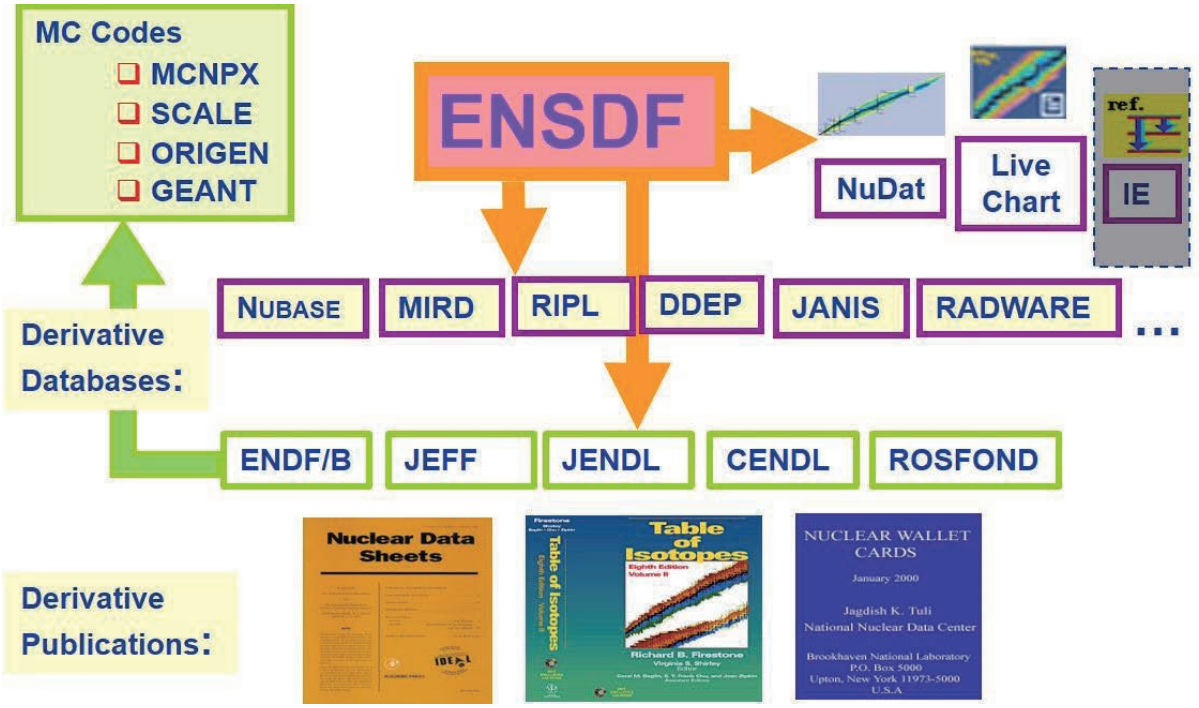

FIG 1. Illustration of how ENSDF is providing evaluated nuclear structure and decay data for a host of other derivative or special-purpose databases.

3. Impact of ENSDF

An example of the importance of having reliable and up-to-date nuclear structure and decay data from ENSDF to evaluations of nuclear reaction cross sections and isomeric ratios up to 20 MeV is given in this section (for more details see Ref. [7]).

Neutron-induced reactions with neutron energies up to 20 MeV are relevant in accelerator driven systems and fusion reactors. In particular, excitation functions of Ni, Co, Fe isotopes are of interest since thy are important components of many types of steel in reactor construction. Ni isotopes for example have large neutron-induced proton emission cross sections that lead to four important residual isotopes ^{56}Co, ^{57}Co, ^{58}Co, ^{60}Co. The activity of the residual isotope ^{58}Co is of concern, namely the cross sections of the following activation reactions for energies up to 20 MeV: ^{59}Co(n,2n)^{58}Co, ^{58}Ni(n,p)^{58}Co, ^{58}Fe(p,n)^{58}Co.

Calculations based on the statistical model and preequilibrium theory are compared with experimental data for the contributions to the total, ground state (gs) and 1st isomeric state in Fig. 2. The differences between the two figures in the left and right panel are attributed to the nuclear structure data used to calculate the transitions to the low-lying discrete states and which are originally taken from ENSDF. In Fig. 2, left panel, the transitions to the 1st isomeric state of ^{58}Co are calculated assuming a value of the multipolarity mixing δ = -0.33 as is recommended in ENSDF [8]. However, other measurements of the isomeric cross-section ratio also support the value δ = -2.3. When using the latter value to calculate the transitions to the 1st isomeric state, one obtains the improved results shown in the right panel. These results confirm the strong dependence of nuclear reaction cross-section calculations on nuclear structure data and highlight the need for maintaining

the currency and quality of the ENSDF database. The ENSDF database has been subsequently updated to include δ = -2.3 in the file.

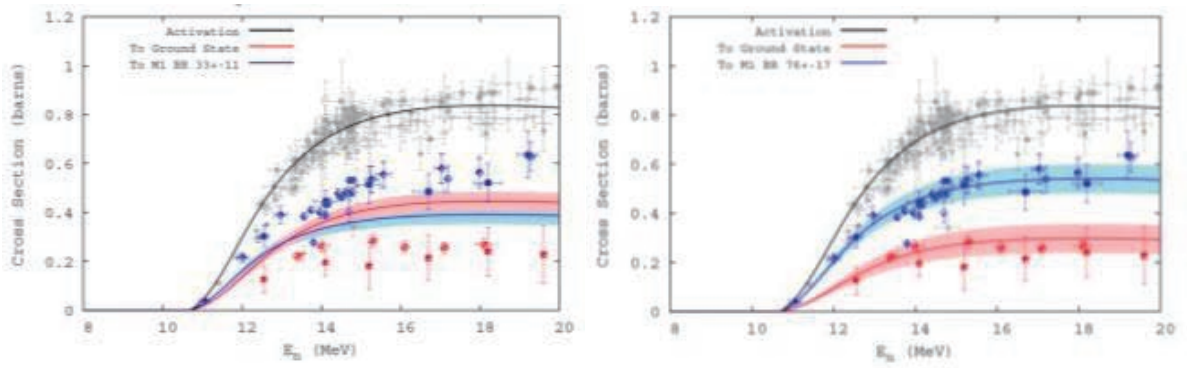

FIG 2. Left panel: Cross sections to the ground state and 1st isomeric state for the reaction $^{59}Co(n,2n)^{58}Co$ using the original value of δ = -0.33 for multipolarity mixing [8]. Right panel: Same cross sections but using the value δ = -2.3 confirmed by measurements (figures from [7]).

4. Future

The evaluation and dissemination of nuclear structure and decay data is an international effort of the NSDD network that is coordinated by the IAEA. For many years now, the network has been facing problems in maintaining and updating the ENSDF database with the same regularity as in the past, due mainly to a shortfall in effort coming from Europe and Asia where the retirement of evaluators was not followed by commensurate replacements. An IAEA initiative to bring together nuclear structure specialists from the European Union and Turkey to discuss the current situation with ENSDF specialists in 2008 [9] lead to some positive outcomes: two new European ENSDF Data Centres joined the network (Hungary, Romania), and a European collaborative effort to support ENSDF through the contribution of mass-chain and horizontal evaluations was formed. Since then a third Data Centre has joined (Bulgaria). However, the three data centers only contribute about 10% of the total effort which is far less than what is expected from a region that is world-known for its technical expertise and output of data from its several top-class, large-scale facilities. A similar trend is seen in Japan, where the contribution to ENSDF has dropped to 2% in the past decade due to the decrease in numbers of evaluators.

The situation is compounded by the recent retirement of senior evaluators from the US national laboratories, and the imminent retirement of more evaluators both in the US and Japan, which may not be commensurated by an equal number of replacements. There is now an imminent risk of losing the technical expertise in addition to the evaluators. Under these circumstances, the worldwide nuclear research and nuclear data community needs to address the following issues:

-is the ENSDF database with recommended nuclear structure data important for their scientific work and for the society at large?

-what would the consequences be (for their current and future projects) if ENSDF were to become outdated

and obsolete?

-is the European and Asian community prepared to step up and take action to avert such a loss of data and expertise?

In an attempt to raise awareness of the situation and the pressing need for action on the part of the European nuclear structure community, the IAEA has liaised with the European NSDD collaboration to promote ENSDF evaluations in Europe which has led to a recognition of the value of nuclear structure and decay data in the newly released Long Range Plan of the Nuclear Physics Expert Collaboration Committee (NuPECC) [10] including recommendations for support of compilation and evaluation of nuclear structure and decay data in Europe.

A similar effort should also be made to engage the nuclear data community of other large nuclear data producing countries, such as Japan. Apart from a long history and successful tradition in serving the nuclear applications community with nuclear data, Japan has a large-scale facility that produces nuclear decay data at a formidable rate (RIKEN). Nuclear structure physicists from RIKEN are already embarking on training schemes and collaborations for compilation of the RIKEN data in the XUNDL database.

However, more effort is needed to maintain the expertise in ENSDF evaluation -which has been ongoing at JAEA for at least 30 years. The active involvement of young nuclear experts at JAEA and RIKEN at this stage is important so that they can profit from the existing expertise before it is too late. The Japan nuclear data community will benefit from maintaining the expertise in the evaluation of both nuclear structure and decay, as well as nuclear reaction data, as it clear that the future of JENDL and ENSDF are inter-connected.

5. Reference

[1] ENSDF, http://www.nndc.bnl.gov/ensdf/

[2] International Network of Nuclear Structure and Decay Data Evaluators, http://www-nds.iaea.org/nsdd/

[3] XUNDL, http://www.nndc.bnl.gov/xundl/

[4] Atomic Mass Data Center, http://amdc.impcas.ac.cn/

[5] N. Stone in Table of Nuclear Magnetic Dipole and Electric Quadrupole Moments, INDC(NDS)-0658, Vienna 2014

[6] Nuclear Moments Database, http://www-nds.iaea.org/nuclearmoments/

[7] C. D. Nesaraja, presented at IAEA Specialized Workshop on Nuclear Structure and Decay Data (NSDD) Evaluations, 27-29 April 2015, IAEA, Vienna: https://www-nds.iaea.org/index_nds_meetings.htm

[8] C.D.Nesaraja, S.D.Geraedts, B.Singh, Nucl.Data Sheets 111 (2010) 897

[9] Summary Report of ENSDF Technical Meeting, 10-11 November 2008, IAEA, Vienna, INDC(NDS)-0543

[10] Nuclear Physics European Collaboration Committee (NuPECC) Long Range Plan, http://www.nupecc.org/

This is a blank page.

11 Unified Coupled-Channels and Hauser-Feshbach Model Calculation for Nuclear Data Evaluation

Toshihiko Kawano
Los Alamos National Laboratory, Los Alamos, NM 87545, USA
Email: kawano@lanl.gov

We present an overview of the coupled-channels optical model and the Hauser-Feshbach theory code CoH_3, which focuses on the nuclear reaction calculations in the keV to tens of MeV region with special attention to the nuclear deformation. The code consists of three major sections that undertake the one-body potential mean-field theory, the coupled-channels optical model, and the Hauser-Feshbach statistical decay. There are other complementary segments to perform the whole nuclear reaction calculations, such as the direct/semidirect radiative capture process, pre-equilibrium process, and prompt fission neutron emission.

1. Introduction

Modern methodology for evaluating nuclear reaction data for medium to heavy mass targets centers a statistical Hauser-Feshbach (HF) code in the evaluation system. The HF theory with the width fluctuation correction gives a compound nuclear reaction cross section when resonances are strongly overlapped; in other words, an energy-averaged cross section is calculated. The HF codes currently available in the market, such as EMPIRE [1], TALYS [2], CCONE [3], and CoH_3 [4], which are capable for multi-particle evaporation from a compound nucleus, provide complete information of nuclear reactions, not only the reaction cross sections, but also the energy and angular distributions of secondary particles, γ-ray production cross sections, isomeric state productions, and so on. One of distinct features in CoH_3 is a unique capability to combine the coupled-channels optical model and the HF theory, where two methods are employed — the generalized transmission coefficients [5] and the Engelbrecht-Weidenmüller transformation [6]. Recently a code comparison was performed amongst the developers of EMPIRE, TALYS, CCONE, and CoH_3, which suggested that the inelastic scattering cross section by CoH_3 tends to be slightly higher than the other codes [7] due to this difference. This paper outlines the reaction theories involved in CoH_3.

2. CoH_3 Code Overview

The CoH_3 code is written in C++, and it consists of about 200 source files including 80 defined classes. For example, the simplest class is `ZAnumber` that has only two private member variables, the Z and A numbers. This class facilitates to calculate the (Z, A) pair of a compound nucleus

emerging in a reaction chain, and it resembles the traditional technique to represent the (Z, A) pair by an index of $1000Z + A$ in the FORTRAN77-age.

CoH_3 has its own optical model solver to generate the transmission coefficients internally. In the deformed nucleus case, a rotational or vibrational model is employed for the coupled-channels (CC) calculation. The nuclear structure properties are determined by reading the nuclear structure database [8]. At higher excitation energies, we use the Gilbert-Cameron level density formula [9] with updated parameters [10]. CoH_3 allows overlapping discrete levels inside the continuum region. The width fluctuation correction is calculated by applying the method of Moldauer [11] with the LANL updated parameters [12] based on GOE (Gaussian Orthogonal Ensemble) [13]. When strongly coupled channels exist, the so-called Engelbrecht-Weidenmüller transformation (EWT) is invoked to diagonalize the S-matrix [6], and the width fluctuation is calculated in the diagonalized channel (eigen-channel) space.

Besides the main HF core part, the code consists of many models. The two-component exciton model [14, 15] is used to calculate the pre-equilibrium process. For fissioning nuclei, the prompt fission neutron spectrum is calculated with the Madland-Nix model [16] including pre-fission neutron emissions. The direct/semidirect (DSD) neutron capture process is calculated with the DSD model [17]. There are three mean-field theories included to calculate the single-particle wave-functions in a one-body potential; FRDM (Finite Range Droplet Model) [18, 19], HF-BCS (Hartree-Fock BCS) [17], and a simple spherical Woods-Saxon.

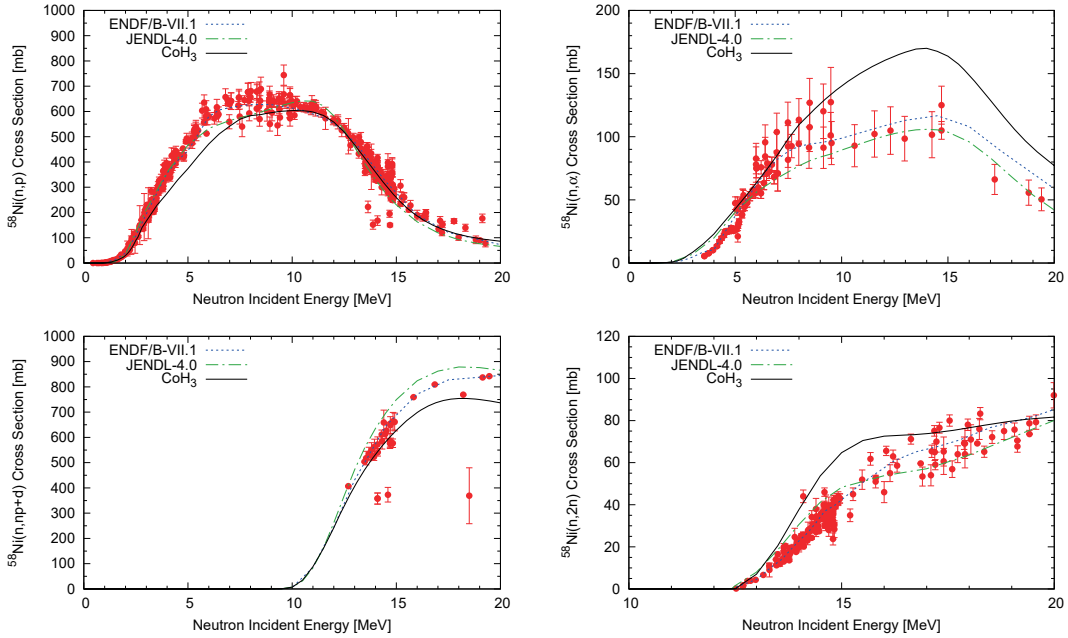

Fig. 1: CoH_3 default calculations for the neutron-induced reactions on ^{58}Ni; (n,p), (n,α), (n,np), and (n,2n) reactions. The (n,np) cross section includes the (n,d) reaction too.

Figure 1 demonstrates some default calculations of neutron-induced reactions on ^{58}Ni, comparing with the evaluated data in ENDF/B-VII.1 and JENDL-4.0, as well as experimental data

in literature (for the sake of simplicity, we use the same symbol for all available experimental data points.) These are relatively well behaved cases, and we suppose the other HF codes provide similar predictions. CoH_3 also produces the emitted particle angular distributions, which are shown in Fig. 2. The left panel shows the neutron elastic scattering that includes both the shape and compound elastic scattering cross sections, and the inelastic scattering to the first, second and third excited states of ^{58}Ni. The center panel is for the proton and the right is the α-particle. The scattering angular distribution in a compound reaction process $a + A \to b + B$ is calculated with the Blatt-Biedenharn formalism [20],

$$\left(\frac{d\sigma}{d\Omega}\right)_{ab} = \sum_L B_L P_L(\cos\theta_b) \ , \tag{1}$$

The B_L coefficient is given by Moldauer's statistical theory as

$$\begin{aligned} B_L &= \frac{1}{4k^2}\frac{(-)^{I_B-I_A+s_b-s_a}}{(2s_a+1)(2I_A+1)}\sum_J (2J+1)^2\frac{1}{N_J} \\ &\times \sum_{l_aj_a}\sum_{l_bj_b} W_{ab}\left\{X_{l_aj_a}(E_a)X_{l_bj_b}(E_b) + \delta_{I_AI_B}\delta_{E_aE_b}Y_{l_aj_a,l_bj_b}(E_a,E_b)\right\} \ , \end{aligned} \tag{2}$$

where k is the incident particle wave number, W_{ab} is the width fluctuation correction factor, I and s are the spin of nucleus and particles, and

$$X_{lj}(E) = Z(ljlj;sL)W(jJjJ;IL)T_{lj}(E) \ , \tag{3}$$

$$\begin{aligned} Y_{l_aj_a,l_bj_b}(E_a,E_b) &= (1-\delta_{l_al_b})(1-\delta_{j_aj_b})\left\{Z(l_aj_al_bj_b;s_aL)W(Jj_aJj_b;I_AL)\right\}^2 \\ &\times T_{l_aj_a}(E_a)T_{l_bj_b}(E_b) \ , \end{aligned} \tag{4}$$

where T_{lj} is the transmission coefficient, Z is the Z-coefficients, and the normalization N_J is given by integrating and summing all possible decay channels from the compound state J,

$$N_J = \sum \int T_{lj}(E)dE. \tag{5}$$

For the Hauser-Feshbach theory, $W_{ab} = 1$ and $Y_{l_aj_a,l_bj_b}(E_a,E_b) = 0$. In Fig. 2 case, the α-particle emission that leaves the residual nucleus in its ground state, the (n,α_0) reaction, shows large anisotropy [21].

3. Diagonalization of Coupled-Channels S-Matrix

When strongly coupled channels exist, such as the direct inelastic scattering to the collective states, the scattering S-matrix contains some off-diagonal elements, hence we cannot apply the standard HF formalism. In CoH_3, the coupled-channels S-matrix is transferred into the diagonalized eigen-channel space (EWT). Since Satchler's penetration matrix

$$P_{ab} = \delta_{ab} - \sum_c \langle S_{ac}\rangle \langle S^*_{bc}\rangle \ , \tag{6}$$

is Hermitian, this can be diagonalized by a unitary transformation [22]

$$(UPU^\dagger)_{\alpha\beta} = \delta_{\alpha\beta}p_\alpha \ , \qquad 0 \le p_\alpha \le 1 \ , \tag{7}$$

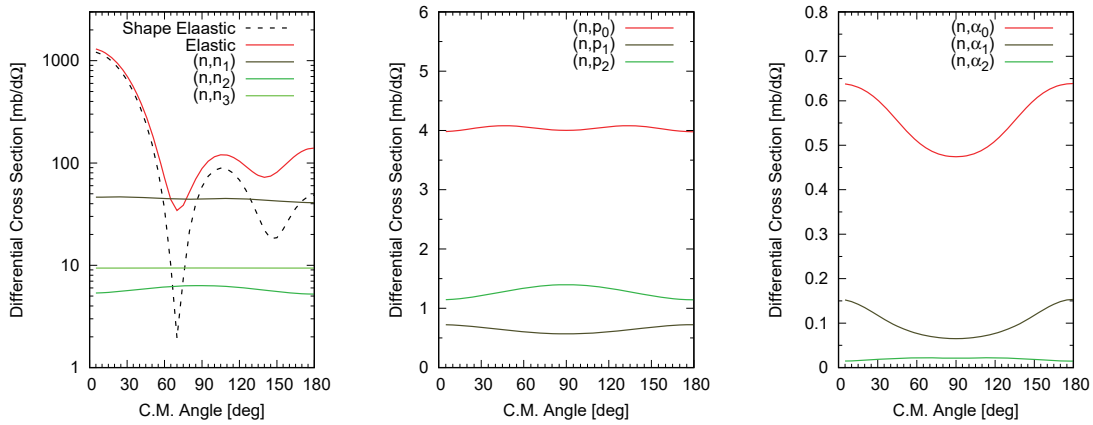

Fig. 2: Calculated secondary particle angular distributions for the neutron-induced reactions on ^{58}Ni at $E_n = 3$ MeV; neutron (left), proton (center), and α-particle (right).

and the same matrix U diagonalizes the scattering matrix,

$$\left\langle \tilde{S} \right\rangle = U \left\langle S \right\rangle U^T \ . \tag{8}$$

Here the Roman letters are for the channel index in the physical space, and the Greek letters are for the eigen-channel. The width fluctuation correction is performed in the eigen-channel, and they are transformed back to the physical space

$$\sigma_{ab} = \sum_{\alpha\beta\gamma\delta} U^*_{\alpha a} U^*_{\beta b} U_{\gamma a} U_{\delta b} \left\langle \tilde{S}_{\alpha\beta} \tilde{S}^*_{\gamma\delta} \right\rangle \ , \tag{9}$$

where $\left\langle \tilde{S}_{\alpha\beta} \tilde{S}^*_{\gamma\delta} \right\rangle$ is the width fluctuation corrected cross section in the eigen-channel. Rewriting Eq. (9) into more convenient form includes a term $\left\langle \tilde{S}_{\alpha\alpha} \tilde{S}^*_{\beta\beta} \right\rangle$, and we estimated this average by applying the GOE technique [6].

This transformation is still optional, since it requires longer computational time when the number of coupled-channels is large. When the transformation is not activated, CoH_3 calculates the generalized transmission coefficients from the coupled-channels S-matrix, where the direct reaction components are eliminated from the compound formation cross section [5], and a usual HF calculation is performed. This approximation works well when the target nucleus is not so strongly deformed. Figure 3 shows comparisons of the calculated elastic and inelastic scattering cross sections for the strongly deformed ^{182}W, and two cases are given; the EWT case (solid curves) and the generalized transmission coefficients (dashed curves). A relatively large difference is seen in the first excited state case.

4. Conclusion

We outlined the coupled-channels Hauser-Feshbach code, CoH_3. The code includes several models that are indispensable for producing evaluated nuclear data in the keV to tens of MeV region. The code is designed to fully utilize the coupled-channels calculation, which is especially

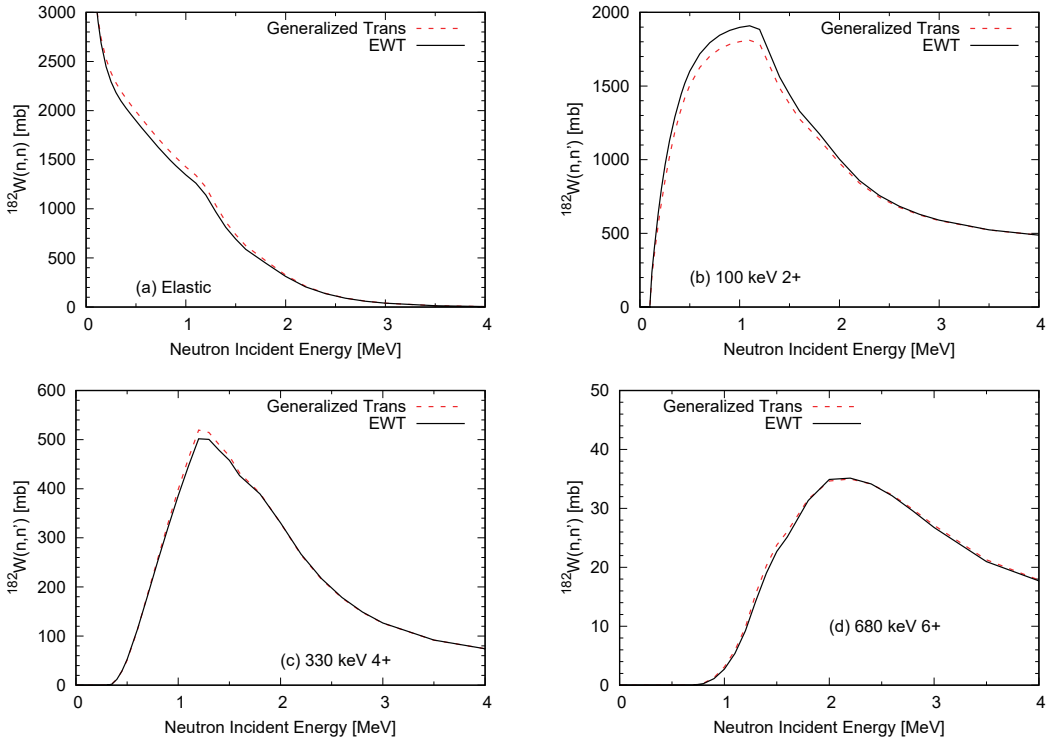

Fig. 3: Comparisons of the calculated (a) elastic and (b) – (d) inelastic scattering cross sections for ^{182}W. The solid curves are the full Engelbrecht-Weidenmüller transformation (EWT) case, while the dashed curves are for the generalized transmission coefficient case.

important for evaluating nuclear data of deformed nuclei such as actinides. As an example, calculations for the neutron-induced elastic and inelastic scattering on ^{182}W were shown, where two methods implemented in CoH_3 to combine the coupled-channels and the Hauser-Feshbach theories are employed.

Acknowledgment

This work was carried out under the auspices of the National Nuclear Security Administration of the U.S. Department of Energy at Los Alamos National Laboratory under Contract No. 89233218CNA000001.

References

[1] M. Herman, *et al.*, INDC(NDS)-0603, International Atomic Energy Agency (2013).

[2] A. J. Koning, S. Hilaire, and M. C. Duijvestijn, EPJ Web of Conferences, pages 211 – 214, (2008), Proc. Int. Conf. on Nuclear Data for Science and Technology, 22 – 27 Apr., 2007, Nice, France, Ed. O. Bersillon, F. Gunsing, E. Bauge, R. Jacqmin, and S. Leray.

[3] O. Iwamoto, J. Nucl. Sci. Technol., **44**, 687 (2007).

[4] T. Kawano, P. Talou, M. B. Chadwick, and T. Watanabe, J. Nucl. Sci. Technol., **47**, 462 (2010).

[5] T. Kawano, P. Talou, J. E. Lynn, M. B. Chadwick, and D. G. Madland, Phys. Rev. C, **80**, 024611 (2009).

[6] T. Kawano, R. Capote, S. Hilaire, and P. Chau Huu-Tai, Phys. Rev. C, **94**, 014612 (2016).

[7] R. Capote, S. Hilaire, O. Iwamoto, T. Kawano, and M. Sin, EPJ Web Conf., **146**, 12034 (2017), ND 2016: Proc. Int. Conf. Nuclear Data for Science and Technology, Bruges, Belgium, September 11 -– 16, 2016, A. Plompen, F.-J. Hambsch, P. Schillebeeckx, W. Mondelaers, J. Heyse, S. Kopecky, P. Siegler and S. Oberstedt (Eds.).

[8] R. Capote, *et al.*, Nuclear Data Sheets, **110**, 3107 (2009).

[9] A. Gilbert and A.G.W. Cameron, Can. J. Phys., **43**, 1446 (1965).

[10] T. Kawano, S. Chiba, and H. Koura, J. Nucl. Sci. Technol., **43**, 1 (2006).

[11] P. A. Moldauer, Nucl. Phys. A, **344**, 185 (1980).

[12] T. Kawano and P. Talou, Nuclear Data Sheets, **118**, 183 (2014).

[13] T. Kawano, P. Talou, and H. A. Weidenmüller, Phys. Rev. C, **92**, 044617 (2015).

[14] C. Kalbach, Phys. Rev. C, **33**, 818 (1986).

[15] A. J. Koning and M.C. Duijvestijn, Nucl. Phys. A, **744**, 15 (2004).

[16] D. G. Madland and J. R. Nix, Nuc. Sci. Eng., **81**, 213 (1982).

[17] L. Bonneau, T. Kawano, T. Watanabe, and S. Chiba, Phys. Rev. C, **75**, 054618 (2007).

[18] P. Möller, J. R. Nix, W. D. Myer, and W.J. Swiatecki, At. Data and Nucl. Data Tables, **59**, 185 (1995).

[19] P. Möller, A. J. Sierk, T. Ichikawa, and H. Sagawa, At. Data and Nucl. Data Tables, **109**, 1 (2016).

[20] T. Kawano and D. A. Brown, J. Nucl. Sci. Technol., **52**, 274 (2015).

[21] T. Kawano, T. Sanami, M. Baba, and H. Nakashima, J. Nucl. Sci. Technol., **36**, 256 (1999).

[22] C. A. Engelbrecht and Hans A. Weidenmüller, Phys. Rev. C, **8**, 859 (1973).

12 Fission Data obtained by Multi-nucleon Transfer Reactions

Katsuhisa Nishio
Advanced Science Research Center, Japan Atomic Energy Agency
Tokai, Ibaraki 319-1195, Japan
e-mail : nishio.katsuhisa@jaea.go.jp

Fission fragment mass distributions (FFMDs) obtained in multi-nucleon transfer (MNT) channels are presented. Experiments were carried out at the JAEA tandem facility in Tokai. The ^{18}O beam is bombarded to several actinide nuclides, instead of using lighter projectile. It is advantageous in a sense that that data for a wider set of nuclei are obtained in one experiment, including neutron-rich nuclei which cannot be accessed by the traditional particle capture reactions. As the total excitation energies of the exit channel E^*_{tot} after MNT reaction distributes widely, we can investigate the excitation energy dependence of the FFMDs. In the MNT reactions, it is not well established how the E^*_{tot} is shared in between ejectile and recoil nucleus. This would bring an uncertainly to identify the excitation energy of the recoiled nucleus. However, some information answering this question would be obtained by comparing the shape of FFMDs and their E^*_{tot} dependence with those for proton-induced fissions that give the same initial compound nuclide with a uniquely identified excitation energy. In the comparison, it is seen that E^*_{tot} is mostly given to the recoiled (fissioning nucleus) up to the energies of around E^*_{tot} = 35 MeV. To explain the shape of FFMD measured in this energy region, the concept of “multi-chance fission” is required to introduce, where neutron emission prior to fission generates less excited nucleus with small number of neutrons, contributing the pronounced peak-to-valley (P/V) structure in mass-asymmetric fission.

1. Introduction

For further public acceptance of nuclear power, it is essential to reduce the already-existing and newly produced nuclear waste. The use of accelerator-driven systems (ADS), for example, is considered as one of the viable options for the incineration and/or transmutation of the long-lived minor actinides into shorter-lived fission products. In the ADS approach, energetic spallation neutrons, produced via high-energy proton impact on a heavy target material such as lead and/or bismuth, could be used to irradiate the fissionable minor actinides. This leads to fission with higher, and more broadly distributed, excitation energies in comparison to those in the thermal-neutron-induced fission in a traditional power reactor. Thus, understanding of fission at high excitation energy is important for nuclear-data evaluations related to ADS developments. Also in the reactors accepting energetic proton beam, fission of larger number of nuclides, not only long-lived nucleus but also short-lived nucleus, occurs. Thus fission data for a wide set of nuclides are required to design the ADS.

Nowadays, the surrogate reaction technique has been widely used for the measurement of neutron-induced fission and capture cross sections, see for example the review article [1]. In JAEA, we are promoting a program to take fission data using multi-nucleon transfer (MNT) reactions [2-4], based on the ^{18}O beam (~9MeV/u) bombarded to various actinide target nuclei. The advantage of using ^{18}O beam, rather than using lighter ion beam, is that various compound nuclides can be populated due to the increased number of transfer channels. Also, in our setup, the total excitation energy E^*_{tot} introduced to the system is widely distributed up to energies as high as ~60 MeV.

Apart from the advantage of the method we have developed, there is an uncertainly in the assignment of the excitation energy of the fissioning nucleus, because in the experiment we can identify only the total excitation energy E^*_{tot} of the exit channel, and the sharing of the excitation energy have not well established theoretically. First of all, we briefly explain the experimental setup, and the obtained data on fission fragment mass distributions (FFMDs) will be shown. The sharing of excitation energy will be discussed, then followed by the concept of multi-chance fission to interpret the FFMD data.

2. Experimental Setup

Figure 1 shows the experimental setup for the fission measurement using MNT reactions at the JAEA tandem facility. Thin targets (typically ~50-100 μg/cm^2), made by electrically depositing the material on a nickel foil of 300 μg/cm^2, are irradiated by an ^{18}O beam at energy of about 9 MeV/u. Transfer channels were identified by detecting the projectile-like nucleus using a silicon ΔE-E telescope, mounted to the forward direction of the target. The thickness of the ΔE layer is 75 μm. Twelve pieces of the ΔE detectors were mounted conically around the beam axis to make an efficient collection of the projectile-like nuclei after MNT reaction. Particles passing through the ΔE detector were detected by a silicon strip E detector (SSD, 300 μm) to measure the residual energy (E_{res}). The E detector is the annular type strip detector, which can accept scattered particle at angles from ~17$^{\mathrm{o}}$ to 31$^{\mathrm{o}}$ relative to the beam direction. Figure 2 shows an example of the projectile-like nuclei plotted on the (E_{res}, ΔE) plane. Oxygen isotopes are clearly separated as well as those of lighter-element isotopes. By choosing a specific transfer channel, we can assign the corresponding compound nucleus by assuming a binary reaction process.

Fission fragments were detected using four multi-wire proportional counters (MWPCs). Each MWPC has an active area of 200×200 mm^2. The MWPC consists of the central cathode which is sandwiched by two wire planes. The wire planes were designed to detect the incident position of a fission fragment. Induced charge in the cathode was used to separate fission fragments from scattered particles and/or lighter ions. Time difference signal, ΔT, from the two facing MWPCs was recorded. Fission fragment masses were determined kinematically using ΔT value and fission fragment directions.

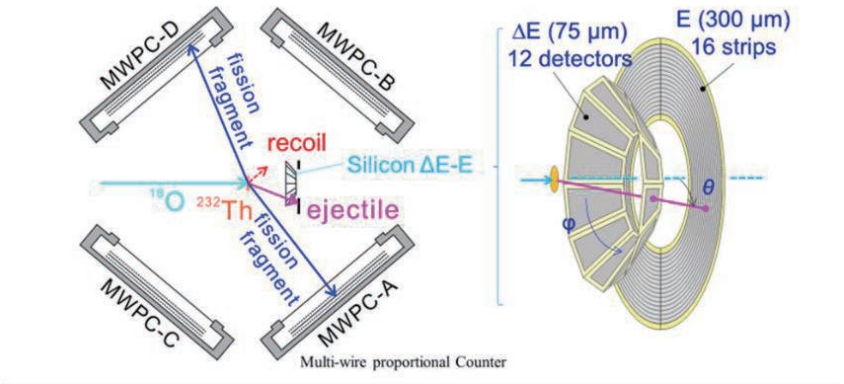

Fig.1 Experimental setup.

3. Experimental Results and Discussions

We show in Fig. 3 fission events recorded on the plane on the fragment mass vs total excitation energy E^*_{tot} of the system, obtained in the MNT channel ^{237}Np(^{18}O,^{19}O)^{236}Np*. The plot defines the threshold for fission at E^*_{tot} =6.3 MeV, from which the fission barrier height can be defined under the assumption that the excitation energy E^*_{tot} is mostly given to the recoiled nucleus, ^{236}Np. The regions of light and heavy fragment groups are clearly identified at lower-excitation energy region, which gradually ambiguous toward the higher energies due to the smearing of the shells responsible for mass-asymmetric fission.

Figure 4 shows the FFMDs of 23 nuclides and their E^*_{tot} dependence, obtained in the MNT channels of the ^{18}O+^{237}Np reaction. At the lowest energy region, all the studied nuclei show the prominent mass asymmetric fissions. The structure tends to be broader symmetric fission at higher excitation energies. It is also found by inspecting the spectra of E^*_{tot} = 20 - 30MeV that peak-to-valley ratio (P/V) gradually decreases with proton number of fissioning nucleus. It is also observed that population of low excited states is hindered in accordance with the number of transferred protons, from the projectile to the target nucleus. One of the plausible interpretation would be that the several nucleons are transferred with the form of cluster, instead of transferring individual nucleons step by step, so that the Coulomb repulsion between the cluster-like nucleus and the target nucleus can be defined and enhanced linearly with protons contained in the cluster.

The FFMDs of ^{236}Np obtained in the MNT channels of ^{237}Np(^{18}O,^{19}O)^{236}Np* (see Fig. 3) are compared with the data of proton-induced fissions of ^{235}U (^{236}Np*) [5][6], see Fig. 5. To make a comparison, center for the total-excitation energy (E^*_{tot}) gate of the MNT channel is adjusted to fit the excitation energy of compound nucleus populated by p + ^{235}U at each incident proton energy [5][6]. Apart from the small and minor disagreement at the highest energy of E^*_{tot} = 33.7-35.7 MeV, the data from MNT reaction agree with the proton-induced fissions. The results support that the total excitation energy a after MNT process is mostly given to the recoiled nucleus (fissioning nucleus) at least up to about E^*_{tot} = 35 MeV. It is highly interesting to make a further systematic comparison to higher excitation-energies of E^*_{tot} =60 MeV.

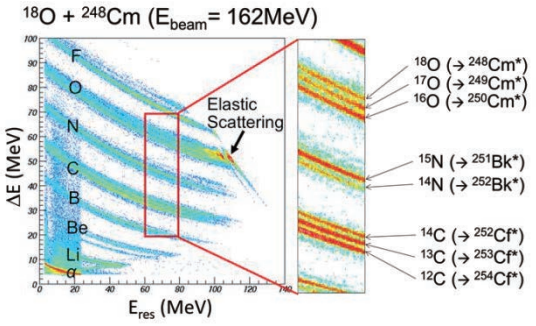

Fig.2 Particle identification with the silicon ΔE-E telescope in the reaction of ^{18}O+^{248}Cm.

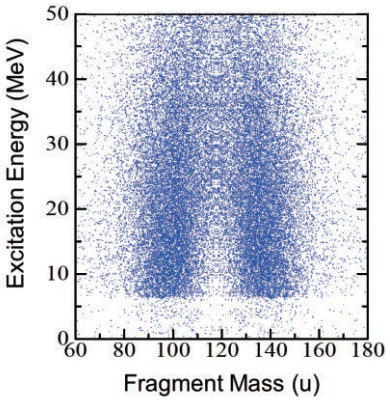

Fig.3 Fission events plotted on the mass vs excitation energy of ^{236}Np.

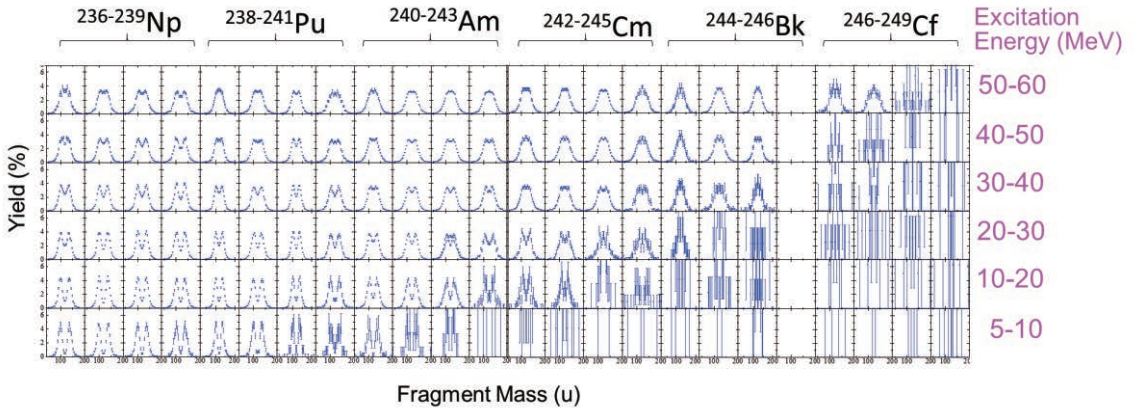

Fig.4 Fission fragment mass distribution obtained in the MNT channels of the ^{18}O+^{237}Np reaction.

Figure 6 shows the FFMDs of uranium, neptunium, and plutonium isotopes obtained in the ^{18}O + ^{238}U reaction [3]. The experimental data are compared with the Langevin calculation [7], where thick and thin curves are the results with and without taking into account the concept of multi-chance fission, i.e. fission after emitting neutrons. By evaporating neutrons before fission takes place, fission fragments from less excited and lighter compound nucleus, are generated and detected in the fission detectors. As the shell-structure responsible for mass-asymmetric fission revives in proportion to pre-fission neutrons, the resultant shape of FFMD tends to have pronounced double-peak structure with larger P/V ratio. Comparing two types calculations, with and without multi-chance fission, it is evident that the FFMDs of the excitation energy E^*_{tot} = 20-30 MeV already require the effects of multi-chance fission, to give better agreement. In the discussion of Fig. 5, total excitation energy after the MNT process is reasonably approximated to the excitation energy of the recoiled nucleus (fissioning nucleus) up to E^*_{tot} =~35 MeV, and the excitation energy taken away by ejectile nucleus is nearly negligible. Reduced P/V ratio of FFMDs at heavier element and enhanced P/V ratio toward neutron-rich isotopes in Fig. 4 and Fig. 6, revealed in the JAEA setup, can be explained only by invoking the concept of multi-chance fission. For the extend calculations, see [8].

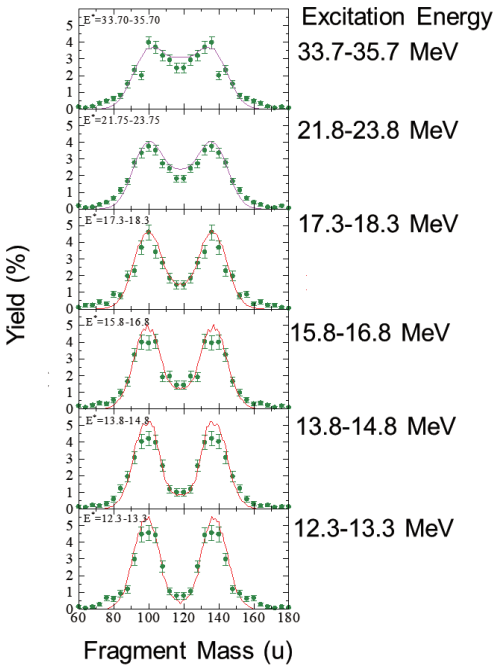

Fig.5 Fission fragment mass distributions of $^{236}Np^{*}$ obtained in the MNT reactions (solid circles) are compared with the data p + ^{235}U of [5] (E_{tot}^{*}=12.3-13.3, 13.8-14.8, 15.8-16.8, 17.3-18.3 MeV) and [6] (E_{tot}^{*}=33.7-35.7, 21.8-23.8 MeV).

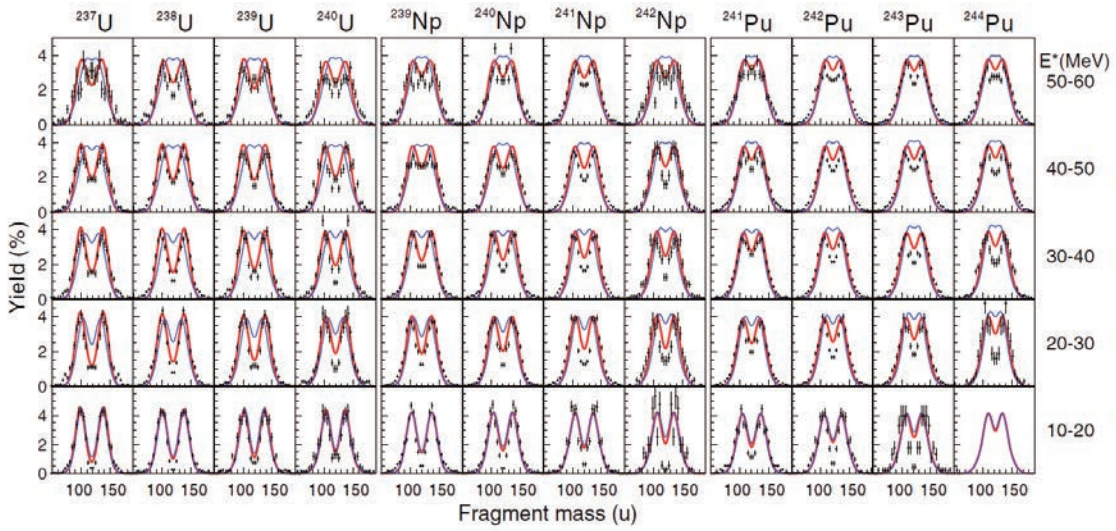

Fig.6 Fission fragment mass distributions obtained in the MNT channels of ^{18}O+^{238}U (solid circles). Thick and thin curves are the Langevin calculating with and without considering the concept of multi-chance fissions. Two sets of the calculation differ with each other already at the total excitation energy range of E^{*}_{tot} =20-30 MeV. Figure is taken from [3].

4. Conclusion

In the MNT reactions using relatively heavier projectile ^{18}O, we show that fission fragment mass distributions for more than 20 nuclides can be obtained in one experiment. Furthermore, dependence on the total excitation energy of the exit channel can be obtained with a significantly large range of E^*_{tot} =5 – 60 MeV. By comparing the FFMDs with the proton induced fissions the total excitation energy E^*_{tot} is mostly stored to the recoil nucleus (fissioning nucleus), up to E^*_{tot} =~ 35 MeV. The structure of obtained FFMDs at these excitation energy range already requires the concept of multi-chance fission in order to explain the data in the framework of Langevin model. It is highly interesting to investigate more precisely to what extent the total excitation energy E^*_{tot} is shared in between outgoing ejectile and recoiled nuclei.

Reference

[1] J. Escher, J. Burke, F. S. Dietrich, N.D. Scielzo, Rev. Mod. Phys. **84**, 353 (2012).

[2] R. Léguillon *et al*., Phys. Lett. B **761**, 125 (2016).

[3] K. Hirose *et al*, Phys. Rev. Lett. **119**, 222501 (2017).

[4] A.N. Andreyev, K. Nishio, K.-H. Schmidt, Reports on Progress in Physics, **81**, 016301(2018)

[5] R.L. Ferguson *et al*., Phys. Rev. C **7**, 2510 (1973).

[6] S.I. Mulgin *et al*., Nucl. Phys. A **824**, 1 (2009).

[7] Y. Aritomo and S. Chiba, Phys. Rev. C **88**, 044614 (2013).

[8] S. Tanaka *et al*., contribution to this proceedings.

13 Reactor power monitoring using neutron induced prompt gamma rays

Koichi OKADA[1]*, Atsushi FUSHIMI[1], Yuichiro UENO[1]
Shun SEKIMOTO[2], Tsutomu OHTSUKI[2]
[1]Center for Technology Innovation - Energy, Research & Development Group, Hitachi, Ltd.
7-2-1 Omika-cho, Hitachi-shi, Ibaraki-ken 319-1221 Japan
[2]Institute for Integrated Radiation and Nuclear Science, Kyoto University
2-1010, Asashiro-nishi, Kumatori-cho, Sennan-gun, Osaka-fu 590-0494, Japan
*E-mail: koichi.okada.nv@hitachi.com

Monitoring of only neutron flux in a nuclear reactor core has an advantage in reactor power monitoring accuracy. We started development of a new nuclear instrumentation based on measurement of prompt gamma rays originating from metals placed at the neutron flux monitoring positions. The thermal neutron flux at the position of each metal can be monitored by measuring the prompt gamma rays as the count rate of each energy. We conducted a neutron irradiation experiment for Ti, V, Ni, Cu and Sm. The energies of high intensity prompt gamma rays of more than 5 MeV showed good agreement between the experiment and nuclear data. And the energy spectra for the metals, excluding Sm, calculated with a Monte Carlo method showed rough agreement with experiments. We confirmed that gamma ray peaks were evaluable in the combined spectrum for Ti, V, Ni and Cu based on an estimation method using the peak ratio. The results indicated that the neutron flux monitoring method based on prompt gamma ray measurement had possible application to monitoring local reactor power at four positions.

1. Introduction

Nuclear instrumentation is the employment of instruments to ensure the proper operation of a nuclear reactor from its startup to its shutdown by controlling and monitoring the reactor power. The main actions consist of monitoring the neutron flux which is the main parameter of the nuclear reactor and emitting a signal for scram or blocking the control rod withdrawn in order to prevent damage to the fuel cladding when reactor power becomes excessive. For rating power monitoring in boiling water reactors (BWRs), local power range monitors (LPRMs) and traversing in-core probes (TIPs) are used. A function of the TIPs is calibration of LPRM detectors. Typically, 52 LPRM assemblies are installed in an advanced BWR core. Four LPRM detectors are installed in one LPRM assembly and they measure the local power at each position in the LPRM assembly. Conventionally, fission chambers are adopted as the LPRM detectors. However, it is difficult to separate neutron detection signals from gamma ray detection signals with a fission chamber in a high dose rate environment. Part of the current value of the fission chamber does not follow the instantaneous changes of the reactor power because decay gamma ray and delayed gamma ray components have a time lag for response. On the other hand, prompt gamma ray and neutron components are able to follow the instantaneous changes of the reactor power. Thus, monitoring for only neutrons present the possibility for improved accuracy of reactor power monitoring.

2. Nuclear power monitoring method using neutron induced prompt gamma rays

We proposed a new nuclear instrumentation method based on a technique to measure only neutrons. Four kinds of metals are placed in the neutron flux monitoring positions in the instrumentation tube which is a dry tube installed in place of LPRM assembly. Prompt gamma rays are emitted by neutron capture reactions between the metals and neutrons. The prompt gamma rays are measured by a gamma ray spectrometer located outside the reactor pressure vessel. The energy distribution of the prompt gamma rays is specific for each metal. The prompt gamma ray intensity is proportional to thermal neutron flux at the position of each placed metal. Therefore, the thermal neutron flux at each metal position can be monitored by measuring the prompt gamma rays as the count rate of each gamma ray energy. One of other advantages of this method is that no detectors need to be installed in the reactor core where radiation dose rate is extremely high. Therefore, this method may facilitate access when maintenance must be carried out.

We limited the prompt gamma ray energy in the range from 5 to 10 MeV. Environmental gamma rays including decay gamma rays from radiated materials and scattering gamma rays mainly have an energy less than 3 MeV. Thus, the lower energy limit of 5 MeV was determined for separation of prompt gamma rays from environmental gamma rays in the energy spectrum. When energy of the gamma rays is more than 10 MeV, probability of the photonuclear reaction like (γ, n) suddenly increases. The reaction causes damage to the sensor material by nuclear transmutation. We chose some metals in consideration of their self-shielding and prompt gamma ray emission cross sections [1][2]. The number of high intensity gamma rays emitted by any one metal was limited to five because too many gamma ray emissions made identification of the gamma rays derived from other candidate metals difficult. When energy of the high intensity gamma rays competed with gamma rays from other candidate metals, we chose those metals with a higher emission rate in consideration of self-shielding. Then, finally we chose Ti, V, Ni, Cu and Sm as our candidate metals for further investigation. Energy of the prompt gamma rays emitted by each candidate metal is shown in Table 1. The gamma ray energy value excluding Sm were in both reference [1] and [2]. However, the 7.21 MeV value from Sm was in reference [2] only.

Table 1 High intensity prompt gamma rays originating from candidate metals

Metal	Ti	V	Ni	Cu	Sm
Energy [MeV]	6.42,6.76	6.46,6.52,6.87,7.16	8.53,9.00	7.31,7.64,7.92	7.21

3. Experiment and evaluation

3.1 Experimental setup

We conducted a thermal neutron irradiation experiment for the candidate metals in the Kyoto University Research Reactor (KUR). We confirmed the emission gamma ray energy of more than 5 MeV from candidate metals. Figure 1 shows the schematic drawing of the experimental setup in the KUR facility. The irradiation neutron flux to the candidate metals was 10^7 $cm^{-2}s^{-1}$. A high-purity germanium semiconductor detector (HPGe) with relative efficiency of 40% was used. The detector was covered with borated polyethylene and Pb blocks.

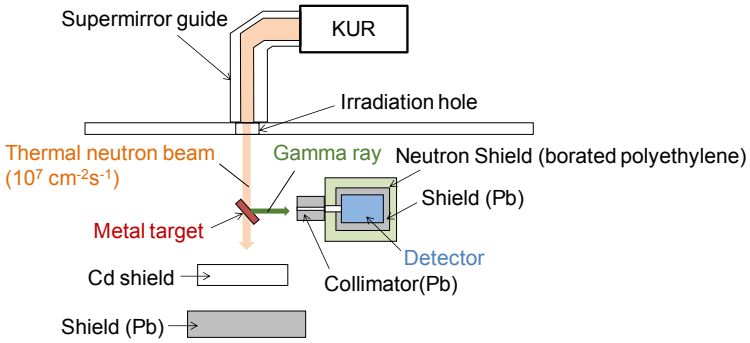

Figure 1 Experimental setup in the KUR facility

3.2 Evaluation of nuclear data and Monte Carlo calculation

Figure 2 compares emission gamma rays from the experiment and reported nuclear data [1][2]. The intensity was normalized by the gamma ray with the maximum intensity (blue characters) for each metal. The gamma ray energy distributions of Ti, V and Ni showed good agreement with nuclear data. As for Cu, the energy of the high intensity gamma ray agreed with the nuclear data. However, measured gamma ray intensities of 7.64 MeV and 7.31 MeV energies were underestimated compared to the nuclear data. This could mean that the nuclear data were overestimated or the experimental results were underestimated.

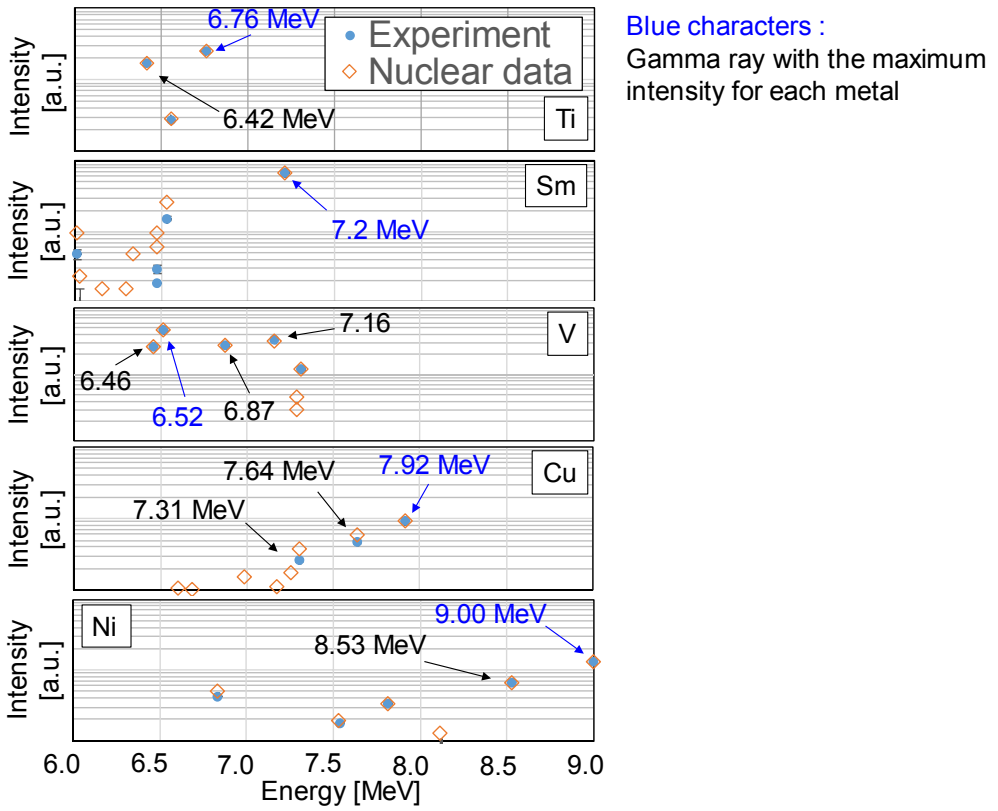

Figure 2 Comparison of energy distributions between experiment and reported nuclear data

As for Sm, we confirmed that the 7.2 MeV gamma ray was emitted. However, the gamma ray energy distribution for less than 6.5 MeV did not necessarily show agreement with the reported nuclear data. In the Sm spectrum, full energy peaks and escape peaks of low intensity prompt gamma rays with energy less than 6.5 MeV overlapped each other. The high intensity gamma rays that we identified for each metal in this experiment might be applicable to our nuclear power monitoring method.

We also confirmed the energy distribution of prompt gamma rays from candidate metals by the Monte Carlo code PHITS version 2.88 and version 3.02[3]. JENLD 4.0 [4] was adopted as the nuclear data library in this calculation. Figure 3 compares energy distribution results for the experiment and the PHITS calculation. The count rate was normalized by the maximum intensity gamma ray for each metal. Ti, V, Ni and Cu spectra were obtained with PHITS version 2.88. Only the Sm spectrum was obtained with PHITS version 3.02 because the gamma rays with energy less than 5 MeV did not appear in the Sm spectrum calculated with PHTS version 2.88.

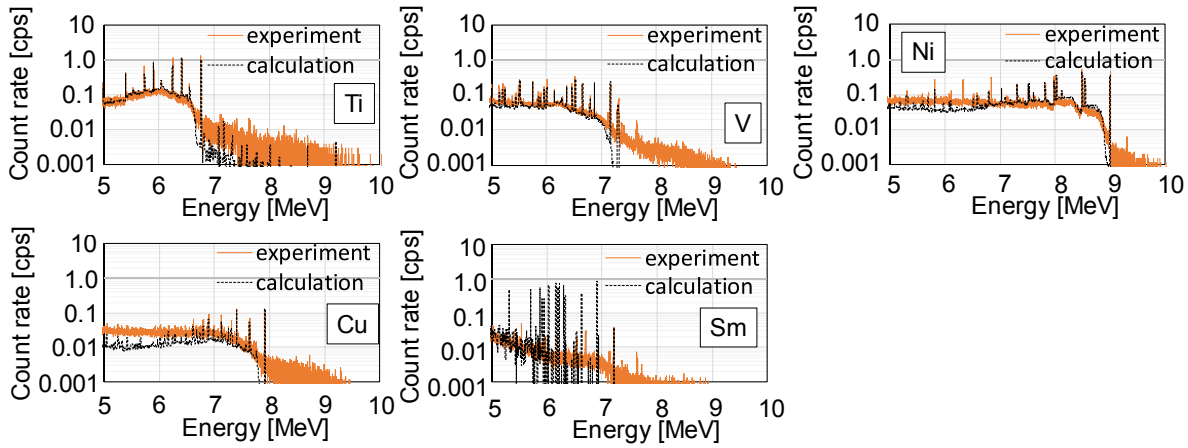

Figure 3 Comparison of energy distributions between experiment and PHITS calculation

The gamma ray energy spectra of Ti and V showed good agreement, even including the escape peaks. As for the Ni spectrum, the gamma ray with the energy of 6.8 MeV did not appear in the PHITS calculation. Thus, the single escape peak of 6.3 MeV, double escape peak of 5.8 MeV and Compton scattering component less than 6.8 MeV did not appear. We guessed that the gamma ray was originating from Ni-63. However, this gamma ray was not important for evaluation of the Ni spectrum because its emission rate was not high relatively. As for the Cu spectrum, energies of high intensity gamma rays showed good agreement but the Compton scattering component was underestimated. The cause for this underestimation was that the 7.92 MeV energy gamma ray which was the maximum intensity gamma ray of Cu was overestimated in the PHITS calculation because measured gamma rays of 7.64 MeV and 7.31 MeV were relatively underestimated in the nuclear data as shown in figure 2. As for the Sm spectrum, many unreported high intensity gamma rays appeared although the gamma ray with the energy of 7.2

MeV was the maximum intensity in the nuclear data and our experiment. We guessed this discrepancy was caused by the lack of nuclear data for the branch ratio during a metastable nuclear de-excitation. Thus, the correct emission gamma ray energy distribution based on nuclear data was not calculated. We eliminated Sm from our candidate metals because it would not be possible to design and evaluate the system with Sm using the PHTS calculation.

3.3 Separation method with non-cooling detector

We used a $LaBr_3$:Ce scintillator with a size of 1.5 inches as a non-cooling gamma ray spectrometer. Energy spectra of the four candidate metals were independently obtained in a similar experiment to that of the HPGe in KUR. Figure 4 shows the combined spectrum for Ti, V, Ni and Cu and their separation ratios. The spectrum of figure 4(a) was obtained using a different weighting to combine the measured spectra of Ti, V, Ni and Cu. Two spectra are shown in figure 4(b) for an expanded scale of the spectrum of figure 4(a) in the range from 5.2 MeV to 6.2 MeV. The upper one is the combined spectrum and the lower one is a spectrum obtained by irradiating V with neutrons.

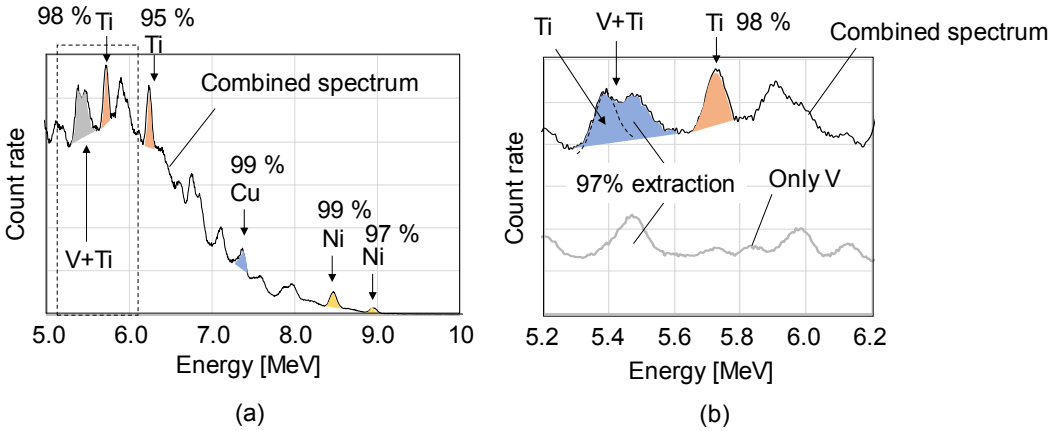

Figure 4 Combined spectrum and separation ratios of the four candidate metals

For Ti, Ni and Cu, the peak count rate in the figure 4(a) spectrum and count rate of the same energy peaks in each individual spectrum showed agreement of more than 95% by simple peak analysis. All V peaks overlapped with other gamma ray components. Therefore, we tried extraction using the peak ratio which consisted of the ratio of the full energy peak to the escape peaks and the emission ratio of prompt gamma ray. The ratio of the full energy peak to escape peaks was unique for sensor shape and the kinds of sensor materials. The gamma ray emission ratio was unique to the metal kind. Thus, peak ratio was uniquely fixed for metal kind and sensor structure. By using the peak ratio which was estimated by the individual spectrum of Ti, the Ti component included in 5.2 MeV to 5.6 MeV of the combined spectrum of figure 4(b) was estimated. And the V component was extracted from the overlapped peak by subtracting the estimated Ti component. Count rate of the extracted V component and count

rate of the same energy range of the individual spectrum that was only the V spectrum of figure 4(b) showed agreement 97%. This result indicated that the four metals had the possibility to be identified in the spectrum obtained by neutron irradiation of the four metals.

4. Summary

Monitoring of only neutron flux in the nuclear reactor core has an advantage in reactor power monitoring accuracy. We started development of a new nuclear instrumentation based on a technique to measure only neutrons. Four kinds of metals are placed in the neutron flux monitoring positions in the instrumentation tube. Prompt gamma rays which were emitted by neutron capture reactions between the metals and neutrons were measured by a gamma ray spectrometer located outside the reactor pressure vessel. The thermal neutron flux at each metal position could be monitored by measuring the prompt gamma rays as the count rate of each energy.

We conducted a thermal neutron irradiation experiment for Ti, V, Ni, Cu and Sm with a HPGe. The energies of high intensity prompt gamma rays of more than 5 MeV showed good agreement between our experiment and reported nuclear data. However, the energy spectrum of Sm calculated with PHITS did not agree the experiment. We guessed this was caused by lack of nuclear data about the branch ratio during metastable nuclear de-excitation. We also obtained the energy spectra of Ti, V, Ni and Cu with $LaBr_3$(Ce) scintillator in a neutron irradiation experiment. Peak count rate of Ti, Ni and Cu in the combined spectrum for the four metals and count rate of the same energy peaks in each individual spectrum showed more than 95% agreement by a simple peak analysis. All V peaks overlapped with other gamma ray components. Therefore, we tried the extraction by the peak ratio which was uniquely fixed for a metal kind and sensor structure. Count rate of the extracted V component and count rate of the same energy range of the individual spectrum showed 97% agreement. These results indicated that the neutron flux monitoring method based on prompt gamma ray measurement had the possibility to monitor local reactor power at four positions.

References

[1] Choi H. D, Firestone R. B, Lindstrom R. M, Molnár G. L, Mughabghab S. F, Paviotti-Corcuera R, Révay Z, Trkov A, Zerkin V, Zhou Chunmei. Database of prompt gamma rays from slow neutron capture for elemental analysis. Vienna: International Atomic Energy Agency, 2007.

[2] Gábor L. Molnár, Handbook of prompt gamma activation analysis with neutron beams. Budapest: Kluwer Academic Publishers Dordrecht, Boston, London; 2004. 7, prompt gamma-ray spectrum catalog; 190-364.

[3] Sato T, Iwaamoto Y, Hashimoto S, Ogawa T, Furuta T, Abe S, Kai T, Tsai P, Matsuda N, Iwase H, Shigyo N, Sihver L, Niita K. Features of particle and heavy ion transport code system (PHITS) version 3.02. J Nucl Sci Technol. 2018; 55: 684-690.

[4] Shibata K, Iwamoto O, Nakagawa T, Iwamoto N, Ichihara A, Kunieda S, Chiba S, Furukawa K, Otuka N, Ohsawa T, Murata T, Matsunobu H, Zukeran A, Kameda S, Katakura J. JENDL-4.0: A new library for nuclear science and technology. J Nucl Sci Technol. 2011; 48: 1-30.

14 Geological Disposal of High-level Radioactive Waste: Long-term Safety and Reduction of Environmental Impact

Hidekazu Asano
Radioactive Waste Management Funding and Research Center
Email: asano@rwmc.or.jp

The long-term safety of high-level radioactive waste in a geological repository is evaluated by numerical analysis based on estimates of the radiation dose received by people living on the surface taking into account a number of possible scenarios. Evaluations include modeling of nuclide migration from vitrified waste in deep underground repository. Safety is ensured by the isolation and confinement of radionuclides using a combination of artificial materials and the natural environment which function as a barrier. In the context of geological disposal and from the perspective of reducing environmental impact, the concept of pursuing integrated multidisciplinary research on nuclide separation with a particular focus on exploiting the relevant nuclear data is elaborated herein.

1. Introduction

In the context of geological disposal, the concepts of securing the long-term safety of radioactive waste and evaluating radiation exposure based on radionuclide migration are specified in the documentation system of the IAEA's safety standards*. Furthermore, countries which pursue geological waste management programs have highlighted the need for long-term safety standards.

Thus, consideration of the estimated annual exposure dose for people living on the surface due to migration of radionuclides from deep repositories is necessary. In Japan, a typical geological formation may contain 40,000 units of vitrified waste** in a repository within granite at depths of 1,000 m and where the maximum annual exposure dose equates to 5×10^{-3} (μSv/year) after approx. 8×10^{5} years of repository closure [1]. This exposure value is several orders of magnitude lower than the value of the dose constraint for geological disposal prescribed by the safety regulations of several countries, with the dominant nuclide for exposure being Cs-135. With respect to nuclides released from vitrified waste, 99% of the total inventory of Np-237, for example, is in the dissolved form and the Np would remain in the area of the engineered barrier after 10^{7} years; furthermore, 95% of the initial inventory of Cs-135 would be in the area of the engineered and natural barriers [1]. Based on such considerations, an approach for reducing the environmental impact of geological disposal is outlined below.

*A hierarchical structure ranging from safety principles (fundamental) [2] to requirements and guides. Refer to SSR-5 [3] for specific safety requirements of radioactive waste disposal (1.10 for the concept and 2.15 for radiation protection in the post-closure period).

**The vitrified waste is enclosed in a metal container, overpacked, surrounded with a buffer material mainly composed of clay, and buried deep in the rock system.

2. Reduction of environmental impact in geological disposal

The environmental impact from geological disposal has been classified into two categories: (1) a radiation effect and (2) a waste volume effect [4]. In the case of the former, relevant data are presented in Table 1 and Fig. 1 [5]. Here, the radiotoxicity per 1 THM of spent fuel is classified into three groups: spent fuel, high-level waste (vitrified waste), and nuclide separation conversion. Also, the time required for the toxicity level to reach the same value of toxicity as that for natural uranium has been estimated. The radiotoxicity depends on the amount and radiation characteristics of the nuclides contained in the spent fuel, as shown in Table 1. From this result, the effect of reducing radiotoxicity by separation and recovery of U and Pu by reprocessing and further separation of minor actinide (MA) nuclides becomes clear.

Table 1 Long-lived nuclides in spent nuclear fuel***
(PWR, 4.5% enrichment, fuel burn-up:45GWd/THM)

Nuclide	$T_{1/2}$ (year)	DCF (μSv/kBq)	Contents (Kg/tonSNF)
U-235	0.7 Billion	47	10
U-238	4.5 Billion	45	930
Pu-238	87.7	230	0.3
Pu-239	24,000	250	6
Pu-240	6,564	250	3
Pu-241	14.3	4.8	1
Np-237	2.14×10^6	110	0.6
Am-241	432	200	0.4
Am-243	7,370	200	0.2
Cm-244	18.1	120	0.06
Se-79	2.95×10^5	2.9	0.006
Sr-90	28.8	28	0.6
Zr-93	1.53×10^6	1.1	1
Tc-99	2.11×10^5	0.64	1
Pd-107	6.50×10^6	0.037	0.3
Sn-126	1×10^5	4.7	0.03
I-129	1.57×10^7	110	0.2
Cs-135	2.30×10^6	2.0	0.5
Cs-137	30.1	13	1.5

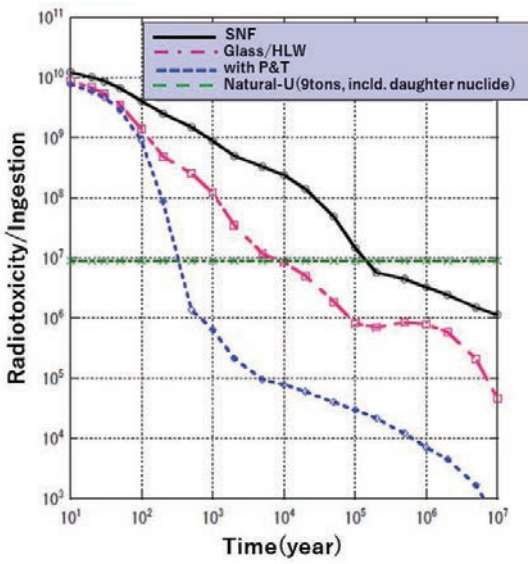

Fig. 1 Time dependency of radiotoxicity/ingestion per 1 THM spent nuclear fuel** (PWR/UO_2, 45GWd/THM, 5 years; Separation: U&Pu /99.5%, MA/99.5%)

***Original data from reference [4]. Transcribed in part from the Japanese to English.

For the latter, the data are presented in Table 2 and Fig. 2 [6]. Here, the pitch for waste emplacement and the tunnel-to-tunnel distance were calculated based on consideration of the mechanical stability of the disposal tunnel and the maximum temperature of the buffer material based on the heat produced by radioactive decay of the nuclides in the vitrified waste in the repository. It is desirable to maintain the temperature of the buffer material below 100 °C to prevent mineralogical alteration. For reference case, assuming an occupation area of 44.4 m^2 for the vitrified waste, the following metrics have been proposed:

10 m for the tunnel-to-tunnel distance and 4.44 m for the waste emplacement pitch as illustrated in Fig. 2. In this case, the heat generation characteristics of the vitrified waste are based on a series of operating conditions for the reactor, and for reprocessing and vitrification as shown in the upper column (green) of Table 3.

Table 2 Specification of the disposal tunnel and the waste package pitch

Emplacement method	Disposal tunnel to tunnel distance [m]	Pitch between waste [m]	Waste occupied area per vitrified waste [m^2]
Vertical emplacement	10	4.44	44.4

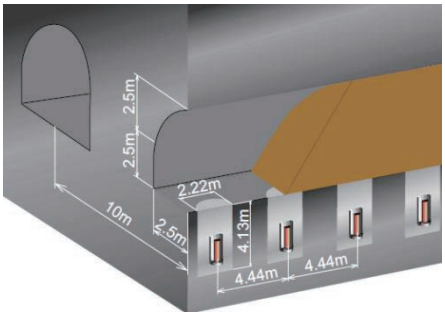

Fig. 2 Layout of disposal tunnel and disposal pit for vertical emplacement method at hard rock repository

Table 3. Combination of various conditions for the fuel cycle, waste treatment and disposal in current/future nuclear energy use

Reactor	Fuel		Spent fuel	Reprocessing			Vitrification			Vitrified waste	Geological disposal
–	UO_2/ MOX	Burn-up	Cooling period	Separation process	Separation ratio	Nuclides	Glass Matrix	Melter operation	Waste loading	Storage period	Waste occupied area
LWR	UO_2	45 GWd/ THM	4	Purex	99.5	U, Pu	-	-	Approx. 20wt%	50 years	44m²/glass
LWR, FR, etc.,	UO_2 MOX/ Pu thermal MOX/ full	Low ～ High	>4 years	Nuclides and their separation ratio	Request from geological disposal	MA: Np, Am, Cm	Measure	–	Higher waste loading	Heat generation	Repository area Waste occupied area Waste emplace-ment method (V,H)
						Cs/Sr	–	–		Heat generation	
						Mo	Measure	Yellow phase		–	
						PGM: Ru, Rh, Pd	Measure	Sedimen-tation		–	

3. Integrated waste management research across the fuel cycle

The conditions for consideration and setting of norms for the current/future use of nuclear energy and the amounts and characteristics of high-level radioactive waste are shown in the lower column (yellow) in Table 3. In comparison with the above reference case, consideration is given to a diversity of conditions for reactor operation, reprocessing, and glass solidification. By interrelating changes in each condition, the occupied area per unit of vitrified waste at a repository was calculated from the heat generation

characteristics of the vitrified waste. The results based on the use of UO_2 fuel are shown in Table 4 [7]. The CAERA (Comprehensive Analysis of Effects on Reduction of disposal Area) index [kg/m^2] shown in Table 4 refers to the weight of radioactive waste in terms of the oxide which is buried in a unit area of the repository [7, 8]. From this table, it is possible to reduce the waste occupied area by one half (or even less) by altering various conditions of the fuel cycle, such as nuclide separation at the reprocessing step and increasing the waste loading ratio of the vitrified waste (glass). In the case of UO_2 fuel, the reduction effect depends on a combination of the following:

- The effects of Cs and Sr as short half-life nuclides and Am as a long-life nuclide due to the length of storage time of the spent fuel
- The separation of the above nuclides
- Further separation for Mo and platinum group metal (PGM), which need to be taken into consideration for the glass vitrification process,
- The waste loading of vitrified waste

Table 4. Reduction of the waste occupied area in consideration of nuclide separation and increasing waste loading for vitrified waste

Case	SNF Cooling period [year]	Cs/Sr separation [wt%]	MA separation [wt%]	Mo/PGM separation [wt%]	Vitrified waste, waste loading [wt%]	CAERA [kg/m^2]	Reduction of waste occupied area [%]
1	4	90	0	70	35	2.25	43
2	15	70	0	70	25	1.35	72
3	20	70	0	70	25	1.15	84
4	30	0	0	0	21	0.97	100
5	40	0	0	0	21	0.97	100
6	50	0	90	70	35	2.25	43
7	100	0	70	70	35	2.25	43

4. Required data

Fig. 3 shows the relationship between the heat generation characteristics and the cooling period of the UO_2 spent fuel with a burn-up of 45 GWd/THM. From this figure, it is understood that as the cooling period becomes longer, the heat generation capacity decreases, but the contribution of Am-241 increases with time. In Table 4, when the cooling period of the spent fuel is 50 or 100 years, the waste-occupied area can be reduced to less than half by separation of MAs due to elimination of Am-241 as the dominant nuclide in heat generation. When the fuel burn-up increases above this value, the heat generation capacity of the spent nuclear fuel (SNF) increases, but at the same time the fuel composition also changes. As a result, in the case of a prolonged cooling period for the SNF, in addition to Am-241, the contribution of Pu-238 increases the heat generation capacity.

Thus, to assess the thermal characteristics of the waste across the fuel cycle and to realize a reduction of the load at the geological disposal site, it is essential to estimate and to evaluate the nuclide composition of

the waste corresponding to the extent of diversification of the various cycle conditions. Moreover, it is clear from Table 3, that the nuclide composition is determined retrospectively from the composition and burn-up of nuclear fuel.

In evaluating the radiation effects with respect to the environmental impact, information on the nuclides in the SNF is indispensable for evaluating nuclide migration or radioactive toxicity in a geological disposal setting.

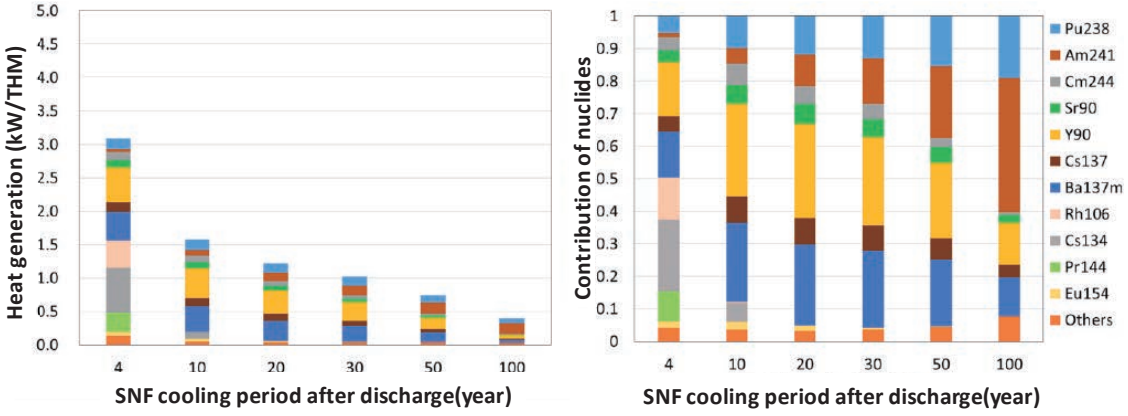

Fig. 3. Heat generation of spent nuclear fuel /UO_2, burn-up 45 GWd/THM

5. Conclusion

In integrated waste management research across the fuel cycle, a detailed evaluation of spent fuel, nuclide separation, use of separated nuclides in recycling (e.g., use of fast reactors), and the vitrification process (glass melting characteristics and quality of vitrified wastes) are necessary, and together with nuclear data, are indispensable to provide technical options for optimizing waste management with a view to reducing environmental impacts.

Acknowledgment

Some of the results of this study were obtained from the RWMC's paper entitled, "Study on the effects of advanced nuclear fuel cycle technology to the geological disposal concept".

References

[1] H12: Project to establish the scientific and technical basis for HLW disposal in Japan, second progress report on research and development for the geological disposal of HLW in Japan, Supporting report 3: Safety assessment of the geological disposal system, TN1410 2000-004, Japan Nuclear Cycle Development Institute (JNC), 2000.

[2] Safety fundamentals No. SF-1, Fundamental safety principles, IAEA safety standards, IAEA, 2006.

[3] Specific safety requirements No. SSR-5, Disposal of radioactive waste, IAEA safety standards, IAEA, 2011.

[4] Sato S., *et al*., Technical options of radioactive waste management for the second half of the 21st century,

in consideration of Pu utilization and less environmentally impacted geological disposal: (1) Background, viewpoints and research plan, 3O13, Proceedings of AESJ 2018 Spring Meeting, 2018 March 26-28, Osaka Univ. (in Japanese)

[5] Text “Nuclear Fuel Cycle, 8-1 Roles of partitioning & transmutation”, K. Tsujimoto, Reprocessing and Recycle Technology Div., Atomic Energy Society of Japan, (in Japanese). Available from: http://www.aesj.or.jp/~recycle/nfctxt/nfctxt.html

[6] H12: Project to establish the scientific and technical basis for HLW disposal in Japan, second progress report on research and development for the geological disposal of HLW in Japan, Supporting report 2: Repository Design and Engineering Technology, TN1410 2000-003, Japan Nuclear Cycle Development Institute (JNC), 2000.

[7] Asano H, Cross-sectoral research on the nuclear energy system for less-impacted radioactive waste management, Vol.25, No. 2, J. Nuclear Fuel Cycle and Environment, 2018 (in Japanese). Available from: https://nuce.aesj.or.jp/journal

[8] K. Kawai, et al., Technical options of radioactive waste management for the second half of the 21st century, in consideration of Pu utilization and less environmentally impacted geological disposal: (3) Effects of various nuclear fuel cycle scenarios on property of spent fuel and waste glass, 3O13, Proceedings of AESJ 2018 Spring Meeting, 2018 March 26-28, Osaka Univ. (in Japanese).

15 Measurement of the Neutron Capture Cross Section of ^{237}Np using ANNRI at MLF/J-PARC

Gerard Rovira[1*], T. Katabuchi[1], K. Tosaka[1], S. Matsuura[1], K. Terada[1]
O. Iwamoto[2], A. Kimura[2], S. Nakamura[2], N. Iwamoto[2]

1) Laboratory for Advanced Nuclear Energy, Tokyo Institute of Technology
2) Japan Atomic Energy Agency
author: rovira.g.aa@m.titech.ac.jp

Abstract

Neutron capture cross section measurements for ^{237}Np have been conducted with the Accurate Neutron Nucleus Reaction Measurement Instrument (ANNRI) at the Materials and Life Science Facility (MLF) of the Japan Proton Accelerator Research Complex (J-PARC) using neutrons with energy ranging from thermal energy to 500 keV. A Time of Flight (TOF) method using a NaI(Tl) detector was employed for this measurement and the data were analyzed based on a pulse-height weighting technique in order to derive a neutron capture cross section. A thermal value for the cross section (σ_{th}) of 176.7 + 0.5$_{sta}$ was obtained. Along with the cross section measurement, the preliminary results of a resonance analysis using the REFIT program are presented.

I. Introduction

As nuclear transmutation of minor actinides (MA) has been established as a solution for high level radioactive waste management, more accurate nuclear data for the neutron capture cross section on minor actinides are required. Numerous types of MA are produced in nuclear reactors and are present in high level radioactive waste (HLW). Current evaluated nuclear data are only suitable for the early stages of the design of nuclear transmutation systems. However, final designs and safety measures require more precise nuclear data with a significant reduction in terms of their uncertainties [1]. ^{237}Np possesses a long half-life of 2.14 x 10^6 years and it is one of the most abundant MA present in spent nuclear fuel. ^{237}Np is also one of the main components of the Accelerator-Driven Systems (ADS) core, a subcritical reactor facility for nuclear transmutation.

The region of interest for the core design is from 0.5 to 500 keV, where JENDL-4.0 includes uncertainties from 6% up to 10%. Current uncertainties in the evaluated nuclear data for the neutron capture cross section of ^{237}Np are an important contributor to the ADS criticality uncertainty. Thus, it is crucial to accurately determine the neutron capture cross section at such energy range, to reduce the uncertainties to 5%, along with an analysis of the resonance region to derive the resonance parameters.

An extensive set of experimental data has been reported on the ^{237}Np (n, γ) reaction using both activation and time-of-flight (TOF) methods [2–17]. In the region of interest for the experiment, from 0.5 to 500 keV, the available experimental data is scarce. Experimental data by activation method exists in the 100-500 keV range but they differ from each other about 30-40% [5, 7–9]. In addition, there are only two sets of reliable data using TOF method, those of Weston *et al* [10] and Esch *et al* [14], but they diverge in the region of interest from 15% to 35% at some energies.

In this paper, preliminary results of the neutron capture cross section for ^{237}Np are presented for incident neutron energy ranging from thermal energy to 500 keV along with details of the early stages of the resonance analysis. Details of the experimental setup and the data analysis are also provided.

II. Experimental Procedure

1. *Experimental Setup*

The experiments were performed using the Accurate Neutron-Nucleus Reaction Measurement Instrument (ANNRI) at the Materials and Life Science Facility (MLF) of the Japan Proton Accelerator Research Complex (J-PARC). An intense pulsed neutron beam was produced by the Japanese Spallation Neutron Source (JSNS) in the MLF using the 3 GeV proton beam of the J-PARC facility. The proton pulses were shot at the spallation target every 40 ms and a beam power of 400 kW.

A TOF method was employed in the present experiment with a flight path of 27.9 m up to the sample position. Emitted γ-rays from the sample were detected by a NaI(Tl) detector surrounded by annular plastic scintillation detectors to suppress cosmic-ray background by anti-coincidence detection. Detected capture events were stored sequentially in a computer as a list format data.

2. *Data Acquisition*

For fast data acquisition purposes, a multi-event time digitizer FAST ComTec MPA4T was employed [19]. The time between a starting trigger event and successive multiple stop events were digitized. The signal coming from the JSNS proton beam monitor was used as a trigger signal for the MPA4T module. Signals coming from the anode of the NaI(Tl) detector were fed into the MPA4T as a stop signal. Time differences between the trigger signal and the NaI(Tl) anode signal were used for the TOF measurement of the incident neutrons. At the same time, signals from the dynode of the NaI(Tl) detector were amplified, shaped and then fed into an analog-to-digital converter (ADC) for pulse height measurement. However, traditional pulse analysis technique using the ADC does not perform adequately in the energy region higher than 1 keV. Strong γ-ray burst from the neutron source after the spallation reaction, known as gamma flash, induce baseline distortion into the analog modules, making pulse height measurement unfeasible in the fast TOF region. Faster data acquisition is needed in such energy region. Thus, along with the pulse height measurement, the pulse width calculated from the time difference between the rising and the falling edges of the anode signal was recorded. The pulse width was converted into pulse height in offline analysis.

3. *Samples*

A 200 mg sample of ^{237}Np with an activity of 5 MBq was used for the measurements. The sample consisted of 227 mg of neptunium dioxide (NpO_2) powder together with 624.5 mg of Al powder. The isotopic purity of ^{237}Np for the sample was 99.99%. The powders were packed into an Al pellet with a 20 mm diameter and 0.4 mm thick walls. A dummy container with the same measurements was also used for a background measurement.

The incident neutron spectrum was reconstructed using γ-rays from the ^{197}Au(n, γ) reaction with a 20 mm in diameter and 1 mm in thickness gold sample and, also, using the 478 keV γ-rays from the ^{10}B(n, α)^{7}Li reaction with a boron sample containing enriched ^{10}B up to 90% and having a diameter of 10 mm and a thickness of 0.5 mm.

Background events due to scattered neutrons were derived using a ^{nat}C sample with a 10 mm diameter and 0.5 mm thickness.

III. Data Analysis

1. *Pulse Width to Pulse Height Conversion*

In order to derive the pulse height value of the γ-ray in the fast TOF region from its pulse width, a conversion relation was obtained between the pulse height and the pulse width. The relation was derived by plotting the pulse height value along with the pulse width value of each detected γ-ray. More information about the pulse width analysis is described by Katabuchi et al [20].

2. *Background Removal*

Several layers of background events have to be removed and other corrections have to be applied so that it is possible to precisely distinguish neutron capture events of ^{237}Np.

A dead time correction is applied to all measurements in order to estimate the count loss in the experiment [20]. The main cause for this count loss is the pile-up of two consecutive signals.

Frame overlaping from previous neutron bursts have to be substacted. Every proton event induces neutron events with a frame length of 40 ms, as the proton beam repetition is 25 Hz. Slow neutrons (TOF > 40 ms) from earlier frames overlap subsequent frames. Overlaping background was estimated using J-PARC's unique operation pattern. A small part of the proton beam pulses from the 3-GeV synchrotron are injected into the 50-GeV synchrotron ring instead of JSNS. As no proton is shot into the JSNS, the measured TOF of the previous proton pulse is extended up to 80 ms, doubling the normal frame length. Hence, the overlap background is estimated from the recorded events from 40 ms to 80 ms . The overlap background is then removed by fitting a curve in the frame spectra from 40 ms to 80 ms and normalizing by referring it to the total number of proton bursts.

Blank background is subtracted using the data retrieved from a measurement with no sample. Likewise, the background events induced due to scattered neutrons at the sample and the events induced by the sample case are removed using the ^{nat}C and the TOF spectra obtained from the aluminum case respectively.

3. *Pulse Height Weighting Technique*

The Pulse Height weighting technique (PHWT) enables the calculation of the neutron capture yields from the pulse height spectrum [21]. The first step to apply the PHWT is to calculate a detector response function using the experimental configuration. This response function ***R(I, E)*** was defined as the probability that a γ-ray with an energy of E was counted in the I channel of the detecting system. This response function was used in order to derive a weighting function ***W(I)***. The weighting function is essential in order to apply the PHWT and it is defined as follows:

$$\sum_I W(I)R(I,E) = E. \tag{1}$$

On the condition that the detection efficiency for γ-rays is so small that only one γ-ray per capture event can be detected, the real capture γ-ray pulse height spectrum ***S(I)*** should be expressed as:

$$S(I) = \sum_i m_i \sum_j R(I, E_{ij}) \tag{2}$$

where E_{ij} is the energy of the j-th γ-ray emitted in the i-th mode and m_i the number of capture events which disintegrated through the i-th mode. At the same time, since the sum energy of the γ-ray cascades emitted per capture event is equal to:

$$\sum_j E_{ij} = B_n + E_n^{'} \tag{3}$$

being B_n the binding energy of the target nucleus and $E_n^{'}$ the incident neutron energy in the center-of-mass system. Finally, as the sum of m_i with respect to i is equal to the capture yield, the neutron capture yield can be expressed as follows:

$$Y = \frac{\sum_i W(I)S(I)}{B_n + E_n^{'}} \tag{4}$$

4. *Self-Shielding and Multiple Scattering Corrections*

Flux attenuation effect through the sample and multiple scattering events caused by scattering at the Al case cannot be ommited in the analysis. The experiment was simulated using the PHITS program [22]. A neutron capture yield and neutron spectrum was obtained and, using both along side

with the sample thickness, a cross section value was deduced. This cross section value included the effects of self-shielding and multiple scattering. In order to isolate those effects, the neutron cross section value of JENDL-4.0 was divided by the obtained cross section to determine and energy dependent correction factor.

5. *Neutron Spectrum*

The neutron spectrum was estimated using the gold and boron samples. The obtained TOF spectrum from both runs was divided by the reaction rate simulated using the PHITS program. Figure 1 shows a good agreement of the incident neutron distribution between the two samples except for the resolved resonance region of gold.

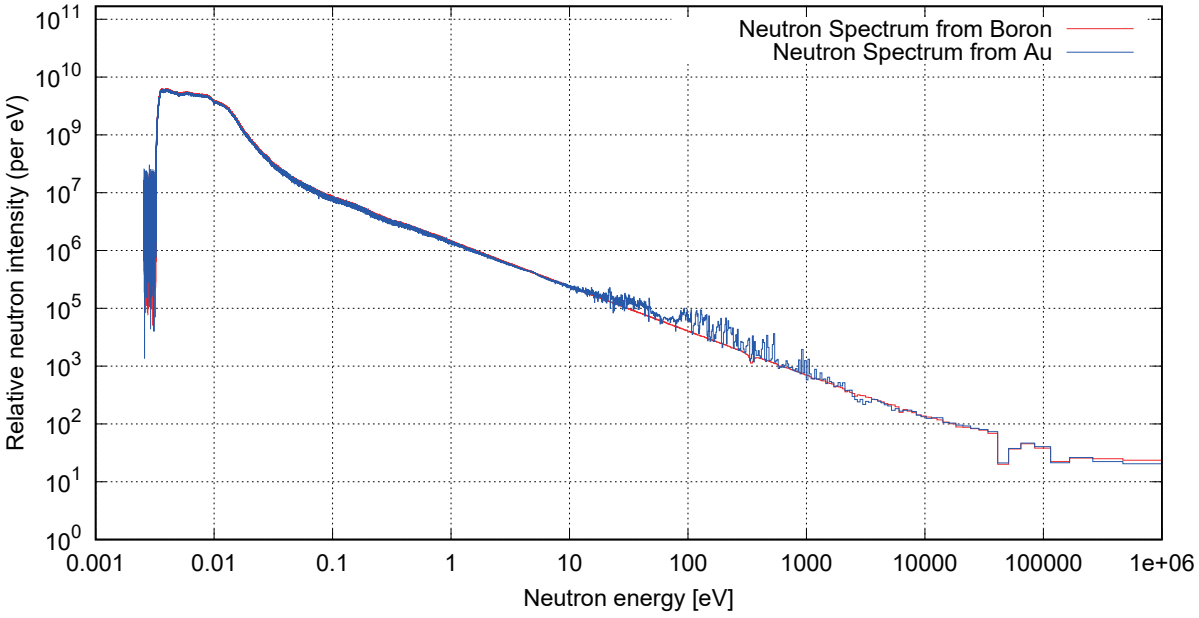

Figure 1: *Incident Neutron Spectrum*

IV. Resonance Analysis

The REFIT fitting program [23] was used to fit the resonances measured in the experiments. This process is still on going and only preliminary results are presented on this paper. Moreover, since no systematic uncertainty analysis has been performed yet for this experiment, the results from the resonance analysis including the average radiation width are subject to change once the uncertainty analysis is finalized.

The averaged radiation width was obtained from 16 resonances below 20 eV as they were presumed to be independent. Using the individual values for $\Gamma_{\lambda,\gamma}$ from each resonance, a mean estimation of 40.1 meV.

For the rest of the resonances, the radiation width was kept fixed at 40.1. Hence, in the fitting process, only the energy and neutron width ($\Gamma_{\lambda,n}$) parameters were retrieved up to 100 eV. Figures 2 and 3 display the fitting process and results with REFIT.

V. Results and Discussion

The neutron capture cross section was derived from the neutron capture yields and the incident neutron spectrum. For comparison, the measured ^{237}Np capture cross section using the neutron spec-

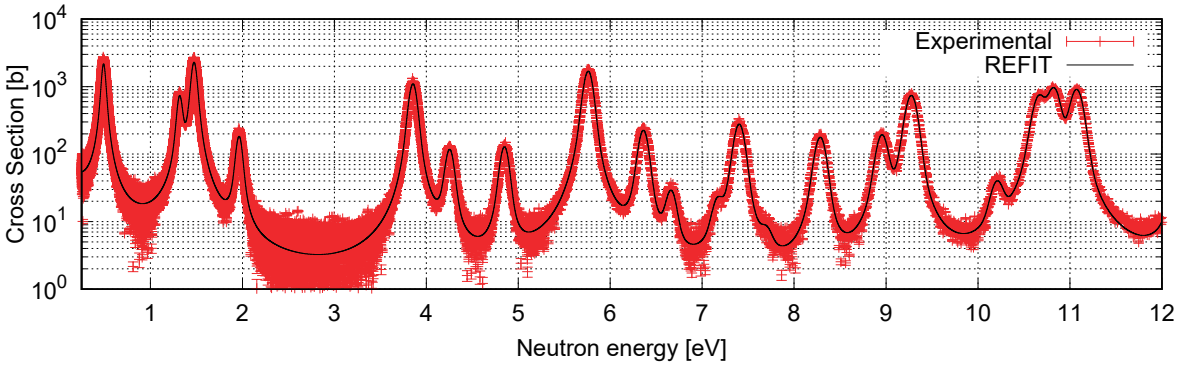

Figure 2: *Resonance fitting using REFIT*

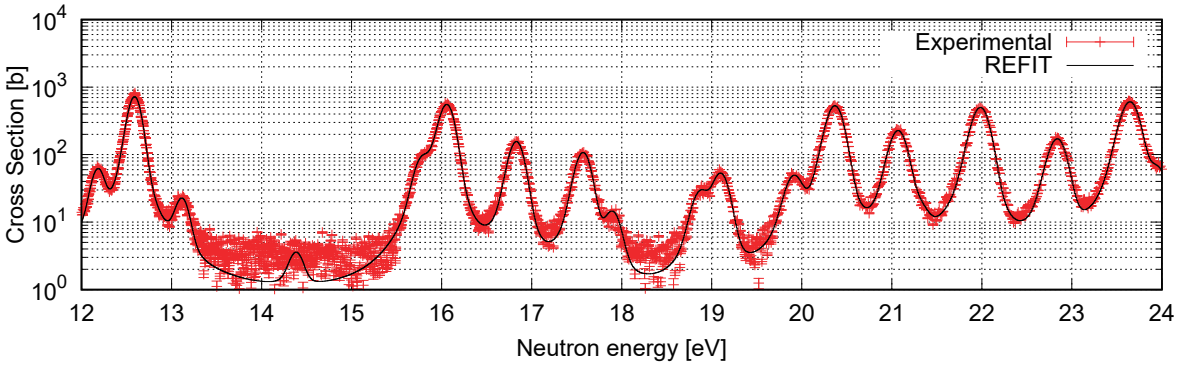

Figure 3: *Resonance fitting using REFIT*

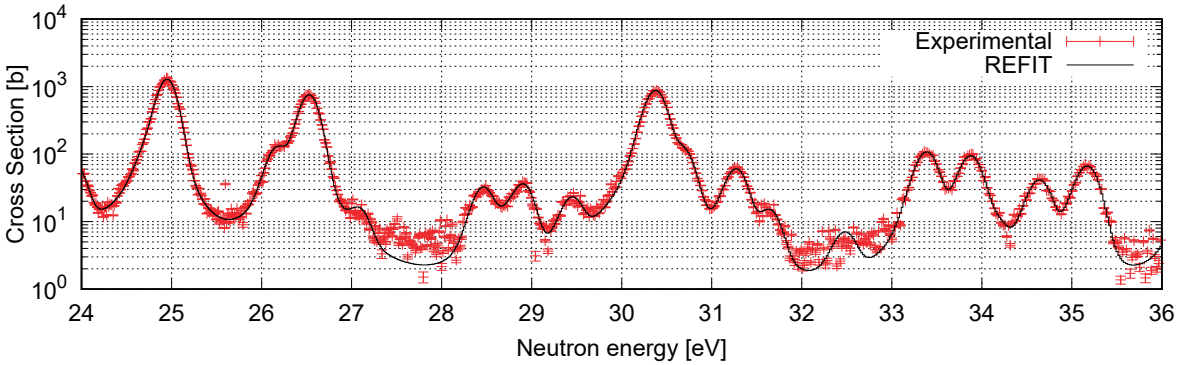

Figure 4: *Resonance fitting using REFIT*

trum with the boron sample is plotted along with evaluated data from JENDL-4.0 (Fig. 5). The capture cross section was measured from thermal energy up to 500 keV. The data was normalized at the JENDL 4.0 first resonance of the cross section. In this work, a thermal value for the cross section (σ_{th}) of 176.7 $\pm$ 0.5$_{sta}$ was obtained. There is a good agreement from thermal region up to 100 keV.

There are two main sets of data available that were measured using the TOF method in the high energy region. Figure 6 portrays a comparison with experimental data from Weston [10] and Esch [14] in the high energy region. The present experimental data has similar values to those experimental data but, over 100 keV, the present data presents lower values. As the present measured data is preliminary,

only the statistical error is included. Uncertainties amount to 5% over the resolved resonance region, higher than 0.5 keV. Further measurements ought to be performed with increased measuring time and beam power. Should the beam power increase to 1 MW, which is the operational goal for J-PARC, with doubling the measuring time, the statistical uncertainties can be reduced below 2.5%.

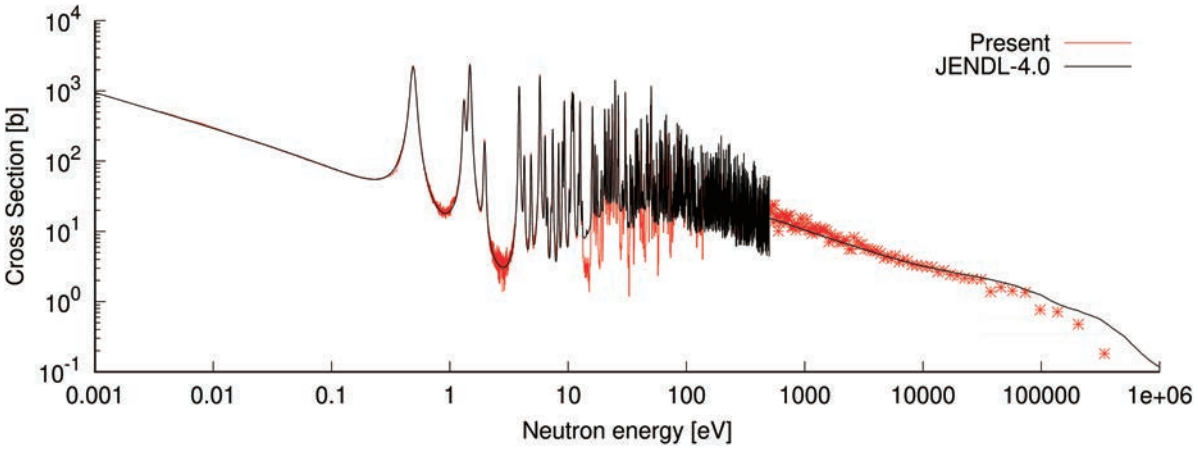

Figure 5: *^{237}Np neutron capture cross section*

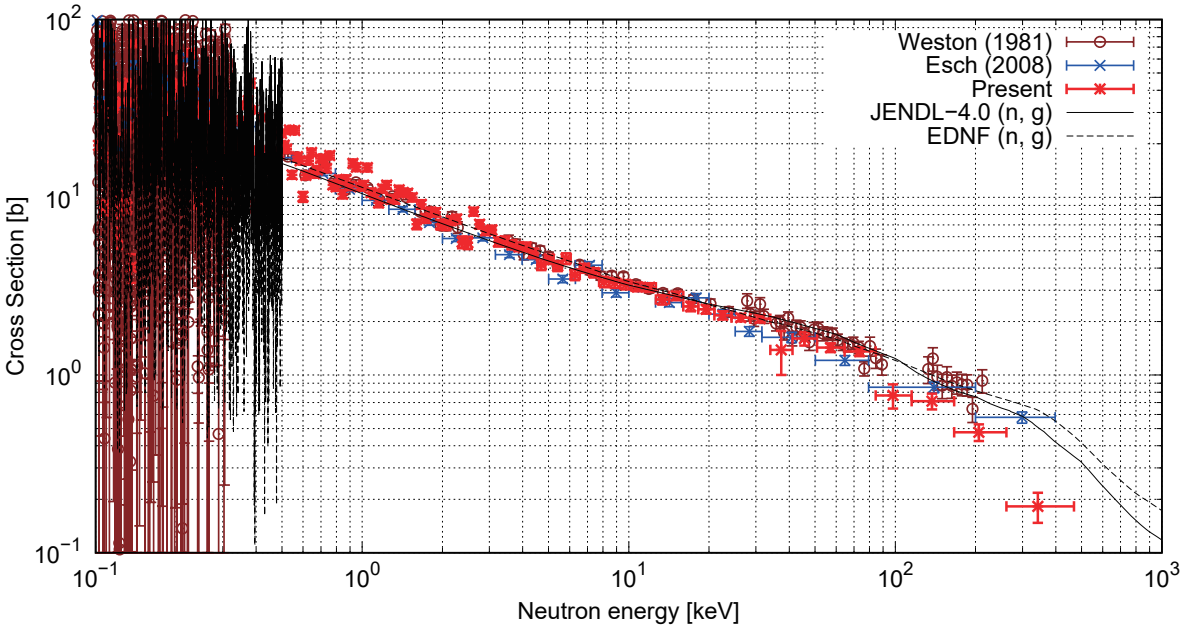

Figure 6: *High energy region of ^{237}Np neutron capture cross section*

For the resonance analysis results, in table 1, the value for the averaged radiation width obtained in this work is presented along with previous results from other authors. Results, albeit not being final, offer a good agreement with prior values.

Table 1: *Comparison of the averaged neutron width with reported data*

Authors	Value (meV)
Paya	40.0 ± 1.2
Mewissen et al.	41.2 ± 2.9
Weston and Todd	~ 40
Gressier	40.0 ± 2.0
Noguere	39.3 ± 1.0
Mughaghab	40.7 ± 0.5
RIPL-3	40.8 ± 1.2
C. Guerrero	40.9 ± 1.8
This work	40.1

The ^{237}Np neutron capture cross section was measured using the pulsed neutron beam generated by the Japanese Spallation Neutron Source in the Materials and Life science Facility at the Japan Proton Accelerator Research Complex. Using pulse width analysis along with pulse-height weighting technique, the neutron capture cross was succesfully dertermined from thermal energy region up to 500 keV. The resonance analysis process still needs to be finalized once the systematic uncertainties have been determined for this experiment. The resonances will then be reanalyzed and the final results will be presented along with uncertainties and statistical properties of the resonances.

References

[1] H. Iwamoto et al. Nuclear Data Sheets 118 (2014) 519-522.
[2] K. Kobayashi et al., J. Nucl. Sci. Technol. 1994; 31:12349-1247.
[3] T. Katoh et al., J. Nucl. Sci. Technol. 2003; 40:559-568.
[4] H. Harada et al. J. Nucl. Sci. Technol. 2006; 43:1289-1297.
[5] N. N. Buleeva et al., AE, 65(6), 1988.
[6] A. Letourneau et al., Appl. Radiat. Isot. 2010; 68:432-438.
[7] Ju. N. Trofimov et al., Conf: 6.All-Union Conf.on Neutron Physics,Kiev,2-6 Oct.1983, Vol.2, p.142 (1983), USSR.
[8] M. Lindner et al., J. Nucl. Sci. Eng. Vol.59, p.381 (1976), USA.
[9] D. C. Stupegia et al., J. Nucl. Sci. Eng. Vol.29, p.218 (1967), USA.
[10] L.W. Weston et al., Nucl. Sci. Eng. 1981; 79:184-196.
[11] K. Kobayashi et al., J. Nucl. Sci. Technol. 2002; 39:111-119.
[12] O. Shcherbakov et al., J. Nucl. Sci. Technol. 2005; 42:135-144.
[13] M. Mizumoto et al., http://doi.org/10.1051/ndata:07463
[14] E-I. Esch et al., Phys. Rev. 2008; C77:034309.
[15] C. Guerrero (n-TOF Collaboration), Phys. Rev. 2012; C85:044616.
[16] M.D. Semon et al., BAP 21, 655 (JE3), 1976.
[17] K. Hirose et al., J. Nucl. Sci. Technol. 2013; 50:188-200.
[18] T. Katabuchi et al., IAEA-TECDOC–1743 332-340, 2014. International Atomic Energy Agency (IAEA).
[19] FAST ComTec MPA4T `https://www.fastcomtec.com/products/mpa/mpa4t0/`
[20] T. Katabuchi et al., Nucl. Ins. and Meth. in Phy. Res. A, 764 (2014) 369-377., Nucl. Ins. and Meth in Phy. Res. A 626-627(2011)58-66.
[21] R. L. Macklin et al., Nuc. Ins. and Meth. in Phy. Res. 91 (1971) 565.

[22] https://phits.jaea.go.jp/lec/phits-introduction-en.pdf
[23] M. C. Moxon, T. C. Ware, and C. J. Dean, UKNSF(2010)P243 (April 2010).

16 Measurement of Low Threshold Energy Spectra of Secondary Protons for 70-MeV Proton-Induced Reactions

Yuji YAMAGUCHI[1], Toshiya SANAMI[2], Yusuke KOBA[3] and Yusuke UOZUMI[1]
[1]Department of Applied Quantum Physics and Nuclear Engineering, Kyushu University
744 Motooka, Nishi-ku, Fukuoka-shi, Fukuoka-ken 819-0395 Japan
[2]High Energy Accelerator Research Organization
1-1 Oho, Tsukuba-shi, Ibaraki-ken 305-0801 Japan
[3]National Institute for Quantum and Radiological Science and Technology
Anagawa, Inage-ku, Chiba-shi, Chiba-ken 263-8555 Japan
e-mail: yyamaguchi@nucl.kyushu-u.ac.jp

We have developed a low threshold detector consisting of Bragg curve counter (BCC) and two built-in solid-state detectors (SSDs) to obtain experimental double-differential cross section (DDX) data for low energy proton production. Since the BCC offers advantages of self particle identification capability and a few μm-thick entrance window, secondary protons down to 1 MeV have been identified and proton spectra down to 1.3 MeV have been obtained. Measured spectra are compared with calculation results of intra-nuclear cascade (INC) plus evaporation models and nuclear data library.

1. Introduction

Energy and angular distributions of evaporated charged particles from energetic proton-nucleus reactions are required to estimate spatial distributions of energy deposition and radiation damage in devices used for accelerator driven system and particle radiation therapy. Since the estimation is performed using model calculation, it is necessary that nuclear reaction models have high predictive power for energy and angular distributions. Two-stage model, which consists of the intra-nuclear cascade (INC) model and the generalized evaporation model (GEM), generally well describes proton production for intermediate energy proton-nucleus reactions, except for low energy proton production from a heavy target. In the recent study [1], poor prediction of energy and angular distributions of low energy protons has been pointed out. The emission of low energy protons is calculated by the GEM after INC stage as evaporation from an excited nucleus with considering Coulomb barrier [2] and a theoretical study on low energy proton emission [3] has been starting to improve GEM.

For the improvement, new series of experimental double-differential cross section (DDX) data are required covering low energy region down to 2 MeV for wide range of target mass and angles because

systematic data are not available in the low energy region due to threshold energy of conventional detector with ΔE–E particle identification. The particle identification is generally performed with a counter telescope consisting of solid-state detectors (SSDs). Since the threshold energy with particle identification is limited by the thickness of the transmission SSD and 150-μm-thick SSD is commercially available as the thinnest SSD for particle identification, most of the data taken with conventional SSDs have threshold energy around 4 MeV.

To obtain the data covering low energy region, we develop a low threshold detector consisting of Bragg curve counter (BCC) [4, 5] and two built-in SSDs.

2. Experiment

The experiment was performed at cyclotron facility of National Institute of Radiological Sciences. The plan view of the experimental setup is shown in Fig. 1. A scattering chamber was connected directly to the beam duct of the cyclotron and evacuated to less than 10^{-3} Pa. Incident protons from the cyclotron hit a target located inside the scattering chamber and entered a Faraday cup consisting of a stainless–steel pipe and a graphite beam dump. The incident proton energy of 70-MeV and targets of ^{nat}C, ^{27}Al, ^{nat}Cu, and ^{197}Au were chosen. The targets were mounted on a target changer. Energy spectra of secondary particles emitted from the target were measured at 60 degrees in the laboratory system with the low threshold detector and a counter telescope consisting of a SSD and a BGO scintillator.

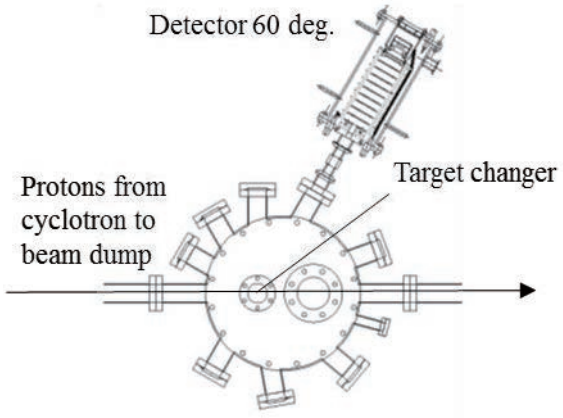

Figure 1. Plan view of experimental setup. Incident protons come from the left side of this view.

The schematic drawing of the low threshold detector is shown in Fig. 2. The threshold energy of 1 MeV is expected with proton identification since the BCC has a thin entrance window and self particle identification capability, as will be described below.

The BCC is a parallel plate ionization chamber with a grid. The chamber is cylindrically shaped and sealed using O-rings to keep Ar + 10 % CH_4 gas as a counting gas. The gas pressure of 53.3 kPa (400 Torr) and

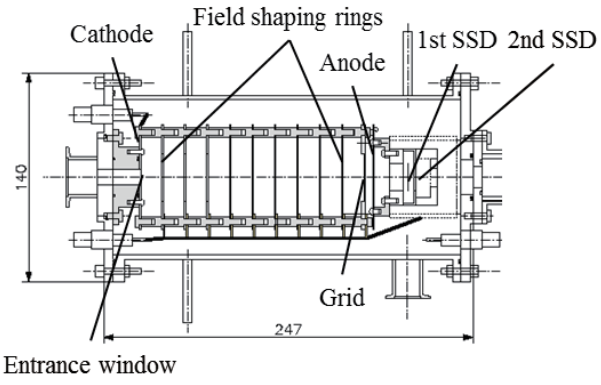

Figure 2. Schematic drawing of low threshold detector. Secondary particles come from the left side of this drawing and pass through the entrance window.

106.6 kPa (800 Torr) were adopted for detection of evaporated protons. The inside electrodes of the BCC consist of the cathode, field shaping rings, grid, and anode. The distances from the cathode to the grid and from the grid to the anode were set to 150 mm and 5 mm, respectively. The distances of 146 mm and 9 mm were also used to improve the ratio of the anode signal to noise for detection of protons. The anode plate is a stainless-steel disk with a central hole 32 mm in diameter. The hole is covered with a 5-μm-thick aluminum foil which is connected with the stainless-steel disk electrically. Thus, the anode allows energetic secondary particles to penetrate with small energy loss. The field shaping rings are arranged at equal intervals to maintain a uniform electric field. The electric field is formed by providing high voltage for the cathode, field shaping rings and grid. The cathode is a stainless-steel disk with a central hole 10 mm in diameter covered with a 2.2-μm-thick aluminized Mylar film. Since the aluminized surface and the stainless-steel disk are connected electrically, the cathode plays the role of a thin entrance window, which introduces secondary charged particles with small energy loss.

The secondary particle stopped in front of the grid produces electron-ion pairs along its trajectory by ionizing the counting gas. Since the number of electrons is proportional to the energy deposited by the secondary particle, distribution of electrons corresponds to Bragg curve. Keeping the distribution, the electrons drift toward the grid due to the electric field, and then all the electrons pass through the grid and reach the anode. In this case, time distribution of the anode signal has inverse shape of the original distribution of electrons (Fig.3). Therefore, the energy (E_{BCC}) and the atomic number of the secondary particle can be deduced from integral and peak height of the anode signal, respectively. The integral of the anode signal is obtained using a long time constant (6 μs) amplifier and the peak height a short time constant (0.25 μs) shaping amplifier.

In Fig. 4, a typical example of E_{BCC} vs Bragg peak height (atomic number) two-dimensional plot is shown. Secondary particles with enough energy to form the

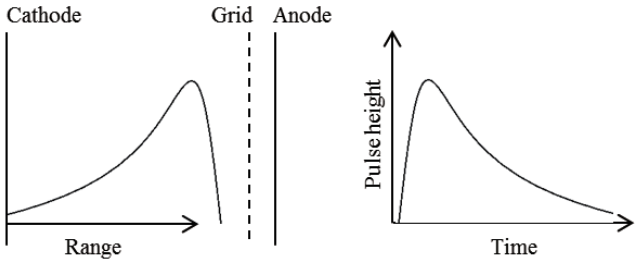

Figure 3. Distribution of electrons produced in BCC (left) and time distribution of anode signal (right).

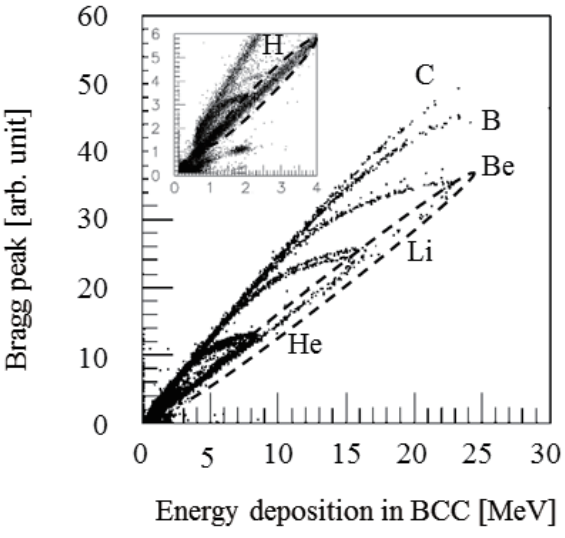

Figure 4. E_{BCC} vs Bragg peak height (atomic number) two-dimensional plot. The inset shows the plot in low energy region up to 4 MeV. The identified secondary particles from H to C are shown. Particles penetrating the anode are identified inside dashed circles.

Bragg peak are identified. For the high energy side of hydrogen, helium, lithium and beryllium, particles penetrating through the anode are observed within dashed circles in Fig.4. These particles are also detected with SSDs behind the anode and identified by applying the ΔE–E method. In this case, the BCC works as a transmission detector. Since the 1st SSD and the 2nd SSD are 400 μm- and 1 mm-thick silicon surface-barrier detectors, respectively, the upper limit energy of proton spectra is limited to be 12 MeV with the low threshold detector. For measurement of proton spectra above 12 MeV, the counter telescope consisting of 500 μm-thick SSD and 12 mm-thick BGO scintillator was used.

The measured data were corrected to remove the effects of background component and energy loss in the target, in the entrance window, and in the anode, and then DDXs were obtained by

$$\frac{\mathrm{d}^2\sigma}{\mathrm{d}\Omega \mathrm{d}E} = \frac{Y}{s\phi\Delta\Omega\Delta E'} \tag{1}$$

where s is the number of target atoms per unit area, ϕ is the number of incident protons, $\Delta\Omega$ is the solid angle determined by α-particle counting using ^{241}Am check source placed instead of the target, ΔE is the energy bin width, and Y is the number of charged particles identified in ΔE.

3. Results and discussion

Figure 5 shows E_{BCC} vs Bragg peak height two-dimensional plot obtained using 53.3 kPa counting gas. In this figure, the high energy region is not shown, but the low energy region is focused to discuss self particle identification capability for hydrogen. In the energy range from 1 MeV to 3 MeV, the hydrogen isotopes of protons, deuterons and tritons are identified because the Bragg peak is characterized by the mass number of the charged particle as well as the atomic number. Since the separation between proton and deuteron is observed above 1 MeV in Fig. 5, the threshold energy of proton identification was determined to be 1 MeV.

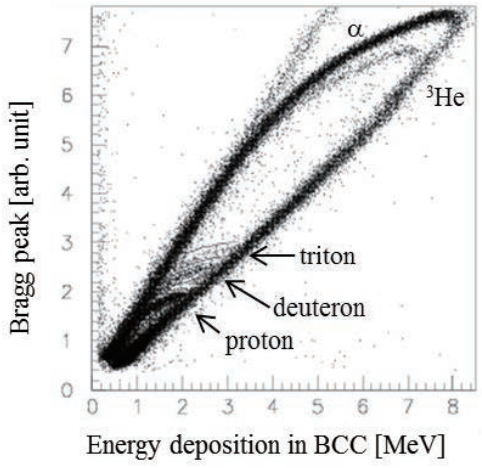

Figure 5. E_{BCC} vs Bragg peak height two-dimensional plot. The identified particles of proton, deuteron, triton, ^{3}He and α are shown.

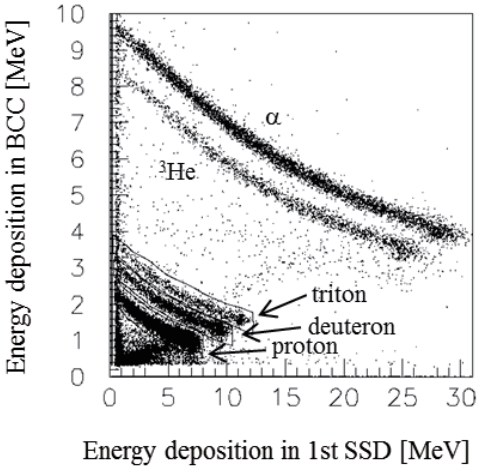

Figure 6. ΔE (BCC) vs E (1st SSD) two-dimensional plot. The identified particles of proton, deuteron, triton, ^{3}He and α are shown.

Figure 6 shows ΔE (BCC) vs E (1st SSD) two-dimensional plot obtained using 106.6 kPa counting gas. The hydrogen isotopes are also identified in this figure because of good energy resolution of the BCC. In Fig. 6, the events of hydrogen and helium isotopes penetrating through the 1st SSD are removed analytically using the signal of the 2nd SSD.

Figure 7 shows proton spectra for 70-MeV incident protons on ^{nat}C, ^{27}Al, ^{nat}Cu and ^{197}Au targets at 60 degrees. Measured spectra were obtained with the low threshold detector below 12 MeV and with the counter telescope above 12 MeV. Since discrepancies between spectrum below 12 MeV and above 12 MeV are observed in ^{27}Al and ^{nat}Cu data, further experiments are planned with a low threshold detector consisting of BCC, SSDs and BGO scintillator. The threshold energy of 1.3 MeV was obtained because of the thin entrance window and self particle identification capability of the BCC. For the ^{197}Au(p, p'x) spectrum, data below 2 MeV show different behavior from data above 2 MeV due to a large contribution of background component and the background component needs to be suppressed.

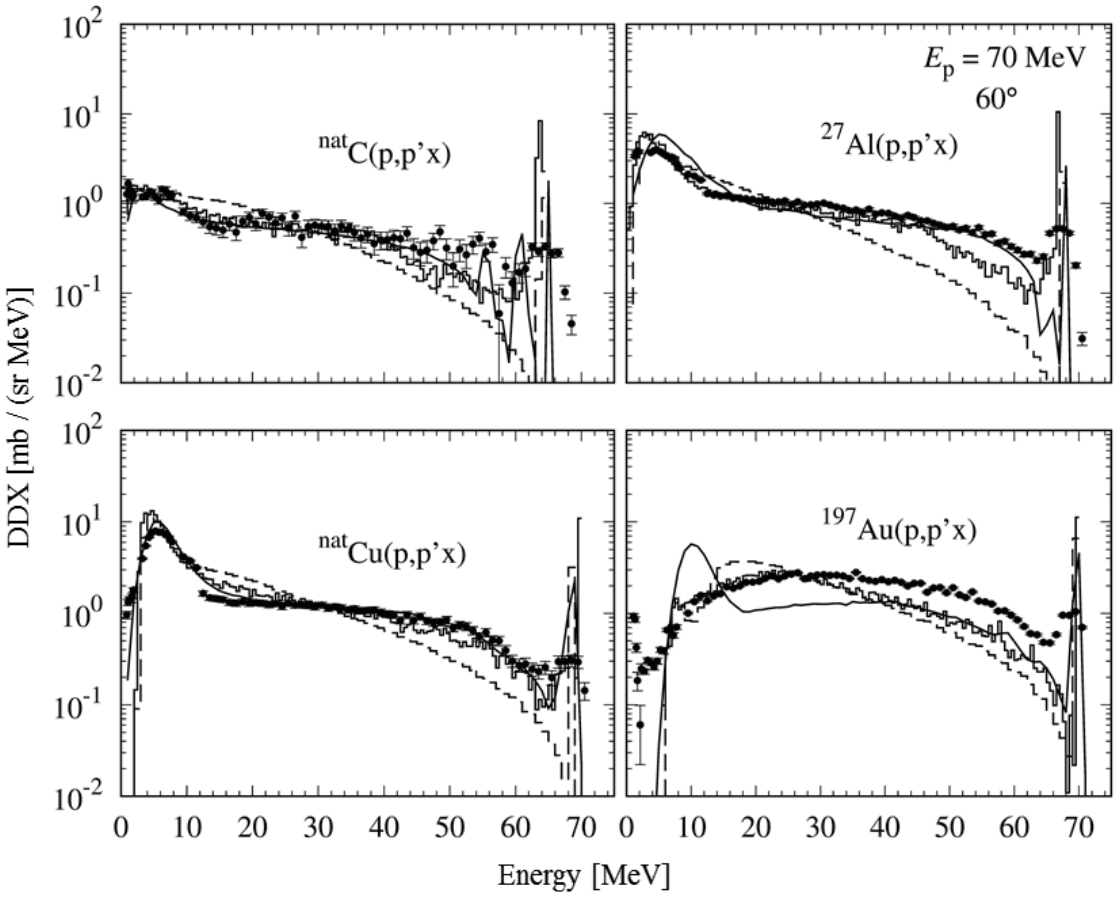

Figure 7. Measured and calculated proton spectra for 70-MeV incident protons on ^{nat}C, ^{27}Al, ^{nat}Cu and ^{197}Au targets at 60 degrees. Measured spectra are shown using closed circles with bar indicating statistical uncertainties. Calculation results of JENDL-4.0/HE, INC-ELF plus GEM and INCL plus GEM are shown with smooth curves, solid histograms and dashed histograms, respectively.

Calculation results of INC-ELF plus GEM and INCL plus GEM are in reasonable agreement with measured data for ^{nat}C, ^{27}Al and ^{nat}Cu targets below 4 MeV, where evaporated protons calculated by GEM are dominant. JENDL results are also in reasonable agreement in the energy region. For the ^{197}Au target, GEM result, which is dominant below 10 MeV has threshold at 6 MeV whereas measured data exist below 6 MeV. The peak in the spectrum of JENDL at 10 MeV is not observed in measured spectrum and should be modified.

4. Conclusion

We developed a low threshold detector consisting of the BCC and two built-in SSDs to obtain experimental data covering low energy region. Using the detector and a counter telescope, proton spectra down to 1.3 MeV were obtained for ^{nat}C to ^{197}Au targets though background component needs to be suppressed for the ^{197}Au target below 2 MeV. Calculation results are in reasonable agreement with measured data for ^{nat}C, ^{27}Al and ^{nat}Cu targets. For the ^{197}Au target, GEM has threshold though measured data exist below the threshold. The peak in the spectrum of JENDL at 10 MeV should be modified.

Acknowledgements

This work was conducted at Joint-use Research Facility for Collaborative Project with NIRS-Cyclotron.

References

[1] Y. Uozumi, T. Yamada and M. Nakano: J. Nucl. Sci. Technol. 52, 264 (2015).
[2] S. Furihata: Nucl. Instr. and Meth. B 171, 251 (2000).
[3] Y. Yamaguchi, Y. Uozumi and M. Nakano: EPJ Web of Conference 122, 1 (2016).
[4] T. Sanami, M. Hagiwara, T. Oishi, M. Baba and M. Takada: Nucl. Instr. and Meth. A 589, 193 (2008).
[5] M. Hagiwara, T. Sanami, T. Oishi, M. Baba and M. Takada: Nucl. Instr. and Meth. A 592, 73 (2008).

17 Double-Differential Cross Sections in the Vicinity of 180 Degrees for Medium-Energy (p, p'x) Reactions

Ryota IMAMURA[1], Yuji YAMAGUCHI[1], Motoharu FUJII[1],
Kazuhito YOSHIDA[1], and Yusuke UOZUMI[1]
[1]Kyushu University, Graduate School of Engineering
Motooka, Nishi-ku, Fukuoka-shi, Fukuoka-ken, 819-0395 Japan
e-mail: imamura@nucl.kyushu-u.ac.jp

For more reliable calculations in the shielding design of accelerator facilities, double-differential cross sections (DDXs) of proton-induced reactions were investigated in the vicinity of 180 degrees. In the present work, we measured DDXs of (p,p'x) reactions at angles of 160, 165 and 171 degrees. The experimental data were obtained for two targets of ^{12}C, and ^{181}Ta by using the 71-MeV proton beam from the cyclotron of National Institute of Radiological Sciences. We compared the measured DDXs with calculations of INC-ELF and CCONE, and found inconsistencies especially at the high-energy region of the DDX spectrum. The INC-ELF involving the improved deflection parameters gives better accounts at 171 degrees.

1. Introduction

High-energy accelerators have found their applications in a variety of fields such as medicine and energy production in addition to fundamental sciences. There is also increasing interest in accelerator driven systems, which transmute long-lived radioisotopes in used nuclear fuel into shorter-lived fission products. Particle transport simulations are essential in R&D of these technologies. Proper shielding design using the simulations is a common challenge for all accelerator facilities. A calculation uncertainty at 180 degrees with respect to the beam is one of the open problems. This is because there are very few experimental data of the double- differential cross section (DDX) in (p, nx), (p, p'x) and other reactions at the angle of more than 150 degrees. For this reason, the nuclear reaction mechanism is not understood sufficiently, and as a result, development of a nuclear reaction model has not advanced.

The problem of energetic particle production at backward angles was opened in Ref.[1,2], where emitted protons of energies up to 400 MeV were measured at 180 degrees with 600- and 800-MeV proton beams. Many theoretical models were proposed in order to explain these observables. For instance, two models are widely known. One is the model considering the high-momentum component of the nucleon Fermi motion [3]. Although it is successful at high energies, it overestimates greatly the experimental data in the low-projectile energies at 200 MeV. The other is the two-nucleon-cluster model [4,5], which can explain data of both high and low energies. It is, however, controversial that this model ignores the multistep process, which

governs reactions [1] with large-energy transfers, and the trajectory deflection due to the nuclear potential, which appears remarkably in the low-incident energies [2].

Some papers [6-8] pointed out that the deflection plays an important role in the Intra-nuclear Cascade (INC) model calculation. Focusing on the deflection effect could be useful in understanding the mechanism of high-energy particle emissions in the vicinity of 180 degrees. Since the reactions below 100 MeV are less affected by the multistep process and the delta particle production and involve the large deflection, they are very useful in revealing the role of the deflection.

In this paper, we report studies on backward proton productions of (p, p'x) reactions below 100 MeV. Experiments are carried out to measure DDX spectra at 71 MeV of the beam energy. The model study with INC is also conducted to explain the experimental observations.

2. Method

Experiment

The experiment was performed at the cyclotron facility of National Institute of Radiological Sciences (NIRS). The experimental arrangement was shown in Fig. 1. The scattering chamber was installed at the C6 beam line. The incident proton energy was 71 MeV, and ^{12}C (100 μm thick) and ^{181}Ta (30 μm thick) were used as the target. The blank target was also used for the background measurement.

The charged particles like protons emitted from the target were detected with counter telescopes placed at 160, 165, and 171 degrees by using ΔE-E technique. The counter telescopes were composed of one or two silicon surface-barrier detectors (SSDs) and a cerium-doped gadolinium silicate; $Gd_2SiO_5(Ce)$ (GSO) crystal detector. The SSDs (0.1 mm, 0.15 mm, 0.4 mm, and 2 mm thick) were used as ΔE-detectors. The GSO(Ce) scintillator is an E-detector of cubic with a 43-mm edge length. A photomultiplier tube (PMT) was connected GSO(Ce) to convert scintillation light into the electric signal and amplify the signal. The general view was shown in Fig. 2.

Electric signals from detectors were fed into a spectroscopic amplifier via a preamplifier. Their pulse heights were analyzed by an amplitude-to-digital converter. The digitized data were transferred to a PC through the CAMAC system, and recorded on hard-drive.

The number of protons passing through the target was counted by a beam monitor placed at the downstream of the chamber. The beam monitor was composed of two plastic scintillators with an Al-foil-scatter. The counts of the beam monitor were calibrated by the Faraday cup placed about 30 cm upstream of the chamber.

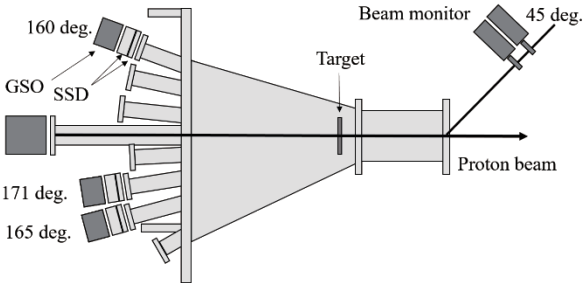

Fig. 1. the measurement system

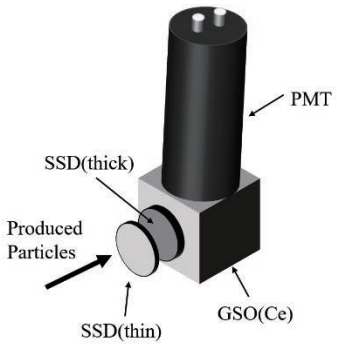

Fig. 2. the general view of the counter telescope

Data analysis

We used the Bethe formula for the energy calibration. In the Bethe formula, the energy loss of a charged particle, *dE/dx* is expressed by the following equation:

$$-\frac{dE}{dx} = 4\pi r_0^2 z^2 \frac{m_e c^2}{\beta^2} NZ \left[\ln\left(\frac{2m_e c^2}{I}\beta^2\right) - \ln(1-\beta^2) - \beta^2\right] \quad (1)$$

where E is the energy, x is the thickness of material traversed, r_0 the classical electron radius, z and $v = \beta c$ the charge and velocity of the moving particle, m_e the electron mass, N the number of atoms in the target material per unit, Z the atomic number of the material, and I the mean excitation energy. The example of the experimental data calibrated is shown in Fig. 3.

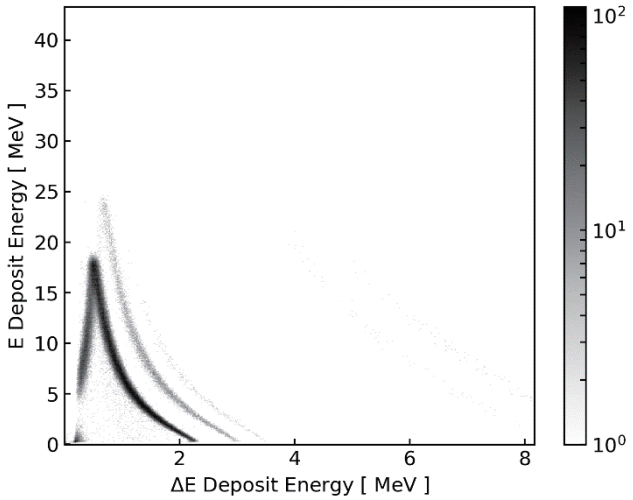

Fig. 3. calibrated data

The particle identification was carried out by using the *PI* parameter:

$$PI = (\Delta E + E)^b - E^b \quad (2)$$

where ΔE and E are the deposit energies on ΔE- and E- detectors, and $b(= 1.75$ in this analysis) is the parameter weakly dependent on energy. Figure 4 shows a sample of a plot of PI versus deposit energy to the detectors. In this figure, three bands correspond to protons, deuterons, and tritons.

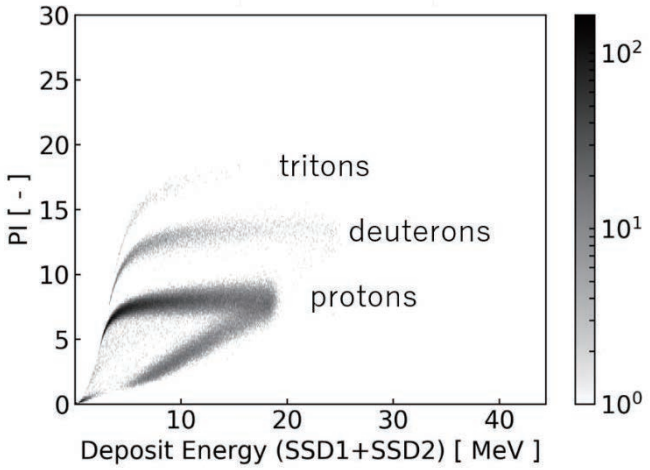

Fig. 4. a two-dimensional plot of PI versus deposit energy to the detectors

DDX was determined by

$$\frac{d^2\sigma}{d\Omega dE} = \frac{Y_p}{\Phi \varepsilon_D \rho_S P \Delta E \Delta\Omega} \tag{3}$$

where Y_p is the counts per energy bin width ΔE, Φ the number of protons of the beam, ε_D the data acquisition efficiency, ρ_S the surface density of the target, P the peak efficiency of the detector $\Delta\Omega$ the detector solid angle.

3. Results and Discussion

The spectra of DDXs for 71-MeV ^{12}C(p, p'x) and ^{181}Ta(p, p'x) reactions at 160, 165, and 171 degrees are shown in Fig. 5 and Fig. 6, respectively. In the Fig. 6, there are lack of data in 15-19 MeV at the angle of 171 degrees. This is because there are air layers and reflective tapes made of aluminum and teflon between SSD and GSO detectors. In other DDXs, we obtained the entire-energy-range spectra by combining two different spectra measured by two kinds of the detector system.

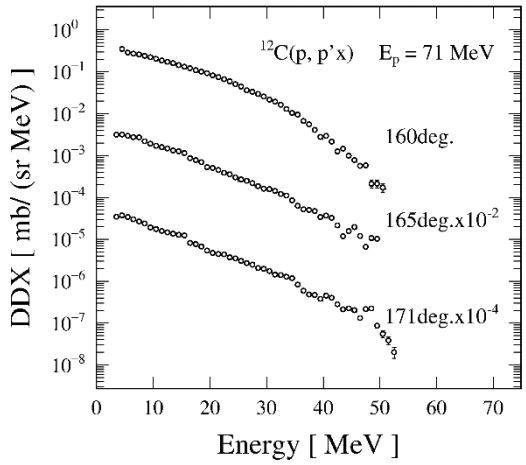

Fig. 5. spectra of DDXs for 71-MeV ^{12}C(p, p'x)

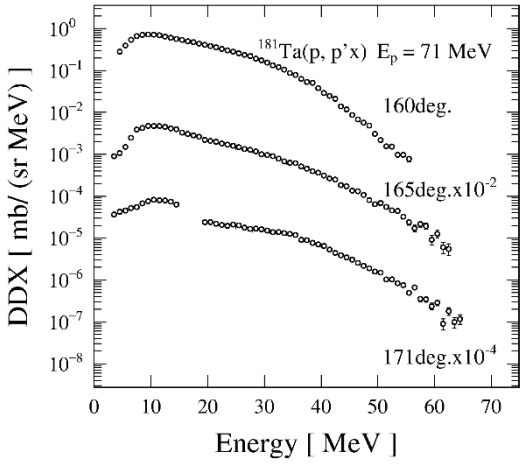

Fig. 6. spectra of DDXs for 71-MeV ^{181}Ta(p, p'x)

Figure 7 and 8 show the experimental data of the $^{12}C(p, p'x)$ reaction at 171 degrees compared with the calculation results of CCONE [9] and INC-ELF [10], respectively. As shown in these figures, both calculation results underestimate experimental values more greatly as the emitted proton energy increases. In CCONE, there is also a significant overestimation in low energies and further improvements are needed in whole. In INC-ELF, an important problem is that there is a large discrepancy in the high-energy range at backward angles, especially in the vicinity of 180 degrees.

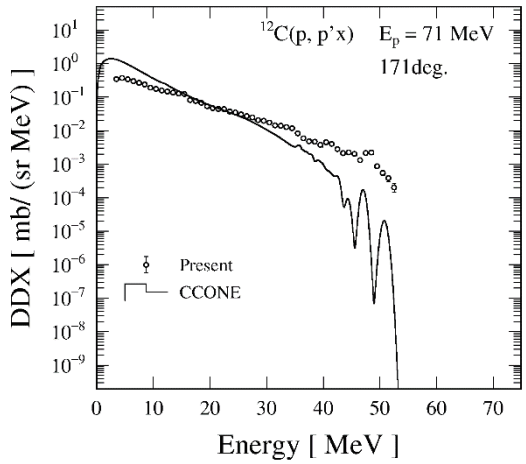

Fig. 7. comparison of (p, p'x) DDX with CCONE

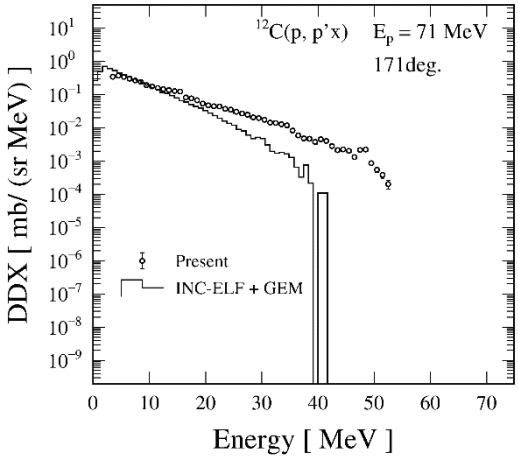

Fig. 8. comparison of (p, p'x) DDX with INC-ELF

Next, we considered the improvement of INC-ELF. The poor deflection might be one of the factors causing the large discrepancy. In INC-ELF, the magnitude of the deflection is determined on the basis of angular distributions of elastic scattering cross-sections. Figure 9 represents the angular distribution of 70-MeV proton elastic scattering of the ^{12}C target. Calculation values in JENDL-4.0/HE [11] are also plotted in this figure. The previous approximation (broken line) was determined only by experimental data at the forward angles because of lack of experimental data at backward, therefore, the probability of bending to backward angles by deflection might be too small. To this end, as in Fig. 9, we determined the modified approximation (solid line) so that the probability above 90 degrees increased.

Figure 10 shows the comparison of previous INC-ELF with modified INC-ELF. Experimental data are also plotted in this figure. As shown Fig. 10, it is found that modified INC-ELF shows remarkable improvement in the high-energy domain. It indicates that the modification about deflection has the potential of improving the INC model. As a next step, we will introduce much better deflection parameter, and validate the model with other angles, targets and energies.

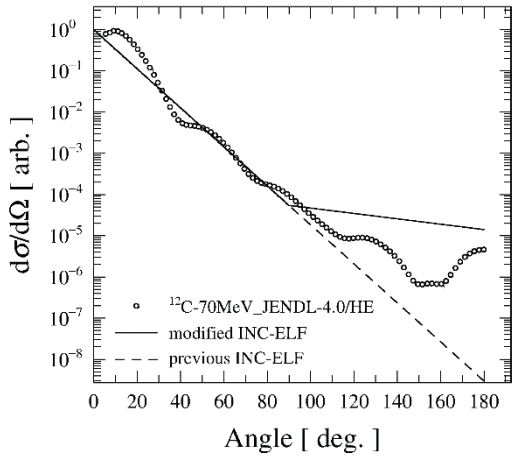

Fig. 9. angular distribution of 70-MeV proton elastic scattering of the ^{12}C target

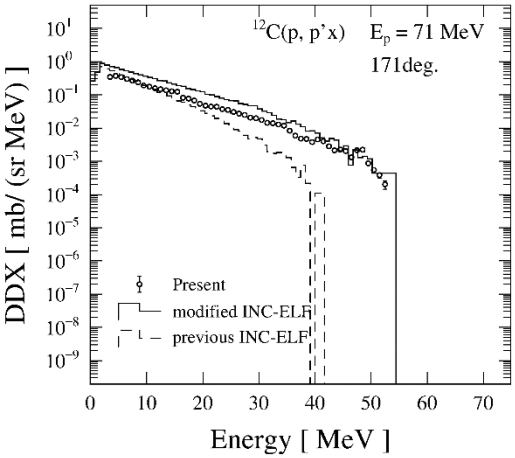

Fig. 10. comparison of ^{12}C(p, p'x) DDX with INC-ELF (previous and modified)

4. Conclusion

We measured DDXs of 71-MeV (p, p'x) reactions at backward angles of 160, 165, and 171 degrees at the cyclotron facility of NIRS. We compared the experimental data with CCONE and INC-ELF, and found that the calculation results underestimated experimental values greatly in high-energy range. This discrepancy in INC-ELF was improved by using new deflection parameters in the ^{12}C(p, p'x) reaction at 171 degees. We will extend the range of the application of this method by checking other conditions.

Acknowledgements

This work was conducted at Joint-use Research Facility for Collaborative Project with NIRS-Cyclotron.

References

[1] S. Frankel, W. Frati, O. Van Dyck, et al., Phys. Rev. Lett. 36, 642 (1976).

[2] S. Frankel, W. Frati, G. Blampied, et al., Phys. Rev. C 18, 1375 (1978).

[3] M. Avan et al., Phys. Rev. C 30, 521 (1984).

[4] Y. Haneishi and T. Fujita, Phys. Rev. C 33, 260 (1986).

[5] Y. Haneishi and T. Fujita, Phys. Rev. C 35, 260 (1987).

[6] Y. Uozumi, T. Yamada, S. Nogamine, M. Nakano, Phys. Rev. C86, 034610 (2012).

[7] Y. Uozumi, T. Yamada, M. Nakano, Jour. Nucl. Sci. Technol., 52, 264 (2015).

[8] M. J. Kobra, G. Watanabe, Y. Yamaguchi, Y. Uozumi, M. Nakano, Jour. Nucl. Sci. Technol., 55, 209 (2018).

[9] O. Iwamoto: J. Nucl. Sci. Technol, 44:5 (2007), 687-697.

[10] Y. Sawada, Y. Uozumi, S. Nogamine, T. Yamada, Y. Iwamoto, T. Sato, and K. Niita, Nucl. Instr. & Meth. B 291, 38-44 (2012).

[11] S. Kunieda et al., JAEA-Conf 2016-004, 41-46 (2016).

18 Effect of the level density on odd-even staggering in proton- and deuteron-induced spallation reactions on ^{93}Zr and ^{107}Pd

Shunsuke Sato and Yukinobu Watanabe
Department of Advanced Energy Engineering Science, Kyushu University
Email: s.s@aees.kyushu-u.ac.jp

We have investigated the effect of level density in the generalized evaporation model (GEM) implemented in PHITS on exaggerated odd-even staggering (OES) seen in calculations of isotopic production in proton- and deuteron-induced spallation reactions on ^{93}Zr and ^{107}Pd. It was found that the level density with a back-shifted Fermi gas model with energy dependence results in weaker OES than the Gilbert and Cameron level density used in the original GEM, and the agreement with the experimental data was improved.

This work was funded by ImPACT Program of Council for Science, Technology and Innovation (Cabinet Office, Government of Japan).

Keyword : GEM, INCL, deuteron-induced reaction, isotopic production cross section, odd-even staggering

1. Introduction

Nuclear transmutation of long-lived fission products (LLFPs) with spallation reactions has been studied in the ImPACT Fujita program, in which Particle and Heavy Ion Transport code System (PHITS) [1] has been used in the simulation of transmutation with spallation reactions in macroscopic LLFP target system. In the PHITS calculation, INCL [2] and GEM [3] models are used to describe the spallation reaction as a two-step process composed of the cascade and evaporation processes, respectively. In the simulations, it is of essential importance to use theoretical models that reproduce nuclear reactions well.

Recently, the PHITS calculation was compared with the latest experimental data of isotopic production cross sections of proton- and deuteron-induced spallation reactions on ^{93}Zr [4]. The calculation reproduced the experimental data generally well, but some discrepancies were found between the calculation and the experimental data. First, the PHITS calculation underestimates the measured cross sections in the neutron deficient region of the produced isotopes adjacent to the target nucleus. The underestimation is expected to be caused by suppression of neutron emission by using the empirical formula of Dostrovsky et al. [5] as the inverse reaction cross section. Since there is a discrepancy between the formula and the experimental data and/or optical model calculation in the low energy region, we have derived a new systematics of the

neutron and proton reaction cross sections based on the optical model calculation with the Koning-Delaroche potential [6]. The new systematics results in improvement of the underestimation. Next, odd-even staggering (OES) is strongly seen in the calculated isotopic distribution of production cross sections, while the experimental data has no such staggering. It was presumed that the OES may be caused by neglect of competition between particle and gamma-ray emissions from unbound states of excited nuclei in the original GEM. To see the effect of the competition on the OES, we considered the competition in GEM [7], but the effect was found to be small. In the present work, we pay attention to the level density used in GEM, and examine how the level density affects the exaggerated OES seen in the calculated isotopic production cross sections.

2. Level density formula

The level density formula of Gilbert and Cameron (GC) [8] is used in GEM. The GC formula is expressed by the Fermi-gas (FG) formula and the constant temperature (CT) formula according to excitation energy. In the statistical model calculations with CCONE [9] and TALYS [10], experimental discrete levels are considered at low excitation energies, while the GC formula is used over the whole excitation energy range in GEM. Our preliminary GEM analysis found that the pairing correction is not sufficient in the low excitation energy region to which the CT formula is applied, resulting in the strong OES effect. To improve this situation, we have implemented a back-shifted Fermi gas model with energy dependence (BSFG-ED) [11] instead of the GC formula:

$$\rho_{BSFG}(E) \propto \frac{e^{2\sqrt{a(E-\Delta)}}}{a^{\frac{1}{4}}(E-\Delta+t)^{\frac{5}{4}}},$$

where Δ is the energy shift, a is the level density parameter, and t is the nuclear temperature, respectively. The level density parameters were determined by fitting of complete level schemes at low excitation energies and the average neutron resonance density at the neutron binding energy. It is noted that the AME2003 mass table [12] was employed in the use of the BSFG-ED formula, instead of the Audi-Wapstra mass table [13] in GEM.

3. Results and Discussion

3.1 Total level density

Figure 1 shows the calculated total level densities of ^{88}Sr and ^{95}Tc produced by proton and deuteron- induced spallation reactions on ^{93}Zr. The strong OES appears in the calculation of ^{88}Sr production and a large discrepancy is seen between calculated and experimental production cross sections of ^{95}Tc as seen in Refs. [4, 14]. The solid and dashed lines denote BSFG-ED and

GC calculations, respectively. In ^{88}Sr, BSFG-ED calculation has an energy gap in the low excitation region. This gap is expected to compensate the deficiency of pairing correction that caused the strong OES in the isotopic production cross section calculated by using the GC formula. In ^{95}Tc, BSFG-ED calculation results in an increase in production cross section as shown in subsection 3.2.

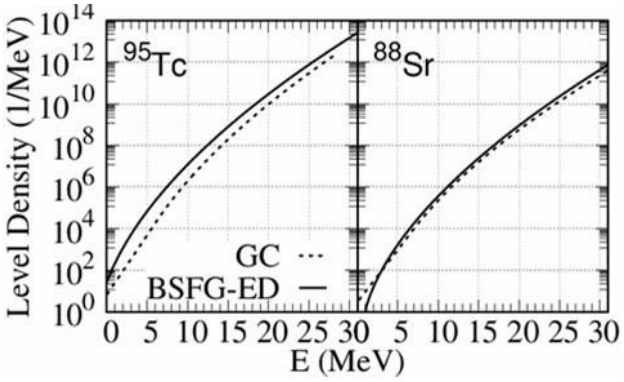

Fig. 1 Total level densities of ^{95}Tc and ^{88}Sr calculated with the GC and BSFG formulae as a function of excitation energy.

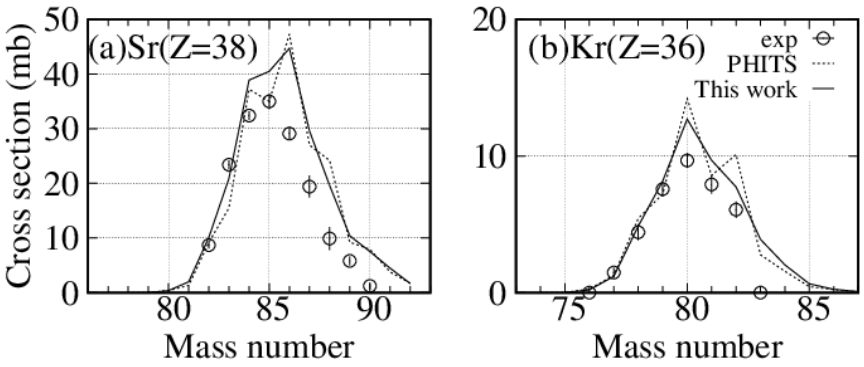

Fig. 2 Isotopic production cross section as a function of mass number for each isotope in the d + ^{93}Zr reaction at 105 MeV/u : (a) Sr (Z = 38), (b) Kr (Z = 36).

3.2 Production Cross Section

Figure 2 shows the experimental data of deuteron-induced reaction on ^{93}Zr at 105 MeV/nucleon and PHITS calculations using the GC formula (dashed line) and the BSFG-ED formula (solid line) for production cross-sections of Sr and Kr isotopes. The calculation with the BSFG-ED formula makes the staggering weaker than that with the GC formula, and the agreement with the experimental data is improved. Fig. 3 shows comparisons of the experimental and calculated production cross sections for Ru, Tc, Mo and Nb isotopes in the deuteron-induced reaction on ^{107}Pd at 196 MeV/nucleon. Table 1 gives the chi-square values χ^2 of individual reactions. It is

found that the use of the BSFG-ED formula makes the OES weaker and agreement with the experimental data is improved. Especially, the χ^2 for the new GEM with the BSFG-ED formula is about 50% better than that for the original GEM in the p + ^{107}Pd reaction at 196 MeV. It is noted that this calculation considers the same systematic of inverse reaction cross section and gamma-ray emission from unbound states as described in section 1 [7].

Table 1 χ^2 of each reaction

Reaction	MeV/u	Original GEM	New GEM	Improvement (%)
^{93}Zr + p	105	48.2	34.1	29.3
^{93}Zr + d	105	93.8	70.6	24.7
^{107}Pd + p	196	10.6	5.3	50.3
^{107}Pd + d	196	71.8	51.0	29.0

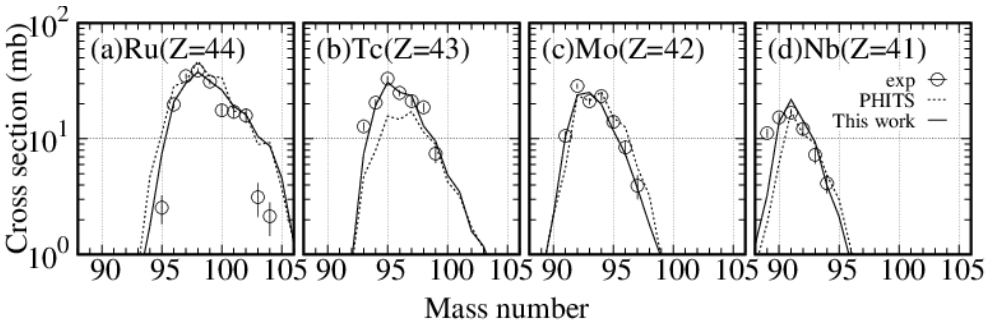

Fig. 3 Isotopic production cross section as a function of mass number for each isotope in the d + ^{107}Pd reaction at 196 MeV/u : (a) Ru (Z = 44), (b) Tc (Z = 43), (c) Mo (Z = 42), (d) Nb (Z = 41).

3.3 Branching Ratio

We focus on the production of Tc isotopes in the d + ^{107}Pd reaction at 196 MeV/u, because ^{95}Tc is one of the most improved isotopes by use of the BSFG-ED formula as shown in Fig. 3. Since proton or neutron emission is dominant in the evaporation process, we have investigated the branching ratio of ^{96}Ru and ^{96}Tc that are parent nuclides of ^{95}Tc in order to understand why the improvement is achieved. Fig. 4 shows the excited energy dependence of the branching ratios. The solid and dashed lines are the branching ratios of neutron and proton emission, respectively. The panels (a) and (c) present the results with the GC formula, while the panels (b) and (d) do those with the BSFG-ED formula. By changing the GC formula to the BSFG-ED one, the proton emission probability of ^{96}Ru changes from some dozen % to about 40% around the

excitation energy of 20 MeV. On the other hand, the proton emission probability is suppressed from several 10% to about 10% in ^{96}Tc. It was found that the change of total level density has a large impact on the branching ratio and leads to an increase in production of ^{95}Tc.

4. Conclusion

We have investigated the effect of level density on the odd-even staggering (OES) seen in the GEM calculation of isotopic production in proton- and deuteron-induced spallation reactions on ^{93}Zr and ^{107}Pd. It was found that the use of the BSFG-ED formula results in weaker OES than that of the GC formula. Based on the result, the GEM model was modified, and then the better agreement with the experimental data of isotopic production cross section was obtained. As a next step, we plan to make further improvement for overestimation seen near the target nucleus in the isotopic distribution of production cross sections. According to Ref. [4], the cascade process described by INCL may be responsible for this overestimation.

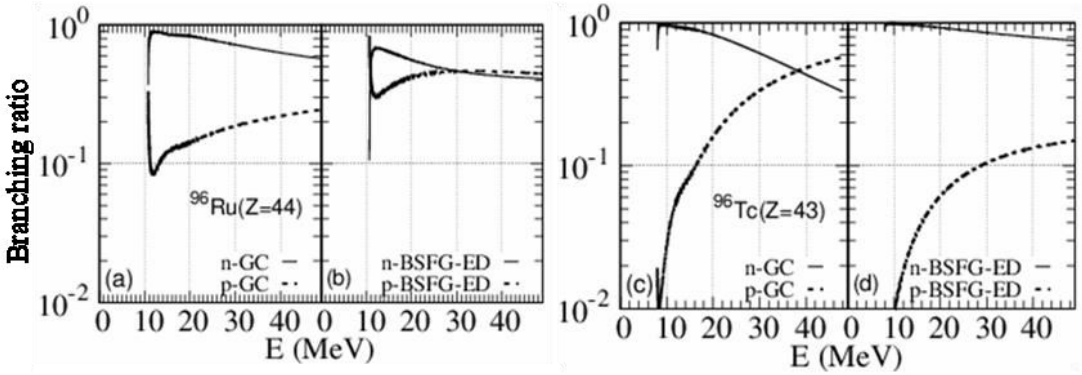

Fig. 4 Branching ratio as a function of excitation energy for ^{96}Ru and ^{96}Tc.

Acknowledgements

We are grateful to T. Ogawa and K. Niita for fruitful discussions.

References

[1] T. Sato *et al.,* J. Nucl. Sci. Technol. **55**, 684-690 (2018).

[2] A. Boudard, J. Cugnon, J.-C. David, S. Leray, and D. Mancusi, Phys. Rev. C **87**, 014606 (2013).

[3] S. Furihata, Nucl. Instrum. Meth. B **171**, 251 (2000).

[4] S. Kawase *et al.*, Prog. Theor. Exp. Phys. **2017**, 093D03 (2017).

[5] I. Dostrovsky, Z. Fraenkel, G. Friedlander, Phys. Rev. 116 (1959) 683.

[6] A.J. Koning and J.P. Delaroche, Nucl. Phys. A 713, 231(2003)

[7] S. Sato *et al.,* Proc, CSS-EEST19, Fukuoka, Japan, Nov. 29- Dec 1, 2017, P095.
[8] A. Gilbert, A.G.W. Cameron, Can. J. Phys. **43** (1965) 1446.
[9] O. Iwamoto, N. Iwamoto, S. Kunieda, F. Minato, and K. Shibata, Nucl. Data Sheets 131, 259 (2016).
[10] A.J. Koning, D. Rochman, Nucl. Data Sheets 113, 2841 (2012).
[11] T. von Egidy and D. Bucurescu, Phys. Rev. C **72**, 044311 (2005); **73**, 049901(E) (2006).
[12] G. Audi, A. H.Wapstra, and C. Thibault, Nucl. Phys. A729, (2003) 337.
[13] G. Audi, A.H. Wapstra, Nucl. Phys. A 595 (1995) 409.
[14] H. Wang et al., Prog. Theor. Exp. Phys. 2017, 021D01 (2017).

19 Measurement of thick target neutron yields from 13.4-MeV deuteron bombardment on LiF, C, Si, Ni, Mo, and Ta

Hayato TAKESHITA[1], Yukinobu WATANABE[1], Keita NAKANO[1], Seiya MANABE[1], Katsumi AOKI[1]
Naoto ARAKI[1], Kosuke YOSHINAMI[1], Tadahiro KIN[1], Nobuhiro SHIGYO[2], Jun KOGA[3], So MAKISE[3],
Tamaki YOSHIOKA[4], Masaomi TANAKA[5], and Takashi TERANISHI[3]
[1]*Department of Advanced Energy Engineering Science, Kyushu University*
[2]*Department of Applied Quantum Physics and Nuclear Engineering, Kyushu University,*
[3]*Department of Physics, Kyushu University*
[4]*Research Center for Advanced Particle Physics, Kyushu University*
[5]*Research Center for Superheavy Elements, Kyushu University*
Email: 2ES17219Y@s.kyushu-u.ac.jp

Double-differential neutron yields from thick target materials (LiF, C, Si, Ni, Mo, and Ta) bombarded by 13.4-MeV deuterons were measured at an emission angle of 0 degrees by using an EJ-301 liquid organic scintillator. Neutron energy spectra were derived by unfolding the measured light output spectra using the FORIST code with the response functions calculated by the SCINFUL-QMD code. The experimental (*d,xn*) spectra were compared with the (*t,xn*) spectra measured at the same incident energy per nucleon, and theoretical model calculations with PHITS and DEURACS.

This work was partially funded by ImPACT Program of Council for Science, Technology and Innovation (Cabinet Office, Government of Japan).

Keyword : double differential neutron yield, deuteron-induced reaction, neutron source

1. Introduction

Neutron production by deuteron-induced reactions has been proposed as a candidate for accelerator-based neutron sources for such applications as transmutation of radioactive waste, production of medical radioisotopes and so on. For the design of these neutron sources, it is important to estimate neutron yields on the basis of experimental data. Up to the present, systematic measurements of deuteron-induced thick target neutron yields (d-TTNYs) from various target materials have been performed in Kyushu University [1-3]. On the other hand, Drosg *et al.* have focused on neutron production with triton irradiation [4] and recently measured triton-induced thick target neutron yields (t-TTNYs) from some target materials at an incident energy of 20.22 MeV [5]. In order to compare d-TTNYs with t-TTNYs from the same materials (LiF, Si, Ni, Mo, and Ta) at the same incident energy per nucleon, or 6.7 MeV/nucleon, we have measured d-TTNYs with 13.4-MeV deuterons in the present work. Moreover, the measured data were compared with theoretical model calculations by Particle and Heavy Ion Transport code System (PHITS) [6] and DEUteron-induced Reaction Analysis Code System (DEURACS) [7], and the reaction models used in the codes were validated.

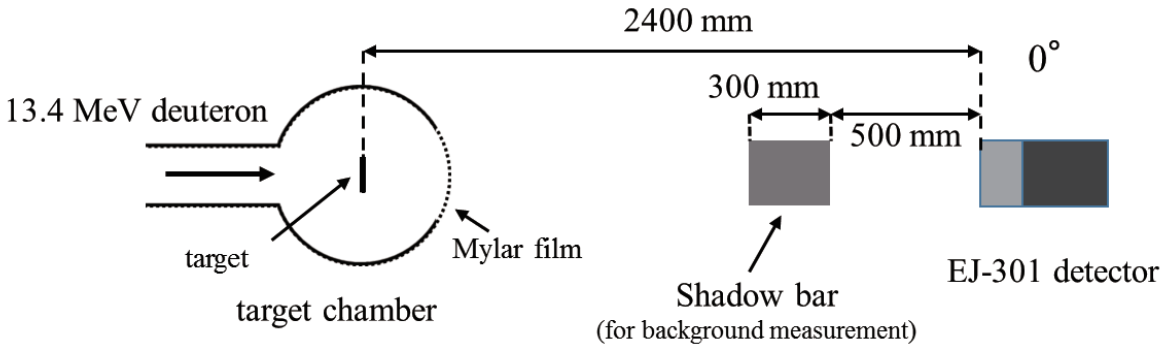

Fig. 1. Schematic drawing of the experimental setup. The shadow bar was placed only in the background measurement.

2. Experiment

The experiment was performed with the 8-MV Tandem accelerator in Kyushu University. The experimental setup is illustrated in Fig. 1. The deuteron beam accelerated to 13.4 MeV was irradiated on the targets placed in a vacuum chamber. The chamber was insulated from the other experimental apparatuses to acquire the whole beam charge induced on the target. In addition, it had a 2-cm-high window covered with a 125-μm-thick Mylar film on the outgoing side in order to reduce the scattering of neutrons in the stainless steel wall. The targets were thick enough to stop incident deuterons completely (2 mm for C, and 1 mm for the others). These thicknesses were determined from the range calculations by the SRIM code [8]. Emitted neutrons were detected by an EJ-301 liquid organic scintillator (5.08 cm by 5.08 cm in diameter and length) placed at the distance of 2.4 m from the target in the emission angle of 0 degrees. In order to estimate the contribution of neutrons scattered from floor and surrounding walls in the experimental room, additional measurements with an iron shadow bar (150 mm wide × 150 mm high × 300 mm thick) placed between the targets and detector were performed.

3. Data Analysis

Particle identification was performed by two gate integration method because the EJ-301 detector is sensitive to gammas as well as neutrons. Figure 2 shows a two-dimensional plot of total and slow components of the EJ-301 light outputs. Neutron events were successfully separated in the region of enough low light output.

Next, the obtained light output spectra of neutron events per ADC channel were converted into those per light output units of electron equivalent (denoted as MeVee). The ADC channels corresponding to the Compton edge for two standard gamma sources, ^{137}Cs (0.662 MeV) and ^{60}Co (1.17 and 1.33 MeV) and for gammas followed by ^{12}C(*d,p*) (3.09 and 3.68 MeV) and ^{13}C(*d,d*) (4.44 MeV) reactions are related to the light output in units of MeVee as shown in Fig. 3. Additional calibration points in higher ADC channels were determined on the basis of the two-body kinematics of the (*d,n*) reactions [9]. Namely, these ADC channels are related to the maximum recoil protons corresponding to neutrons from ^{12}C(*d,n*) and ^{7}Li(*d,n*) reactions.

Finally, neutron energy spectra were derived by an unfolding method using the response functions of the EJ-301 detector calculated by the SCINFUL-QMD code [10] (Fig. 4). The unfolding of the measured light output spectra was performed by the FORIST code [11] based on the least-square method.

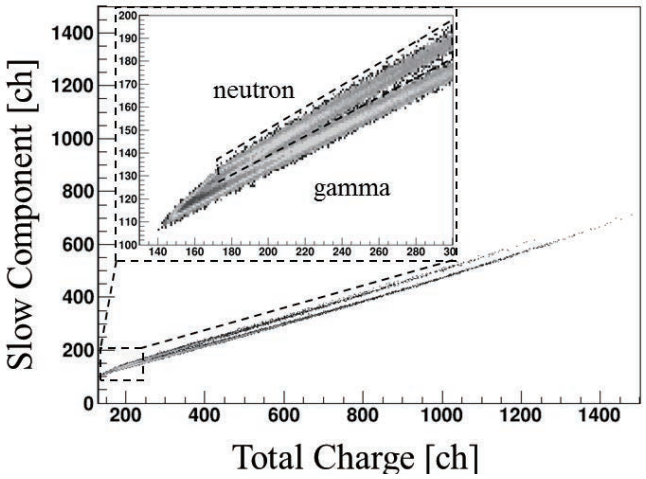

Fig. 2. Two-dimensional plot of pulse integration of total (x-axis) and slow components (y-axis)

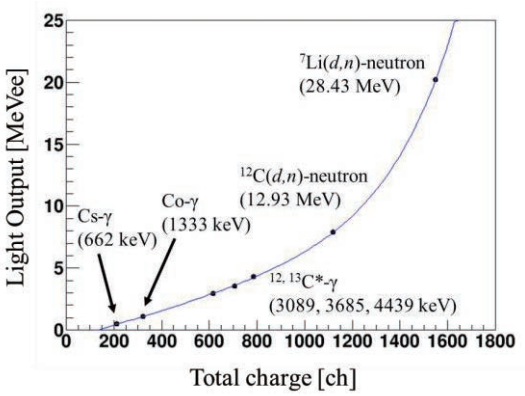

Fig. 3.Relation between integrated charge amount given by ADC channel and light output

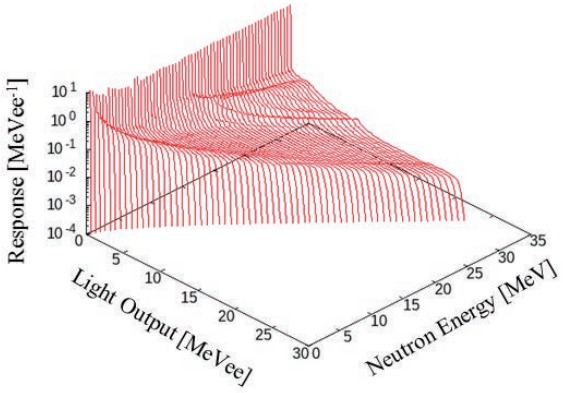

Fig. 4. Neutron response functions of the EJ-301 detector calculated by SCINFUL-QMD code [10]

4. Results and Discussion

In Fig. 5, the measured d-TTNY from C target are compared with the existing data of Weaver *et al.* [12] measured by using the time-of-flight method. It should be noted that the latter data were taken at the incident energy of 14.05 MeV and the emission angle of 3.5 degrees. Although the two data were measured by different experimental methods, reasonably good agreement with each other is confirmed. Figure 5 also shows model calculations with PHITS and DEURACS. In the PHITS calculation, the dynamical process and the subsequent evaporation process were described by the Intra-Nuclear Cascade of Liège (INCL-4.6) [13] and the Generalized Evaporation Model (GEM) [14], respectively. The default options were used for the PHITS calculation except for the option of deuteron reaction cross section, for which the MWO formula [15] was employed. The PHITS calculation generally reproduces the spectral shape but underestimates the magnitude in the neutron energy range lower than approximately 10 MeV. DEURACS calculation was performed for only C, where neutron multiple scattering in the target was not considered because it is negligible. The calculation result is in fairly good agreement with the experimental data. Since the INCL was developed originally for intermediate energy reactions >100 MeV/nucleon, its applicability may be worse for low incident energies below 20 MeV. On the other hand,

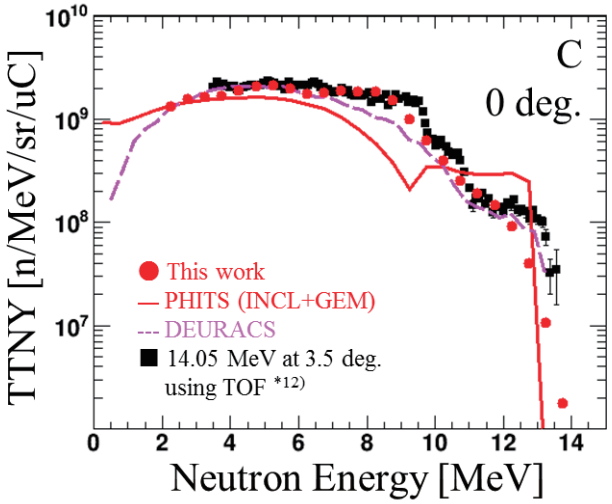

Fig. 5. Deuteron-induced TTNYs of C target: this work (circle), Weaver's data [12] (square), and calculation results by PHITS [6] (solid line) and DEURACS [7] (dashed line). The error bars of the experimental data represent the statistical error. Note that the data of Weaver et al. was taken at the incident energy of 14.05 MeV and emission angle of 3.5 degrees.

DEURACS can consider the breakup and stripping processes associated particularly with deuteron-induced reactions, leading to more sound result.

In Fig. 6, the d-TTNY spectra for the other targets are compared with the t-TTNY spectra measured at the same incident energy of 6.7 MeV/nucleon. In the d-TTNY spectra, broad peaks are characteristically observed around the emission energy of 5 MeV for LiF and Si targets although such structure is not observed for the other targets. In contrast, all the t-TTNYs decrease monotonically as the emission energy increases. This might be due

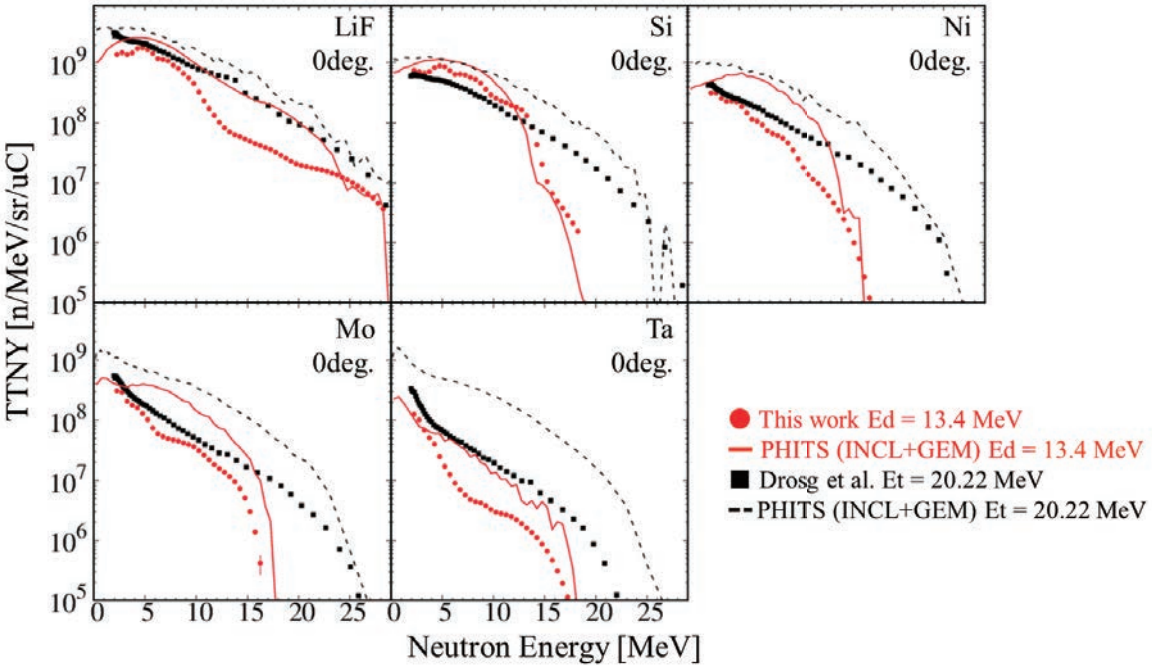

Fig. 6. Experimental TTNYs from LiF, Si, Ni, Mo, and Ta by irradiation of deuteron (circle) and triton (square) at 6.7 MeV/nucleon. Calculation results by PHITS are also shown by the solid (d) and dashed lines (t).

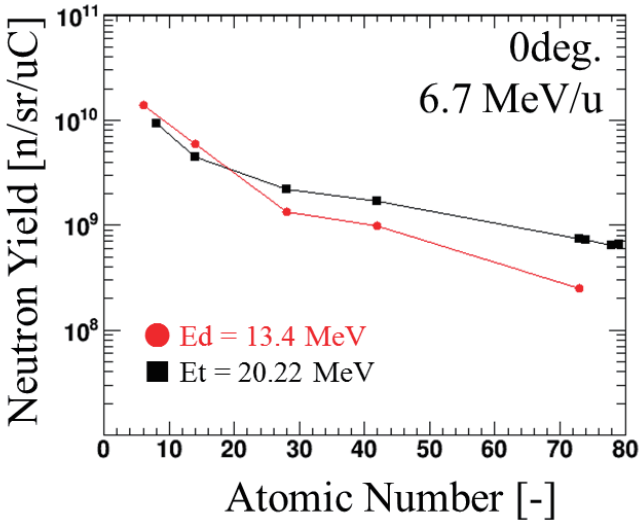

Fig. 7. Total neutron yields at 0 degrees as a function of the atomic number of target nuclei. The experimental data of the other target materials [5] are also included in the triton data denoted by the closed squares.

to the difference of involved reaction mechanisms. As mentioned in [1-3], the broad peaks caused by the breakup processes were observed at half of the incident energy in the measured d-TTNY spectra because the deuteron binding energy (2.22 MeV) is quite small. We presume that the broad peak caused by the breakup processes is not observed in the t-TTNYs because the triton is not easily dissociated owing to the larger binding energy per nucleon (8.48 MeV).

Figure 6 also shows the simulation results of d- and t-TTNY spectra by PHITS code. In the calculated d-TTNY spectra, broad peaks are observed for targets except Ta although such peaks are seen in the experimental results only for LiF and Si targets. However, these peaks are broader than those in the experimental results. This is because the INCL model is not appropriate to describe the reaction processes unique to deuteron-induced reactions at low incident energies. For the t-TTNY spectra, the PHITS calculation reproduces the spectral shapes well, but overestimates the magnitudes of the spectra. The default option with the KUROTAMA model [16] was used in the PHITS calculation. This option has not yet been validated because experimental data of triton reaction cross sections are insufficient, which may be one of the reasons for the overestimation seen in Fig. 6.

Finally, the measured TTNY spectra were integrated over the neutron energy from 2 MeV to the maximum emission energy. Figure7 shows the results as a function of target atomic number. The yields for the other materials measured in [5] are also plotted as the triton data. For the deuteron and triton incidences, the total neutron yields decrease gradually with increasing atomic number. The deuteron incidence produces more neutrons for low Z targets and decreases more rapidly for high atomic numbers than the triton incidence. It is presumed that the enhancement of neutron production from deuteron-induced reactions on light nuclei is mainly due to the deuteron breakup process leading to forward neutron emission, while the neutron emission from the subsequent evaporation process is dominant as the atomic number increases. Further theoretical analysis will be necessary for more detailed discussions about the difference between deuteron- and triton-induced neutron productions.

5. Summary and outlook

Deuteron-induced thick target neutron yields (d-TTNYs) from six target materials (LiF, C, Si, Ni, Mo, and Ta) bombarded by 13.4-MeV deuterons were measured at the emission angle of 0 degrees. To investigate the difference in neutron production by deuterons and tritons that have the same incident energy per nucleon, the measured d-TTNYs were compared with the existing data of 20.22-MeV triton-induced thick target neutron yields (t-TTNYs). The broad peaks were observed in the d-TTNY spectra from LiF, C, and Si around half of the incident energy, while no peak was observed in the t-TTNY spectra for the same targets. In addition, the total neutron yields integrated over the neutron emission energy were derived for the measured d-TTNYs and t-TTNYs at 0 degrees. Both the neutron yields decrease gradually as the target atomic number increases. The deuteron incidence produced more neutrons in LiF, C and Si than the triton incidence, while the opposite tendency was observed for Ni, Mo, and Ta.

The measured d-TTNY spectra were compared with the theoretical model calculations using PHITS and DEURACS. The DEURACS calculation was performed only for C target in this work, which was in better agreement with the experimental data than the PHITS calculation.

In the future, further theoretical analysis with DEURACS will be performed for other target materials, and the difference between d-TTNYs and t-TTNYs will be discussed in more detail.

References

[1] S. Araki *et al*., Energy Procedia 71 197-204 (2015).

[2] Y. Tajiri *et al*., Progress in Nuclear Science and Technology Vol. 4 582-586 (2014).

[3] N. Shigyo J. Kor. Phys. Soc. 1725-1728 (2010).

[4] M. Drosg *et al*., Nucl. Sci. Technol. 106, 183-191 (1990).

[5] M. Drosg *et al*., Nucl. Sci. Eng. 182,.256 (2016).

[6] T. Sato *et al*., J. Nucl. Sci. Technol. 55 684-690 (2018).

[7] S. Nakayama *et al*., Phy. Rev. C 94, 014618 (2016).

[8] J.F. Ziegler *et al*., Nucl. Instr. Meth. in Phys. Res. B 268, 1818-1823 (2010).

[9] N. Nakao *et al*., Nicl. Instr. Meth. in Phys Res. A 463, 275-287 (2001).

[10] D. Satoh *et al*., JAEA-Data/Code 2006-023.

[11] R. H. Johnson *et al*., Nucl. Instr. Meth. 145 337-346 (1977).

[12] K. A. Weaver *et al*. ,Nucl. Sci. Eng. 52, 35-45 (1973).

[13] A. Boundard *et al*., Phys. Rev. C 87 (2013).

[14] S. Furihara *et al*., Instr. Meth. in Phys. Res. B 171 251 (2000).

[15] K. Minomo *et al*., J. Nucl. Sci. Technol. 54, 127-130 (2017).

[16] K. Iida *et al*., J. Phys. Soc. Japan 76, 044201 (2007), and L. Sihver *et al.*, Nucl. Instr. & Meth. B 334, 34-39 (2014).

20 Microscopic Calculations for the Charge Polarization of Fission Fragments

S. Ebata[1], S. Okumura[2], C. Ishizuka[3], S. Chiba[3]
[1] School of Environment and Society, Tokyo Institute of Technology, 152-8550 Tokyo, Japan
[2] Nuclear Data Section, International Atomic Energy Agency, A-1400 Vienna, Austria
[3]Laboratory for Advanced Nuclear Energy, Tokyo Institute of Technology, 152-8550 Tokyo, Japan
e-mail: ebata.s.ab@m.titech.ac.jp

We suggest a new method of theoretical evaluation for the charge distribution of fission fragments. The distribution is a very important quantity that affects the delayed neutron yields emitted from fission products. Our method is based on the microscopic calculations which are resulted from the constrained Skyrme Hartree-Fock plus BCS theory represented in three-dimensional Cartesian coordinate. We compared our result on charge polarization with that in Wahl's systematics, and on delayed neutron yields obtained by the Hauser-Feshbach statistical decay and the summation calculations for $^{235}U+n_{Thermal}$ fission reaction.

The initial charge distribution of fission fragments is an important parameter that relates the delayed neutron yields and the decay heat, because emission of neutrons following beta decay changes the initial mass distribution of independent fission product yield (FPY). The parameter is also important in the calculation for the solar system abundances of elements derived from the rapid neutron capture process on which the heavy neutron-rich nuclei fission [1]. While the importance is well known, it is difficult to measure the distribution directly from the nuclear fission experiment. The unchanged charge distribution (UCD) assumption is used in evaluations by Wahl et al. [2] to obtain the deviation of the most probable charge (Z_p), $dZ=Z_p-Z_{UCD}$. Under the UCD assumption, the fragments keep the proton-neutron ratio of the fissile parent nucleus. However, an actual independent charge distribution slightly deviates from the UCD. The deviation from the UCD is called the charge polarization. Although the amplitude of the charge polarization is less than $dZ = 1.0$, its influence becomes large in the delayed neutron yields. For limited fission reactions with $Z = 90$, 92 and 98, their evaluated charge polarizations are compiled in Wahl's systematics [3].

In order to provide the charge polarization of fragments generated from known and unknown fissile nuclei without empirical ways, a new method based on the microscopic theory is suggested. We employ a mean-field theory which is the constrained Skyrme Hartree-Fock plus BCS (HF+BCS) theory represented in the three-dimensional Cartesian coordinate [4]. The calculated charge polarization was used for Hauser-Feshbach calculation code; $HF^3D(CoH_3/BeoH)$ [5]. To confirm availability of our method, we show

the polarization on the ^{235}U with thermal neutron fission, and compare it with that in Wahl's systematics. The delayed neutron yields were calculated using the summation calculation method.

First, we prepare the potential energy surface (PES) of ^{236}U with respect to quadrupole (Q_{20}) and octupole (Q_{30}) moment which correspond to elongation and mass asymmetry of fissile nucleus, respectively. The PES is obtained from the constrained Skyrme HF+BCS in which SkM* parameter set and the constant monopole model are used for the particle-hole interaction and the nuclear pairing, respectively. The constraint terms in the form of parabola are added to the single-particle Hamiltonian [4]. The constraint ranges are from 435 to 13,050 (fm^2) for Q_{20}, and from 0 to 65,000 (fm^3) for Q_{30}. Second, the nucleon numbers of nuclei are calculated at the points of fission or having a clear neck structure on the PES. Although nuclei with small mass asymmetry are deformed with 15 times quadrupole moment of the ground state, they did not reach fission. In these cases, we obtain approximately their nucleon numbers from the integration of the region separated at the smallest neck. The charge polarization is calculated from the nucleon numbers at fission or at the maximum quadrupole moment of the PES. Finally, we obtain delayed neutron yields by combining the Hauser-Feshbach calculation code HF^{3}D using the calculated charge polarizations in present and in Wahl's systematics with the summation calculation.

Figure 1 means the PES of ^{236}U on which the ground state, the second minimum and the valley toward the fission are shown. The finite Q_{30} around the second minimum is favored in energy. The energy reduction along the mass symmetric Q_{20} elongation is smaller than that in the mass asymmetric Q_{20} elongation, which is consistent with the small amount of symmetric fission fragments.

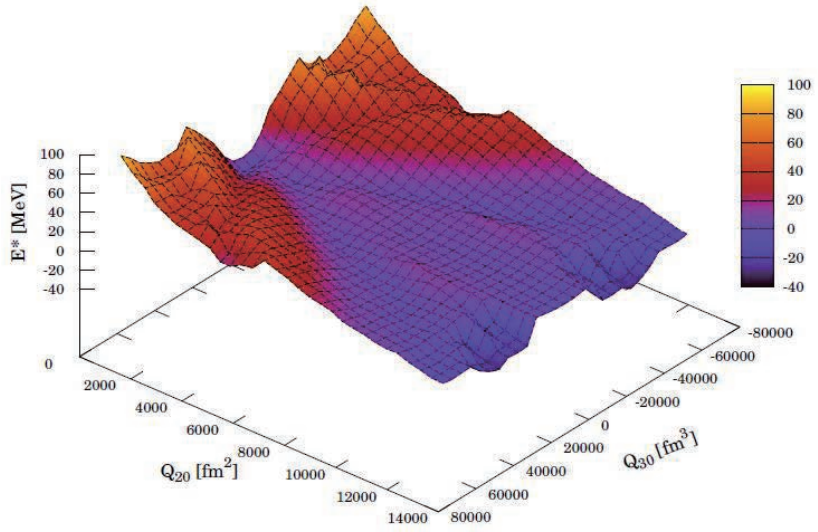

Fig. 1: Potential energy surface of ^{236}U with respect to Q_{20} and Q_{30}, which is calculated by the constrained Skyrme HF+BCS with SkM* parameter set and the constant monopole pairing.

Figure 2 shows the charge polarizations of the present calculation (cross) and of Wahl's systematics (square). The raw data obtained by our method and the interpolated data used in the HF^{3}D are plotted in the upper and lower panels, respectively. The maximum amplitude of our polarization is comparable with

Wahl's that. The mass numbers at the maximum correspond to magic numbers, Z=50 and N=82, which indicates the shell effects on the fission. A big difference of behavior appears around the fragments of symmetric fission.

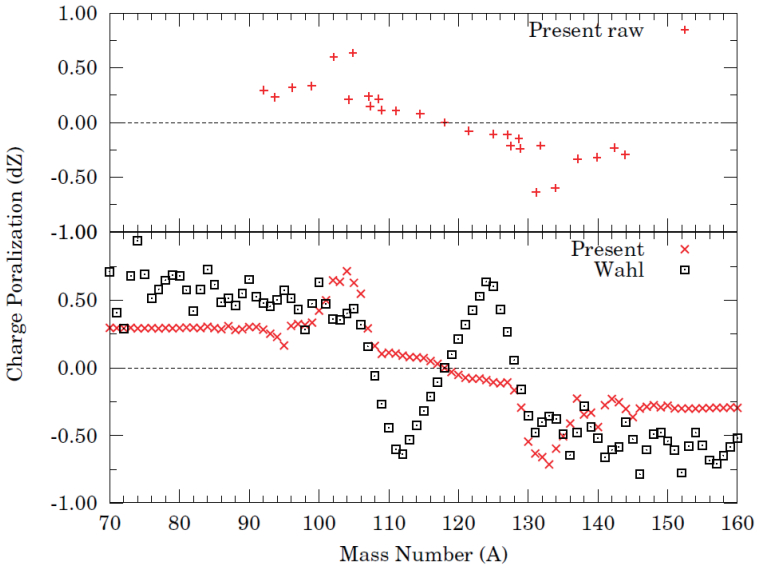

Fig. 2: Charge polarization with respect to mass number. The present raw data and interpolated data are shown in upper and lower panels. The square symbols mean those in Wahl's systematics.

We calculate also the delayed neutron yields using the independent FPYs that incorporate the present charge polarization, and compare ours among those of Wahl's systematics and UCD, which is shown in Fig.3. The yield on UCD assumption is the largest. Although the present result shows about 1.5 times of experimental yields, ours are better than those of UCD. The peak position is consistent with that of JENDL.

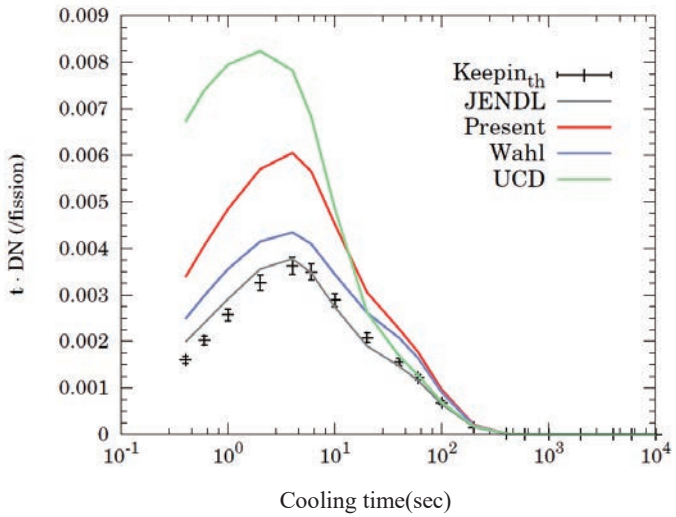

Fig. 3: Comparison among delayed neutron yields calculated with the present, Wahl's charge polarization and UCD assumption. Symbols correspond to the experimental data [6] and the gray line is taken from JENDL/FPY-11 [7]

In summary, we suggest the new method to provide the charge polarization of fission fragments. In order to provide the charge polarization of any fissile nucleus, the method is based on the microscopic theory which is the constrained Skyrme HF+BCS theory. The PES of ^{236}U with respect to quadrupole and octupole moment is calculated for the fission reaction of ^{235}U injected thermal neutron. Then, we calculate nucleon numbers from the density distribution at the fission and at the end of the PES. The charge polarization obtained from the nucleon numbers is consistent with that of Wahl's systematics on its amplitude, but the behavior around symmetric fission is much different. Our results indicate automatically the shell effects in the charge polarization. Furthermore, we calculate the delayed neutron yields through the Hauser-Feshbach calculation; HF^{3}D using the charge polarization, and the summation calculation. Although our results are better than those of UCD assumption, they are overestimated as 1.5 times of the experimental data.

In future work, we will extend the PES with respect to octupole moment, because the present PES does not cover the region less than A=90. Furthermore, the charge polarizations of other fissile nuclei, for instance more neutron-rich nuclei, will be investigated to clear the dependence on nucleon numbers and to improve our method, simultaneously.

References

[1] Eichler M., Arcones A., Käppeli R. *et al.,* The Impact of Fission on R-Process Calculations; J. Phys. Conf. Ser., 665, 012054.

[2] Wahl A.C., Nuclear-charge distribution and delayed-neutron yields for thermal-neutron-induced fission of ^{235}U, ^{233}U, and ^{239}Pu and for spontaneous fission of ^{252}Cf; At. Data Nucl. Data Tables, **39**, 1, 1988.

[3] Wahl A.C., Systematics of Fission-Product Yields. Los Alamos National Laboratory; 2002. LA-13928.

[4] Ebata S,, Nakatsukasa T., Octupole deformation in the nuclear chart based on the 3D Skyrme Hartree-Fock plus BCS model ; Phys. Scr. **92** (2017) 064005.

[5] Okumura S., Kawano T., Jaffke P. *et al.*, ^{235}U(n, f) Independent fission product yield and isomeric ratio calculated with the statistical Hauser–Feshbach theory; J. Nucl. Sci. Technol., **55** (2018) 1009.

[6] Keepin G.R., Wimett T.F., Zeigler R.K., 1957. Delayed Neutrons from Fissionable Isotopes of Uranium, Plutonium, and Thorium, Physical Review, **107**, 1044-1049.

[7] JENDL/FPY-11; JENDL FP Fission Yields Data File 2011: https://wwwndc.jaea.go.jp/ftpnd/jendl/jendl-fpy-2011.html

21 Theoretical Study on Fission Process at High Excitation Energy with a Concept of Multi-chance Fission

Shoya TANAKA[1,3], Kentaro HIROSE[3], Katsuhisa NISHIO[3], Yoshihiro ARITOMO[2,1]

[1]*Graduate School of Science and Engineering, Kindai University*
[2]*Faculty of Science and Engineering, Kindai University*
Higashi-Osaka, Osaka 577-8502, Japan
[3]*Advanced Science Research Center, Japan Atomic Energy Agency*
Tokai, Ibaraki 319-1195, Japan
e-mail: tanaka.shoya9071@gmail.com

To understand nuclear fission from highly excited states is essential for development of Accelerator Driven System (ADS) aiming to transmute long-lived minor actinide into short-lived fission products. In this study, we aim to clarify fission fragment mass distributions (FFMDs) from a highly excited heavy nucleus by using dynamical model calculation including multi-chance fission (MCF). The results showed that the behavior of FFMDs at high excitation energy was obviously attributed to the effect of MCF.

1. Introduction

Management of nuclear waste of long-lived minor actinide is one of the most important issues in the use of nuclear power. For further public acceptance of nuclear power, it is essential to reduce the already-existing and newly produced nuclear waste. The use of accelerator-driven systems (ADS) is considered as one of the viable options for the incineration and/or transmutation of the long-lived minor actinides into shorter-lived fission products. In the ADS approach, energetic spallation neutrons, which are produced via high-energy proton impact on a heavy target material such as lead and/or bismuth, could be used to irradiate the fissionable minor actinides. This leads to fission with higher, and more broadly distributed, excitation energies in comparison to those in the thermal-neutron-induced fission in a traditional power reactor. Thus, understanding of fission at high excitation energy is important for nuclear-data evaluations related to ADS developments.

With increasing excitation energy, two competing processes are expected to occur. First of all, due to a reduced importance of shell effects, the transition to predominantly symmetric (liquid-drop) type fission should occur, which is indeed demonstrated by many experiments. The other process is multi-chance fission (MCF), or fission after consecutive neutron

evaporations, where the fissioning nuclei with less neutrons will have lower excitation energy, thus showing stronger shell effects than in the initial compound nucleus. The latter effect is then supposed to favor the asymmetric fission of typical actinides after neutron evaporation.

It was only recently that the effect of MCF on fission fragment mass distributions (FFMDs) was introduced in theoretical studies. However, the validity of the calculated FFMDs for each fission chance was not shown because of the lack of experimental data. The purpose of this study is an estimation of FFMDs by dynamical model calculation including MCF effects.

2. Model

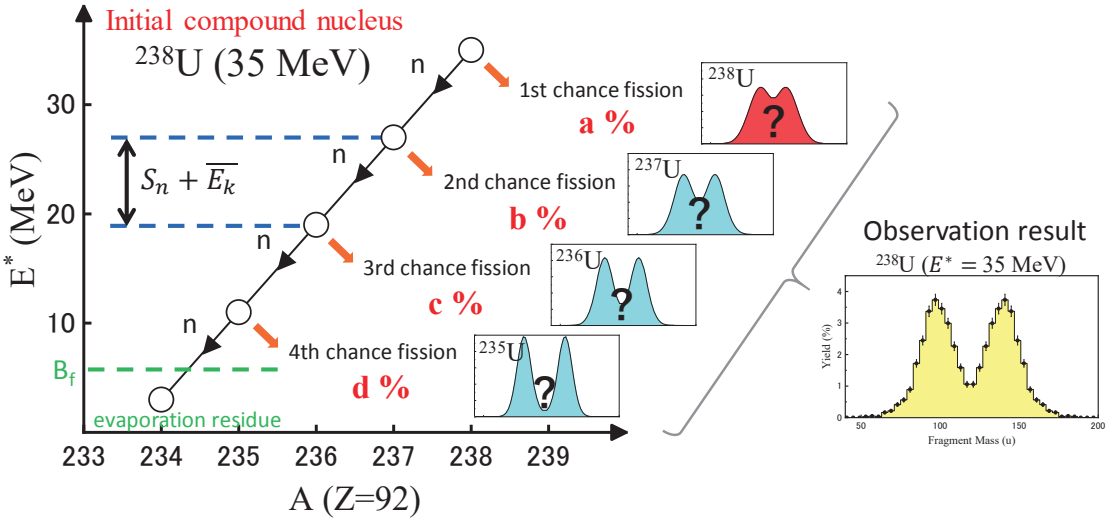

Figure 1 Schematic diagram of multi-chance fission process at ^{238}U (E* = 35 MeV).

A calculation procedure of FFMDs with MCF effects can be divided into two steps based on MCF concept, as shown in Figure 1. At the first step, FFMDs for each fission chance are calculated by the fluctuation dissipation model. At the second step, the fraction for each fission chance is calculated by the statistical model using the GEF model code [1]. FFMDs for each fission chance which multiplied by the fraction are summed to obtain the distribution to be compared with the experimental data.

We use the fluctuation-dissipation model and employ Langevin equations to investigate the dynamics of the fission process [2]. The nuclear shape is defined by the two-center parametrization, which has three deformation parameters, z_0, δ, and α to serve as collective coordinates: z_0 is the distance between two potential centers, while $\alpha = (A_1 - A_2)/(A_1 + A_2)$ is the mass asymmetry of the two fragments, where A_1 and A_2 denote the mass numbers of heavy and light fragments. The symbol δ denotes the deformation of the fragments, and is defined as $\delta = 3(R_{\parallel} - R_{\perp})/(2R_{\parallel} + R_{\perp})$, where $R_{\parallel}$ and $R_{\perp}$ are the half length of the axes of an ellipse in the z_0 and ρ directions of the cylindrical coordinate, respectively. We use the fixed neck parameter ε for each fissioning nuclei. The three

collective coordinates may be abbreviated as q, $q = \{z, \delta, \alpha\}$.

For a given value of the temperature of a system T, the potential energy is defined as a sum of the liquid-drop (LD) part, a rotational energy and a microscopic (SH) part:

$$V(q, l, T) = V_{\mathrm{LD}}(q) + \frac{\hbar^2 l(l+1)}{2I(q)} + V_{\mathrm{SH}}(q, T), \quad (1)$$

$$V_{\mathrm{LD}}(q) = E_{\mathrm{S}}(q) + E_{\mathrm{C}}(q), \quad (2)$$

$$V_{\mathrm{SH}}(q, T) = E^0_{\mathrm{shell}}(q)\Phi(T), \quad (3)$$

$$\Phi(T) = \exp\left(-\frac{aT^2}{E_{\mathrm{d}}}\right). \quad (4)$$

Here, the potential energy V_{LD} is calculated with the finite-range liquid drop model, given as a sum of the surface energy E_{s} and the Coulomb energy E_{c}. The shell correction energy V_{SH} is evaluated by the Strutinski method from the single-particle level of the two-center shell model. The shell correction energy has a temperature dependence expressed by a factor $\Phi(T)$ in which the shell damping energy E_{d} is chosen as 20 MeV and a is the level density parameter. At the zero temperature ($T = 0$), the shell correction energy reduces to that of the two-center shell model values E^0_{shell}. The second term on the right-hand side of Eq. (1) is the rotational energy for an angular momentum l, with a moment of inertia $I(q)$ at q.

The multidimensional Langevin equations are given as

$$\frac{dq_i}{dt} = (m^{-1})_{ij} p_j,$$

$$\frac{dp_i}{dt} = -\frac{\partial \mathrm{V}}{\partial q_i} - \frac{1}{2}\frac{\partial}{\partial q_i}(m^{-1})_{jk} p_j p_k - \gamma_{ij}(m^{-1})_{jk} p_k + g_{ij} R_j(t), \quad (5)$$

where $i = \{z, \delta, \alpha\}$ and $p_i = m_{ij} dq_j/dt$ is a momentum conjugate to coordinate q_i. The summation is performed over repeated indices. In the Langevin equation, m_{ij} and γ_{ij} are the shape-dependent collective inertia and the friction tensors, respectively. The wall-and-window one-body dissipation is adopted for the friction tensor which can describe pre-scission neutron multiplicities and total kinetic energy of fragments. A hydrodynamical inertia tensor is adopted with the Werner-Wheeler approximation for the velocity field. The normalized random force $R_i(t)$ is assumed to be that of white noise, i.e., $\langle R_i(t) \rangle = 0$ and $\langle R_i(t_1) R_j(t_2) \rangle = 2\delta_{ij}\delta(\mathrm{t}_1 - \mathrm{t}_2)$. The strength of the random force g_{ij} is given by the Einstein relation $\gamma_{ij} T = \sum_k g_{ij} g_{jk}$.

The fission events are determined in our model calculation by identifying the different trajectories in the deformation space. Fission from a compound nucleus is defined as the case that a trajectory overcomes the scission point on the potential energy surface.

The reduction of the excitation energy of the compound nucleus due to neutron emission was calculated from neutron binding energies [3] and a mean energy for the emitted neutron, ~1.9 MeV, obtained by the PACE2 code [4].

3. Results and discussion

As a summary of all the calculation results, Figure 2 shows the FFMDs for the twenty-one compound nuclides $^{234\text{-}240}$U, $^{236\text{-}242}$Np and $^{238\text{-}244}$Pu with the excitation energy range of E^* =15-55 MeV. A 10 MeV interval of the excitation energy was chosen as a compromise between the available statistics and a reasonable increment of E^*. To understand these trends, the calculation results compared with the experimental FFMDs as [5,6]. In Fig. 2, there are several blanks of experimental data, because the experimental data does not have enough statics.

And, Table 1 shows neutron binding energy obtained by [3] and the mean number of neutron emission calculated by GEF code [1] for twenty-one nuclides of calculation range.

The calculation considering the MCF (red curves in Fig. 2) reproduced the experimental data, and peak position and peak-to-valley (P/V) ratio agree well for all the measured excitation-energy range by including MCF. Three characteristics (excitation energy, atomic number and neutron number dependence) of FFMDs are reproduced at high excitation energy.

1. Excitation energy dependence

In contrast to the results without MCF (blue curves in Fig. 2), the calculation with MCF (red curves in Fig. 2) well explains the excitation-energy dependence which FFMDs are clearly preserved double-humped shape up to the highest measured energy in experiment. The apparent asymmetric shape of FFMDs for given initial high excitation energy originates from fission of less excited lighter isotopes produced via the neutron evaporation.

2. Atomic number dependence

To fix the excitation energy (boxed by pink frame in Fig. 2), P/V ratio of calculation results decreases as well as experimental data toward larger atomic number. This behavior can be also understood by the MCF effect, or easiness of neutron evaporation. To increase atomic number, two neutron binding energy also increases, and the mean neutron emission number decreases. It means that a highly excited nucleus cannot be deexcited by neutron emission effectively. This tendency is also confirmed in the other neutron number.

3. Neutron number dependence

To fix the excitation energy (boxed by light blue frame at Fig. 2), P/V ratio of calculation results increases as well as experimental data toward larger neutron number. To increase neutron number, two neutron binding energy decreases. It means that as the number of neutrons increases, a highly excited nucleus becomes easy to emit neutron and deexcite to repair the shell structure.

The calculation results without MCF (blue curves in Fig. 2) show predominantly symmetric fission due to washing out nuclear shell structure at highest excitation energy in this study. This result indicates proper picture of the fission originated form highly excited nucleus, and we expect this single peak FFMDs of mass asymmetric fission is also observed

in experiment at a high excitation energy.

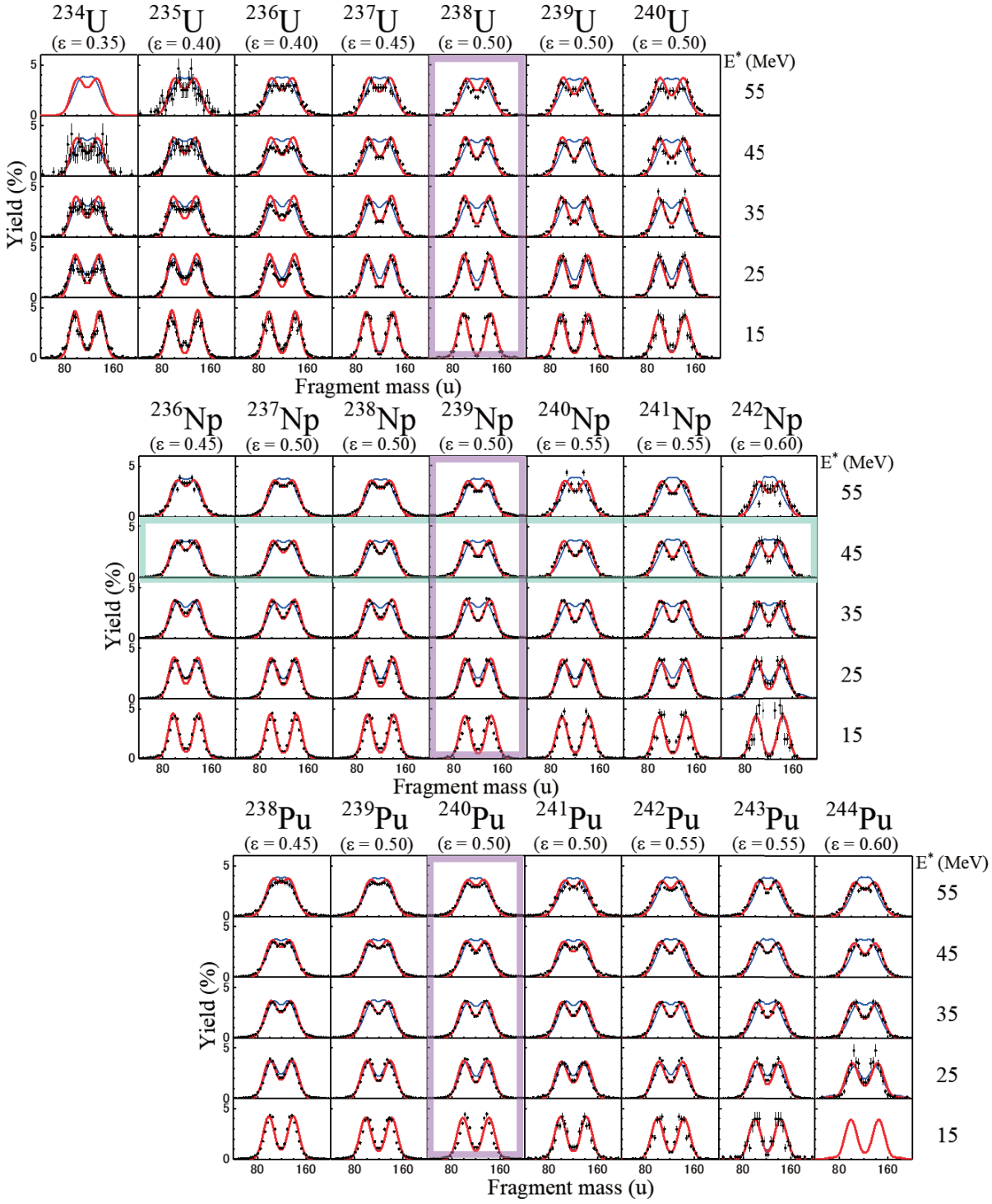

Figure 2 Calculation results of FFMDs of without (blue curves) and with (red curves) the inclusion of multi-chance fission at the U, Np and Pu isotopes and their dependence on excitation energy in the range of E^*=15-55 MeV. The calculation FFMDs are compared with experimental data (points with error bars).

Table 1 One and two neutron binding energy are each defined as S_n and S_{2n} obtained by [3]. The mean number of neutron number is defined as $\langle \upsilon \rangle$ calculated by GEF code [1].

Z	N	A	S_n (MeV)	S_{2n} (MeV)	E (MeV)	< ν >	Z	N	A	S_n (MeV)	S_{2n} (MeV)	E (MeV)	< ν >	Z	N	A	S_n (MeV)	S_{2n} (MeV)	E (MeV)	< ν >
92	142	234	8.74	16.40	15	0.16	93	143	236	7.58	16.46	15	0.16	94	144	238	8.90	16.68	15	0.09
					25	0.69						25	0.57						25	0.45
					35	1.22						35	1.04						35	0.90
					45	1.72						45	1.51						45	1.35
					55	2.20						55	1.96						55	1.81
	143	235	7.20	15.94	15	0.29		144	237	8.52	16.10	15	0.14		145	239	7.55	16.45	15	0.17
					25	0.87						25	0.65						25	0.61
					35	1.47						35	1.19						35	1.10
					45	2.00						45	1.69						45	1.60
					55	2.52						55	2.20						55	2.08
	144	236	8.44	15.64	15	0.26		145	238	7.39	15.91	15	0.29		146	240	8.43	15.98	15	0.12
					25	0.92						25	0.83						25	0.61
					35	1.61						35	1.42						35	1.19
					45	2.21						45	1.97						45	1.74
					55	2.75						55	2.48						55	2.26
	145	237	7.03	15.47	15	0.41		146	239	8.11	15.50	15	0.14		147	241	7.14	15.57	15	0.22
					25	1.14						25	0.78						25	0.75
					35	1.85						35	1.51						35	1.37
					45	2.49						45	2.10						45	1.96
					55	3.06						55	2.66						55	2.51
	146	238	8.05	15.08	15	0.26		147	240	7.07	15.18	15	0.25		148	242	8.21	15.35	15	0.14
					25	0.99						25	0.94						25	0.73
					35	1.97						35	1.62						35	1.43
					45	2.61						45	2.30						45	2.06
					55	3.25						55	2.90						55	2.65
	147	239	6.71	14.76	15	0.35		148	241	7.92	14.99	15	0.22		149	243	6.93	15.14	15	0.24
					25	1.29						25	0.88						25	0.92
					35	1.97						35	1.71						35	1.57
					45	2.80						45	2.37						45	2.24
					55	3.48						55	3.03						55	2.87
	148	240	7.82	14.53	15	0.25		149	242	6.82	14.74	15	0.35		150	244	7.92	14.85	15	0.14
					25	0.79						25	1.27						25	0.80
					35	1.95						35	1.80						35	1.61
					45	2.69						45	2.53						45	2.27
					55	3.53						55	3.23						55	2.94

4. Conclusion

In this study, we explain three characteristics (excitation energy, atomic number and neutron number dependence) of FFMDs at high excitation energy only by taking into account MCF for the first time. This result suggests that the consideration of MCF is essential to interpret and evaluate fission observables.

References

[1] K.-H. Schmidt, B. Jurado, C. Amouroux, and C. Schmitt, Nucl. Data Sheets **131**, 107 (2016), Special Issue on Nuclear Reaction Data.

[2] Y. Aritomo and M. Ohta, Nucl. Phys. A **744**, 3 (2004).

[3] P. Möller, A. J. Sierk, T. Ichikawa, H. Sagawa, Atomic Data and Nuclear Data Tables **109–110**, 1–204 (2016).

[4] A. Gavron, Phys. Rev. C **21**, 230 (1980).

[5] R. Léguillon, *et al.*, Phys. Lett. B **761**, 12 (2016).

[6] K. Hirose, K. Nishio, S. Tanaka, *et al.*, Phys. Rev. Lett. **119**, 222501 (2017).

22

The Evaluation Method for independent Yield including the Effect of the Shell Correction

Kohsuke TSUBAKIHARA, Shin OKUMURA, Chikako ISHIZUKA, Tadashi YOSHIDA
and Satoshi CHIBA
Laboratory for Advanced Nuclear Energy, Tokyo Institute of Technology
Email: tsubakihara.k.aa@m.titech.ac.jp

The fission product yields play a crucial role to determine the property of the decay heat (DH) and the delayed neutron (DN) and they strongly affect to the calculation about the post-irradiation examination data of nuclear reactors. In this work, we estimate how the isobaric independent yields increase or decrease from systematic Gaussian distribution depending on the *Z* and *N* number of produced nucleus, which is regarded as odd-even effects. We propose a new formula for fission product yield evaluation as a form of Boltzmann factor calculated with shell correction energies ΔE_{sh} which are estimated by a theoretical mass formula and paring energies. Based on this formula, independent yields are calculated, where the model parameters are searched so as to reproduce odd-even staggering from Gaussian distribution. Derived independent yields are validated from DH and DN in burst fission. We find the present formula has enough reproduction power and an isomer ratio has a decisive role to DN and tend to enhance it. Finally, based on the generalized least square (GLS) method, we also report how to derive the errors and covariance matrix of the independent yields which obey the constraints to the fission product yield, e.g., chain yields and their errors.

1. Introduction

Evaluation of fission product yield (FPY) of long-lived fission products (LLFP) is highly important when we consider the burn-up calculation and the transmutation of LLFP in fast reactors [1] and aim to make them precise. In addition, FPY plays a crucial role to determine the property of the decay heat (DH) and the delayed neutron (DN). They also affect to the calculation about the post-irradiation examination data of nuclear reactors. There are, however, less available data of fast-neutron-induced fission reactions. Thus, it is strongly needed to establish the method which is applicable in wide ranges of mass numbers and excitation energies.

These isobaric independent yields tend to increase or decrease from systematic Gaussian distribution depending on the Z and N numbers of produced nucleus, which is regarded as odd-even effects. The pairing effects between nucleons are known as one of candidates to make an even-even nucleus more energetically stable than an odd-odd nucleus. In previous work by Wahl [2], the odd-even effects are treated phenomenologically and parameters concerning about them are determined so as to reproduce experimental independent yields. This model has been quite successful, but it is less predictive: it cannot be applied to the system where there are not enough experimental data. The stability coming from the odd-even effects determines how much each nucleus is produced as independent fission products, and it should be considered if we aim to establish a theoretical framework to evaluate FPY based on the knowledge of

nuclear theory.

In this work, we propose a new formula for FPY evaluation as a form of the Boltzmann factor calculated with a shell correction energy ΔE_{sh} which is estimated by theoretical mass formula [3]. Based on this formula, independent yields are calculated systematically, where the model parameters are fixed so as to reproduce odd-even staggering from Gaussian distribution. Derived independent yields are validated by calculating DH and DN in a burst fission.

2. Methods

According to the scission point model by Fong [4] and Wilkins [5], the independent yields $Y_I(Z,A)$ can be calculated based on the Boltzmann factor of the potential at the scission point as,

$$Y_I(Z,A) \propto \exp\left[-\frac{E_{\mathrm{LD}}(Z,A)+\Phi(E^*)\Delta E_{\mathrm{sh}}(Z,A)}{T(Z,A)}\right] .$$

In this work, we assume this Boltzmann factor can be divided into two parts: normalized Gaussian distribution on each isobar and the damping factor estimated by the shell correction energy. Then, $Y_I(Z,A)$ can be calculated as the product of them as follows,

$$Y_I(Z,A) = Y(A) \times F_{\mathrm{oe}} \times \frac{1}{\sqrt{2\pi}\sigma(A)} \int_{-0.5}^{0.5} \exp\left[-\frac{\left(Z - Z_p(A) + t\right)^2}{2\sigma(A)^2}\right] dt$$

$$F_{\mathrm{oe}} = \exp\left[-\frac{\Delta E_{\mathrm{sh}}(Z,A)}{E\,(A)}\right]$$

where we employ the Boltzmann-factor-type weight F_{oe} to represent a fine structure from odd-even effect, which schematic view is shown in Fig. 1; FPYs of even-even (odd-odd) nuclei tend to be larger (smaller) than expected Gaussian distribution. KTUY mass formula [3] is applied to estimate the shell correction energy $\Delta E_{\mathrm{sh}}(Z,A)$. Paring energies are included in $\Delta E_{\mathrm{sh}}(Z,A)$ with a simple form as,

$$E_{\mathrm{pair}} = {}^{12}/_{\sqrt{A}} \text{ MeV(odd-odd nucleus)}, \ -{}^{12}/_{\sqrt{A}} \text{ MeV(even-even nucleus)}, 0 \text{ (the others)} ,$$

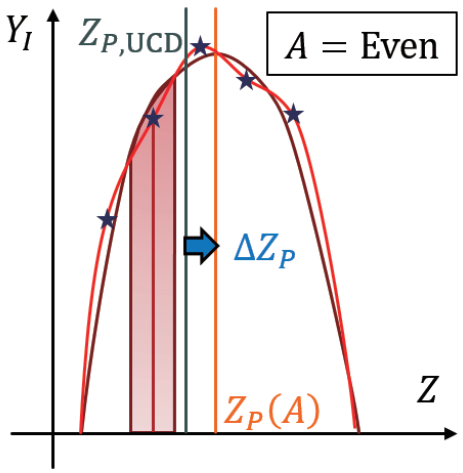

Figure 1: Schematic view of the independent yields $Y_I(Z,A)$ on even-mass-number isobars

respectively. By comparing experimental data taken from EXFOR database [6] and evaluation data, JENDL/FPY-2011 and JEFF, the parameters in the formula, $\sigma(A), Z_{\mathrm{p}}(A)$ and $E_{\mathrm{d}}(A)$ are determined on each mass number, A. Hereafter, we rewrite the parameter $Z_{\mathrm{p}}(A)$ by using a deviation $\Delta Z_{\mathrm{p}}(A)$ from UCD (Unchanged Charge Density) ansatz where the ratio between Z and A numbers is "unchanged" after the scission compared to the one of compound nucleus. Based on this anstaz, $Z_{\mathrm{p}}(A)$ is reprezented as,

$$Z_{\mathrm{P,UCD}}(A) = \left({}^{Z_{\mathrm{comp}}}\!/_{A_{\mathrm{comp}}} \right) \times A, Z_{\mathrm{p}}(A) = Z_{\mathrm{P,UCD}}(A) + \Delta Z_{\mathrm{p}}(A),$$

where Z_{comp} and A_{comp} are the charge and mass numbers of the compound nucleus. Calculated FPY should be validated by estimating the decay heats and the delayed neutrons in burst fission and we compute them by applying Oyak-code[7].

In addition we also estimate not only the errors of independent yields but also their covariance which is consistent with several constraints listed below;

1. Mass number normalization $\sum_i A_i Y_i = A^t Y = A_{\mathrm{CN}} - \bar{\upsilon}_P - A_{\mathrm{LCP}}$: The sum of the product of the fission product mass number A_i and its independent yield Y_i should be equal to the mass of compound nucleus except for $\bar{\upsilon}_P$ and A_{LCP} (the mass number of light charge particle, LCP).
2. Charge number normalization $\sum_i Z_i Y_i = Z^t Y = Z_{\mathrm{CN}} - Z_{\mathrm{LCP}}$: The sum of the product of the fission product charge number Z_i and its independent yield Y_i should be equal to the charge of compound nucleus except for the charge of LCP.
3. Total yield normalization $\sum_i Y_i = I^t Y = 2$: The sum of all independent yields should be 2.

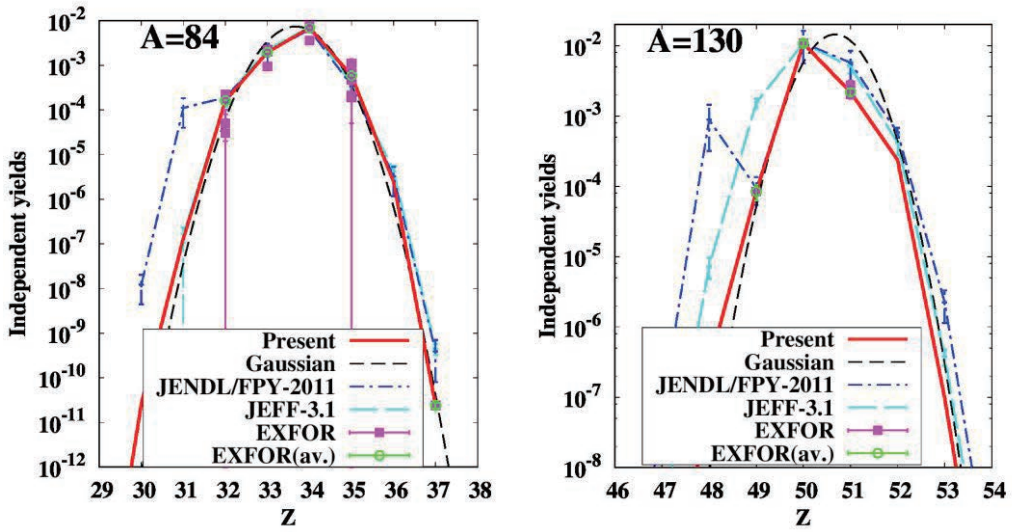

Figure 2: The charge number distributions of $Y_I(Z, A)$ at A=84 (left panel) and A=130 (right panel) on ^{235}U+n_{th} reaction. Red lines show the results of the present formula. Black lines present the results of pure Gaussian distributions without odd-even effects. Blue and cyan lines correspond to the result of evaluation database, JENDL/FPY-2011 and JEFF 3.1, respectively. Magenta and green points are experimental independent yields taken from EXFOR and their averages, respectively.

4. Heavier yield normalization $\sum_{A_i \geq \frac{A_{CN}-\bar{\nu}_P}{2}} Y_i = H^t Y = 1$: The sum of the independent yields of heavier fission product should be 1.
5. Calculated chain yields based on independent yields should be consistent with evaluated chain yields.

Obeying these five constraints, the errors and their covariance can be updated by using genelarized least square (GLS) method where updated (posterior) information can be calculated with prior information as,

$$y = S^t \theta,$$
$$\theta_{\text{upd.}} = \theta_a + V_a S^t (S V_a S^t + V)^{-1} (\eta - y_a),$$
$$V_{\text{upd.}} = V_a - V_a S^t (S V_a S^t + V)^{-1} S V_a.$$

In this case, calculated independent yields can be regarded as prior information θ_a and their prior covariance matrix is represented by V_a. S^t is design matrix (or vector) in order to calculate the quantity to be examined by GLS update process. y is the calculated quantity to be compared with the constraints listed before. η and V are the data and their covariance known by experiments (or by definition). After GLS update process, we can obtain the covariace which is consistent with the constaints where they have already been precisely known althogh each independent yield has large uncertainty, respectively.

3. Results

First, we present how well odd-even staggering is explained by the present formula. In Fig. 2, calculated FPYs at *A*=84 (left panel) and A=130 (right panel) are plotted as functions of charge number *Z* and compared with evaluated database, JENDL/FPY-2011 and JEFF-3.1, and experimental data taken from EXFOR. With the present formula, the distributions which are distorted from pure Gaussian distribution shown by black lines can be well reproduced at both light and heavy mass distributions as shown in Fig. 2.

In Fig. 3, $Y_I(Z,A)$ of the isotopes of LLFP are shown as a function of mass number A. As shown in these figures, LLFPs locate at the skirt of $Y_I(Z,A)$ distribution except for ^{126}Sn. Thus, that implies cumulative yields are important in these LLFP region. We will derive them based on statistical decay based on newly-calculated independent yields and we will examine their properties around LLFP regions.

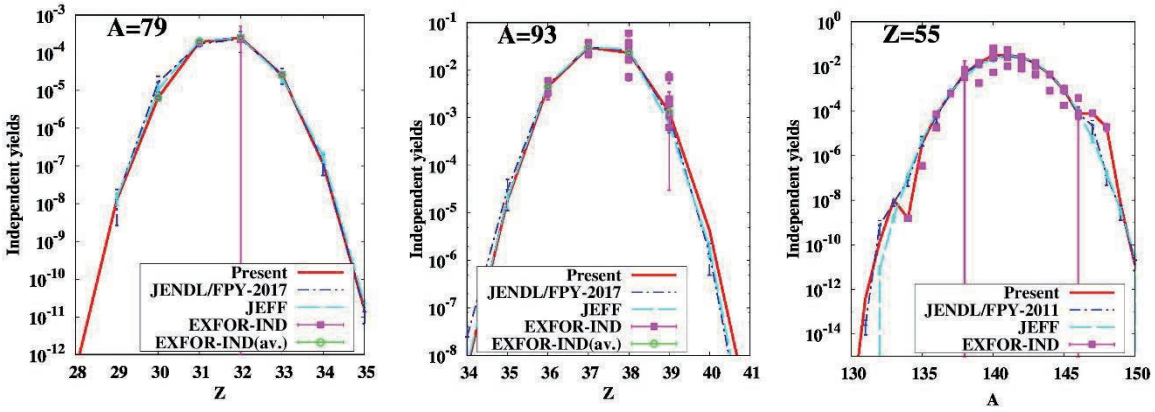

Figure 3: Independent yields in the region where LLFP are included. All legends are same as Fig. 2.

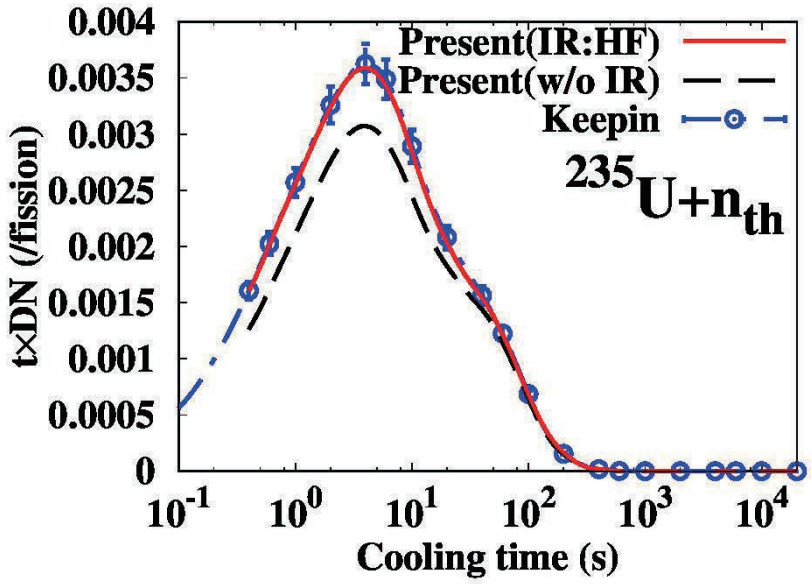

Figure 4: Calculated delayed neutrons (DN) on $^{235}U_{th}$ as a function of cooling time. Black and red lines correspond to the results with or without isomer ratio contribution, respectively. Experimental DNs estimated by Keepin[8] are also plotted by blue points.

Calculated DNs with the present formula are revealed in Fig. 4. Experimental data are also presented with the legend "Keepin." [8] In this calculation, we employ same isomeric ratio (IR) as the one calculated by Hauser-Feshbach model. From these results, DN should be enhanced if IR is introduced to FPY and by including IR, DN of $^{235}U_{th}$ as shown by red line in Fig. 4.

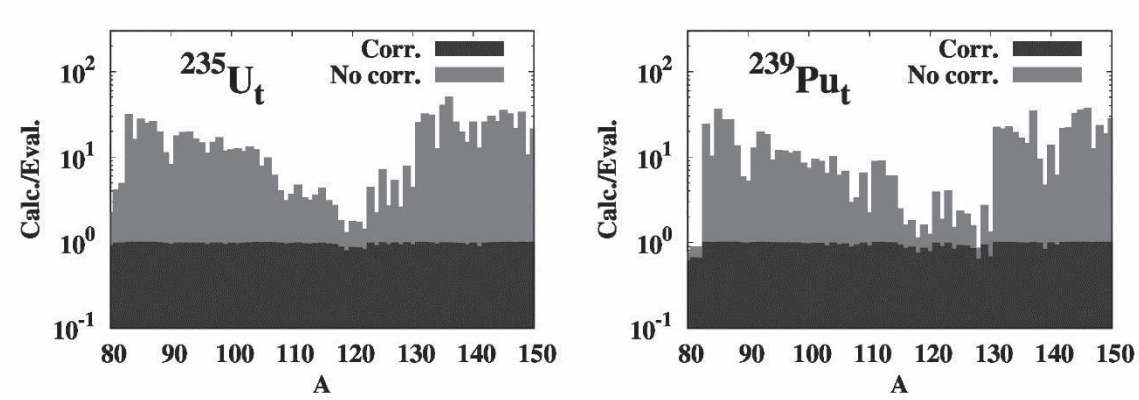

Figure 5: The ratio of calculated mass yield errors on $^{235}U_t$ and $^{239}Pu_t$ to the evaluated ones, C/E as functions of the mass number of the fission fragments. Red and blue histograms correspond to the results with or without the contributions of correlations enumerated in the text, respectively. Evaluated mass yield errors are taken from England-Rider [9].

Finally, calculated errors of $^{235}U_t$ and $^{239}Pu_t$ mass yields based on GLS method are presented by comparing the ratio to evaluated errors, i.e. C/E where C means calculated mass yield errors and E corresponds to evaluated mass yield errors. In Fig. 5, C/E on mass yields of $^{235}U_t$ and $^{239}Pu_t$ are presented by histograms. Red histograms are calculated directly from newly calculated independent yields. As clearly seen, too larger errors are derived compared to evaluated mass yield errors from Ref. [9]. On the other hand, the calculated results including the correlation taken into account by GLS update process are presented by blue histograms in Fig. 5. From these results, we find most of C/E based on the errors with correlations populate around unity and that means estimated mass yield errors are consistent with already-evaluated mass yield errors and this agreement is derived by considering the covariance among independent yields updated by GLS method.

4. Summary

We present a new type of evaluation formula including nuclear shell effects as a Boltzmann factor form. As the result, this formula can reproduce experimental and evaluated independent yields systematically. With this factor, especially the odd-even staggering on the Z-distribution of FPY are reasonably reproduced by tuning model parameters. With calculated FPY, the data of DN and DH are also well explained by including isomeric ratio calculated by Hauser-Feshbach model. Covariance matrix can be calculated so as to be consistent with several constraints: mass number normalization, charge number normalization, total yield normalization heavier yield normalization, and consistency with well-known cumulative mass yields. By GLS method, the independent yield errors and their covariance satisfy these constraints and updated covariance can derive consistent mass yield and errors with existing evaluated mass yield and errors.

Acknowledgements

This study comprises the results of “Research and development of an innovative transmutation system of LLFP by fast reactors”, entrusted to the Tokyo Institute of Technology by the Ministry of Education, Culture, Sports, Science and Technology of Japan (MEXT).

References

[1] S. Chiba *et al.*: Scientific Reports **7**, 13961 (2017).
[2] A.C. Wahl: LA-13928 (2002).
[3] H. Koura, T. Tachibana, M. Uno and M. Yamada: Prog. Theor. Phys., **113**, 305 (2005).
[4] P. Fong: Phys. Rev., **102**, 434 (1956).
[5] B.D. Wilkins, E.P. Steingerg and R.R. Chasman: Phys. Rev. C, **14**, 1832 (1976).
[6] EXFOR: https://www-nds.iaea.org/exfor/exfor.htm
[7] K. Oyamatsu: Proc. 1998 Sympo. on Nucl. Data, JAERI-Conf. 1999.
[8] G.R.Keepin, T.F.Wimett, and R.K.Zeigler, Phys. Rev. **107**, 1044 (1957).
[9] T.R. England and B.F. Rider, LA-UR **94** 3106 (1993).

23 Fission Barrier Heights of Actinide Nuclei Obtained in Multi-Nucleon Transfer Reactions of ^{18}O + ^{237}Np

K. R. Kean[1], K. Nishio[2], K. Hirose[2], M. Vermeulen[2], H. Makii[2], R. Orlandi[2], K. Tsukada[2], Y. Iwata[1], A.N. Andreyev[2,3], I. Tsekhanovich[4] and S. Chiba[1]

[1]*Laboratory for Advanced Nuclear Energy, Institute for Innovative Research, Department of Trans-disciplinary Science and Engineering, School of Environment and Society,Tokyo Institute of Technology, 2-12-1-N1-19, Ookayama, Meguro-ku, Tokyo 152-8550, Japan*

[2]*Advanced Science Research Center, Japan Atomic Energy Agency(JAEA), Tokai, Ibaraki 319-1195, Japan*

[3]*Department of Physics, University of York, York YO10, United Kingdom*

[4]University of Bordeaux, 351 Cours de la Libration, 33405 Talence Cedex, France

Abstract

The validity of multi-nucleon transfer approach for the measurements of fission barrier heights, using heavy ion beam ^{18}O with ^{237}Np target, was investigated in JAEA tandem accelerator facility. In this study, fission barrier heights were obtained for ^{239}Np and ^{239,240}Pu isotopes, and these results are compared with literature data and some theoretical calculations. We demonstrate that our approach has a large potential to generate fission barrier data for a large number of nuclide, hard to access by other methods, not investigated so far.

E-mail: kean.r.aa@m.titech.ac.jp, ratha.angkor@yahoo.com

1 Introduction

Fission barrier height is very essential to evaluate fission cross sections, and also critical to assign fissile or fissionable nucleus. Experimental determination of barrier height for a number of short-lived actinide nuclei by neutron-induced method is often difficult or even impossible due to the lack of available target materials. Neutron-induced fission can give fission barrier data only for fissionable nucleus, and thus available data are extremely limited. Instead, a multi-nucleon transfer reaction technique can generate fission barrier data for a wide range of nuclei. In this approach, the nucleus of interest is created in collisions of a beam with target nuclei, via the exchange of nucleons between them. The compound nucleus of interest is formed in an excited state and may therefore de-excite via fission, emission of gamma-rays, neutrons, etc. The basics of this technique are explained in [1].

Some data obtained so far with multi-nucleon transfer reactions' method stem from the transfer of just a few nucleons, based on light ion beams, such as ^{2,3}H and ^{3,4}He beams. However, JAEA

makes use of the heavier projectile, ^{18}O, which allows one to increase the number of transferred nucleons and thus to obtain, and to study fission properties of a wider range of compound nuclei [2, 3].

In this work, we report on the measurement of the barrier heights of ^{239}Np and ^{239,240}Pu isotopes at the JAEA tandem facility. The obtained data are compared with the literature data and theoretical models.

2 Experiments and Data Analysis

2.1 Experiments

We employed ^{18}O + ^{237}Np reaction in the direct kinematic for this study. The ^{18}O beam (162.0 MeV, ∼0.5 pnA) was supplied by the JAEA tandem accelerator in Tokai, Japan. The target was made by electro-deposition of the ^{237}Np material with the thickness 76.3 μg/cm^2 on a nickel backing (300 μg/cm^2). The impurity in ^{237}Np target is negligible. For the detailed information of the impurity, see [10]. The detection system was composed of four Multi-Wire Proportional Counters (MWPCs) to identify fission fragments and a ΔE-E silicon telescope to catch ejectile nuclei. The detailed description of experimental set-up is shown in [2].

The ΔE-E silicon telescope enables us to measure the energy and identify ejectiles, thus the specific transfer channel. This, in turn, allows to uniquely determine the fissioning nucleus and its excitation energy, based on the kinematics of the reaction. The energy of an ejectile, E_{total}, was measured as a sum of its energy loss, ΔE, in one of twelve ΔE detectors (75 μm thick) and the remaining energy (residual energy), E_{res}, deposited in one of the 16 annular strips of the E detector of 300 μm in thickness ($E_{total} = \Delta E + E_{res}$).

The experiment was also performed using natural nickel target (300 μg/cm^2 thick) with the same experimental conditions as the above target. Note that the nickel target and the nickel backing of ^{237}Np target have the same thickness. This measurement serves for the subtraction of the background generated by the target backing.

2.2 Data Analysis

An example of a ΔE-E_{total} Particle Identification plot (PID) for one pair of ΔE-E combinations (out of 16x10=160 combinations) is shown in Fig.1. panels (a) and (b) provide the data for the ^{237}Np target (with Ni backing) and for the Ni target, respectively. Consequently, the ejectiles associated with different (A, Z) lines are clearly identified and distinguished by these plots. On each plot, we made gates, using a functional for charge and mass identification in ΔE-E telescope as reported in [11], to fit these lines so that we are able to extract the kinetic energy of each ejectile. Moreover, applying the conservation of linear momentum and energy, the excitation energies of the compound nucleus, E^*, can be calculated. For the interpretation of the experimental data hereafter, we assume that no excitation of ejectile happens, and the whole E* is contained in the fissioning nucleus.

Fig.2 shows an example of our analysis for the specific transfer channel of ^{237}Np(^{18}O,^{15}N)^{240}Pu. Fig.2(a) shows a continuous singles energy spectrum of ^{15}N ejectiles recorded with the ^{237}Np target (blue rectangle), and with dumb Ni target (yellow triangle). The red points show the result of their subtraction, after the normalization of Ni data was done to the total beam dose. Fig.2(b) shows the number of ^{15}N ejectiles in coincidence (blue rectangle) and random coincidence (black stars) with fission events measured by MWPC. The random fission events were selected by choosing the time

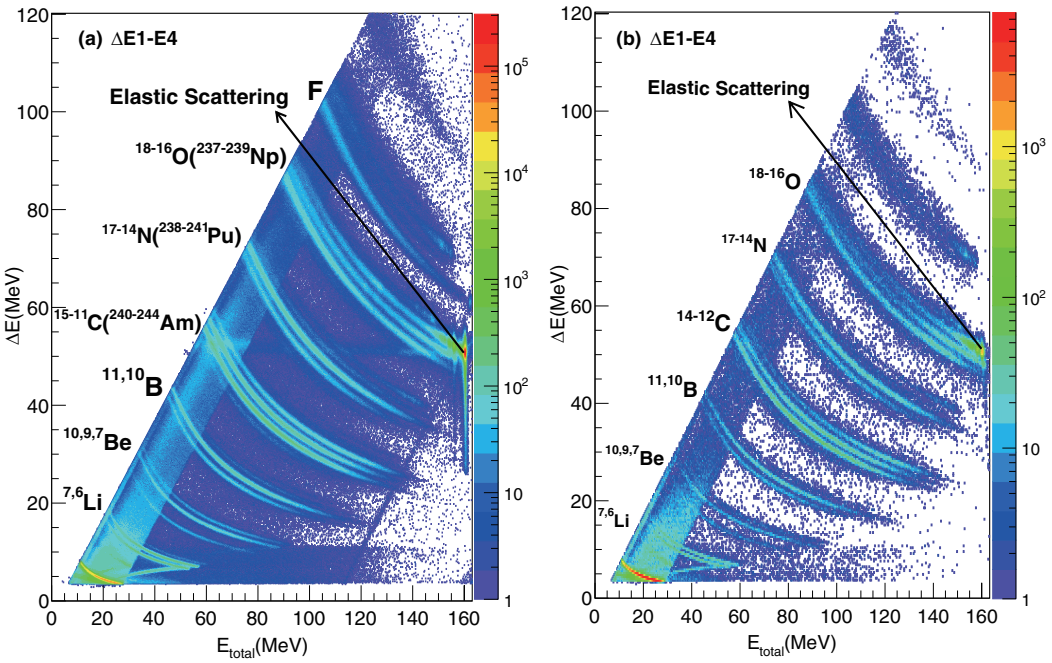

Figure 1: Energy loss versus total energy obtained from ΔE and E detector. Panel (a) for the ^{18}O + ^{237}Np reaction and Panel (b) for the ^{18}O + ^{58}Ni reaction with the average beam dose of 2.0×10^{6} and 8.2×10^{5}, respectively.

interval outside the prompt ejectile-fission time window of 2000 ns. The random coincidences are very significant for $^{18-16}$O ejectiles, and the rests of the ejectiles are negligible. The red rectangles show the result of their subtraction. Fig.2(c) shows the probability spectrum, which is obtained by dividing the background-subtracted coincidence spectrum from Fig.2(b) by the background-subtracted singles spectrum from Fig.2(a) after the correction for the detection geometry efficiency of the MWPCs ($\varepsilon(E^*) \approx 7\%$), according to, [1].

$$P_{fis} = \frac{N_{ej}^{coin}(E^*)}{N_{ej}^{sing}(E^*)\varepsilon(E^*)} \tag{1}$$

This plot shows several features: the onset of fission around 6.50 MeV (1^{st} chance fisson) and the 2^{nd} chance fission at ∼14 MeV.

The uncertainty of an ejectile kinetic energy , $\Delta E_{ej} = 0.38$ MeV, is obtained from the resolution of E_{total} (FWHM = 0.9 MeV). We choose 0.8 MeV for a bin size of each histogram as a compromise between bin statistics and the expected precision of the barrier determination. By using the same procedure, the P_{fis} was also deduced for ^{239}Pu and ^{239}Np. The deduced $P_{fis}(E^*)$ are shown in Fig.2(d,e,f).

In order to obtain fission barrier heights, we fitted the experimental data with the Hill-Wheeler' s expression for the barrier penetration probability [12],

$$P = \frac{P_0}{1 + \exp\left(\dfrac{2\pi(B_f - E^*)}{\hbar\omega}\right)}. \tag{2}$$

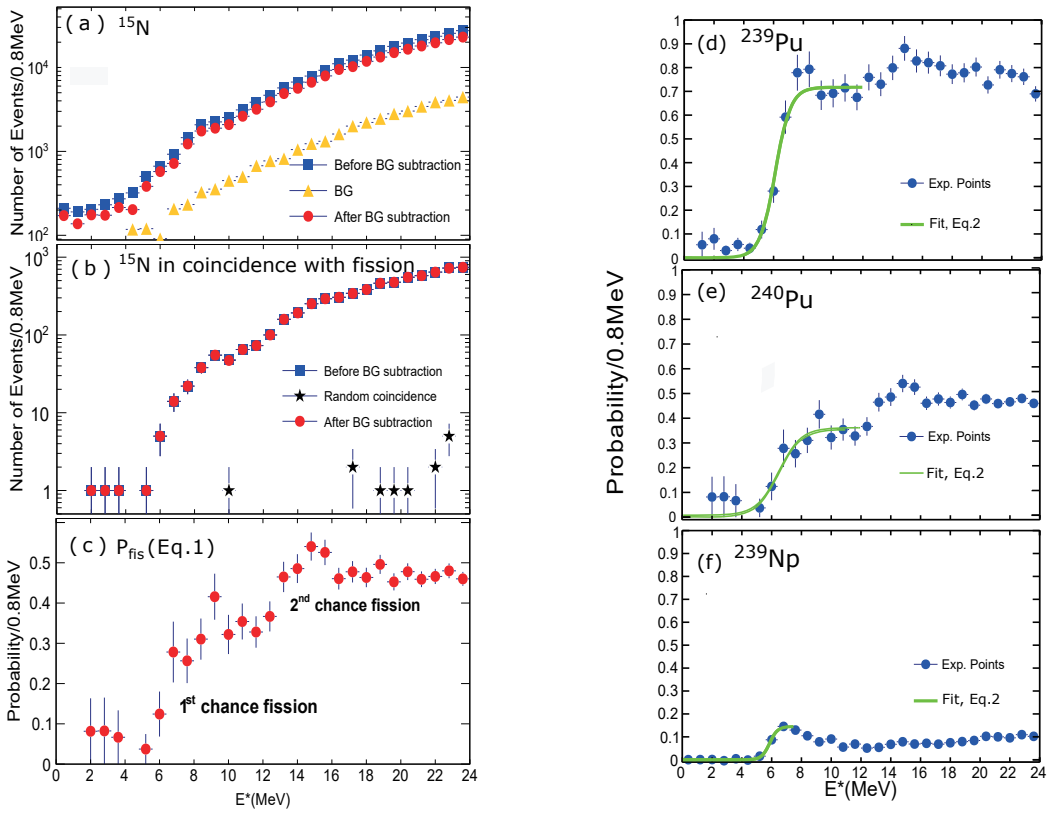

Figure 2: (a) Singles spectrum, (b) coincident spectrum, and (c) probability spectrum for ^{237}Np(^{18}O,^{15}N)^{240}Pu reaction are illustrated. Fission probability as a function of the excitation energies for (a) ^{239}Pu, (b) ^{240}Pu and (c) ^{239}Np. The experimental data are fitted with the Hill-Wheeler's expression from Eq.(2) (solid line) [12].

Table 1: Fission barrier heights (Bf) in MeV for 3 isotopes of this experiment are shown. Those of RIPL2 [4], GEF [9], the recent FRLDM [5], and Skyax (SLy4 [7] and SkM* [8]) calculations are also listed.

Isotopes	Bf (this work)	Bf (RIPL2)	Bf (GEF)	Bf (FRLDM)	Bf (SLy4)	Bf (SkM*)
^{239}Np	5.64	Not exist	5.60	5.57	10.3	8.50
^{239}Pu	6.25	6.20	6.08	5.74	10.1	8.25
^{240}Pu	6.24	6.05	5.70	5.98	10.6	8.76

where E^* is excitation energy, and three fitting parameters P_0, B_f and $\hbar\omega$ represent fission probability, fission barrier height and a curvature, respectively. Fitting, as illustrated in Fig.2(d,e,f) (green solid curve), was performed using CERN ROOT code with Chi-square method.

3 Results and Discussions

Fission barrier heights of three nuclei ^{239}Np and ^{239,240}Pu were determined from fitting of respective data: $B_f(^{239}\text{Np}) = 5.87 \pm 0.09$ MeV, $B_f(^{239}\text{Pu}) = 6.11 \pm 0.12$ MeV and $B_f(^{240}\text{Pu}) = 6.48 \pm 0.37$ MeV, see Table 1. The uncertainties represent 1.53%, 1.96% and 5.71% with respect to the barrier heights, accordingly. This shows a good accuracy of our measurements because of good resolutions of ΔE detectors. These barrier heights are compared with the literature data from RIPL2 [4]. Our data agree well with the empirical data from RIPL2 within 1.45 % for ^{239}Pu and 7.11 % for ^{240}Pu. Note that the data for ^{239}Np is not listed in the RIPL3 compilation. We compare with RIPL2 because it provides reliable data which are originated from neutron induced fission. These small deviations show the validity of our approach. Our data also agree well with GEF [9]. The comparison with theoretical predictions, such as FRLDM [5] and Skyax-BCS (SkM* [8], SLy4 [7]), are also shown. We found that the estimations of the recent FRLDM are slightly smaller than our data. For SLy4 and SkM*, we observe that there are very large discrepancies compared to our data.

4 Summary and Perspective

In summary, our method is a good experimental tool to determine barrier heights for a wide range of nuclei. We preliminarily obtained the barrier heights of ^{239}Pu and ^{240}Pu which, in general, agree very well with those from RIPL2. This evidence shows the validity of our method. Our data have as well good agreement with GEF code. The FRLDM model shows smaller fission barriers than our data. The SkM* and SLy4 calculations generate significantly larger values.

Acknowledgements

The work is partially supported by the "Comprehensive study of delayed-neutron yields for accurate evaluation of kinetics of high burn-up reactors", by the Ministry of Education, Culture, Sports, Science and Technology of Japan (MEXT), and MEXT scholarship program for Cambodian students. We express our gratitude to Dr. F. Minato in JAEA for Skyax code. We thank the tandem accelerator operators who provided the beam with very good conditions.

References

[1] Q. Ducasse et al., Phys. Rev. C 94, 024614 (2016) .

[2] R. Léguillon et al., Phys. Lett. 761, 125-130 (2016).

[3] K. Hirose et al., Phys. Rev. Lett. 119, 222501 (2017)

[4] T. Belgya et al., Handbook for calculations of nuclear reaction data, RIPL-2. IAEA-TECDOC-1506 (IAEA, Vienna, 2006) .

[5] P. Möller et al., Phys. Rev. C 91, 024310 (2015) .

[6] P.-G. Reinhard et al., Phys. Rev. C 60, 014316 (1999) .

[7] E. Chabanat et al., Nucl. Phys. A635, 231 (1998); A643, 441(E) (1998).

[8] J. Bartel et al., Nucl. Phys. A386, 79 (1982).

[9] K.-H. Schmidt et al., Nuclear Data Sheets 131, 107-221 (2016).

[10] T. Ohtsuki et al., Phys. Rev. C 44, 1405 (1991) .

[11] L. Tassan-Got, Nucl. Instr. Meth. Phys. Res. B 194, 503-512 (2002).

[12] D. L. Hill and J. A. Wheeler, Phys. Rev. 89, 1102 (1953).

24 α-cluster structures and dipole excitations in medium-heavy nuclei

M. Nakao[1], H. Umehara[2], S. Ebata[3] T. Okuno[1], F. Tani[1], Y. Hirata[1], and M. Ito[1,4,†]

[1]Department of Pure and Applied Physics, Kansai University, Yamatecho, 3-3-35, Suita 564-8680, Japan
[2]Department of Physics, Osaka University, Machikaneyama-cho, 1-1, Toyonaka 560-0043, Japan
[3]Laboratory for Advanced Nuclear Energy, Institute of Innovative Research, Tokyo Institute of Technology, 2-12-1-N1-16 Ookayama, Meguro-ku 152-8550, Japan
[4]Research Center for Nuclear Physics (RCNP), Osaka University, Mihogaoka 10-1, Suita 567-0047, Japan

† itomk@kansai-u.ac.jp

Abstract Continuum strength function of the isoscalar dipole (IS1) transition for ^{44}Ti $\rightarrow \alpha + {}^{40}$Ca is investigated on the basis of the orthogonality condition model (OCM) under the absorbing boundary condition (ABC). The nuclear potentials are constructed from the double folding procedure with the effective nucleon-nucleon interaction of the density-dependent Michigan three range Yukawa (DDM3Y). The OCM + ABC calculation predicts that the enhancement in the IS1 strength induced by the excitation of the α – ^{40}Ca relative motion occurs at the lower excitation energy of $E_x \leq 10$ MeV. The IS1 strength is larger than the strength by a single nucleon excitation. The low-lying enhancement in the E1 strength for ^{135}Cs $\rightarrow \alpha + {}^{131}$I is also discussed.

I. INTRODUCTION

Basic properties of ground state in nuclei can be described by mean field picture, in which individual nucleons perform single particle motions in a self-consistent mean field [1]. Coherent excitations of such the single particle motion generate various collective excitations of the nuclei [1]. On the contrary, the so-called α cluster structures are known to be realized in the excited states of the nuclei. The α particle is quite stable and inert and hence, it becomes a subunit, which is a building block in constructing the intrinsic structures of the nuclear systems. The α cluster structure has been especially discussed in $N = Z$ systems [2–4]. The typical examples of such the α cluster state are $^{8}\mathrm{Be} = 2\alpha$, $^{12}\mathrm{C} = 3\alpha$, $^{16}\mathrm{O} = \alpha + {}^{12}$C and $^{20}\mathrm{Ne} = \alpha + {}^{16}$O in the lighter mass region.

The picture of the α cluster structures is extended to much heavier systems beyond $A = 40$, such as $^{44}\mathrm{Ti} = \alpha + {}^{40}$Ca [5–10], neighboring nuclei of $^{94}\mathrm{Mo} = \alpha + {}^{90}$Zr [10–12], and $^{212}\mathrm{Po} = \alpha + {}^{208}$Pb [10, 11, 13–15]. In the studies of the heavy systems, the macroscopic α cluster model, in which the local potential for the system of α – residual nucleus is an initial ingredient, are mainly applied. Amongst, the ^{44}Ti nucleus is the most deeply analyzed not only by the local potential approaches [5, 6, 10] but also by the full microscopic approaches, such as resonating group method (RGM) [8] and the anti-symmetrized molecular dynamics (AMD) [9] with the deformed basis [16]. The local potential approach is very effective for this nucleus, and the structure and scattering features are descried in a unified manner.

The cluster state mainly appears as the first excited 0^+ state or the yrast 1^- state, which corresponds to the negative parity partner of the parity doublet with the ground 0^+ state. The typical examples of such the 1^- state can be seen in the asymmetric cluster systems, such as $^{20}\mathrm{Ne} = \alpha + {}^{16}$O and $^{44}\mathrm{Ti} = \alpha + {}^{40}$Ca [2, 3]. Recently, the isoscalar dipole (IS1) transition has been proposed as a useful probe to identify the 1^- cluster excitation [17, 18]. The IS1 transition sheds new light upon the studies of α cluster state with $N = Z$ systems because the lowest electric dipole (E1) transition is completely forbidden in the α cluster model and hence, the analyses about the E1 strength in the clustering phenomena are restricted in $N \neq Z$ systems [19–23]. The pioneering works in Refs. [17, 18] have clearly demonstrated that the IS1 strength induced by the α cluster excitation in ^{20}Ne and ^{44}Ti is comparable to the respective strength for the single particle excitation [17].

In this report, we extend the local potential model in $^{44}\mathrm{Ti} = \alpha + {}^{40}$Ca and investigate the continuum strength of the IS1 transitions in more realistic manner. We employ the orthogonality condition model (OCM) [24, 25] and the absorbing boundary condition (ABC) [26–28] to discuss the continuum strength. One of the great advantage in the local potential model is that the continuum boundary condition is possible to impose and hence, the continuum strength, which corresponds to the direct observable in experiments, can be easily calculated. Since the IS1 strengths in continuum of ^{44}Ti are not discussed experimentally, it is valuable to predict the IS1 continuum strength before the measurement. We also discuss the fraction of energy weighted sum rule (EWSR) as well as the continuum strength. As for the α

– ^{40}Ca potential, we use the double folding (DF) potential with the effective nucleon-nucleon interaction of density-dependent Michigan three range Yukawa (DDM3Y) [29–34].

We also extend the present application to the heavier nuclei, such as ^{135}Cs = α + ^{131}I, which is a kind of long lived fission products (LLFP) in nuclear wastes. The α threshold of this nucleus is about 2.6 MeV and hence, we expect that the α cluster model works nicely in this system. In this situation, there is a possibility that the low-lying enhancements in the dipole strength will be effective in nuclear transmutation. We also discuss the strength function of the E1 transition as a simple example.

The organization of this article is as follows. In Sec. II, the theoretical framework about the DF potential, OCM and ABC are explained. In Sec. III, the continuum strengths of the dipole excitation for ^{44}Ti and ^{135}Cs are presented. The final section is devoted to the summary and the future subject.

II. FRAMEWORK

In this section, we explain the framework for calculation of the continuum strength of ^{44}Ti $\to \alpha +$ ^{40}Ca. The extension to ^{135}Cs $\to \alpha +$ ^{131}I can be achieved in a straight forward manner.

A. $\alpha -$ ^{40}Ca Double folding potential

The nuclear potential of α and ^{40}Ca is calculated from the double folding (DF) model [29–31], which is symbolically written as a function of the $\alpha -$ ^{40}Ca relative coordinate $\mathbf{R}$,

$$U_{\rm DF}(\mathbf{R}) = \iint \rho_\alpha(\mathbf{r}_\alpha)\rho_{40}(\mathbf{r}_{40}) \times v_{\rm NN}^{\rm DDM3Y}(s,\rho){\rm d}\mathbf{r}_\alpha{\rm d}\mathbf{r}_{40} \tag{1}$$

with $s = |\mathbf{r}_{40} - \mathbf{r}_\alpha - \mathbf{R}|$. Here $\mathbf{r}_\alpha$ ($\mathbf{r}_{40}$) denotes a coordinate measured from the center of mass in α (^{40}Ca). $\rho_\alpha(\mathbf{r}_\alpha)$ is the density of α particle, which reproduces the charge form factor, while $\rho_{40}(\mathbf{r}_{40})$ represents the density of ^{40}Ca, which is calculated by the mean-filed model [35].

In Eq.(1), $v_{\rm NN}^{\rm DDM3Y}$ represents the effective nucleon-nucleon (NN) interaction which acts between a pair of nucleons contained in the α particle and the ^{40}Ca nucleus. In the present calculation, we adopt the DDM3Y (density-dependent Michigan three range Yukawa) interaction [32–34]. The validity of the DF potential with DDM3Y in ^{44}Ti = α + ^{40}Ca has been checked by the previous work in Refs. [6, 7, 30]. In recent studies, the DF potential was applied to the systematic studies of the $A \sim 50$ region in recent studies [36].

B. Orthogonality condition model with absorber

First, we calculate the energy spectra of the compound system of ^{44}Ti = α + ^{40}Ca from the DF potential. In the calculation of the energy levels, we apply the orthogonality condition model (OCM) [24, 25] under the absorbing boundary condition (ABC) [26–28].

The OCM equation for ^{44}Ti = α + ^{40}Ca with the total Hamiltonian H and the absorber $-i\eta\mathcal{W}$ is

$$(H - i\eta\mathcal{W})\,\Psi^\eta \;=\; E^\eta\Psi^\eta \tag{2}$$

Here the total Hamiltonian H is given by

$$H \;=\; T \,+\, \bar{U}_{\rm int} \tag{3}$$

$$\bar{U}_{\rm int} \;=\; N_R \times U_{\rm DF} + V_{\rm C} + V_{\rm PF} \;\;, \tag{4}$$

which contains the kinetic energy T and the interaction of $\bar{U}_{\rm int}$ composed of the nuclear potential $U_{\rm DF}$ multiplied by N_R, and the Coulomb potential $V_{\rm C}$. In Eq. (4), $V_{\rm PF}$ means the pseudo potential, which excludes Pauli's forbidden states from the computational space. In ^{44}Ti = α + ^{40}Ca, the oscillator quanta N for the α – ^{40}Ca relative motion is restricted to $N \geq 12$ if the internal structure of α and ^{40}Ca is assumed to the lowest shell model configurations, such as the closed $0s$ and $1s0d$ shells configurations, respectively. Thus, the Pauli forbidden states with $N \leq 10$ should be excluded in the computational space. In the similar manner, the lowest allowed state in ^{135}Cs = α + ^{131}I should have the total oscillator quanta of $N \geq 18$ if we assume a simple harmonic oscillator configuration of ^{110}Zr $\otimes$ $\pi(2s1d0g)^{13}$ and $\nu(2p1f0h)^8$

for ^{131}I. Thus, the Pauli forbidden states with $N \leq 16$ should be excluded in the computational space in the ^{135}Cs = α + ^{131}I system.

In Eq. (2), $-i\eta\mathcal{W}$ denotes the negative absorptive potential with the strength of η, which is introduced to impose the absorbing boundary condition (ABC) [26–28]. In the ABC calculation, the wave function Ψ^η and energy eigenvalue E^η depend on the strength η. According to the previous studies [26–28], the functional form of $\mathcal{W}$ is set to the shifted polynomial function like

$$\mathcal{W}(R) \ = \ \theta(R - R_a) \times (R - R_a)^p \ . \tag{5}$$

A starting point of the absorber R_a should be taken to the outside of the physical interaction region, and we set $R_a = 12$ fm. The power of the polynomial is set to be $p = 1$ in the present calculation.

Secondly, the continuum strength function is calculated from the wave function obtained in the above ABC calculation. A general definition of the strength function for the transition from the initial ground state Ψ_i, which is induced at the energy of E

$$\mathcal{S}_\lambda(E) \ = \ \sum_\nu \left| \left\langle \Psi_\nu \left| \hat{O}_\lambda \right| \Psi_i \right\rangle \right|^2 \delta(E - E_\nu) \ , \tag{6}$$

where Ψ_ν is a final state having the energy eigenvalue E_ν. In Eq. (6), $\hat{O}_\lambda$ denotes the operator of an external field with a multi-polarity of λ. This strength function is calculated by introducing the extended completeness relation (ECR) in the ABC solution [28].

As for the operator of the external field, we consider the dipole operator ($\lambda = 1$) generated by the electric (E1) and isoscalar (IS1) field for the α – core nucleus relative motion, such as

$$\hat{O}^E_{\lambda=1} \ = \ \sqrt{3} \times \frac{4 \cdot Z_C - A_C \cdot 2}{A} R Y_{1,0}(\hat{\mathbf{R}}) \quad \text{for E1} \tag{7}$$

$$\hat{O}^{IS}_{\lambda=1} \ = \ \sqrt{3} \times (\hat{O}^{IS(1)}_{\lambda=1} - \hat{O}^{IS(2)}_{\lambda=1}) \quad \text{for IS1} \tag{8}$$

with the definition of

$$\hat{O}^{IS(1)}_{\lambda=1} \ = \ \frac{5}{3} \left(\frac{A_C}{A} \sum_{i \in \alpha} \xi_i^2 - \frac{4}{A} \sum_{i \in \text{core}} \xi_i^2 \right) R Y_{1,0}(\hat{\mathbf{R}}) \tag{9}$$

$$\hat{O}^{IS(2)}_{\lambda=1} \ = \ \frac{4 \times A_C \times (4 - A_C)}{A^2} R^3 Y_{1,0}(\hat{\mathbf{R}}) \ , \tag{10}$$

where A and A_C represent the total mass and the mass of the core nucleus ($A = A_C + 4$) [17, 18]. In these expressions, $\mathbf{R}$ means the α – core relative coordinate, whereas ξ_i denotes the nucleon coordinate measured from the center of mass in α particle or core. A factor of $\sqrt{3}$ in Eqs. (7) and (8) arises from the Wigner-Eckert theorem, which corresponds to the calculation of the reduced matrix element.

III. RESULTS

In this section, the continuum strength function of $S_\lambda(E)$ for the isoscalar dipole (IS1) transition is discussed. In addition to $S_\lambda(E)$, we investigate the integrated strength over the continuum energies with the k-th energy moment, such as

$$m^\lambda_k(E) \ = \ \int_0^E \varepsilon^k S_\lambda(\varepsilon) \mathrm{d}\varepsilon \ . \tag{11}$$

The integrated values in Eq. (11) are compared with the single particle strength ($M^\lambda_{\text{s.p}}$) or the energy weighted sum rule value, EWSR (M^λ_{sum}).

A. Isoscalar dipole strength in ^{44}Ti $\rightarrow \alpha +$ ^{40}Ca

In the ABC calculation of ^{44}Ti = α + ^{40}Ca, two 1^- resonances are obtained; the 1^-_1 state at $E_R = 5.3$ MeV with $\Gamma_R \sim 10^{-5}$ and the 1^-_2 state at $E_R = 12.7$ MeV with $\Gamma_R = 4.4$ MeV with respect to the

α threshold. The former state corresponds to the negative parity partner of the ground state with $N = 13$, while the latter state has the higher nodal quanta of $N = 15$. The resonance energy of the calculated 1^-_1 state ($E_R = 5.3$ MeV) corresponds to the energy of the observed 1^- state ($E_R = 7.2$ MeV) [37], although the theoretical energy is a little lower than the experimental energy. As for the 1^-_2 state, there is no experimental identification but a considerable mixture of the 1^- strength is confirmed in the 0^+ resonance at $E_R = 10.9$ MeV [37]. Since the 0^+ ($E_R = 10.9$ MeV and $\Gamma_R = 0.7$ MeV) and 1^-_2 ($E_R = 12.7$ MeV and $\Gamma_R = 4.4$) resonances in the calculation overlap each other in energy, the considerable mixture of the 0^+ and 1^- strengths in the experiment is consistent to the theoretical calculation.

The IS1 strength of $S_{\lambda=1}(E)$ plotted as a function of the excitation energy is shown in Fig. 1. In this figure, we can clearly see the strong and sharp enhancement at the excitation energy of 5 MeV. This peak is generated by the 1^-_1 resonance with $N = 13$. Since the decay width of the 1^-_1 state is quite sharp, we have calculated the IS1 strength by the bound state approximation without the absorber. The magnitude of the IS1 matrix element from the ground 0^+ state to the 1^-_1 resonant state is 83.53 fm^3.

A broad peak appears around the excitation energy of 15 MeV. This broad peak is due to the higher resonance, the 1^-_2 state, corresponding to the one higher nodal state from the lower resonance, 1^-_1. The dot with the error bar shows the centroid energy ($E_R = 12.7$ MeV) and the decay width ($\Gamma_R = 4.4$ MeV) of the 1^-_2 resonance, which are reflected in the broad bump structure in the strength function.

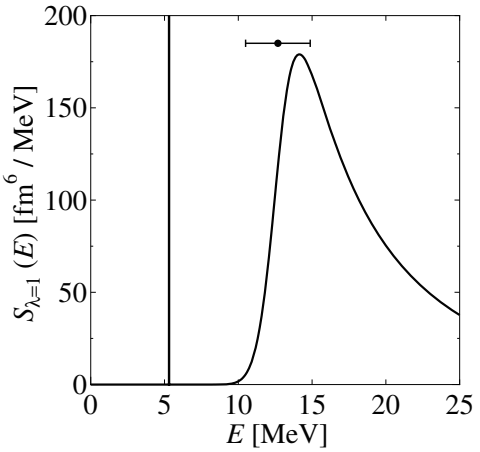

FIG. 1: IS1 continuum strength. The ordinate and abscissa represent the strength and excitation energy, respectively. The dot with the error bar shows the resonant energy with the width.

To confirm the anomalous feature of the IS1 strength, the ratio of the IS1 strength to its single particle strength, such as $\sqrt{m^1_0(E)}/M^1_{\rm s.p.}$, is calculated. At the resonance energy of the 1^-_1 state (~ 5 MeV), the IS1 strength exceeds the respective single particle strength by a factor of 4. In the simple mean field picture, the excitation to the 1^- state requires the $1\hbar\omega$ excitation, which corresponds to about 12 MeV. In the case of the α – ^{40}Ca relative excitation, the enhanced strength occurs at a half of the energy in the single particle excitation, say about 5 MeV. Thus, the low-lying 1^- strength induced by the α excitation is anomalous feature in comparison to the mean field picture. The contribution from 1^-_2 (the dot with the width) further increases the total ratio of $\sqrt{m^1_0(E)}/M^1_{\rm s.p.}$, and the ratio finally reaches about a factor of about 6 in the energy integration up to 15 MeV.

The low energy feature of IS1 can also be confirmed in the fraction of EWSR. The EWSR fraction exceeds about 4 % at the resonance energy of the 1^-_1 state (about 5 MeV), and it reaches about 5% around the excitation energy of the 1^-_2 resonance (about 13 MeV). The EWSR fraction obtained by the random phase approximation (RPA) for ^{208}Pb is about 7% in the energy range of $2 \le E_x \le 17$ MeV [38]. Thus, we can conclude that the appearance of the considerable fraction (~ 4 %) at the low excitation energy of $E_R = 5$ MeV is peculiar phenomenon to the α cluster excitation.

B. Electric dipole strength in ^{135}Cs $\rightarrow \alpha +$ ^{131}I

We have also calculated the E1 strength for ^{135}Cs $\rightarrow \alpha +$ ^{131}I. The E1 strength distribution plotted as a function of the excitation energy is shown in Fig. 2. In this figure, the solid curve shows the B(E1) strength of the dissociation into $\alpha +$ ^{131}I. We can clearly see the strong and sharp enhancements at the excitation energy of 6 MeV. and 18 MeV, which are generated by the $L = 1$ resonances. The former and latter peaks correspond to the $L = 1^-_1$ and 1^-_2 states with the decay width of $\Gamma_\alpha \approx 10^{-4}$ MeV and $\Gamma_\alpha \sim 0.3$ MeV, respectively although the precise determination of the former width is a little difficult in the numerical calculation. On the contrary, the dotted curve represents the strength of the dissociation into $p +$ ^{134}Xe, in which a simple dipole transition of $0g \rightarrow 0h$ is assumed for the proton orbit.

The strength for the first $L = 1$ resonance appear at the lower energy than the peak of the proton excitation, say about 9 MeV, which is same as $1\hbar\omega$ excitation energy in a simple mean filed picture. The

ratio of the strengths for the α excitation to that for the proton excitation are $\sqrt{m_0^1(E)/M_{\rm s.p.}^1} = 0.8$ and 0.1 for the 1_1^- and 1_2^- resonances, respectively. Thus, the total strength for the lower resonance is comparable to the single particle strength of $0g \to 0h$ (or Weisskopf Unit (W.U.)), while the strength for the higher resonance is not so strong. The EWSR fraction of 1_1^- and 1_2^- is totally about $m_1^1/M_1^1 \times 100 = 0.9\%$.

In both of Figs. 1 and 2, we have confirmed a strong enhancement in the transition to the 1_1^- resonance but this strong enhancement will be fragmented into several states in the realistic observation. In fact, a systematic experiments about the dipole transition in the rare-earth region demonstrated that the discrete B(E1) strengths are distributed over the energy range of $2 \sim 4$ MeV in the excitation energy [39–41]. For example, in the case of ^{144}Nd, the individual levels carry the strength of B(E1) $\approx 2.2\times10^{-3}$ e^2fm^2 in average, corresponding to 1.2×10^{-3} W.U., and the total strength below $E_x \leq 4$ MeV reaches about 1.8×10^{-2} W.U. (3.3×10^{-2} e^2fm^2) [40].

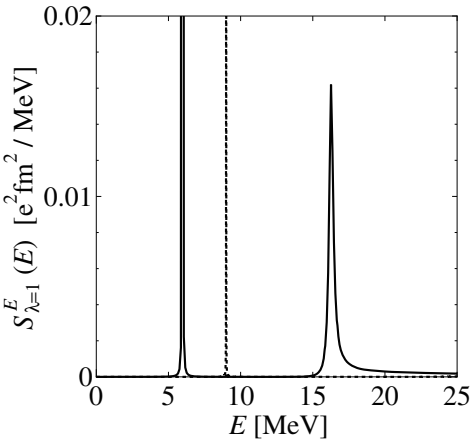

FIG. 2: Continuum strength for E1 transition. The solid curve shows the strength of the dissociation of ^{135}Cs into α + ^{131}I, while the dotted curve shows the strength calculated by the single proton excitation in p + ^{134}Xe with $0g \to 0h$.

According to the observation of the fragmented strength, the 1_1^- resonant states with a pure α cluster configuration should be considered as the doorway state, which finally decays into the more complicated compound states [42]. Such the coupling to the compound state can be handled by the so-called spreading width $\Gamma^\downarrow$ [42]. We speculate $\Gamma^\downarrow$ by assuming that the fraction of about 2×10^{-2} W.U. in B(E1) for 1_1^- (0.8 W.U.) distributes over the energy range of 2 MeV above the α threshold. The resultant spreading width is about $\Gamma^\downarrow = 0.1$ MeV, which is much larger than the α decay width of $\Gamma_\alpha \approx 10^{-4}$ MeV.

IV. SUMMARY AND DISCUSSION

In summary, we have discussed the anomalous feature in the continuum strength of the isoscalar dipole (IS1) transition for the ^{44}Ti = α + ^{40}Ca by applying the orthogonality condition model (OCM) under the absorbing boundary condition (ABC). The IS1 strengths are calculated from the prescription of the extended completeness relation (ECR) in ABC [28]. The analyses about IS1 in the cluster picture has already been done [17, 18] but the previous calculations are based on the bound state approximation. Thus, the prediction of the continuum strength, which is a direct observable in future experiments, is quite important.

We have confirmed the anomalous feature in the IS1 strength; specifically, the strong enhancement in IS1, which is larger by a factor of four than the single nucleon excitation, appears at the excitation energy of about 5 MeV, which is a half of $1\hbar\omega \sim 12$ MeV for the single nucleon excitation. The fraction of EWSR is about 4 %. This strong enhancement is originated from the formation of the negative parity partner in the parity doublet [2, 3]. The similar enhancement occurs at the low excitation energy in the E1 dissociation of ^{135}Cs $\to$ α + ^{131}I. The E1 dissociation occurs at the lower energy, say about 6 MeV, than the energy of the nucleon emission through the giant resonance (about 15 MeV). If this story is true, the transmutation of ^{135}Cs may be possible in non-accelerator based systems. This is because a low-energy photon source ($E_\gamma \leq 10$ MeV) can be generated from a blend material with α emitters.

Although the enhanced dipole transition is expected to occur in the macroscopic α potential model, we should be careful for the effect of the spreading width after the α cluster formation, in which the doorway α cluster state decays into the more complicated compound state. In fact, the 1_1^- state in ^{44}Ti is observed as the fragmented states [37] in the α transfer reaction, while the B(E1) strength in rare-earth region seems to spread in the energy range of about 2 MeV [39, 40]. In future studies, we should analyze the effect of the spreading width as well as the formation of the α cluster structure excited as the doorway state in the discussion of the enhanced dipole strength at the low-lying state. In order to obtain the information of the spreading width, it is important to apply the α cluster model to the rare-earth nuclei, where the α cluster structure was discussed on the basis of the interacting boson model [41]. The analysis of the rare-earth nuclei is now underway.

Acknowledgments

We would like to thank Mr. S. Sonoda and all the members of the Quantum Many-body Physics Laboratory at Kansai University for their useful discussions and kind support. One of the authors (M. I.) thanks Profs. M. Kimura at Hokkaido University, T. Yamada, Y. Funaki at Kanto-Gakuin University, K. Ikeda at RIKEN and Dr. K. Minomo at RCNP for their valuable discussions, useful comments and encouragements.

References

[1] P. Ring and P. Schuck, 2004 Nuclear Many-Body Problem1st edn (Berlin: Springer), and references therein.
[2] K. Ikeda *et al.*, Prog. Theor. Phys. Suppl. **68**, 1 (1986).
[3] H. Horiuchi *et al.*, Suppl. Prog. Theor. Phys. **192**, 1 (2012), and references therein.
[4] M. Freer, Rep. Prog. Phys. **70**, 2149 (2007).
[5] B. Bukc, C. B. Dover, and J. P. Vary, Phys. Rev. C **11**, 1803 (1975).
[6] U. Atzrott, P. Mohr, H. Abele, C. Hillenmayer, and G. Stadt, Phys. Rev. C **53**, 1336 (1996).
[7] S. Ohkubo, Y. Hirabayashi, and T. Sakuda, Phys. Rev. C **57**, 2760 (1998), and references therein.
[8] T. Wada and H. Horiuchi, Phys. Rev. C **38**, 2063 (1988).
[9] M. Kimura and H. Horiuchi, Nucl. Phys. A **767**, 58 (2006).
[10] F. Michel, S. Ohkubo and G. Reidmeister, Suppl. Prog. Theor. Phys. bf132, 7 (1998), and references therein.
[11] B. Buck, A. C. Mearchant, and S. M. Perez, Phys. Rev. C **51**, 559 (1995).
[12] M. A. Souza and H. Miyake, Phys. Rev. C **91**, 034320 (2015).
[13] F. Hoyler, P. Mohr, and G. Staudt, Phys. Rev. C **50**, 2631 (1994).
[14] S. Ohkubo, Phys. Rev. Lett. **74**, 2176 (1995).
[15] Y. Suzuki and S. Ohkubo, Phys. Rev. C **82**, 041303(R) (2010).
[16] M. Kimura and H. Horiuchi, Phys. Rev. C **69**, 044319 (2004).
[17] Y. Chiba, M. Kimura and Y. Taniguchi, Phys. Rev. C **93**, 034319 (2016).
[18] Y. Chiba, Y. Taniguchi and M. Kimura, Phys. Rev. C **95**, 044328 (2017).
[19] Y. Alhassid, M. Gai, and G. F. Bertsch, Phys. Rev. Lett. **49**, 1482.
[20] M. Gai, M. Ruscev, A. C. Hayes, J. F. Ennis, R. Keddy, E. C. Schloemer, S. M. Sterbenz, and D. A. Bromley, Phys. Rev. Lett. **50**, 239 (1983).
[21] M. Gai, J. F. Ennis, M. Ruscev, E. C. Schloemer, B. Shivakumar, S. M. Sterbenz, N. Tsoupas, and D. A. Bromley, Phys. Rev. Lett. **51**, 646 (1983).
[22] A. Astier, P. Petkov, M.G. Porquet, D. S. Delion, and P. Schuck, Phys. Rev. Lett. **104**, 042701 (2010).
[23] D. S. Delion, R. J. Liotta, P. Schuck, A. Astier, and M.G. Porquet, Phys. Rev. C **85**, 064306 (2012).
[24] S. Saito, Suppl. Prog. Theor. Phys. **62**, 11 (1977).
[25] H. Masui, K. Kato and K. Ikeda, Phys. Rev. C **75**, 034316 (2007).
[26] M. Ito and K. Yabana, Prog. Theor. Phys. **113**, 1047 (2005).
[27] Y. Takenaka, R. Otani, M. Iwasaki, K. Mimura, and M. Ito, Prog. Theor. Exp. Phys. **2014**, 113D04 (2014).
[28] M. Iwasaki, R. Otani, Y. Takenaka and M. Ito, PTEP **2015**, 023D01, and references therein.
[29] G. R. Satchler and W. G. Love, Phys. Rep. **55** (1979).
[30] M. Nakao, H. Umehara, S. Ebata and M. Ito, Proceedings of the 2017 Symposium on Nuclear Data; November 16-17, 2017, page 185, iVil, Tokai-mura, Ibaraki, Japan, (DOI) https://doi.org/10.11484/jaea-conf-2018-001
[31] M. Ito, Y. Hirabayashi and Y. Sakuragi, Phys. Rev. C **66**, 034307 (2002), and references therein.
[32] A. M. Kobos *et al.*, Nucl. Phys. A **384** (1982); A. M. Kobos, B. A. Brown, R. Lindsay and G. R. Satchler, Nucl. Phys. A **425**, 205 (1984).
[33] M. El-Azab Farid and G. R. Satchler, Nucl. Phys. A **438**, 525 (1985).
[34] M. E. Brandan and G. R. Satchler, Nucl. Phys. A **487**, 477 (1988).
[35] S. Ebata, T. Nakatsukasa, T. Inakura, K. Yoshida, Y. Hashimoto, and K. Yabana, Phys. Rev. C **82**, 034306 (2010).
[36] P. Mohr, Open Nucl. & Part. Phys. J. **1**, 1 (2008).
[37] T. Yamaya, K. Katori, M. Fujiwara, S. Kato and S. Ohkubo, Suppl. Prog. Theor. Phys. **132**, 73 (1998), and references therein.
[38] I. Hamamoto and H. Sagawa, Phys. Rev. C **66**, 044315 (2002).
[39] H. Friedrichs *et al.*, Phys. Rev. C **45**R, 892 (1992).
[40] T. Eckert *et al.*, Phys. Rev. C **56**, 1256 (1997).
[41] M. Spieker, S. Pascu, A. Zilges, and F. Iachello, Phys. Rev. Lett. **114**, 192504 (2015).
[42] A. M. Lane, R. G. Thomas and E. P. Wigner, Phys. Rev. **98**, 693 (1955).

25 Evaluations of neutron induced reaction cross sections for ^{35,36,37}Cl

Jeong-Yeon Lee[1], Shin Okumura[2], Kohsuke Tsubakihara[1], Satoshi Chiba[1]
[1]Tokyo Institute of Technology, [2]International Atomic Energy Agency
Email: lee.y.ay @m.titech.ac.jp

We have performed evaluations of cross sections for neutron induced reactions, e.g., (n,tot), (n,el), (n,γ), (n,p), and (n,α), on ^{35,36,37}Cl for molten salt reactors, where chloride U, Pu and/or Th are used as nuclear fuel. We have included covariances in our evaluations. We have also obtained random files for Total Monte Carlo analyses of integral quantities.

1. Introduction

There is a project on design of molten salt reactors (MSR), where chloride U, Pu and/or Th are used as nuclear fuel. MSR is a type of nuclear reactor that uses liquid fuel instead of solid fuel rods used in conventional nuclear reactors. Using liquid fuel provides many advantages: simplicity of design, unparalleled safety, and a solution to nuclear waste and stockpiles of plutonium.

There are two stable isotopes of chlorine: ^{35}Cl(75.76%) and ^{37}Cl(24.24%). However, by neutron capture, ^{36}Cl will be populated and its half life is 3.01x10^{5} years. The produced ^{36}Cl will affect reactor performance and also will be problematic radioactive nuclear waste. The value of radioactivity concentration of ^{36}Cl contained in a material should be less than 1Bq/g for a material to be treated as non-radioactive waste (clearance level) [1]. In addition, neutron capture reaction on ^{36}Cl will produce ^{37}Cl. Therefore, evaluations of neutron induced reaction cross sections for ^{35,36,37}Cl are very important for a design of MSR.

2. Evaluations of neutron induced reaction cross sections for ^{35,36,37}Cl

There are evaluated nuclear data files for neutron induced reaction cross sections for ^{35,36,37}Cl. However, the evaluated results do not include covariances. Therefore, we aimed at evaluations of the reactions cross sections for ^{35,36,37}Cl with covariance data. First, we have surveyed the status of experimental [2] and evaluated nuclear data [3] for neutron induced reactions, e.g., (n,tot), (n,el), (n,γ), (n,p), and (n,α), on ^{35,36,37}Cl and have compared the data. Next, we have performed evaluations of the cross sections for neutron induced reactions on ^{35,36,37}Cl with covariances using the T6 code package including the TALYS and the TARES codes [4] as well as many other codes. The TALYS code deals with nuclear reactions taking into account nuclear structure, optical model, direct and compound reaction models,

preequilibrium model, and many other reaction models to describe cross sections in the different reaction channels in the fast neutron energy region. The TARES code deals with resonance parameters for calculations of cross sections in the resonance region.

Figures 1-4 show our evaluated results of cross sections for neutron induced reactions on ^{36}Cl using the T6. Figure 1 shows our calculated cross sections for neutron capture reaction on ^{36}Cl, showing good agreement with the corresponding experimental data and other evaluated nuclear data. Figure 2 shows results of random number calculations for obtaining the ^{36}Cl(n,γ)^{37}Cl reaction cross sections using the Total Monte Carlo analyses [5]. Figure 3 shows calculated cross sections for ^{36}Cl(n,p)^{36}S reaction, showing overall agreement with experimental data over the thermal and fast neutron energy regions, while the resonances in the excitation function are not reproduced in the resonance energy region. We have obtained covariances. The correlation matrix of covariance between Δσ/σ vs. E for ^{36}Cl(n,tot) and Δσ/σ vs. E for ^{36}Cl(n,inel) reactions are shown in Fig. 4. Figure 5 shows our evaluated results for ^{35}Cl(n,el) reaction cross sections, compared with other evaluated nuclear data. Our evaluated result shows good agreement with previous evaluated data. Figure 6 shows our evaluated cross sections of ^{35}Cl(n,α)^{32}P reaction. Our result shows good agreement with the experimental data over the thermal and fast neutron energy regions, while our result does not show the resonances which are shown in the EAF-2010 evaluation data in the resonance region. Figures 7 and 8 show our evaluated cross sections for the reactions ^{37}Cl(n,tot) and ^{37}Cl(n,γ)^{38}Cl, respectively. The evaluated files include covariances and the cross sections show good agreement with the experimental and evaluated data over the whole energy range in the figures.

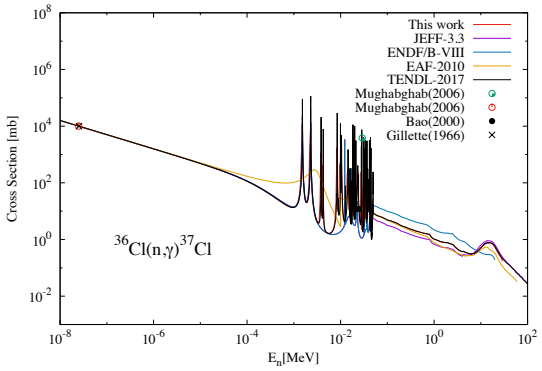

Fig. 1. Neutron capture cross sections for ^{36}Cl.

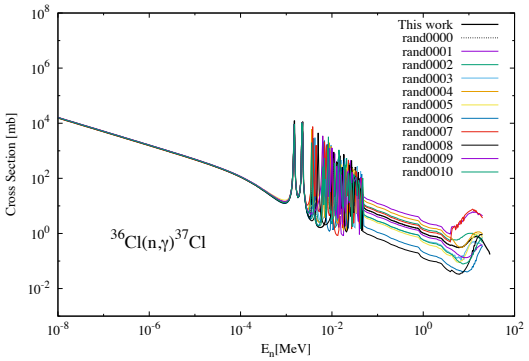

Fig. 2. Random files via Total Monte Carlo analysis.

3. Conclusion

We have performed evaluations of cross sections for neutron induced reactions, e.g., (n,tot), (n,el), (n,γ), (n,p), and (n,α), on ^{35,36,37}Cl for a design of molten salt reactor and have compared our evaluated results with the corresponding experimental data and other previous evaluated nuclear data. We have included covariances in our evaluations and have also obtained random files for Total Monte Carlo analyses of integral quantities. Our evaluated results for the reactions on ^{35,36,37}Cl show good agreements with the experimental data and other previous evaluated data.

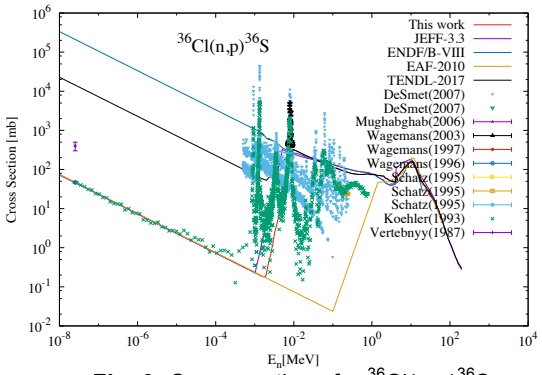

Fig. 3. Cross sections for ^{36}Cl(n,p)^{36}S.

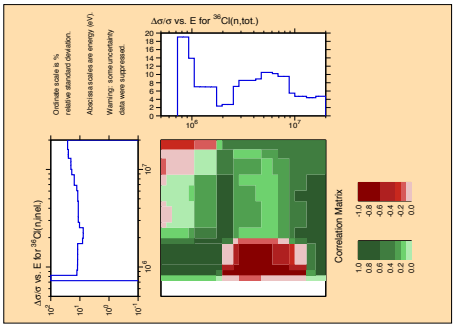

Fig. 4. Correlation matrix.

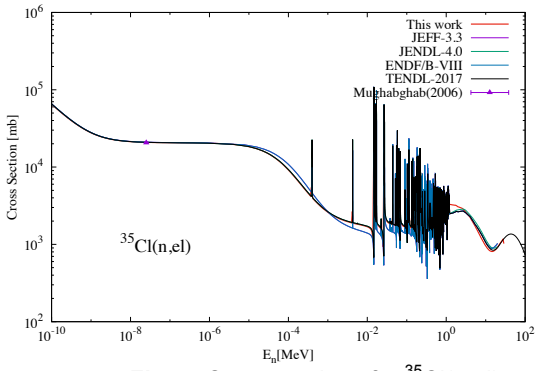

Fig. 5. Cross sections for ^{35}Cl(n,el).

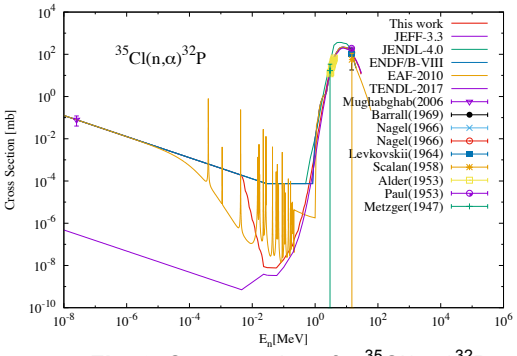

Fig. 6. Cross sections for ^{35}Cl(n,α)^{32}P.

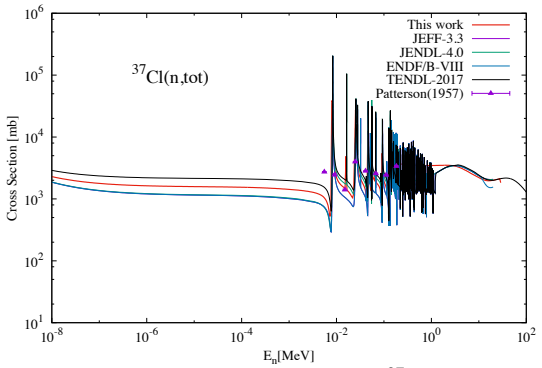

Fig. 7. Cross sections for ^{37}Cl(n,tot).

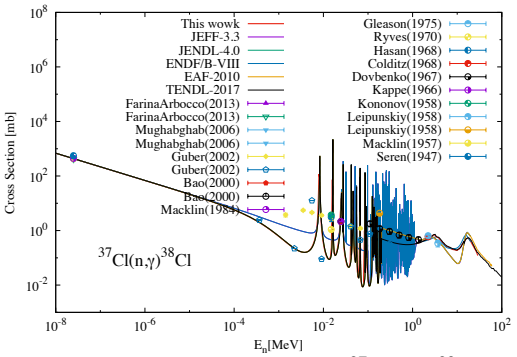

Fig. 8. Cross sections for ^{37}Cl(n,γ)^{38}Cl.

References

[1] IAEA Safety Guide, No. RS-G-1.7 (2004).

[2] EXFOR, available at https://www-nds.iaea.org/exfor/.

[3] ENDF, available at https://www-nds.iaea.org/exfor/endf.htm.

[4] A.J. Koning and D. Rochman, '*Modern nuclear data evaluation with the TALYS code system*', Nuclear Data Sheets **113** (2012) 2841.

[5] A.J. Koning, '*Bayesian Monte Carlo method for nuclear data evaluation*', European Physical Journal A **51** 184 (2015) 1.

26 A SYSTEMATIC TDDFT DATA FOR NUCLEAR FISSION ANALYSIS - SV MODELS -

TAKASHI NISHIKAWA[1*], YORITAKA IWATA[2], AND SATOSHI CHIBA[2]

[1]NUCLEAR ENGINEERING LTD, OSAKA 550-0001, JAPAN
[2]TOKYO INSTITUTE OF TECHNOLOGY, TOKYO 152-8550, JAPAN
*E-MAIL: RG12F090@GMAIL.COM

Abstract. Quantum dissipation during nuclear reactions is studied by means of TDDFT+ Langevin model. Much attention is paid to the energy dependent role of symmetry energy in the friction coefficient. In this article, following the preceding work showing a systematics on $Z = 92$ to 100 nuclei, macroscopic friction coefficients are obtained by employing all the SV-type nuclear interaction models. The comparison between different SV models clarifies the influence of several nuclear matter properties on the quantum dissipation. That is not only the completion of a systematic theoretical database, but also identifying the dissipation effect on astrophysical nuclear-matter objects.

1. Introduction

The SV-model interaction sets [1] are design for identifying the relation between the effective nuclear force and the nuclear matter property. There are 15 different parameter sets in the SV models: SV-min, SV-bas, SV-K218, SV-K226, SV-K241, SV-mas07, SV-mas08, SV-mas10, SV-sym28, SV-sim32, SV-sym34, SV-kap00, SV-kap02, SV-kap60, and SV-tls. Among these interactions, SV-bas is the basic interaction, and SV-min is the interaction determined with less requirements, and SV-tls is the interaction adjusted including the spin-current tensor contribution. The incompressibilities are examined via the power of density dependence α in SV-K, and the effective mass in SV-mas, the symmetry energy in SV-sym, and the sum-rule enhancement in SV-kap.

In this article, following the preceding work [2] showing a systematics on $Z = 92$ region (Uranium, Plutonium isotopes and so on) using conventional SkM* and SLy4 models, the dissipation in many-nucleon systems is studied using SV moldels. A systematic calculation of friction coefficients for SV-models is carried out based on the TDDFT+Langenvin model. In terms of dissipation effect, the unknown physical effect of imcompressibility, effective mass, symmetry energy and sum-rule enhancement is possibly clarified by these results. The effect of symmetry energy is explored in the fission dynamics of ^{236}U. According to the fitting protocol of SV-models, the symmetry energy $a_{\rm sym}$ is fitted to be equal to 28, 32, and 34 for SV-sym28, SV-sim32, and SV-sym34, respectively. The other fitting conditions are intentionally taken to be exactly the same. The comparison between the three interactions is expected to show the symmetry-energy dependence of the dissipation effect.

2. Proposed method

The analysis of quasi-fission events is made based on the TDDFT+Langevin model being introduced by Nishikawa *et al.* [2] after our preparatory works on nuclear fission[3, 4, 5, 6, 7], where the terminology "TDDFT" stands for the time-dependent density functional theory. The TDDFT+Langevin model is explained in Ref. [2]. The numerical code Sky3D [8] is employed for the TDDFT calculations, and fission dynamics is calculated by 4D Langevin code [9]. For the TDDFT calculations, we employ 15 different effective nuclear interactions being proposed in Ref. [1]. We carried out the TDDFT calculations of quasi-fission

Numerical computation was carried out at a workstation system at Tokyo Institute of Technology (AEGIS system). This work was supported by JSPS KAKENHI Grant No. 17K05440. Authors are grateful to Dr. N. Hinohara for a useful suggestion.

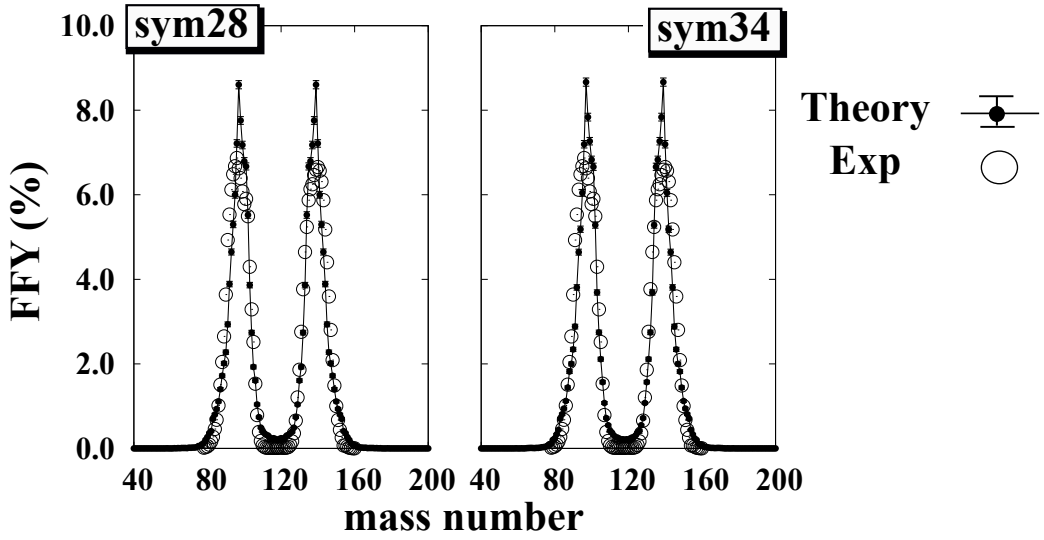

Figure 1. (Color online) Fission fragment yields (FFYs) of ^{236}U calculated by the TDDFT+Langevin model, where $a_{\rm sym}$=28 for SV-sym28, and $a_{\rm sym}$=34 for SV-sym34 interactions. The FFY at the excitation energies 0.085 per nucleon is calculated. Open circles are experimental data Ref. [11, 12]. For SV-bas and SV-sym, the corresponding fission probabilities are 9 %.

processes by symmetric central collision reactions

$$ {}^{A}Z + {}^{A}Z \ \rightarrow \ {}^{2A}2Z \ \rightarrow \ {}^{A}Z + {}^{A}Z \ , \tag{1}$$

where A and Z are a mass number and a proton number respectively. In particular, Z and A are fixed to $Z = 92$ and $A = 236$ in this research. Here the energy E is taken as the initial energy of the collision, and E/A is from 3 MeV to 7 MeV. The distance $R(t)$ between the center-of-mass of two colliding nuclei is extracted from the TDDFT wave function. For the details of $R(t)$, see Ref. [10]. The averaged friction coefficient is calculated by the $R(t)$

$$ \overline{\gamma}(E) = \frac{\{\frac{1}{2}\mu\dot{R}^2(t_i) + V(t_i)\} - \{\frac{1}{2}\mu\dot{R}^2(t_f) + V(t_f)\}}{\int_{t_i}^{t_f}\{\dot{R}(t)\}^2 dt} \ , \tag{2}$$

where $\overline{\gamma}(E)$ is averaged for time t. t_i and t_f are usually taken as the initial and the final time of reaction. Note that $\overline{\gamma}(E)$ values at extra-ordinary energies, which are too low or too high to be treated by the TDDFT, are also obtained using the extrapolation method being explained in Ref. [2].
The $\overline{\gamma}(E)$ at the extrapolated lower energy is substituted to the Langevin coefficient γ_{11}, and fission dynamics is obtained by Langevin calculation. γ_{11} is the friction coefficient of the motion along $R(t)$. Detailed explanation of Langevin calculation is shown in Ref. [9]. By this procedure, both stochastic aspect and microscopic aspect of fission dynamics are incorporated.

3. Result

Figure 1 shows the fission fragment yields (FFYs) for ^{236}U with SV-sym interaction set. Two things are remarkable. First, according to the comparison with the experiment, the both of two interactions reproduce the FFY well. It briefly shows the validity of the proposed method. Second, according to the comparison between the results from two interactions, the symmetry energy does not play a significant role in the fission (for both fission probability and FFY). The second issue, which corresponds to a kind of the Skyrme interaction dependence, should be further studied by considering the fission of other Uranium isotopes.

Table 1. The friction coefficients $\overline{\gamma}(E)$ of unit $\hbar$ calculated for ^{236}U by 15 effective nuclear interactions. The energy is taken for 3 MeV, 5 MeV, 7 MeV and 0.085 MeV per nucleon, where 0.085 MeV corresponds to the total excitation energy 20 (i.e., 0.085×236 = 20). In the row "Average", the averaged values for these 15 interactions are shown.

SV-prameter	3MeV	5MeV	7MeV	0.085MeV
bas	100.12	91.20	83.61	119.78
min	102.81	91.96	85.85	119.87
K218	100.65	85.94	80.46	117.33
K226	103.19	85.01	82.04	111.98
K241	108.25	94.36	86.36	124.13
kap00	110.05	93.80	83.23	128.00
kap02	107.58	91.77	83.57	125.33
kap06	103.18	87.10	84.77	110.44
sym28	106.90	91.53	83.59	123.95
sym32	99.22	91.16	83.37	117.88
sym34	98.93	89.86	82.68	120.04
mas07	89.72	69.60	54.12	110.27
mas08	94.58	80.67	67.97	118.01
mas10	116.76	100.50	96.23	125.70
tls	111.63	93.56	90.86	119.12
Average	103.57	89.20	81.91	119.46

The calculated friction coefficient $\overline{\gamma}(E)$ is shown in Table 1. Fission at or around the Coulomb barrier energy (E/A = 0.085 MeV) is useful to analyze the low-energy fission events such as quasi-fission, photo-fission, neutron-induced fission and so on. The other cases are more important to see the higher energy fission or fragmentation events, as well as to see the energy dependence. There is a similar energy dependence for all the interaction parameters. Although there is no significant difference in fission property (Fig. 1), several percents of difference can be found in the $\overline{\gamma}(E)$ values for SV-sym28 and SV-sym34 interactions as shown in Fig. 2. Since the $a_{\rm sym}$ values for the most of SV-type interactions are set to 30 [1], the obtained results suggest that larger $a_{\rm sym}$-value results in the smaller friction coefficient. In addition, as a common trend, the amplitude of $\overline{\gamma}$ becomes smaller for higher energies. Such a trend is reasonable, because the shorter duration time in higher energy collisions should lead to the smaller amount of dissipated energy in reaction processes. Furthermore there is no remarkable quantitative difference among the three cases. It supports the fact that the symmetry energy does not play a role in both the fission and the dissipation (represented by the friction coefficient). Consequently, using different SV-models, the influence of symmetry energy on the fission is found out to be quite limited.

4. Summary

We have demonstrated a systematic calculation of TDDFT+Langevin model using SV type interactions. The TDDFT+Langevin with SV models is expected to be a powerful tool to pin down the physical role of incompressibility, the effective mass, the symmetry energy, the sum-rule enhancement, and the spin-current tensor effects in the fission dynamics.

In this article, within the limited number of pages, we focus on the symmetry energy. The agreement between the theory and experiment is remarkable. As our main discovery, the TDDFT+Langevin with SV models found a quite limited role of symmetry energy in the dissipation and the fission dynamics. The symmetry energy effect on fission was found out to be weakened for higher energies, which is still quite low compared to the energy scale of intermediate energy heavy-ion collisions. Table 1 provides a part of theoretical database of systematic friction coefficients. The detials of incompressibility, the effective mass, and the sum-rule enhancement on the fission dynamics are expected to be examined in our forthcoming publications.

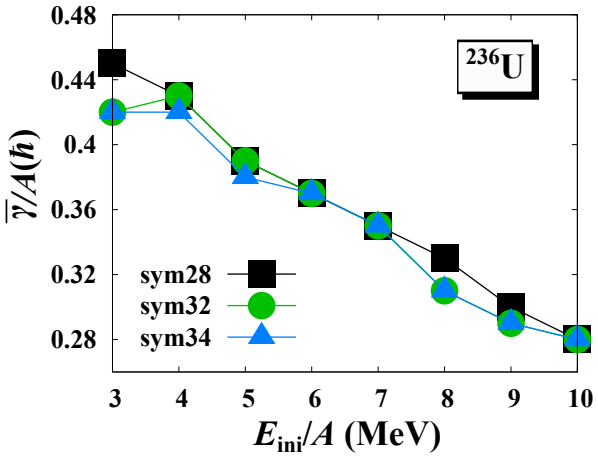

Figure 2. (Color online) Energy dependence of friction coefficient $\overline{\gamma}$ per nucleon, where A denotes the mass number. The results with SV-sym28, SV-sym32 and SV-sym34 are compared. The amplitude of $\overline{\gamma}$ stands for the amount of dissipated energy at a given excitation energy.

References

[1] P. Klüpfel, P.-G. Reinhard, J. Bürvenich, and J. A. Maruhn, Phys. Rev. C **79** 034310 (2009).
[2] T. Nishikawa, Y. Iwata, and S. Chiba, in preparation.
[3] T. Nishikawa, Y. Iwata, and S. Chiba, to appear in JAEA-Conf 2018-001(2018).
[4] T. Nishikawa, Y. Iwata, and S. Chiba, to appear in JAEA-Conf 2019-001(2019).
[5] Y. Iwata and S. Heinz, Exotic Nuclei, EXON-2012, World Scientific, 153 (2013).
[6] Y. Iwata and S. Heinz, CERN Proceedings 2012 - 002, 241 (2013).
[7] Y. Iwata, JAEA-Conf 2015-003, INDC(JPN)-201, 93 (2015).
[8] J. A. Maruhn, P.-G. Reinhard *et al.*, Comput. Phys. Commun. **185** 2195 (2014).
[9] M. D. Usang, F. A. Ivanyuk, C. Ishizuka, and S. Chiba, Phys. Rev. C **94** 044602 (2016).
[10] Y. Iwata, H. Feldmeier, and J. A. Maruhn, AIP Conf. Proc. 1377, 365 (2011).
[11] C.Straede, C.Budtz-Jørgensen, H.H.Knitter, Nucl. Phys. A **462** 85-108 (1987) .
[12] S.Zeynalov, W.Furman, F.J.Hambsch, ISINN-13. 2006

27 Compilation for Chart of the Nuclides 2018: A Comprehensive Decay Data

Hiroyuki Koura
Advanced Science Research Center, Japan Atomic Energy Agency
Shirakata 2-4, Tokai-mura, Ibaraki 319-1195, Japan
Jun-ichi Katakura
Department of Nuclear System Safety Engineering, Nagaoka University of Technology
Kamitomioka-machi 1603-1, Nagaoka, Niigata 940-2188, Japan
Takahiro Tachibana
Research Institute for Science and Engineering, Waseda University
Okubo 3-4-1, Shinjuku-ku, Tokyo 169-8555, Japan
Futoshi Minato
Nuclear Data Center, Nuclear Science and Engineering Center, Japan Atomic Energy Agency
Shirakata 2-4, Tokai-mura, Ibaraki 319-1195, Japan
e-mail: koura.hiroyuki@jaea.go.jp

Abstract:

A chart of the nuclides 2018 version is now preparing to be published from JAEA. This will be the latest successive version of the chart since 1976, and continues as 1980, 1984, 1988 1992, 1996, 2000, 2004, 2014 and 2018. This chart includes decay data of isotopes as half-lives, decay modes, isotopic abundance, and isomeric states with certain long half-lives. In addition, the periodic table of elements, fundamental physical constants, characteristic X-rays, thermal neutron capture and fission cross sections are listed and tabulated. The latest version is now compiled with recent experimental data until the end of June in 2018, with some additional improvements. The number of nuclides experimentally identified is totally 3,299, which includes 3,062 half-life-measured nuclides. Regarding the theoretical prediction, five decay modes are considered: alpha decay, beta decay, spontaneous fission, one- and two-proton emission. In addition, the experimental proton and neutron drip lines, and the boundary line of beta-delayed neutron are drawn.

1. Introduction

A comprehensive evaluated nuclear decay data set as “Chart of the Nuclides 2018” is being constructed from Japan Atomic Energy Agency (JAEA). This is the successive version of a nuclear chart on nuclear decay. The first version was published in 1976, and continues as 1980, 1984, 1988 1992, 1996, 2000, 2004, 2010 and 2014. The first eight series were published from Japan Atomic Energy Research Institute, and last one is from JAEA, which is the preceding institute by joining Japan Nuclear Cycle Development Institute. These charts include nuclear decay data of isotopes as half-lives, decay modes, isotopic abundance, and isomeric states with certain long half-lives. In addition, the periodic table of elements, fundamental physical constants, characteristic X-rays, thermal neutron capture cross sections were listed and tabulated.

In the previous version in 2014, we did a major revision. Consequently, we published totally 16 sheets of the chart, 4 sheets more than the previous version in 2010 [1]. The current version (2018) has only small changes in the construction, however, there are constantly new and revised nuclear decay data since 2014. In this report, we show current results of the chart before the finalization which will be done in the end of March of 2019.

2. New naming and element symbols

In 2016, International Union of Pure and Applied Chemistry (IUPAC) announced that the naming and element symbols are officially approved for the 113th, 115th, 117th and 118th elements as nihonium (Nh), moscovium (Mc), tennessine (Ts) and oganesson (Og) [2]. These new element symbols are adopted both in the nuclear chart and in the periodic table of element in the sheets.

3. Construction of the chart

The chart has totally 16 sheets as in Fig. 1. The construction is as follows.

Front side:

・Main part of the nuclear chart: page 1-12

・Explanation of the main part: page 13-14

・Overview chart: page 15-16

Back side:

・Periodic table of elements: page 1-2

・Fundamental physical constants: page 3

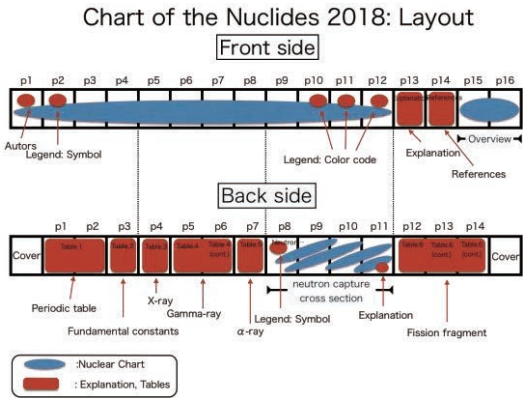

Figure 1: Construction of the Chart of the Nuclides 2018.

4. Main nuclear chart

(1) Experimental data

The main points in experimental data are as follows:

i. Adopted experimental data: Basically, we adopt experimental decay data from both of the 2018 March version of Evaluated Nuclear Structure Data File (ENSDF) and Nuclear Data Sheet. In addition, recent experimental results from published peer-review papers are adopted. The cutoff date for Nuclear Data Sheets and journal papers is set as **June 30, 2018**. Finally, we adopted experimental data from the following seven journal papers: *Physical Review Letters*, *Physical Review C*, *Nuclear Physics A*, *European Physical Journal A*, *Physics Letters B*, *Journal of the Physical Society of Japan*, and *Nuclear Instruments and Method in Physics Research B*.

ii. Lighter mass region: Neutron- or proton-emitting unstable nuclides are adopted. These nuclides have been well studied in the lighter nuclear mass region, and many of resonant states were reported these several years. Subsequently 34 nuclei are listed including ^{4}n, $^{4\text{-}7}$H, $^{5,\,7,9\text{-}10}$He, $^{4,5,\,10,12\text{-}13}$Li, etc.

iii. Border of unstable nuclides against particle nucleon emission: The neutron and proton drip lines are drawn by the difference of the ground-state masses of nuclides. The lines are defined as the borders of neutron or proton separation energies. The 2016 Atomic Mass Evaluation [3] is adopted to obtain the ground-state masses of nuclides. We also draw the boundary line of the beta-delayed neutron emission in the same manner.

(2) Theoretical data

The main points in theoretical prediction are as follows:

i. Description of five decay modes: Until the 2014 version, we adopted three decay modes in the theoretical prediction as beta-decay, alpha decay (since 2000), and spontaneous fission (2010). In the 2014 version, we added theoretical predictions of one-proton and two-proton emissions. Totally five partial half-lives are adopted. In the current 2018

version, the theoretical decay modes are appeared in the same. These partial half-lives are listed for first-three shortest ones, however, the values are put only for the half-lives within 10^6 times longer comparing with the shortest one. These partial half-lives are ordered as p, 2p, f, β, and α for one-proton emission, two-proton emission, spontaneous fission, beta-decay and alpha-decay, respectively. See References [4-8] for the actual calculations.

Figure 2 shows an overview of the 2018 chart. The rectangle line corresponds to actual region of the chart in the sheet. The number of nuclides experimentally identified is totally 3,299, which includes 3,062 half-life-measured nuclides.

Transition of number of nuclides since 1976 obtained from the previous charts is shown in Fig. 3. In 1976, number of identified nuclides is less than 2,000. The number of nuclides increases, and almost reaches 3,300 in the current version of the chart.

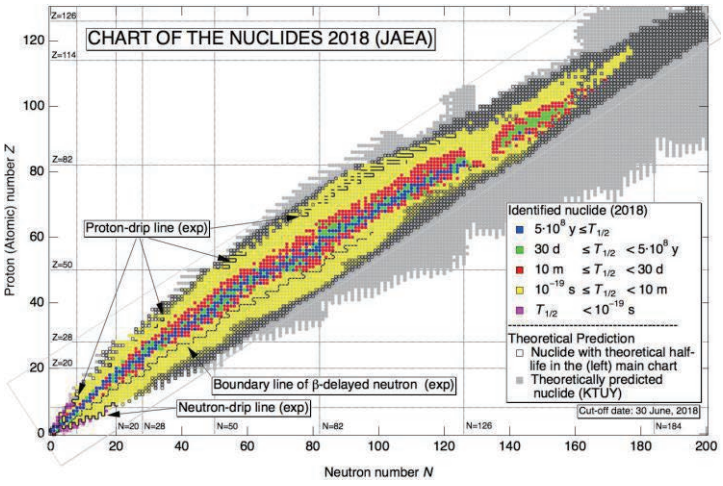

Figure 2: Overview of the 2018 chart.

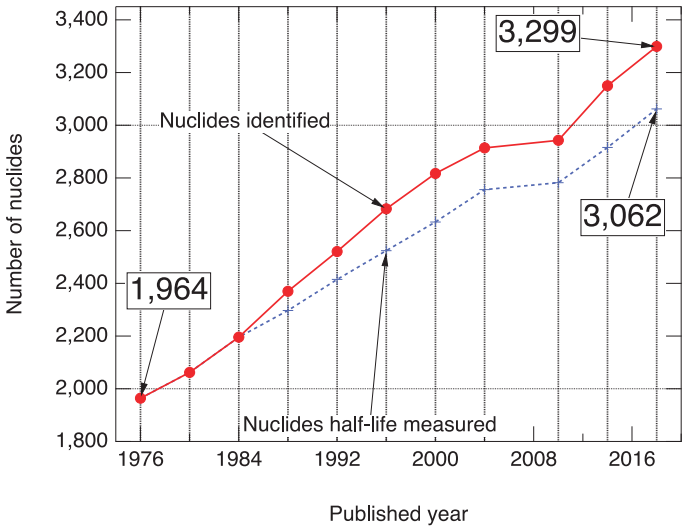

Figure 3: Transition of number of nuclides identified in the JAEA (JAERI) chart of the nuclide since 1976.

5. Periodic table of the element

Figure 4 is the summary of the periodic table of the element. From the previous periodic table, we remake the table with the use of the 2017 handbook of chemistry and physics [8]. In addition, the recent experimental results of the first ionization potentials are adopted. In the 2014 version, we adopted the first experimental data for technetium, astatine, and actinium [9-11]. In the 2018 version, we newly add the ionization potential for lawrencium, which was firtly measured in 2015

[12].

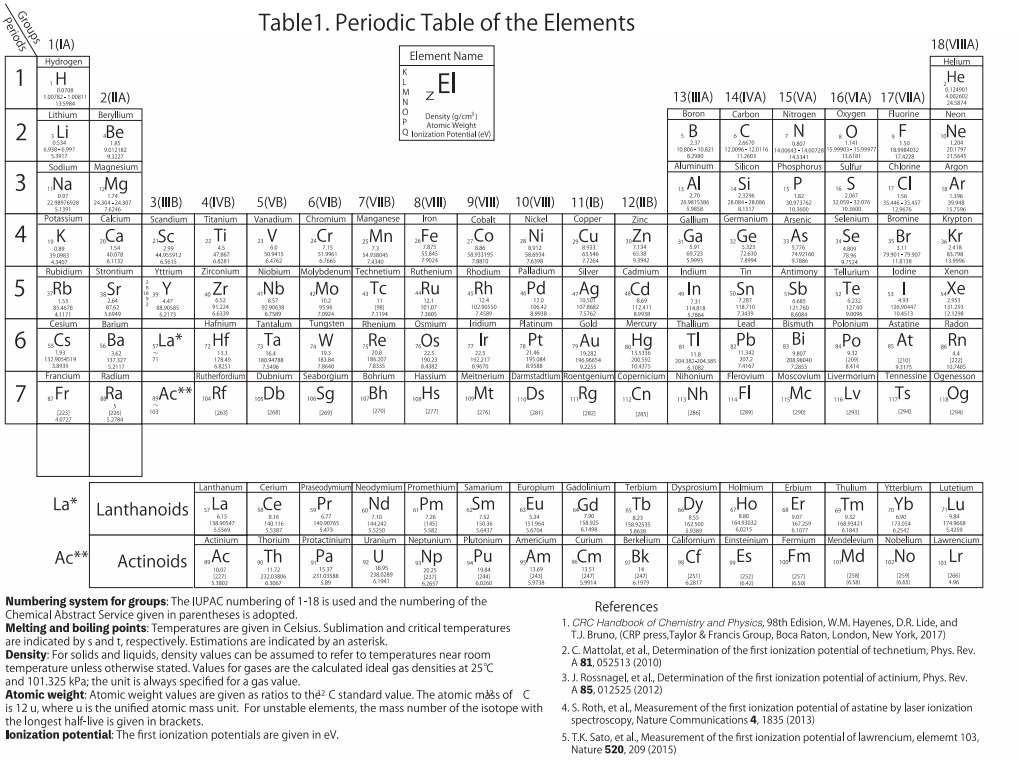

Figure 4: Periodic table of the elements. New element symbols, Nh (113th), Mc (115th), Ts (117th), and Og (118th) are shown.

6. Other data

In the sheets, we also put other quantities as listed in the section 2. The fundamental physical constants are adopted from the latest data, CODATA2014 [13]. The thermal neutron-capture and fission cross section for U-235 are adopted as a form of nuclear chart. The data are taken from JENDL-4.0 [14]. The cumulative fission yield from thermal neutron for ^{233,235}U and ^{239}Pu are also tabulated. The data are taken from JENDL FP Fission Yield Data File 2011 [15].

References

[1] H. Koura, J. Katakura, T. Tachibana and F. Minato, *Compilation of Chart of the Nuclides 2014, A comprehensive Decay Data*, JAEA-Conf 2015-003, pp.147-152 (2015).

[2] L. Ohrström, and J. Reedijk, *Names and symbols of the elements with atomic numbers 113, 115, 117 and 118 (IUPAC Recommendations 2016)*, Pure Appl. Chem., **88**, 1225–1229 (2016).

[3] M. Wang, G. Audi, F.G. Kondev, W.J Huang, S. Naimi, and X. Xu, *The AME2016 atomic mass evaluation (II), Tables, graphs and references,* Chinese Physics C **41**, 030003-1-442 (2016).

[4] H. Koura, T. Tachibana, M. Uno and M. Yamada, *Nuclidic mass formula on a spherical basis with an improved even-odd term*, Prog. Theor. Phys. **113**, 305-325 (2005), http://wwwndc.jaea.go.jp/nucldata/mass/KTUY04_E.html

[5] H. Koura, *Phenomenological formula for alpha-decay half-lives*, J. Nucl. Sci. Technol., **49**, 816-823 (2012).

[6] T. Tachibana, M. Yamada, Proc. Int. Conf. on exotic nuclei and atomic masses, Arles, 1995, *eds.* M. de Saint Simon and O. Sorlin (Editions Frontueres, Gif-sur-Yvette, 1995) p. 763, and references therein.
https://wwwndc.jaea.go.jp/nucldata/beta-decay-properties.pdf

[7] H. Koura, *Ground-state properties of heavy and superheavy nuclei predicted by nuclear mass models*, Tours symposium on nuclear physics V (AIP Conf. **704**, Melville, New York, 2004) pp. 60-69

[8] H. Koura and T. Tachibana, *How far does the area of superheavy element extend? – Decay modes of heavy and superheavy nuclei predicted by a mass formula*, BUTSURI (Bulletin of the Physical Society of Japan) **60**, pp. 717-724 (2005) (in Japanese).

[8] *CRC Handbook of Chemistry and Physics*, 98th Edition, W.M. Hayenes, D.R. Lide, and T.J. Bruno, (CRP press, Taylor & Francis Group, Boca Raton, London, New York, 2017).

[9] C. Mattolat, *et al.*, *Determination of the first ionization potential of technetium*, Phys. Rev. A **81**, 052513 (2010).

[10] J. Rossnagel, *et al.*, *Determination of the first ionization potential of actinium,* Phys. Rev. A **85**, 012525 (2012).

[11] S. Roth, *et al.*, *Measurement of the first ionization potential of astatine by laser ionization spectroscopy,* Nature Communications **4**, 1835 (2013).

[12] T.K. Sato, *et al.*, *Measurement of the first ionization potential of lawrencium, element 103*, Nature **520**, 209 (2015).

[13] P.J. Mohr, B.N. Taylor and D.B. Newell, *CODATA Recommended Values of the Fundamental Physical Constants: 2014*, J. Phys. Chem. Ref. Data **45**, 043102 (2016) and Rev. Mod. Phys. **88**, 035009 (2016).

[14] K. Shibata, *et al.*, *JENDL-4.0: A New Library for Nuclear Science and Engineering*, J. Nucl. Sci. Technol. **48**, 1-30 (2011).

[15] J. Katakura, *JENDL FP Decay Data File 2011 and Fission Yield Data File 2011*, JAEA-Data/Code 2011-025 (2012), 73p.

28 CHF+BCS CALCULATIONS FOR SUPERHEAVY $^{284}120$ NUCLEUS

KUN RATHA KEAN[1,2], TAKASHI NISHIKAWA[3], YORITAKA IWATA[1,*], AND SATOSHI CHIBA[1]

[1]TOKYO INSTITUTE OF TECHNOLOGY, TOKYO 152-8550, JAPAN
[2]JAEA, TOKAI, IBARAKI 319-1184, JAPAN
[3]NUCLEAR ENGINEERING LTD, OSAKA 550-0001, JAPAN

Abstract. Chemical elements with their proton numbers 119 and 120 correspond to the next unnamed chemical elements. For realizing the first synthesis of $Z = 120$ in experiments, the supportive theoretical result is an urgent issue. In this article, based on the constrained Hartree-Fock calculations with the BCS type paring interaction, the potential surface structure is studied by focusing on $^{284}120$ nucleus to provide a standard benchmark of the superheavy research.

1. Introduction

The synthesis of superheavy nuclei is a popular issue under the worldwide competition for the naming rights of new chemical elements. The nuclei with their proton number $Z = 120$ collect special attention since they are the next unnamed element at this point. By focusing on $^{284}120$ nucleus, the potential structure and some related physics is fully discussed by using widely-used SkM* interaction. This result will provide a standard property of superheavy region.

In this article, since the fission is an important process of de-excitation of superheavy nuclei, the potential structure along the symmetric fission channel is studied by the Constrained Hartree-Fock calculations with the BCS type pairing (CHF+BCS). Fission barrier height and their potential structure are shown for $^{284}120$ nucleus. The corresponding fission probability is calculated by the TDDFT + Langevin model [1, 2, 3, 4, 5].

2. Method

2.1. **Constrained Hartree-Fock+BCS theory.** For carrying out the density functional calculations, the constrained Hartree-Fock+BCS theory (CHF) is utilized to impose a constraint on the quadrupole-deformation. The master equation is obtained by the variational principle:

$$\delta \langle \psi | \mathcal{H} - \beta Q | \psi \rangle = 0,$$

where $\mathcal{H}$ means the Hamiltonian operator of many nucleon systems [6], the quadrupole parameter β plays a role of the Lagrangian multiplier for the quadrupole constraint βQ, and the trial function ψ is taken as the Slater determinant. In the obtained equation, the nuclear Skyrme interaction, the Coulomb interaction and the BCS-type pairing interactions are included at the level of one-body mean-field formalism (for textbooks, see [7, 8]). Each deformed state and the corresponding energy surface are obtained by choosing the values of β.

The calculation is performed by the SkyAX code [9] in which the quadrupole deformation is given on the three-dimensional Cartesian coordinate. In the SkyAx code, the octupole moment is optimized by adding a small octupole moment to the initial wave functions under the quadrupole constraint. Although the axial symmetry is assumed for the SkyAX calculations, it does not require anything more for the quadrupole constraint calculations. Indeed, the quadrupole-deformed nuclei can be fully described within the axial

Key words and phrases. Superheavy nuclei, fission barrier, CHF+BCS.
Numerical computation was carried out at a workstation system at Tokyo Institute of Technology (AEGIS system). This work was supported by JSPS KAKENHI Grant No. 17K05440.

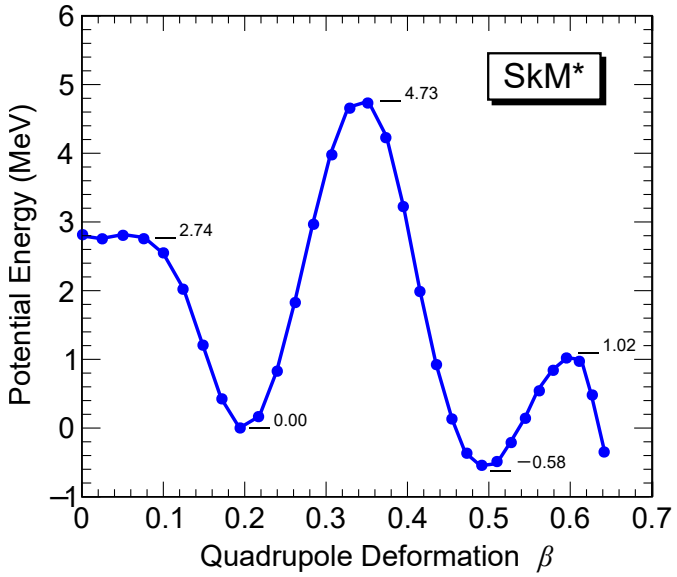

Figure 1. (Color online) The potential energy surface of $^{284}120$ nucleus calculated by CHF+BCS with SkM* interaction. Each point is obtained by imposing the quadrupole deformation, and lines are drawn to guide eyes. The zero point of the potential energy is taken as the minimum energy located at $\beta = 0.2$.

symmetric framework. A widely-used nuclear effective interaction SkM* [10] is employed with the density dependent-type pairing interaction.

2.2. **TDDFT+Langevin model.** The fission probability is obtained based on the TDDFT+Langevin model being introduced by Nishikawa *et al.* [5], where the terminology "TDDFT" stands for the time-dependent density functional theory. The detail of TDDFT+Langevin model is explained in Ref. [5]. The numerical code Sky3D [11] is employed for the TDDFT calculations, and the fission dynamics is calculated by 4D Langevin code [12]. In accordance with the CHF+BCS calculations, SkM* interaction is adapted to the TDDFT calculations. Both the stochastic aspect and microscopic aspect of fission dynamics are incorporated into the TDDFT+Langevin model. Furthermore it is advantageous with respect to the scientific progress that the fission probability is obtained in associated with certain Skyrme parameter sets.

3. Result

A superheavy nucleus $^{284}120$ is calculated by the CHF+BCS. The binding energy of the ground state is calculated to be 1962.3 MeV (6.9 MeV per nucleon). This value is quite small by comparing to a doubly-magic heavy nucleus (^{208}Pb: 7.9 and 7.9 MeV per nucleon for SkM* calculation and experiment [13], respectively), and to a typical heavy nucleus (^{236}U: 7.7 and 7.5 MeV per nucleon for SkM* calculation and experiment [13], respectively).

The calculated potential surface along the quadrupole deformation is shown in Fig. 1. The inner fission barrier height measured from $\beta = 0.2$ state is 4.7 MeV, and the outer barrier height measured from $\beta = 0.5$ state is 1.6 MeV. The inner barrier height is rather similar to those obtained for heavy nuclei, and the outer barrier height is significantly lower than those obtained for heavy nuclei; indeed, the inner barrier height of ^{236}U is 7.5 and 5.0 MeV per nucleon for SkM* calculation and experiment [14] respectively, and the outer barrier height of ^{236}U is 6.2 and 5.7 MeV per nucleon for SkM* calculation and experiment [14] respectively. On the other hand, the fission barrier is thin with its width $|\beta| = 0.1$ by measuring at almost half hight 2.4 MeV. Since this value is smaller than $|\beta| \sim 0.2$ calculated with SkM* for Uranium isotopes (for example, see Fig. 2 of [15]), more quantum tunneling towards the fission is expected in this case. It is remarkable that the flat dependence is found around the spherical state. More substantially, the roles of ground state and

fission isomer state are opposite in this case; the ground state is located at $\beta = 0.5$ in this case. Note that the fission barrier calculated by SkM* tends to be higher than the experimental values, one solution for this discrepancy is discussed in our recent work [15].

The double well structure is a typical potential structure for heavy nuclei. It is also found in case of superheavy ^{284}120. In particular, it is remarkable that the two wells have almost the same bottom energies, though it is not necessarily true for heavy nuclei. While the most stable state is located at $\beta = 0.5$, a larger well can be found at $\beta = 0.2$. That is, it is not easy to identify the ground state of ^{284}120. These states are expected to co-exist in a natural situation, and makes things more complicated. The two wells are definitely shallow as much as 3.0 MeV or 1.0 MeV depth. It simply tells us the difficulty of preserving ^{284}120 for a long time.

The corresponding fission probability is helpful to understand this complicated structure of superheavy ^{284}120 . According to the TDDFT + Langevin model, the fission probability of ^{284}120 is calculated as 39% for E/A =0.2 MeV. Although the fission probability of $Z = 120$ isotopes has been reported to be smaller for lower energies [4], the present fission probability is large enough for fission to be an efficient decay process of ^{284}120.

4. Summary

The potential surface of ^{284}120 along the symmetric fission channel is studied by the Constrained Hartree-Fock calculations with the BCS type pairing. It shows the potential with a double well structure with almost the same bottom energies. The inner fission barrier, which achieves almost the similar height by comparing to those of heavy nuclei, is rather thin, and the outer fission barrier is not so high as much as 1.0 MeV height. These facts are expected to make fission happen easily. Not only α decays, but also the fission can be main decay processes for ^{284}120. This conclusion is also supported by TDDFT+Langevin model calculations. As a conclusion, according to the potential structure, the co-existence of different deformed states are suggested in ^{284}120.

References

[1] T. Nishikawa, Y. Iwata, and S. Chiba, to appear in JAEA-Conf 2018-001(2018).
[2] T. Nishikawa, Y. Iwata, and S. Chiba, to appear in JAEA-Conf 2019-001(2019).
[3] T. Nishikawa, Y. Iwata, and S. Chiba, to appear in CERN report (2019).
[4] T. Nishikawa, Y. Iwata, and S. Chiba, to appear in Special issue, World Scientific (2019).
[5] T. Nishikawa, Y. Iwata, and S. Chiba, in preparation.
[6] D. Vautherin, and D. M. Brink, Phys. Rev. **C 5** 626 (1972).
[7] P. Ring, and P. Schuck, "The nuclear many-body problem", Springer-Verlag, 1980.
[8] W. Greiner, and J. A. Maruhn, "Nuclear Models", Springer-Verlag, 1996.
[9] P.-G. Reinhard, D.J. Dean, W. Nazarewicz, J. Dobaczewski, J. A. Maruhn, and M. R. Strayer, Phys. Rev. **C 60** 014316 (1999).
[10] J. Bartel, P. Quentin, M. Brack, C. Guet, and H.B. Hakansson, Nucl. Phys. **A 386**, 79 (1982).
[11] J. A. Maruhn, P.-G. Reinhard *et al.*, Comput. Phys. Commun. **185** 2195 (2014).
[12] M. D. Usang, F. A. Ivanyuk, C. Ishizuka, and S. Chiba, Phys. Rev. C **94** 044602 (2016).
[13] NuDat 2: https://www.nndc.bnl.gov/nudat2/
[14] RIPL-2: https://www-nds.iaea.org/RIPL-2/
[15] K. Kean, Y. Iwata, and S. Chiba, submitted; arXiv.

This is a blank page.

29

Neutron Induced Nonelastic Cross-sections below 50 MeV based on the Intranuclear Cascade Model

Masahiro Nakano[1,2] and Yusuke Uozumi[2]

[1]Junshin Gakuen University, Chikushigaoka, Minami-ku, Fukuoka, Japan

[2]Kyushu University, Motooka, Nishi-ku, Fukuoka, Japan

e-mail: nakano@med.uoeh-u.ac.jp

The intranuclear cascade (INC) model is generalized for an explanation of a low energy neutron induced nonelastic cross-section of ^{27}Al in two points. One is a method to construct the ground state of the target nucleus. The generalization of the ground sate brings a better energy dependence of the reaction cross-section. The other is a method of taking the effective two-body cross-sections between two nucleons, one of which exists in the nucleus. Our two body cross-sections, which are modified from free NN cross-sections as a result of medium effects, bring a satisfactory fit to the experimental data. It is concluded that the INC can be generalized to explain neutron induced nonelastic cross-sections in a low energy region from 10 MeV to 100 MeV.

1. Introduction

The intranuclear cascade (INC) model followed by the generalized evaporation model (GEM) explains well various reactions such as (p,p'x), (p,dx), (p,αx) in very wide energies and angles [1-4]. On the other hand, the INC model has not been applied to neutron induced reactions in the low energies below 50 MeV. Experimental data on the neutron induced nonelastic cross-sections in a range from 10 MeV to 100 MeV are taken for several target nuclei. The purpose of this paper is to generalize the INC model to apply to neutron induced nonelastic cross-sections in a low energy region below 100 MeV.

In this paper, we chose ^{27}Al as a target of our calculations since the data points below 100MeV are comparatively well determined [5] as shown in Fig.1.

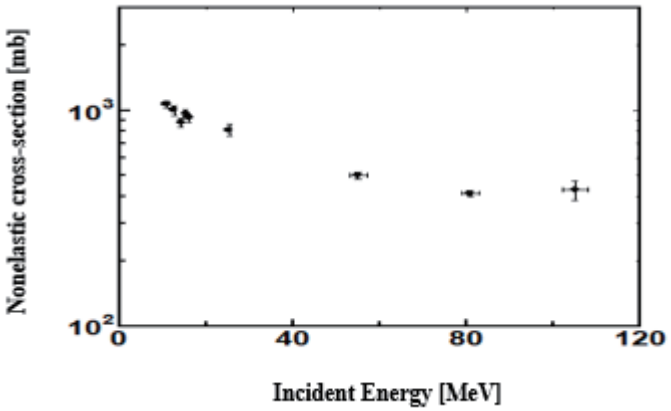

Fig.1 Experimental data of neutron induced nonelastic cross-section of ^{27}Al with error bars.

2. Generalizations in the INC Model

An explanation of INC model is available in Refs. [1-4]. The INC model has been developed for applications to higher energy collisions than 50 MeV. Therefore the straight forward application of INC to neutron induced reactions below 50 MeV does not reproduce the experimental data, thus it should be modified in few points. For the generalization, two considerations are necessary to reproduce the data. One point is how to make up the ground state of the target nucleus. The other point is how to select the nuclear two body cross-sections in such a low energy. We explain these two points in the following sections.

2.1 Constitution of the ground state

Usually, the ground state preparation is based on a random sampling both on the positions and momentums. On the positions of the particles in the nucleus, we use random numbers so as to reproduce the Wood-Saxon density distribution in a probabilistic way, while the momenta are randomly chosen so as to reproduce a uniform distribution. However, the nonelastic cross-section calculated using this ground state of the random sampling brings a peak around Ein =40 MeV as shown in Fig.2.

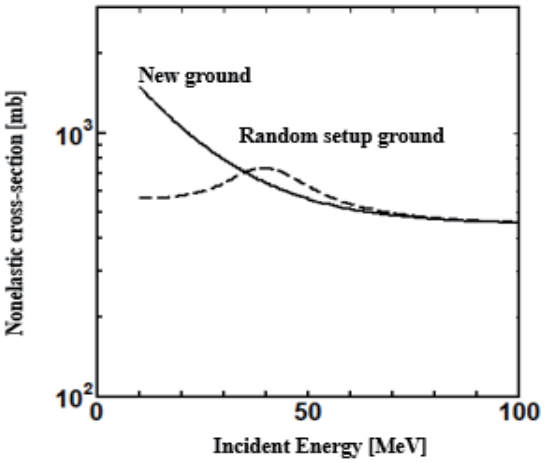

Fig.2 Nonelastic reaction cross-sections calculated with the ground state constructed by a random method (dashed line) and new one (solid line). The same two-body cross-section in eq.(6) is taken for both calculations.

In this work, we have chosen a new ground state based on the local dependent momentum. On the positions, the same procedure is taken as the random setup. Thus the density of radial direction is a Woods-Saxon distribution. On the other hand, the momenta are determined according to the effective nucleon mass at the particle position. The effective nucleon mass is determined by a local dependent formula,

$$M^*(r)=M+U(r). \quad (1)$$

where the potential U(r) has a Wood-Saxon shape, and the radius r_0=2.840 and the diffuseness a_0=0.569 are chosen from the experimental data of charge distribution of ^{27}Al by electron scattering experiments [6].
Using this effective nucleon mass, the maximum momentum at r is given by

$$\mathrm{P}_{max}(\mathrm{r}) = \sqrt{\mathrm{E}_f^2 - \mathrm{M}^*(\mathrm{r})^2} \tag{2}$$

where $\mathrm{E_f}$ is the Fermi energy. The momenta of particles are determined by random numbers, which are chosen in a probabilistic way from zero to the maximum momentum $\mathrm{P_{max}(r)}$. As a result, the new ground state has nucleons with a smaller momentum in the peripheral of target. This brings a completely different curvature in the total reaction cross-sections from the calculated result of the random setup in low energies below 70 MeV as shown in Fig.2.

2.2 Effective two body cross-sections between two nucleons

Originally, Cugnon *et a*l. [7] shows a set of parameters of the total reaction cross-sections of two nucleons including elastic cross-sections, which is shown by dashed curves in Fig.3. The two-body cross-sections S are expressed by the following equations for each energy interval:

$$\begin{aligned}
&for \quad pp \\
&\quad \mathrm{S} = 41 + 60(p_G - 0.9)\exp(-1.2p_G) && for\ 1.5GeV/c < p_G < 5GeV/c \\
&\quad \mathrm{S} = 23.5 + 24.6/(1 + \exp(-(p_G - 1.2)/0.1)) && for\ 0.8GeV/c < p_G < 1.5GeV/c \\
&\quad \mathrm{S} = 23.5 + 1000(p_G - 0.7)^4 && for\ p_G < 0.8GeV/c \\
&for \quad pn \\
&\quad \mathrm{S} = 42 && for\ p_G > 2GeV/c \\
&\quad \mathrm{S} = 24.2 + 8.9\ p_G && for\ 1GeV/c < p_G < 2GeV/c \\
&\quad \mathrm{S} = 33 + 196\,\mathrm{abs}(\ p_G\ - 0.95)^{2.5} && for\ p_G < 1GeV/c
\end{aligned} \tag{3, 4}$$

where p_G is the relative momentum in the unit of GeV/c.

The INC model calculations using above two body cross-sections explained well various experimental data in a higher energy region [1-4]. However, on the experimental total cross-sections, the calculations using Cugnon's underestimate in the low energy region as shown Fig.4.

Cugnon *et al*. introduced improved two body cross-sections given by following equations for better fits to low energy phenomena. The low energy parts are replaced in the momentum region for p_G<0.4 *GeV/c*. They say that this interaction was made to reproduce the free NN cross-sections, and is valid down to p_G=0.1 *GeV/c.*

$$\begin{aligned}
&\mathrm{S} = 34(\ p_G\ /0.4)^{-2.104} && for \quad pp \\
&\mathrm{S} = 6.3555\ {p_G}^{-3.2481}\ \exp(-0.377(\ \ln p_G)^2\ ) && for \quad pn
\end{aligned} \tag{5}$$

The defect of these two body cross-sections is that the derivatives of the energy dependence of the cross-sections have jumps at the junctions since the two body cross-sections are given separately for each interval of energy, and furthermore the value itself jumps at p_G=0.4 *GeV/c*.

The INC model calculations using the improved two body cross-sections by Cugnon overestimate the data as

shown in fig.4. Therefore we introduced a new set of effective two body cross-sections. Our two body cross-sections are a smooth function, since they consist of a sum of continuous functions. There are many possibilities to express the functions. One example of the expression is given for $p_G < 2GeV/c$ as follows:

$$S = (Y1 + Y2)(0.19 + 0.81/(1 + \exp(-(p_G - 0.8)/0.3))) + 0.36\,Y3 \quad (6)$$

where the functions $Y1, Y2$ and $Y3$ are given as follows:

$$\begin{aligned} &for \quad pp \\ &Y1 = 250\exp(-p_G{}^{1.2}/0.1) \\ &Y2 = 26.5/(1+\exp(-(p_G - 1.178)/0.122)) + 22 \\ &Y3 = 3300\exp(-p_G{}^{0.8}/0.07) + 80000\exp(-p_G{}^{0.86}/0.02) \end{aligned} \quad (7)$$

$$\begin{aligned} &for \quad np \\ &Y1 = 67\exp(-(p_G - 0.12)^2/0.15) \\ &Y2 = (10\ p_G + 23)(1+0.2\exp(-(p_G - 0.5)/0.15)) \\ &Y3 = 8000\exp(-p_G/0.064) \end{aligned} \quad (8)$$

These two body cross-sections are smaller than the two body cross-sections by the Improved Cugnon in the momentum range smaller than 1.5 *GeV/c* as shown in Fig.3. This implies that the free cross-sections are reduced as a result of the medium effects in the nuclear matter, since the interaction of the particle inside nucleus is considered to be modified. The calculated result using the proposed two body cross-sections reproduce well the experimental data of neutron total reaction cross-section as is shown in Fig.4. The sharp curvature of this calculation well fits the data in the energy region less than 50 MeV.

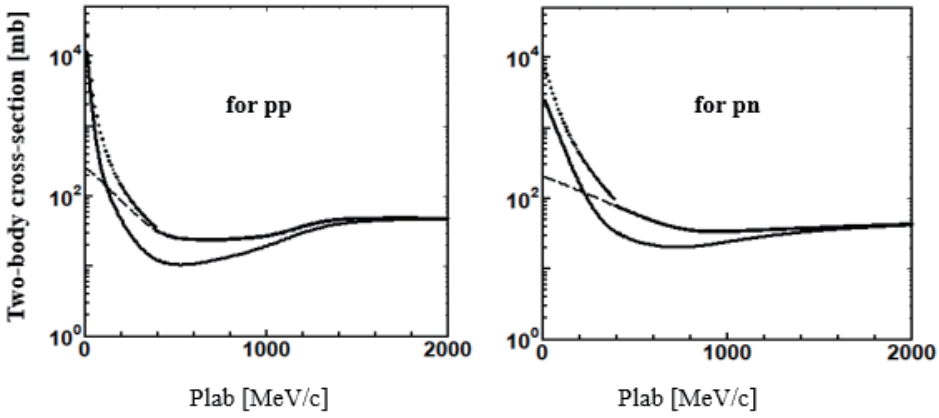

Fig.3 Two-body cross-sections for pp (left) and pn (right). Ours (solid) in eq.(6) are illustrated together with Cugnon (dashed) in eqs.(3) and (4) and improved Cugnon (dotted) in eq.(5).

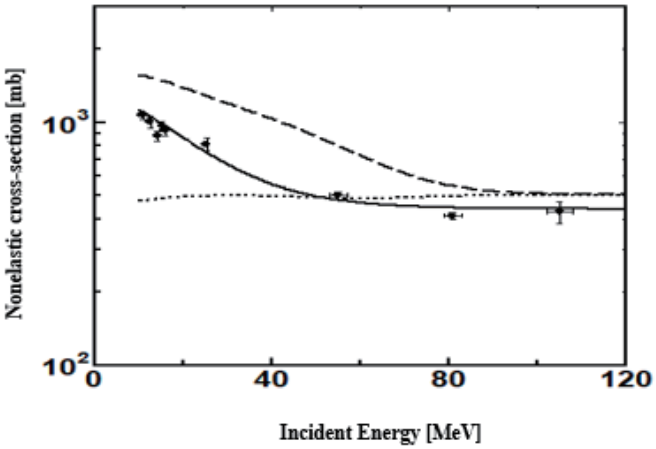

Fig.4 Nonelastic cross-sections calculated by Cugnon (dotted), improved Cugnon (dashed) and ours(solid curve). The black dot is experimental data point from 10 MeV to 120 MeV[5].

3. Discussions

The INC model is not a phenomenological fitting model, but a kind of dynamic model, which traces sequential collisions of two nucleons inside the target nucleus. The collisions are treated in a relativistic way. Therefore, all the reaction processes are counted explicitly in the INC model.

Our calculation includes (n,x) reactions, where x=n, p, 2p, 3p, … and so on, furthermore it includes contributions from 3 processes occurring inside the nucleus. One is the collective excitations of nucleus whose excitations are confined within one major shell [2]. The incident nucleon excites the collective states of the target nucleus. This process is important relatively in a low energy region. The second is the contribution from the giant quadrupole resonance (GQR) whose excitations are over one major shell. The third is the contribution from (n,d) reactions. This includes proton pickup reactions and d-knockout reactions. The contributions from these processes are at most 25 percent in these energy region as shown in Fig.5. The INC model includes the effect of the Pauli blocking. The nucleons in the target nucleus exist below Fermi sea inside the nuclear potential. The process is forbidden when the energy of any scattered particle is below Fermi sea. This is the Pauli blocking in the INC model.

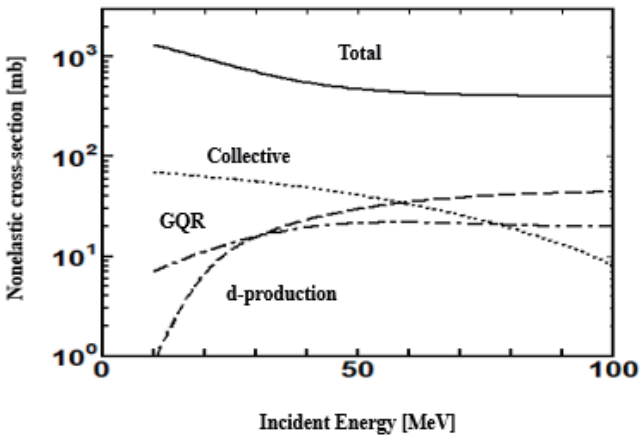

It is interesting that there is a big difference between low energy reactions and high energy ones. In a low momentum region, the two body cross-sections have a very long range, for example, over 10fm in the range of p<50MeV/c. It is longer than the radius of Al (r_0=2.84 fm). Then the incident neutron can interact from the outside of the nucleus. This contributes to bring a sharp curvature in the energy dependence of the total reaction.

Fig.5 Contributions from 3 processes; collective excitations, giant quadrupole resonance (GQR) and deuteron productions.

4. Conclusion

In order to explain neutron induced nonelastic cross-sections, the INC model has been generalized in two points. One is the way of making the ground states of the target nucleus. The other is the effective cross-sections of two nucleons. The INC model calculations using the two sets of two body cross-sections proposed by Cugnon cannot reproduce the experimental data of the total reaction cross-section of ^{27}Al. One, which is used for higher energy region, underestimates the data at the low incident energy, and the other, which reproduces the free NN cross-sections, overestimates the data. We proposed the new effective two body cross-sections which is similar to the two body cross-sections proposed by Cugnon. Our two body cross-sections are a little weak in lower momentum region compared with the free NN cross-sections. This implies the two-body cross-section in the nuclear matter should be weaken from the free one in low energy collisions as a result of medium effects, while unchanged in high energy collisions. The INC model generalized in this way can explain neutron induced nonelastic cross-sections in the low energy region from 10 MeV to 100 MeV.

Acknowledgements

We are grateful for Dr. Yuji Yamaguchi and Dr. Gaku Watanabe, who continuously supported this work.

References

[1] Yusuke Uozumi, Yusuke Sawada, Aleksandre Mzhavia, Sho Nogamine *et a*l.: “Deuteron-production double-differential cross sections for 300- and 392-MeV proton-induced reactions deduced from experiment and model calculation”, Physical Review C, 84, 064617, 1-11, (2011).

[2] Yusuke Uozumi, Takahiro Yamada, Sho Nogamine, Masahiro Nakano: “Intranuclear cascade model including collective excitations and trajectory deflections for (p,p'x) reactions around 50 MeV”, Physical Review C ,86,034610, 1-7, (2012).

[3] Yusuke Uozumi, Taiki Mori, Akifumi Sonoda, Masahiro Nakano: “Extended Intranuclear Cascade model for pickup reactions induced by 50-MeV-range protons”, The proceedings of the fifth international workshop on Compound-Nuclear Reactions and Related Topics (CNR*15), EPJ Web of Conferences 122, 04001 (2016).

[4] Yusuke Uozumi, Yuji Yamaguchi, Gaku Watanabe, Yuki Fukuda, Ryota Imamura, Monira Jannatul Kobra, and Masahiro Nakano: “Direct pickup and knockout processes in inclusive (p,dx) reactions at 42-392MeV”, Phys. Rev. C97, 034630, 1-7 (2018).

[5] EXFOR Experimental Nuclear Reaction Data: https:// www-nds.iaea.org/exfor/exfor.htm.

[6] H.De.Vries, C.W.De Jager and C.De Vries, "Nuclear Charge-Density-Distribution Parameters From Elastic Electron Scattereing", Atomic Data and Nuclear Data Table 36, 495-536 (1987).

[7] J. Cugnon, D.L.Hote, J.Vandermeulen: “Simple parametrization of cross-sections for nuclear transport studies up to the GeV range”, Nucl. Instr. and Meth. B111, 215 (1996).

30

Problems of TENDL-2015 official ACE files

Chikara Konno[1], and Saerom Kwon[2]
[1]Japan Atomic Energy Agency
[2] National Institutes for Quantum and Radiological Science and Technology
Email: konno.chikara@jaea.go.jp

Recently we tested the official ACE files of TENDL-2015 and found the following problems in the files,

- no p-table data except for those of ^{235}U, ^{235m}U and ^{238}U in the neutron sub-library,
- no secondary gamma data for a lot of nuclei in the neutron, proton, deuteron, triton, He-3, and alpha sub-libraries.

By a simple calculation, it was demonstrated that effects of the issues were not so small as follows,

- the effect of no unresolved resonance data in ACE files was large in a special case as pure niobium,
- secondary gammas produced in neutron-gamma coupling MCNP calculations were not correct because wrong data were used as secondary gamma data.

The issues were probably caused by simple mistakes of NJOY processing. Note that the issues also occur partially in the official ACE files of TENDL-2017.

1. Introduction

TENDL (TALYS-based Evaluated Nuclear Data Library) [1] is a nuclear data library which is mainly produced with the TALYS code [2]. It is notable that TENDL-2015 (TENDL released in 2015) [3] contains sub-libraries of neutron, gamma, proton, deuteron, triton, He-3 and alpha injections for nuclei more than 2800, up to 200 MeV, with covariance data. TENDL has been used as a standard nuclear data library worldwide, particularly in Europe. Since 2016 we also have used the official ACE (A Compact ENDF) files [3] of TENDL-2015 for our study, where we found the following two problems.

1) There are no probability table (p-table) data in the neutron sub-library ACE files of most of the nuclei with unresolved resonance data.
2) There are no secondary gamma data in a lot of the ACE files not only of the neutron sub-library but also of the proton, deuteron, triton, He-3, and alpha sub-libraries.

We investigate these issues and demonstrate their effects in detail.

2. Problem of no probability table

A lot of nuclei (2513 nuclei) in the neutron sub-library of TENDL-2015 have unresolved resonances, where averaged resonance parameters are given in nuclear data libraries, as shown in Fig. 1. The unresolved resonance data are also important for the self-shielding effect in shielding analyses. However, there are no p-table data of unresolved resonances in the official ACE files of the neutron sub-library except for three nuclei (^{235}U, ^{235m}U and ^{238}U). Thus, the self-shielding correction in the unresolved resonance

region is incomplete if most of the official ACE files are used. The effect of no unresolved resonance data in the ACE files of the TENDL-2015 neutron sub-library was demonstrated with a simple test; we calculated and compared neutron spectra inside a natural niobium (a mono-nuclidic element with unresolved resonance data) sphere of 1 m in radius with a 20 MeV neutron source at the center as shown in Fig. 2 by using the MCNP [4] code with the official ACE file (without p-table data) and JAEA TENDL-2015 ACE file (with p-table data, processed by using NJOY2012.50 [5]). The calculated neutron spectra at 50 cm from the niobium sphere center are shown in Fig. 3. The effect of no p-table data is large in a special case such as this calculation. The solution of this issue is easy, just to use the PURR module of the NJOY code in the processing, though it takes time.

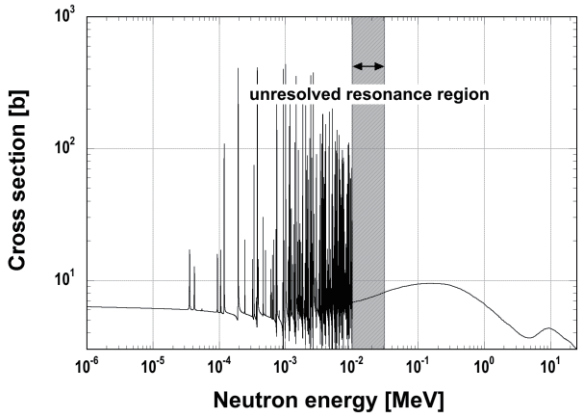

Fig. 1 Total cross section of ^{93}Nb in TENDL-2015

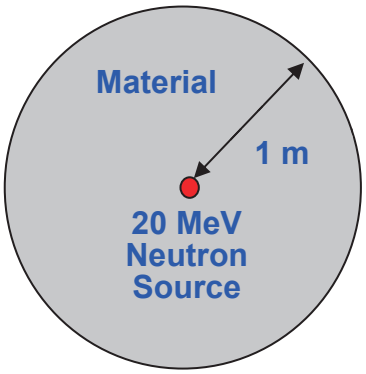

Fig. 2 Calculation model

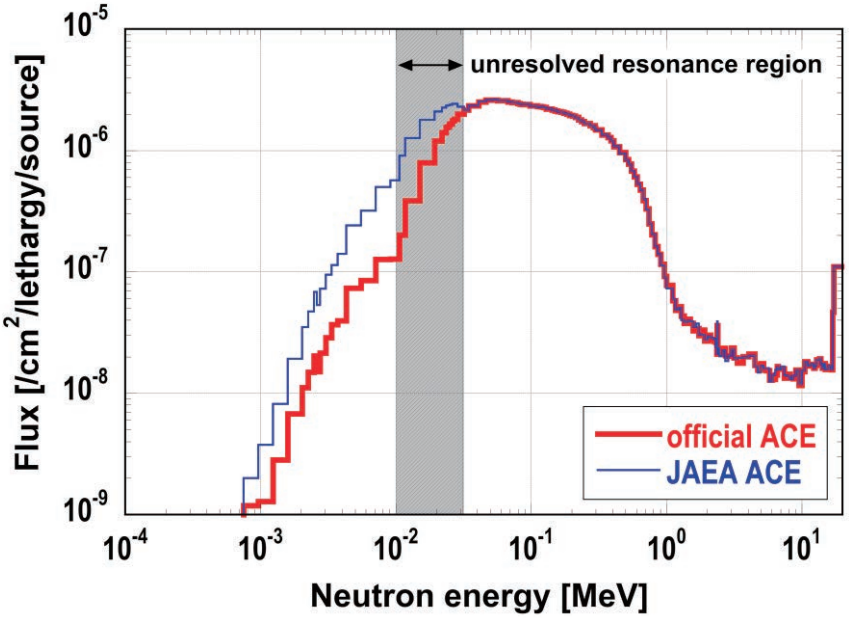

Fig. 3 Neutron spectra at 50 cm from niobium sphere center

3. Problem of no secondary gamma data

The secondary gamma data are required in neutron-gamma coupling calculations. However, there are no secondary gamma data in the official ACE files of the neutron sub-library except for 13 nuclei (^{1}H, ^{2}H, ^{6}Li, ^{7}Li, ^{9}Be, ^{10}B, ^{11}B, ^{12}C, ^{14}N, ^{15}N, ^{16}O, ^{19}F and ^{239}Pu). Thus, secondary gammas are not produced in neutron-gamma coupling MCNP calculations with the official ACE files. In order to demonstrate this effect, neutron and gamma spectra inside a natural iron (a typical structural material) sphere of 1 m in radius with an isotropic neutron source of 20 MeV at the center (Fig. 2) were calculated with MCNP by using the official ACE file (without secondary gamma data) and JAEA TENDL-2015 ACE file (with secondary gamma data, processed by using NJOY2012.50) files. Figure 4 shows the calculated neutron spectra at 50 cm from the iron sphere, where the both spectra are the same. On the contrary, the calculated gamma spectrum with the official ACE file at 50 cm from the iron sphere is a strange shape and is drastically different from that with the JAEA ACE file as shown in Fig. 5. Strange to say, the MCNP calculation with the official ACE file produces gamma despite no secondary gamma data in the official ACE file. We examined the official ACE files in more detail and found that MCNP misused particle production data (mt=5 data) as secondary gamma data and produced wrong secondary gammas with the particle production data. If the particle production data in the ACE file are set to 0.0, no secondary gammas are produced in the MCNP calculation.

We guessed the reason of no secondary gamma data in the official ACE files.

- "iopp" (input parameter for "detailed photons", 0=no, 1=yes) in the ACER input of NJOY2012 was set to 0, which required obsolete 20x30 photon matrix data. Probably the obsolete 20x30 photon matrix data were not supplied in the NJOY processing. Thus, only gamma production cross section data were included in the official ACE files, but outgoing photon energy data (secondary gamma data) were not included.
- It is not known why iopp=0 was used in processing of TENDL-2015.

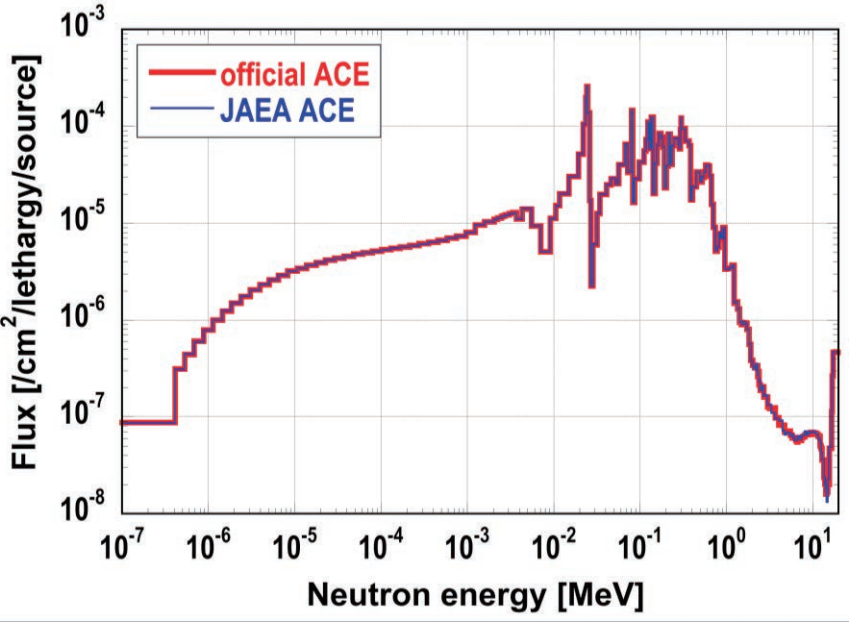

Fig. 4 Neutron spectra at 50 cm from iron sphere center

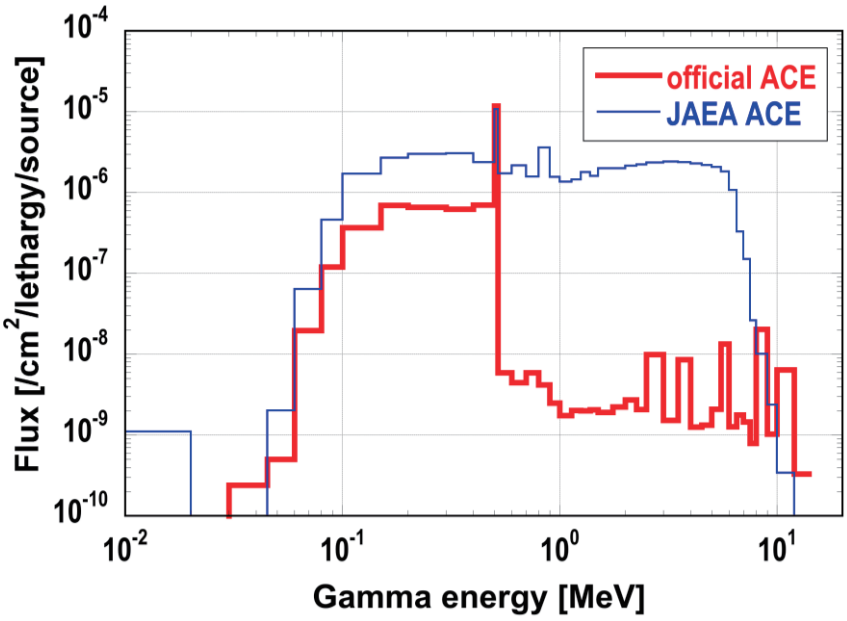

Fig. 5 Gamma spectra at 50 cm from iron sphere center

It is noted that this issue also occurs in the official ACE files of the proton, deuteron, triton, He-3, and alpha sub-libraries.

4. TENDL-2017

We reported the issues of the TENDL-2015 official ACE files to the TENDL developers in 2017 and expected that the issues would be improved in the next version TENDL. The latest TENDL, TENDL-2017 [6], was released in the end of 2017 with the official ACE files. However, the official ACE files had the same problems first. The ACE files of main nuclei (556 nuclei for the neutron sub-library and 283 nuclei for the proton sub-library) were improved in March, 2018. In the end of 2018, there exist two different ACE files of the main nuclei in the web site of TENDL-2017 [6]; one is a correct one in a tar file (see a box in Fig. 6) and the other is a wrong one with the issues in an individual file (see a box in Fig. 7). We are so afraid that users use not only the correct ACE files but also the wrong ones because of no announcement for the issues in the web site of TENDL-2017.

5. Summary

We found that the official ACE files of TENDL-2015 had no unresolved resonance data in the neutron sub-library except for those of ^{235}U, ^{235m}U and ^{238}U and no secondary gamma data in a lot of the ACE files not only of the neutron sub-library but also of the proton, deuteron, triton, He-3, and alpha sub-libraries. Thus, the effects and reasons of the issues were examined. The effect of missing unresolved resonance data in ACE files was large in a special case as pure niobium. Secondary gammas produced in neutron-gamma coupling MCNP calculations were not correct because wrong data were used as secondary gamma data. We suggested that the issues were due to inadequate NJOY processing. It is noted that these issues also occur partially in the official ACE files of the latest TENDL, TENDL-2017.

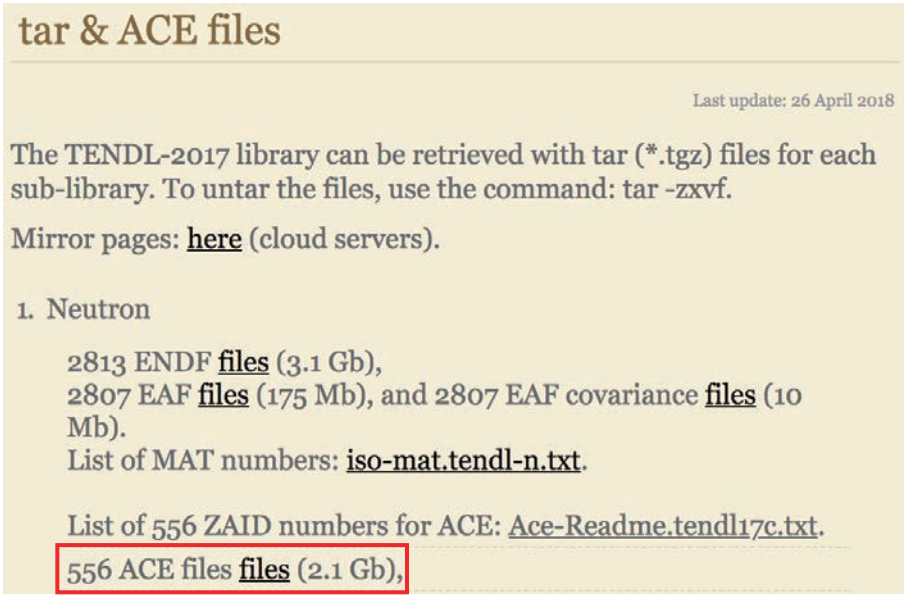

tar & ACE files

Last update: 26 April 2018

The TENDL-2017 library can be retrieved with tar (*.tgz) files for each sub-library. To untar the files, use the command: tar -zxvf.

Mirror pages: here (cloud servers).

1. Neutron

2813 ENDF files (3.1 Gb),
2807 EAF files (175 Mb), and 2807 EAF covariance files (10 Mb).
List of MAT numbers: iso-mat.tendl-n.txt.

List of 556 ZAID numbers for ACE: Ace-Readme.tendl17c.txt.
556 ACE files files (2.1 Gb),

Fig. 6 A part of https://tendl.web.psi.ch/tendl_2017/tar.html

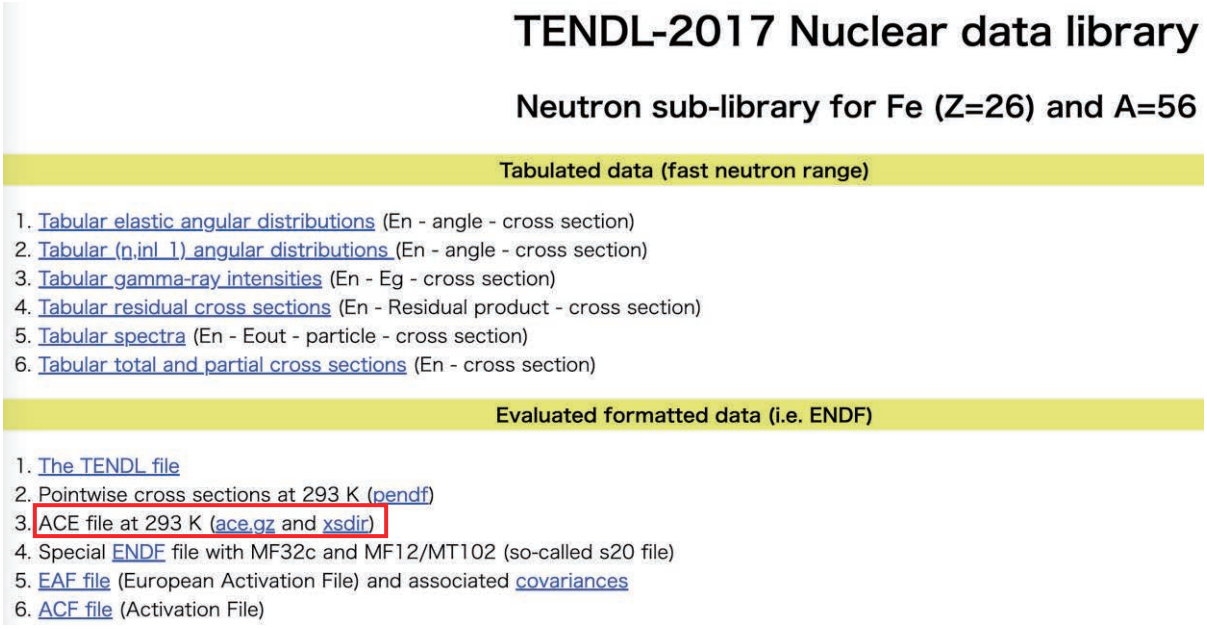

TENDL-2017 Nuclear data library

Neutron sub-library for Fe (Z=26) and A=56

Tabulated data (fast neutron range)

1. Tabular elastic angular distributions (En - angle - cross section)
2. Tabular (n,inl_1) angular distributions (En - angle - cross section)
3. Tabular gamma-ray intensities (En - Eg - cross section)
4. Tabular residual cross sections (En - Residual product - cross section)
5. Tabular spectra (En - Eout - particle - cross section)
6. Tabular total and partial cross sections (En - cross section)

Evaluated formatted data (i.e. ENDF)

1. The TENDL file
2. Pointwise cross sections at 293 K (pendf)
3. ACE file at 293 K (ace.gz and xsdir)
4. Special ENDF file with MF32c and MF12/MT102 (so-called s20 file)
5. EAF file (European Activation File) and associated covariances
6. ACF file (Activation File)

Fig. 7 A part of https://tendl.web.psi.ch/tendl_2017/neutron_html/Fe/NeutronFe56.html

References

[1] A.J. Koning and D. Rochman, Modern Nuclear Data Evaluation With The TALYS Code System, Nuclear Data Sheets **113** (2012) 2841-2934.

[2] http://www.talys.eu/home/ (current as of Jan. 2019).

[3] https://tendl.web.psi.ch/tendl_2015/tendl2015.html (current as of Jan. 2019).

[4] X-5 Monte Carlo Team, MCNP - A General Monte Carlo N-Particle Transport Code, Version 5, LA-UR-03-1987 (2005).

[5] A.C. Kahler, *et al*, The NJOY Nuclear Data Processing System, Version 2012, LA-UR-12-27079 (2012).
[6] https://tendl.web.psi.ch/tendl_2017/tendl2017.html (current as of Jan. 2019).

31 Gamow-Teller Strength Distribution of Nickel Isotopes with Odd Number of Neutron

Futoshi Minato[1]
[1]Nuclear Data Center, Japan Atomic Energy Agency, Tokai 319-1195, Japan
Email: minato.futoshi@jaea.go.jp

We study the effect of particle vibration coupling (PVC) on Gamow-Teller transitions of nickel isotopes with the odd number of neutron. The single particle bases are calculated by the Skyrme HFB and the vibrational phonons are obtained by using the QRPA. Our calculation clarifies the PVC gives a remarkable change in spectroscopic factors of a single particle level and GT distributions. The β-decay half-lives of nickel isotopes are calculated and it turns out that the odd-even straggling found in a calculation of the independent particle model is slightly mitigated.

1. Introduction

Mean-field theory and its expansion to superfluid states such as Hartree-Fock-BCS (HFBCS) and Hartree-Fock-Boboliubov (HFB) theories are a powerful tool to investigate the ground state properties of light to heavy nuclei. However, most of study using them targets even-even nuclei one hand, there are much fewer works on odd-even and odd-odd nuclei (hereafter odd nuclei) on the other hand. This is because the calculation of even-even nuclei is much easier than that of odd nuclei; for even-even nuclei, time reversal symmetry can be assumed due to the spin-parity $J^{\pi} = 0^{+}$ in the ground state and time-odd terms in the mean-field are vanished accordingly. By utilizing the fact, we can reduce computational tasks considerably. If one wants to study odd-nuclei, blocking effect in pairing correlation and the time-odd terms in the mean-field has to be considered. The situation remains the same in calculating excited states by using quasiparticle-random-phase-approximation (QRPA) which uses the HFBCS or HFB as the wave-function basis. These complications attributed from the calculation of odd nuclei are a big barrier to perform a systematical calculation, for example, of mass, γ-strength function, and β-decay of nuclei in the nuclear chart, which are relevant to studies of r-process and nuclear data evaluation of unstable nuclei.

To avoid the computational problems concerning odd nuclei approximately, a simple approach called equal filling approximation (EFA) has been suggested. The EFA has been applied for various studies of odd nuclei. This approximation has been compared with the exact blocking method, and it turned out that the EFA was able to provide a very close result to the exact blocking method [1]. Using the EFA, a systematical investigation of β-decay was recently performed [2].

Besides the EFA, one may assume that odd mass nuclei are composed of even-even core and valence nucleon(s). In this sense, odd-nuclei is depicted by a cluster model, and one has to consider an interaction between the core and valence nucleon(s), which induces a polarization effect to the core nucleus. In contrast, the EFA is based on the picture of the mean-filed theory. To describe the core polarization effects, particle vibration coupling (PVC) is frequently used. The PVC is applied to many research interests, however, there is no work to study its effect along with isotopes systematically to my knowledge. In this study, we focus on the Gamow-Teller (GT) transition of nickel isotopes aiming at future application to β-decay.

The contents of this paper are the following. Section 2 describes the effect of PVC briefly and Sec. 3 demonstrates theoretical framework. The result is discussed in Sec. 4 and the summary and the future perspectives are given in Sec. 5.

2. Coupling of Valence Particle and Core Phonon

Let us consider a system composed of one even-even core nucleus and one valence nucleon. The valence nucleon is at an orbit of discrete state (the lowest level above the Fermi energy) of the mean-field potential produced by the even-even core. If there is no interaction between the core and the nucleon, the core remains the ground state and the nucleon also stays at the lowest orbit above the Fermi energy forever. This picture is exactly the same as the independent particle model (IPM). In a practical case, however, there exists a residual interaction, which wasn't taken into account in the mean-field theory, between the core and the nucleon. Provided that a residual interaction is present, the nucleon is scattered into higher orbits and the core is excited both vibrationally and rotationally. Then, the valence nucleon occupies various orbits. The perturbation due to the residual interaction between the core and the nucleon is not properly included in the EFA. A schematic picture of the PVC effect on the spectroscopic factor of $s_{1/2}$ states is illustrated in Fig. 1.

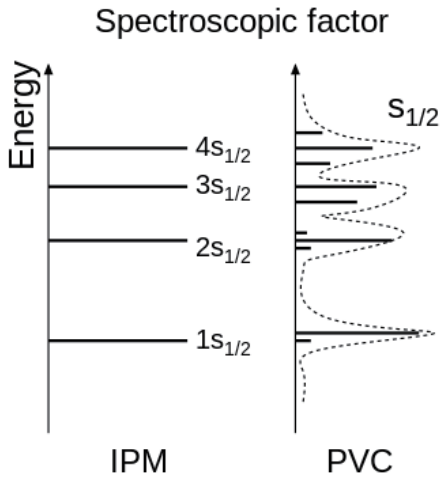

Fig.1: A schematic picture of the PVC effect on the spectroscopic factor of $s_{1/2}$ states.

3. Theoretical Framework

The model Hamiltonian of this study is

$$H = \frac{\vec{p}^2}{2\mu} + V(\vec{r}) \ldots (1),$$

where μ is the reduced mass and p is the momentum of the valence particle. The potential $V(\vec{r})$ is given in the form

$$V(\vec{r}) = V_{static}(\vec{r}) + \sum_{\nu,c=IS,IV,CX} \int \frac{\delta V}{\delta \rho_c}(\vec{r} - \vec{r}')\delta\rho_{\nu,c}(r')d\vec{r}' \ldots (2).$$

The first term of Eq. (2) is the static potential and the second term is the dynamic potential which

governs core vibrational effects. If we omit the second term, the framework corresponds to the IPM. The single particle states are calculated by Skyrme HFB with the SGII [3] interaction. We assume the unperturbed states are

$$H_0 \equiv \left(\frac{\vec{p}^2}{2\mu} + V_{static}(\vec{r})\right)\varphi(\vec{r}) = \varepsilon\varphi(\vec{r}) \ldots (3).$$

The continuum states are discretized by introducing a boundary box size 30 fm and the calculation was carried out by a step size $dr = 0.1$ fm. We assume the core nuclei (^{70,72,74,76}Ni) are spherical, so that we did not take into account the coupling with rotational collective modes.

The residual interaction $\delta V/\delta\rho_c$ can be derived from the second derivative of energy density with respect to densities. However, it is complicated to calculate it, so that we approximate it with the Landau-Migdal force [4] given as

$$\frac{\partial V}{\partial \rho_{IS}} = \left(\frac{3}{4}t_0 + \frac{t_3}{16}(\alpha+1)(\alpha+2)\rho^\alpha(r) + \frac{1}{8}k_f^2\left(3t_1 + t_2(5+4x_2)\right)\right)\delta(\vec{r}-\vec{r}') \ldots (4)$$

$$\frac{\partial V}{\partial \rho_{IV}} = \left(-\frac{t_0}{4}(1+2x_0) - \frac{t_3}{24}(1+2x_3)\rho^\alpha(r) + \frac{1}{8}k_f^2\left(t_2(1+2x_2) - t_1(1+2x_1)\right)\right)\delta(\vec{r}-\vec{r}') \ldots (5)$$

$$\frac{\partial V}{\partial \rho_{CX}} = -\frac{1}{4}t_0 - \frac{1}{24}t_3\rho^\alpha(r) + \frac{1}{8}k_f^2(t_2 - t_1) \ldots (6),$$

where $t_0, t_1, t_2, t_3, \alpha$ are the conventional Skyrme parameters (see [4]). Phonon states are calculated by the QRPA in the canonical basis, where the phonon creation operator is given by

$$Q_\nu^\dagger = \sum_{kk'} X_{kk'}^\nu \alpha_k^\dagger \alpha_{k'}^\dagger - Y_{kk'}^\nu \alpha_k^\dagger \alpha_{k'}^\dagger \ldots (7).$$

We define the QRPA ground state as $\Phi^{L=0}(\xi, \nu = 0)$ and the phonon state is then described by $\Phi^{L_\nu}(\xi, \nu) = \mathrm{Q}_\nu^\dagger \Phi^0(\xi, 0)$, where ξ is the degree of freedom of the core nucleus. The QRPA coefficients are obtained by solving the QRPA equation,

$$\begin{pmatrix} A & B \\ -B^* & -A^* \end{pmatrix}\begin{pmatrix} X^\nu \\ Y^\nu \end{pmatrix} = E_\nu \begin{pmatrix} X^\nu \\ Y^\nu \end{pmatrix} \ldots (8).$$

The transition density is defined as

$$\delta\rho_{\nu,c}(r) = \sum_{kk'}(X_{kk'} + (-1)^{L_\nu}Y_{kk'})(u_k v_{k'} + (-1)^{L_\nu} v_k u_{k'})\varphi_k\varphi_{k'}\langle k||F||k'\rangle \ for\ c = IS, IV \ldots (9)$$

$$\delta\rho_{\nu,c}(r) = \sum_{kk'}(u_k v_{k'} X_{kk'} + v_k u_{k'} Y_{kk'})\varphi_k\varphi_{k'}\langle k||F||k'\rangle \ for\ c = CX \ldots (10).$$

The operator F takes $F = rY_{L_\nu}(\hat{r})$, $F = rY_{L_\nu}(\hat{r})\tau_z$ for the isoscalar and isovector transitions, respectively, and $F = \sigma\tau_\pm$ for the Gamow-Teller transition ($c = CX$). The coefficients, u_k and v_k are the amplitudes of the canonical basis of HFB. The QRPA calculation is performed by imposing a cutoff energy of two quasiparticle energy 80 MeV.

The model Hamiltonian of Eq.(1) is diagonalized by the following model wave function

$$\Psi^{IK}(r,\xi) = \sum_{\alpha\nu} c_{\alpha\nu}[\varphi_\alpha(r)\Phi^L(\xi,\nu)]^{IK}$$

$$= \sum_{\alpha\in j=I} c_{\alpha 0}[\varphi_\alpha(r)\Phi^0(\xi,0)]^{IK} + \sum_{\alpha,\nu\neq 0} c_{\alpha\nu}[\varphi_\alpha(r)\Phi^{L_\nu}(\xi,\nu)]^{IK} \ldots (11),$$

where $\alpha = (n, j, l)$ is the quantum numbers of the single particle state. We include both isoscalar and isovector phonons of natural parity and the GT phonon with a fraction of non-energy weighted sum-rule being above 5 % and phonon energy being less than 30 MeV.

A one-body operator $\hat{O}$ with rank L can be expressed by the sum of the valence nucleon and core parts as

$$\hat{O} = \hat{O}_1 + \hat{O}_\xi \ldots (12).$$

The operators O_1 and O_ξ operate the valence nucleon and core nucleus, respectively. The reduced transition matrix of the one-body operator is calculated by

$$\begin{aligned}
\langle \Psi^{I'} \| \hat{O} \| \Psi^{I} \rangle = & \sum_{\alpha' \in I', \alpha \in I} c^*_{\alpha' 0} c_{\alpha 0} \langle \varphi_{\alpha'} \| \hat{O}_1 \| \varphi_\alpha \rangle \\
& + \sum_{\alpha' \alpha \nu} c^*_{\alpha' \nu} c_{\alpha \nu} (-1)^{j' + L_\nu + I + L} \hat{I} \hat{I}' \begin{Bmatrix} j' & I' & L_\nu \\ I & J & L \end{Bmatrix} \langle \varphi_{\alpha'} \| \hat{O}_1 \| \varphi_\alpha \rangle \\
& + \sum_{\alpha \nu} c^*_{\alpha 0} c_{\alpha \nu} (-1)^{L_\nu + L} \hat{I} \hat{I}' \begin{Bmatrix} 0 & I' & I' \\ I & L_\nu & L \end{Bmatrix} \langle \Phi^0 \| \hat{O}_\xi \| \Phi^{L_\nu} \rangle \\
& + \sum_{\alpha \nu} c^*_{\alpha \nu} c_{\alpha 0} (-1)^{I + I' + L} \hat{I} \hat{I}' \begin{Bmatrix} L_\nu & I' & I \\ I & 0 & L \end{Bmatrix} \langle \Phi^{L_\nu} \| \hat{O}_\xi \| \Phi^0 \rangle \\
& + \sum_{\alpha \nu \nu'} c^*_{\alpha \nu} c_{\alpha \nu} (-1)^{j' + L_\nu + I' + L} \hat{I} \hat{I}' \begin{Bmatrix} L_{\nu'} & I' & J \\ I & L_\nu & L \end{Bmatrix} \langle \Phi^{L_{\nu'}} \| \hat{O}_\xi \| \Phi^{L_\nu} \rangle \ldots (13)
\end{aligned}$$

In this work, we did not take into account the last term of Eq. (13), which is expected to be a small contribution to the reduced transition matrix. We also calculate the spectroscopic factor defined as

$$S(\alpha) = |\langle \Psi^{IK} | \varphi_\alpha \Phi^0(0) \rangle|^2 = \left| \sum_{\alpha'} c_{\alpha' 0} \langle \varphi_{\alpha'} | \varphi_\alpha \rangle \right|^2 = \left| \sum_{\alpha'} c_{\alpha' 0} \delta_{\alpha' \alpha} \right|^2 \ldots (14).$$

4. Result

We will discuss the effect of PVC by comparing with the result of IPM and experiment. First, we discuss the effect of PVC on the single particle state. Figure 2 shows the spectroscopic factor $S(\alpha)$ of the proton $g_{9/2}$ state of ^{73}Cu. The rectangles with the dotted and the solid lines are the results of IPM and PVC, respectively. In the case of IPM, the spectroscopic factor gives only unity for every single particle state. If one considers the PVC, each spectroscopic factor of the single particle levels decreases and distributes in a wide energy region, as illustrated in Fig. 1.

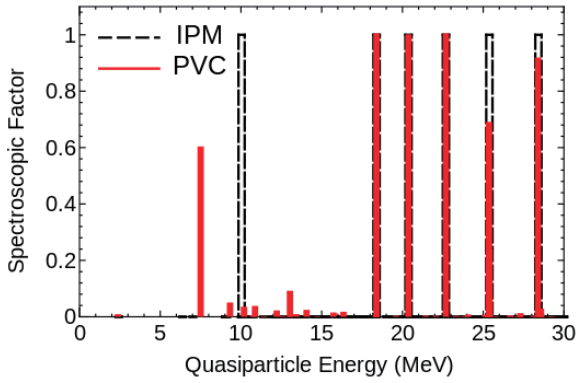

Fig.2: Spectroscopic factor $S(\pi g_{9/2})$ of ^{73}Cu. The rectangles with the dashed and the solid lines are the results of IPM and PVC, respectively.

Figure 3 illustrates the GT distribution of ^{73}Ni as a function of the excitation energy of the daughter nucleus, ^{73}Cu. The ground state energy of ^{73}Ni is shown by the arrow in the figure. Excited states of ^{73}Cu are calculated in the same way as ^{73}Ni by replacing neutron to proton as the valence nucleon. We can see, by including the PVC effect, the GT distribution is significantly varied for a whole energy region. In a region above E=10 MeV, the GT distribution shifts to higher energies and the strengths become smaller a little. We can also see the variation at a low energy region below the ground state of ^{73}Ni. In particular, a new peak about at E=7 MeV appears in the PVC result. This will give a change in the β-decay half-life.

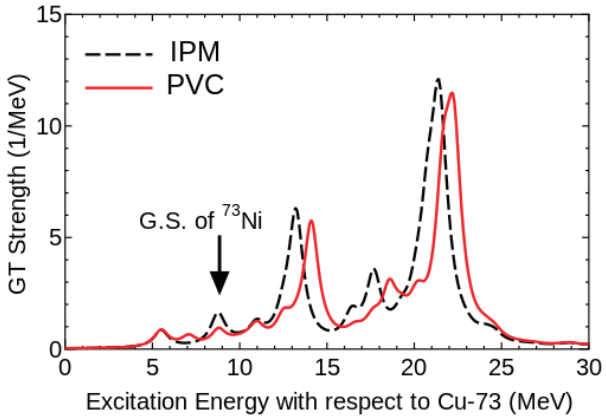

Fig.3: GT distribution of ^{73}Ni as a function of excitation energy with respect to the ground state of ^{73}Cu. The dashed and solid lines are the results of IPM and PVC, respectively. The ground state energy of ^{73}Ni (E=8.9 MeV) is shown by the arrow.

Figure 4 shows the β-decay half-lives of nickel isotopes calculated by using the results of GT distribution. We did not take into account the forbidden transitions in this work. Even-even nuclei are calculated in the same way, namely HFB+QRPA, both for IPM and PVC, so that the results are identical to each other. We can see that the half-lives of PVC for ^{73,75,77}Ni become shorter than those of IPM and the odd-even straggling found in IPM is slightly mitigated. The half-life of PVC for ^{71}Ni is also shorter than the result of

IPM, however, it is difficult to see in the scale given in the figure.

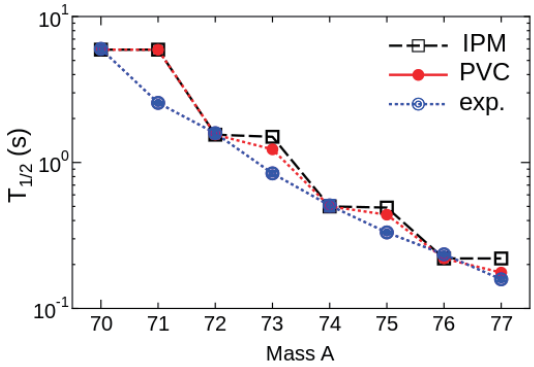

Fig.4: β-decay half-lives of nickel isotopes. The square, circle, and double circle are the results of IPM, PVC, and experiment, respectively. The lines are just for guiding eye.

5. Summary and Future Perspectives

We introduced the PVC to the Skyrme HFB + QRPA framework in order to calculate the GT distributions and β-decay half-lives of nickel isotopes with odd number of neutron. We first demonstrated the PVC effect on the spectroscopic factor of ^{73}Ni. By considering the PVC, the spectroscopic factor significantly changed and distributed in a wide energy region. The GT distribution of ^{73}Ni was shown comparing the result of IPM, and it was found that the PVC effect remarkably changed the GT distribution both at low energy and giant resonance regions. The β-decay half-lives are calculated by using the GT distributions of $^{71\text{-}77}$Ni and it was found that the PVC effect shortened the half-lives and the odd-even straggling found in the IPM was mitigated.

Our work was performed with one effective interaction, namely SGII force. It will be important to study the PVC effects on GT distributions with different forces. We are also interested in studying the PVC effect on the forbidden transitions in the future. We also plan to extend our framework to other nuclei than nickel isotopes for a systematical calculation of β-decay half-life.

References

[1] N. Schunk, J. Dobaczewski, J. McDonnell, J. Moré, W. Nazarewicz, J. Sarich, and M. V. Stoitsov, One-quasiparticle states in the nuclear energy density functional theory, Phys. Rev. C **81** (2010) 024316.

[2] T. Shafer, J. Engel, C. Fröhlich, G. C. McLaughlin, M. Mumpower, R. Surman, β decay of deformed *r*-process nuclei near A=80 and A=160, including odd-A and odd-odd nuclei, with the Skyrme finite-amplitude method, Phys. Rev. C **94** (2016) 055802.

[3] Nguyen Van Giai and H. Sagawa, Spin-Isospin and pairing properties of modified Skyrme Interactions, Phys. Lett. **106**B (1981) 379.

[4] I. Hamamoto and H. Sagawa, Core polarization charges of quadrupole transitions in neutron drip line nuclei, Phys. Rev. C **54**, 2369 (1996).

32 Preliminary Experiment for Temperature-dependent Thermal Neutron Spectrum in Solid Moderator

Jaehong Lee[1], Tadafumi Sano[1], Jun-ichi Hori[1], Rei Kimura[2], Takayuki Sako[3], Akira Yamada[2], and Jun Nishiyama[4]

[1] Institute for Integrated Radiation and Nuclear Science, Kyoto University, Kumatori-cho, Sennan-gun, Osaka, 590-0494, Japan

[2] Toshiba Energy Systems & Solutions, 72-34 Horikawa-cho, Saiwai-ku, Kawasaki-shi, Kanagawa 212-8585, Japan

[3] Toshiba Energy Systems & Solutions, 2-4, Suehiro-cho, Tsurumi-ku, Yokohama, Kanagawa, 230-3699, Japan

[4] Laboratory for Advanced Nuclear Energy, Institute of Innovative Research, Tokyo Institute of Technology, 2-12-1-N1-19 Ookayama, Meguro-ku, Tokyo, 152-8550, Japan

e-mail: lee.jaehong@jaea.go.jp

To measure the temperature-dependent thermal neutron spectrum in the solid moderator, a preliminary experiment was conducted for two purposes. The first purpose was to examine the possibility of the neutron scattering measurement at the Kyoto University Institute for Integrated Radiation and Nuclear Science - Linear Accelerator (KURNS-LINAC). The second was to obtain the thermal neutron spectrum in the solid moderator. To achieve these goals, we have carried out the neutron transmission measurements of the polyethylene (CH_2) samples with thickness 0.2, 1.0 and 2.0 cm using the time-of-flight (TOF) method at the KURNS-LINAC.

In this experiment, we were able to observe the thermal neutron spectrum generated by the CH_2 with thickness 2.0 cm. The future plan is to measure the temperature-dependent thermal neutron spectrum in the CaH_2 moderator material using the heater.

1. Introduction

In order to provide reliable energy for long-duration crewed missions to the moon or Mars, the nuclear reactor is being suggested as a power source [1]. Especially, the small high-temperature reactor using a solid moderator is being studied as a space reactor [2]. As a

solid moderator, the metal hydrides such as the CaH_2 having a high melting point are suggested for the high-temperature operation. Since neutronics characteristics is changed by the increase of temperature, the reactivity of the solid moderated reactor is largely impacted by the temperature-dependent thermal neutron spectrum in the moderator. Therefore, it is necessary to experimentally investigate the temperature-dependent thermal neutron spectrum in the moderator to accurately design the reactor.

In order to carry out the experiment to measure the temperature-dependent thermal neutron spectrum in the solid moderator, a preliminary experiment was conducted for two purposes. The first purpose was to examine the possibility of the neutron scattering measurement at the Kyoto University Institute for Integrated Radiation and Nuclear Science - Linear Accelerator (KURNS-LINAC). The second was to obtain the thermal neutron spectrum in the solid moderator.

To achieve these goals, we have carried out the neutron transmission measurements of the polyethylene (CH_2) samples, which is well known as one of moderator materials to produce thermal neutron spectrum, with thickness 0.2, 1.0 and 2.0 cm. The present time-of-flight (TOF) measurements were performed by using the Kyoto University Institute for Integrated Radiation and Nuclear Science - Linear Accelerator (KURNS-LINAC) as a pulsed neutron source and by using a gas electron multiplier (GEM) detector as a neutron detector.

We obtained the transmitted neutron measurement results of the CH_2 samples, and investigated the thermal neutron spectrum generated by the CH_2 samples.

2. Experiment

2.1 Experiment procedure

The transmission measurements of the CH_2 samples have been carried out by the TOF method at the KURNS-LINAC. The experimental arrangement is shown in **Fig. 1**.

Bursts of fast neutrons were produced from a water-cooled Ta target [3], 5 cm in diameter and 6 cm in length, as a photoneutron target. The Ta-target was set a water tank packed in a graphite scatterer [4], 50×40×40 cm^3, packed in an Al container, 0.5 cm thickness walls, as a neutron scatterer. The neutron flight path used in the experiment was in the

direction of 135° to the LINAC electron beam. In order to reduce the γ-flash generated by the electron burst from the Ta-target, a lead shadow bar, 5×5 cm^2 in area and 20 cm in length, was placed in front of the Ta-target. A gas electron multiplier (GEM) detector having a low sensitivity to γ-rays was used to detect the transmitted and scattered neutrons. The neutron flight length between the Ta-target and the GEM detector was 12.60±0.03 m.

The KURNS-LINAC was operated with a pulse width of 4 μs, a repetition rate of 50 Hz, an average current of 100 μA and an electron energy of 30 MeV.

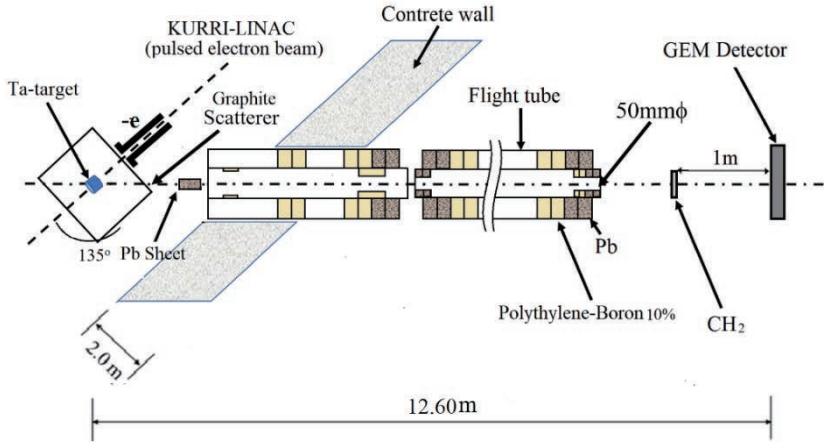

Fig. 1. Experimental arrangement for the neutron transmission measurements

2.2 Samples and measurements

To obtain the thermal neutron spectrum in the CH_2 moderator material, the high density polyethene samples (0.95 g/cm^3) with thickness 0.2, 1.0 and 2.0 cm were used to the present experiment. The information about samples is listed in **Table 1**.

The transmitted and scattered neutrons from the CH_2 samples were detected with the GEM detector. The GEM detector was operated with Ar and CO_2 in 70/30 mixing ratio with 90 ml/min flow rate at -2500 V and 354 μA. Output signals from the GEM detector were summed up and stored in a personal computer as the TOF data. The data taking system of the GEM detector is shown in **Fig. 2**.

In the present measurements, we obtained the incident neutron spectrum by measuring a TOF spectrum without the sample (blank run). We also obtained the TOF measurement by the resonance filters of In (1.46 eV), Co (132 eV) and Mn (336 eV) to evaluate the

background level. The measuring times of each measurement run are listed in **Table 2**.

Table 1. Information of sample

Sample name	CH_2
Density (g/cm^3)	0.95
Isotopic composition	99.95%
Shape	Plate
Size (cm^3)	20.0×20.0×0.2
	20.0×20.0×1.0
	20.0×20.0×2.0

Table 2. List of measuring times

Samples	Measurement	Measurement time (h)
Blank	Neutron spectrum	0.5
CH_2 (0.2 cm)	Foreground	0.5
CH_2 (1.0 cm)	Foreground	0.5
CH_2 (2.0 cm)	Foreground	0.5
Resonance filters	Background	0.5

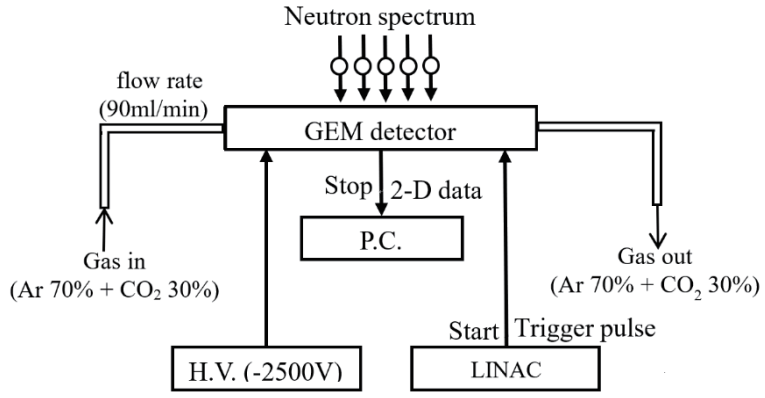

Fig. 2. Data acquisition system for the present experiment

3. Results and Discussion

In the present experiment, we have obtained the transmitted and scattered neutron spectra of the CH_2 samples thickness with 0.2, 1.0 and 2.0 cm. The present results are compared with each other as shown in **Fig. 3**.

For the blank measurement, the thermal neutron peak is observed in the TOF region around 3.5 ms. However, we think this peak would be due to the thermal neutron component decelerated by the cooling water in the Ta-target.

For the measurements of the CH_2 samples, as can be seen in the figure, the thermal neutron spectrum generated by the CH_2 sample with thickness 2.0 cm is observed in the TOF region around 370 μs, although the thermal neutron spectrum is not observed by the CH_2 sample with thickness 0.2 cm and 1.0 cm. It indicates that the experiment for

temperature-dependent thermal neutron spectrum in solid moderator is possible at the KURNS-LINAC by using the TOF method, if sufficiently thick samples are used.

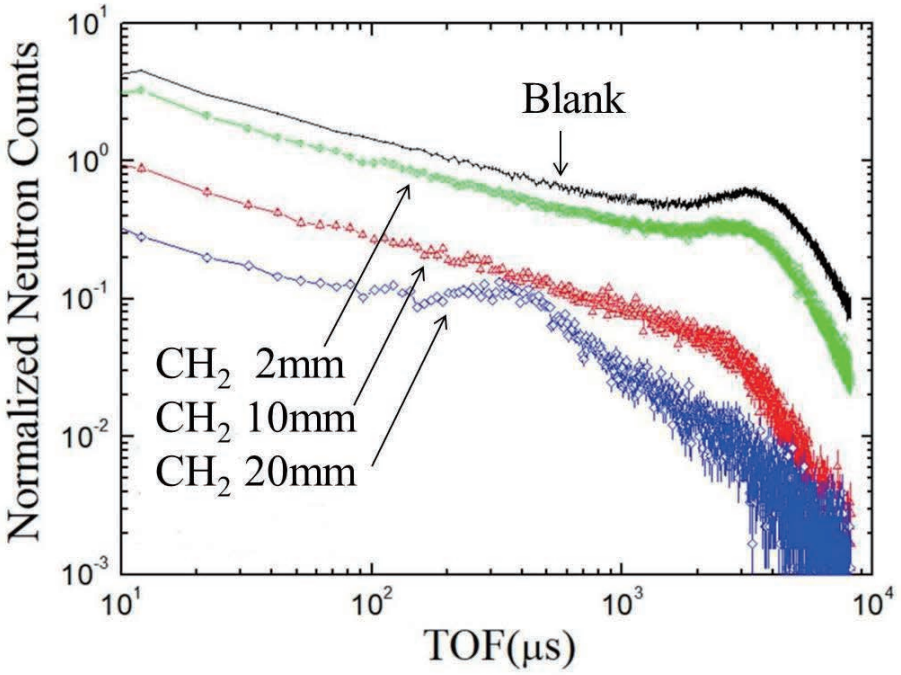

Fig. 3. TOF spectra for the CH_2 samples and blank

4. Conclusions

In the present study, the preliminary experiment for the temperature-dependent thermal neutron spectrum in solid moderator were performed by the TOF method at the KURNS-LINAC. We obtained the transmitted and scattered neutron spectra of the CH_2 samples with thickness 0.2, 1.0 and 2.0 cm, and the obtained neutron spectrum results are compared with each other.

In this experiment, we were able to observe the thermal neutron spectrum generated by the CH_2 with thickness 2.0 cm. We confirmed that the experiment for temperature-dependent thermal neutron spectrum in solid moderator is possible at the KURNS-LINAC by using TOF method.

The future plan is to measure the temperature-dependent thermal neutron spectrum in the CaH_2 moderator material using the heater.

Acknowledgements

This research is a collaborative effort of Toshiba Energy Systems & Solutions, Tokyo Institute of Technology and Kyoto University.

References

[1] P. McClure, D. Poston, Design and Testing of Small Nuclear Reactors for Defense and Space Applications, LA-UR-13-27054, Los Alamos National Laboratory, Sep, 2013.

[2] R. Kimura, S. Wada, T. Yoshida, Y. Nishioka, Y. Hyodo, K. Hoshino, Small nuclear reactor for dispersed power systems 1): conceptual design of the reactor system for Luna and Mars surface missions, Atomic Energy Society of Japan, 2016 Fall Meeting, 3I08, Sep, 2016.

[3] K. Kobayashi, G. Jin, S. Yamamoto, K. Takami, Y. Kimura, T. Kozuka, Y. Fujita, KURRI-LINAC as a Neutron Source for Irradiation, Osaka: Research Reactor Institute of Kyoto University, Report no.22, 142 1987.

[4] Y. Takahashi, Y. Kiyanagi, K. Watanabe, A. Uritani, T. Sano, J. Hori, Ken Nakajima, Development of a neutron source for imaging at the electron linac facility in Kyoto University Research Reactor Institute, Physica B: Condensed Matter, 2018, 4page, DOI: 10.1016/j.physb.2018.06.009.

33 Production Cross Sections of ^{89}Zr by Deuteron-induced Reactions on ^{89}Y

Michiya SAKAGUCHI[1], Masayuki AIKAWA[2,3*], Moemi SAITO[3], Naoyuki UKON[4], Yukiko KOMORI[5], Hiromitsu HABA[5]

[1] *School of Science, Hokkaido University, Sapporo 060-0810, Japan*

[2] *Faculty of Science, Hokkaido University, Sapporo 060-0810, Japan*

[3] *Graduate School of Biomedical Science and Engineering, Hokkaido University, Sapporo 060-8638, Japan*

[4] *Advanced Clinical Research Center, Fukushima Medical University, Fukushima 960-1295, Japan*

[5] *Nishina Center for Accelerator-Based Science, RIKEN, Wako 351-0198, Japan*

*e-mail: aikawa@sci.hokudai.ac.jp

Production cross sections of the ^{89}Y(d,2n)^{89}Zr reaction were measured up to 24 MeV. The stacked foil activation method and the γ-ray spectrometry were used to derive the cross sections. A stacked target consisting of ^{89}Y and ^{nat}Ti metallic foils were irradiated at the RIKEN AVF cyclotron. The γ rays emitted from the irradiated target foils were measured using a high resolution HPGe detector. Cross sections of the reaction were determined and compared with literature data. Our result is consistent with the three out of the seven literature data.

1. Introduction

Many radioisotopes are used for nuclear medicine, e.g. diagnosis and therapy. One of such medical radioisotopes is ^{89}Zr ($T_{1/2}$ = 78.41 h), which is a positron emitter and available for positron emission tomography (PET). The radioisotope can be produced by charged-particle induced reactions using accelerators.

There are several reactions to produce ^{89}Zr. Among the reactions, we focused on the ^{89}Y(d,2n)^{89}Zr reaction. Several studies of the reaction [1–7] could be found in the EXFOR database [8]. There is, however, a large discrepancy among the experimental data. Therefore, we performed an experiment to measure cross sections of the ^{89}Y(d,2n)^{89}Zr reaction.

2. Experimental

The experiment was performed using the RIKEN AVF cyclotron. The stacked foil activation method and the high resolution γ-ray spectrometry were used.

A stacked target consisted of ^{89}Y and ^{nat}Ti foils. Pure metallic foils of ^{89}Y (99% purity, Goodfellow Co., Ltd., UK) and ^{nat}Ti (99.6% purity, Nilaco Corp., Japan) were purchased. The ^{nat}Ti foils were used for the

monitor reaction and assessment of target thicknesses and beam parameters. The sizes and weights of the foils were measured and the thicknesses of the ^{89}Y and ^{nat}Ti foils were found to be 28.6 and 20.3 mg/cm^2, respectively. The foils were cut into small pieces (8 × 8 mm^2) to fit a target holder served also as a Faraday cup.

The target was irradiated by a 23.6-MeV deuteron beam. The incident energy of the beam was measured by the TOF method [9]. The irradiation with an average intensity of 102.4 nA lasted for 1 hour. Energy degradation in the target was calculated by the SRIM code [10]. The beam parameters were assessed by the monitor reaction.

The γ-ray spectra of irradiated foils were measured by a high resolution γ-spectrometer with a HPGe detector. The detector was calibrated by a multiple standard γ-ray point source (^{57,60}Co, ^{85}Sr, ^{88}Y, ^{109}Cd, ^{113}Sn ^{137}Cs, ^{139}Ce, ^{203}Hg and ^{241}Am).

3. Results

Cross sections of the ^{nat}Ti(d,x)^{48}V monitor reaction were derived to assess the target thicknesses and the beam parameters. The characteristic γ-line at 983.525 keV (99.98%) from the decay of ^{48}V ($T_{1/2}$ = 15.9735 d) was measured after a cooling time of 14 days. During the period, an interfering by-product of ^{48}Sc ($T_{1/2}$ = 43.67 h) decayed completely.

Our result of the monitor reaction is shown in Fig. 1. It is compared with the IAEA recommended values [11], which were updated in 2017 from the data in 2001 [12]. We could find good agreement between our result and the recommended values.

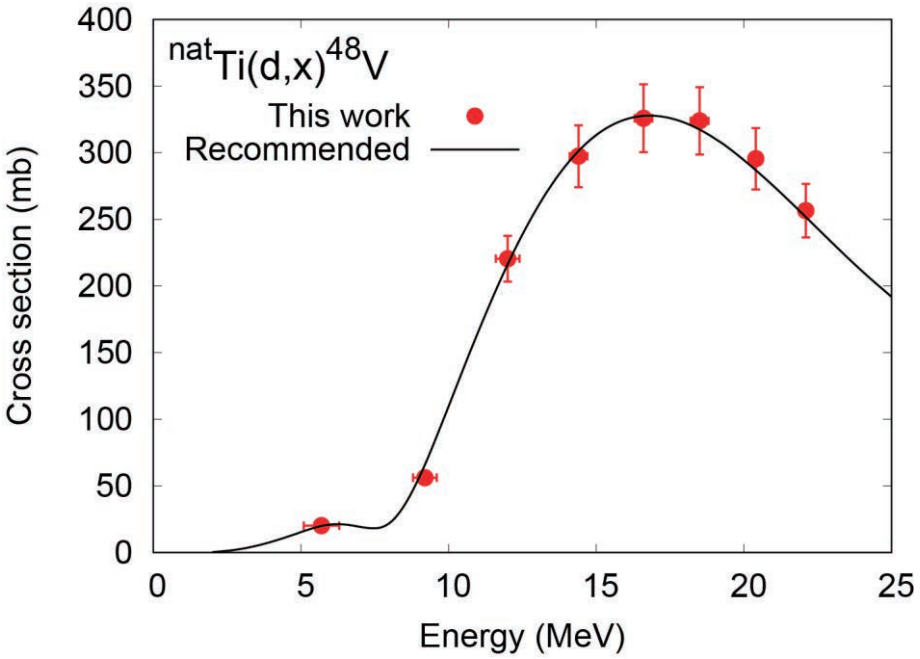

Fig. 1: Cross sections of the ^{nat}Ti(d,x)^{48}V monitor reaction with the IAEA recommended values [11].

Cross sections of the ^{89}Y(d,2n)^{89}Zr reaction were derived from the measurement of the 909.15 keV γ-line (99.04%) decayed from ^{89}Zr ($T_{1/2}$ = 78.41 h). The radionuclide ^{89}Zr has a metastable state with a short half-life ($T_{1/2}$ = 4.161 min), which decays to ^{89g}Zr (IT: 93.77%) and ^{89}Y (ε+β$^+$: 6.23%). The net counts measured after a cooling time of 14 days were cumulative ones of the ground and part of the excited state. Therefore, only cumulative cross sections could be obtained from the γ-line measurement. The result is compared with the previous studies [1–7] and the TENDL-2017 data [13]. Our result is in good agreement with the three [5–7] out of the seven previous studies.

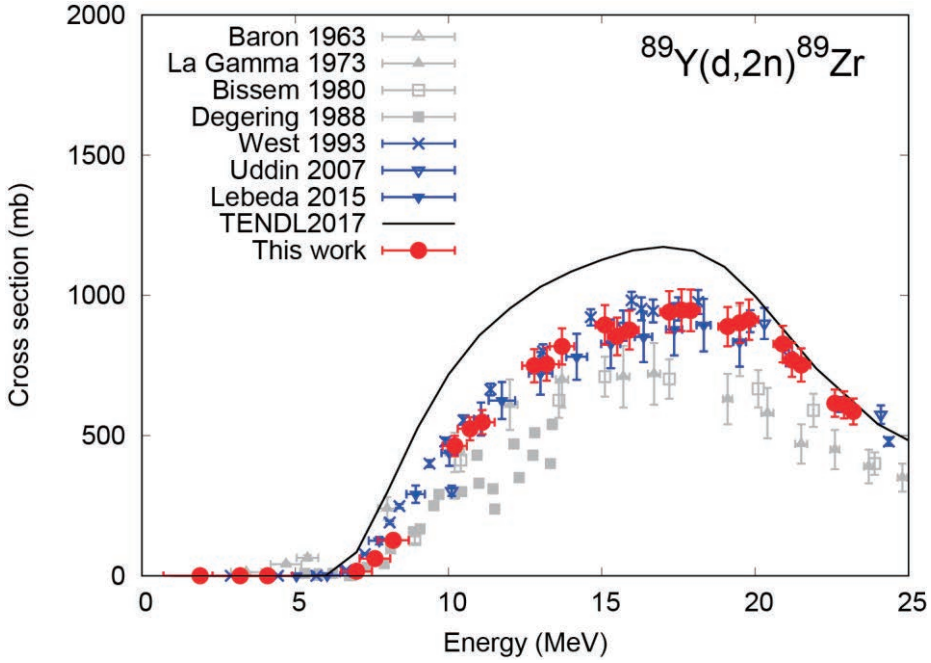

Fig. 2: Cross sections of the ^{89}Y(d,2n)^{89}Zr reaction with the previous data [1–7] and the TENDL-2017 data [13]

4. Summary

We measured cross sections of the ^{89}Y(d,2n)^{89}Zr reaction up to 24 MeV. The standard methods, stacked target activation technique and high resolution γ-spectrometry, were used. The measured data were compared with the previous experimental data and the TENDL-2017 data. Our result is consistent with the three out of the seven previous studies.

Acknowledgements

This work was carried out at the RI Beam Factory operated by RIKEN Nishina Center and CNS, University of Tokyo Japan. This work was partly supported by JSPS KAKENHI Grant Number 17K07004.

References

[1] Baron N, Cohen BL. Activation cross-section survey of deuteron-induced reactions. Phys. Rev. 1963;129:2636–2642.

[2] La Gamma AM, Nassiff SJ. Excitation Functions for Deuteron-Induced Reactions on ^{89}Y. Radiochim. Acta. 1973;161–162.

[3] Bissem HH, Georgi R, Scobel W, et al. Entrance and exit channel phenomena in d- and ^{3}He-induced preequilibrium decay. Phys. Rev. C. 1980;22:1468.

[4] Degerign D, Unterricker S, Stolz W. Excitation function of the ^{89}Y(d,2n)^{89}Zr reaction. J. Radioanal. Nucl. Chem. Lett. 1988;127:7–11.

[5] West Jr. HI, Lanier RG, Mustafa MG, et al. Some light-ion excitation-function measurements on titanium, yttrium, and europium, and associated results. West Jr. HI, editor. Livermore, California: Lawrence Livermore National Laboratory; 1993.

[6] Uddin MS, Baba M, Hagiwara M, et al. Experimental determination of deuteron-induced activation cross sections of yttrium. Radiochim. Acta. 2007;95:187–192.

[7] Lebeda O, Štursa J, Ráliš J. Experimental cross-sections of deuteron-induced reaction on ^{89}Y up to 20 MeV; comparison of ^{nat}Ti(d,x)^{48}V and ^{27}Al(d,x)^{24}Na monitor reactions. Nucl. Instruments Methods Phys. Res. Sect. B. 2015;360:118–128.

[8] Otuka N, Dupont E, Semkova V, et al. Towards a More complete and accurate experimental nuclear reaction data library (EXFOR): International collaboration between nuclear reaction data centres (NRDC). Nucl. Data Sheets. 2014;120:272–276.

[9] Watanabe T, Fujimaki M, Fukunishi N, et al. Beam energy and longitudinal beam profile measurement system at the RIBF. Proc. 5th Int. Part. Accel. Conf. (IPAC 2014). 2014. p. 3566–3568.

[10] Ziegler JF, Biersack JP, Ziegler MD. SRIM: the Stopping and Range of Ions in Matter [Internet]. 2008. Available from: http://www.srim.org.

[11] Hermanne A, Ignatyuk A V., Capote R, et al. Reference Cross Sections for Charged-particle Monitor Reactions. Nucl. Data Sheets. 2018;148:338–382.

[12] Tárkányi F, Takács S, Gul K, et al. Beam monitor reactions. Charg. Part. cross-section database Med. Radioisot. Prod. IAEA-TECDOC-1211. 2001.

[13] Koning AJ, Rochman D. Modern Nuclear Data Evaluation with the TALYS Code System. Nucl. Data Sheets. 2012;113:2841–2934.

34 Nuclear Fission of the Neutron-deficient Mercury Isotopes using 4D-Langevin Model

Chikako Ishizuka[1], Mark D. A. Usang[2],Yoko Ishii[1], Fedir A. Ivanyuk[3], and Satoshi Chiba[1,4]
[1]Tokyo Institute of Technology, [2]Malaysian Nuclear Agency, [3]Kiev Institute for Nuclear Research, [4]NAOJ
Email: chikako@lane.iir.titech.ac.jp

In this study, we use four-dimensional (4D) Langevin model, which can well explain the experimental results in actinide region, to understand what controls the fission fragment mass distribution (FFMD) by varying E* for ^{180}Hg and ^{190}Hg. We successfully reproduced FFMDs of neutron-deficient (proton-rich) isotopes in Pb region, although the further investigation is necessary to reproduce qualitative properties of fission fragments in ^{180,190}Hg. The Langevin model can also provide reasonable total kinetic energy (TKE) of fission fragments, and its variance.

1. Introduction

Recently, precise evaluation of fission products (nuclear species and their amounts) of actinides has attracted attention in decommissioning of nuclear power plants, to reduce its cost. However, measurements of nuclear fissions of actinide region still have been limited. Therefore, we need a theoretical model with a strong prediction power to various nuclei. Such theoretical model may solve the open problems on nuclear fission, i.e., sudden shape transitions in FFMDs, energy dependence of prompt neutrons and rotations of fission fragments. Sudden change of FFMD shapes in isotopes and/or isotones is the one of the motivation why we need a theoretical model with enough prediction power. For example, Fm-isotopes up to N=157 have double peak FFMDs (asymmetric fission is dominant), while those above N=157 have single peak FFMDs (symmetric fission mainly takes place). In actinides, we found that our 4D-Langevin model can explain FFMD transitions [1], and can reproduce both FFMDs and TKEs quantitatively. Thus our 4D-Lanvegin model works very well in actinides. However it is still opaque whether our model can describe the fission phenomena far from actinides, where the FFMD is controlled by different mechanism from that in actinides. In actinides, asymmetric FFMD is mainly dominated by double-magic ^{132}Sn. On the other hand, FFMD of ^{180}Hg is not symmetric around double-magic ^{90}Zr, but asymmetric. In order to examine prediction power of our model, we studied neutron-deficient Hg isotopes, $^{180, 190}$Hg.

2. Methods

Langevin model [2] describes nuclear fission as the time evolution of nuclear shape of a compound nucleus till scission using a solution of the following Langevin equation

$$\frac{dq_i}{dt} = (m^{-1})_{ij} p_j$$

$$\frac{dp_i}{dt} = -\frac{\partial F}{\partial q_i} - \frac{1}{2}\frac{\partial}{\partial q_i}(m^{-1})_{jk} p_j p_k - \gamma_{ij}(m^{-1})_{jk} p_k + g_{ij} R_j(t)\,,$$

where $g_{ik}g_{kj} = T^*\gamma_{ij}$, with $T^* = \frac{\hbar\omega}{2}\coth\frac{\hbar\omega}{2T}$. Here, the variable q_i is $q_i=(z_0, \delta_1, \delta_2, \alpha)$, which is the Two-center Shell-model parametrization. These variables correspond to elongation (z_0), deformations of the outer parts of the fragment (δ_1,δ_2),and mass asymmetry (α). In the current model, we fixed the neck parameter $\varepsilon=0.35$. We also the local frequency of collective motion ω, which gives the effective temperature as $\hbar\omega=2$. Shell corrections to the free energy F were calculated directly starting from their formal definitions without any additional approximations [3]. For comparison, we also used Ignatyuk shell damping formula to evaluate the shell corrections. Collective inertia tensor $m_{\mu\nu}$ is calculated based on the Werner-Wheeler approximation of the liquid drop mass tensor. The friction tensor $\gamma_{\mu\nu}$ is calculated from the wall-window friction formulation.

3. Results

We performed the Langevin calculations at the excitation energy E*=23.9MeV for ^{180}Hg system, and E*=27.6MeV for ^{190}Hg system, respectively. As shown in Table 1, the difference of shell correction does not affect the peak position of fission fragments very much in the case of ^{180}Hg, while the exact shell correction makes the mean mass number of light fragments (AL) larger by 2.79, and that of heavy fragments (AH) smaller by 2.79 than the experimental result in ^{190}Hg. In ^{190}Hg system, we found that the discrepancy between the calculation and the experiment becomes very large when we use well-known Ignatyuk shell damping formula.

	Peak positions
Hg-180 (Experiment)	AL=79 AH=101
Presnet model with exact shell corr. E*=23.9MeV, ^{180}Hg	**AL= 78.44 AH= 101.56**
Present model with Ignatuk corr. E*=23.9MeV, ^{180}Hg	**AL= 79.35 AH= 100.65**
Hg-190 (Experiment)	AL=83 AH=107
Presnet model with exact shell corr. E*=27.6MeV, ^{190}Hg	**AL= 85.79 AH= 104.21**
Present model with Ignatuk corr. E*=27.6MeV, ^{190}Hg	**AL= 87.04 AH= 102.96**

Table 1 Comparison of the mean two peak-positions of fission fragments of 180Hg fission at E*=23.9MeV, and 190Hg fission at E*=27.6MeV. AL is the mean mass number of light fragments, while AH is that of heavy fragments.

Table 2 is the comparison of various mean TKEs in nuclear fission of ^{180}Hg and ^{190}Hg. We compared two calculation results with different shell corrections, the experimental result with corresponding energy to calculations for fission, and experimental result of beta-delayed fission of ^{180}Tl. In addition to them, we also show the mean TKE suggested by Viola systematics. In both cases, the mean TKEs of Langevin calculations are between experimental values and Viola systematics. In the mass region around actinides, the TKE follows Viola systematics in general. In that sense, the experimental <TKE> is too small. However, it is not clear whether Viola systematics can be valid in Hg region. Therefore, we need further investigation of nuclear fission in the mass region far from actinides.

Table 2 The mean TKEs, <TKE>s, are listed in the case of ^{180}Hg and ^{190}Hg fission.

	<TKE>
Present, ^{180}Hg* at E^*_{eff}=23.9MeV with exact shell corr.	**137.92 MeV**
Present, ^{180}Hg* at E^*_{eff}=23.9MeV with Ignatuk corr.	**138.90 MeV**
Nishio+2015, ^{180}Hg* at E^*_{eff}=23.9MeV	131.7(10) MeV
βDF study of ^{180}Tl	133.2(14) MeV
Viola systematics, ^{180}Hg	142.1 MeV
Present, ^{190}Hg* at E^*_{eff}=27.6MeV with exact shell corr.	**134.12 MeV**
Present, ^{190}Hg* at E^*_{eff}=27.6MeV with Ignatuk corr.	**137.43 MeV**
Nishio+2015, ^{190}Hg atE^*_{eff}=27.6MeV	132.5(10) MeV
Viola systematics, ^{190}Hg	139.7 MeV

Present calculations are compared with Nishi+2015 [4], beta-delayed fission case [5] and the estimated value by Viola systematics [6].

4. Summary

We calculated ^{180,190}Hg nuclear fission using our 4D-Langevin model, which can reproduce both experimental FFMD and TKE very well in actinide region, with two types of shell correction, i.e., exact one and standard shell-correction formula of Ignatyuk. As a result, difference of shell correction does not strongly affect FFMD and TKE in ^{180}Hg, while the discrepancy between the Langevin calculation and the experiments became larger when we use the standard Ignatyuk shell correction in ^{190}Hg. We conclude that our 4D-Langevin model can successfully reproduce both FFMD and TKE, although the agreement with experimental data in ^{180,190}Hg has room for discussion, compared to that in actinides.

References

[1] M. D. Usang F. Ivanyuk, C. Ishizuka, S. Chiba, Scientific Reports (2019) in press.

[2] C. Ishizuka, M. D. Usang, F. A. Ivanyuk, J. A. Maruhn, K. Nishio, S. Chiba, Phys. Rev. C **96** (2017) 064616.

[3] F. A. Ivanyuk, C. Ishizuka, M. D. Usang, S. Chiba, Phys. Rev. C **97** (2018) 054331.

[4] K. Nishio *et al*, Phys. Lett. B **748** (2015) 89–94.

[5] A.N. Andreyev, *et al.*, Phys. Rev. Lett. **105** (2010) 252502.

[6] V. E. Viola, *et al.*, Phys. Rev. C **31** (1985) 1550.

This is a blank page.

35 Neutron Capture Reaction Data Measurement of Minor Actinides in Fast Neutron Energy Region for Study on Nuclear Transmutation System

Tatsuya KATABUCHI[1)]*, Osamu IWAMOTO[2)], Jun-ich HORI[3)], Nobuyuki IWAMOTO[2)], Atsushi KIMURA[2)], Shoji NAKAMURA[2)], Yuji SHIBAHARA[3)], Kazushi TERADA[1)]

1) Tokyo Institute of Technology

2) Japan Atomic Energy Agency

3) Kyoto University

*E-mail: buchi@lane.iir.titech.ac.jp

A research project entitled *"Study on accuracy improvement of fast-neutron capture reaction data of long-lived MAs for development of nuclear transmutation systems"* started in 2017 as a four-year project. The purpose of the project is to improve the neutron capture cross sections of minor actinides in the fast neutron energy region that is particularly important for study on a nuclear transmutation system. The outline of the project is reported.

1. Introduction

Nuclear waste from nuclear power plants contains long-lived minor actinides (MA), some of which keep their radiotoxicities for more than a thousand years. Currently planned geological disposal of nuclear waste has been a long-standing issue for public acceptance. In order to solve the issue, nuclear transmutation, by which long-lived MAs are transmuted to stable or shorter-lived nuclides via neutron-induced reactions, has been suggested. In recent years, accelerator-driven systems (ADS) are considered as feasible candidates of MA burners and several ADS projects are ongoing or planned. Detailed core design of an ADS requires accurate, reliable nuclear reaction data of MAs but the uncertainties of the current cross section data in evaluated nuclear data libraries in the fast neutron energy region that is most relevant for ADS are not small enough to satisfy the requirement [1,2].

A research project entitled *"Study on accuracy improvement of fast-neutron capture reaction data of long-lived MAs for development of nuclear transmutation systems"* started in 2017. The project aims at improving the accuracies of neutron capture cross sections of MAs (^{237}Np, ^{241}Am, ^{243}Am) in the fast neutron energy region. In order to improve the capture

reaction data of MAs, an intense pulsed neutron beam from a spallation neutron source of the Japan Proton Accelerator Research Complex (J-PARC) is utilized in time-of-flight (TOF) experiments to measure capture cross sections. In previous research projects, we worked on building and commissioning the Accurate Neutron Nucleus Reaction Measurement Instrument (ANNRI), a neutron beam line for nuclear data measurement in the Materials and Life Science Experimental Facility (MLF) of J-PARC [3]. ANNRI now becomes one of the leading neutron beam lines for nuclear data measurement in the world.

One of the major reasons why previous measurements of MA capture cross sections were not able to achieve high accuracies is that samples were radioactive. A radioactive sample emits decay γ-rays that become background for the detection of neutron capture γ-rays. The large decay γ-ray background hinders accurate capture cross section measurement. The J-PARC high-intensity pulsed neutron beam solves the issue by increasing neutron capture reaction rates in a sample. The rate of capture events to background events can be improved, consequently achieving small uncertainties of cross sections.

Another difficulty to deal with a radioactive sample is to assay sample characteristics such as total mass, isotopic composition and impurities. Sample characteristic assay of radioactive samples cannot be carried out easily. It needs special apparatus and radiation-controlled areas for handling unsealed radioactive material. In many past nuclear data measurements using radioactive samples, this technical barrier leads to the situation that sample characteristics were not assayed by an experimental group themselves and, instead, rely completely on sample spec sheets provided by a manufacture. Uncertainties of manufacture measurements are not easily testable, often not small enough and sometimes not mentioned at all. This is why uncertainties of radioactive sample characteristics often dominate systematic uncertainties of cross sections. In this project, we plan to analyze sample characteristics of MA samples by ourselves.

The project consists of four tasks: (1) development of neutron beam filter system in J-PARC, (2) neutron capture cross section measurement, (3) sample characteristic assay, and (4) theoretical reaction model study. The following sections describe details of the items.

2. Neutron Beam Filter System

The neutron beam filter is designed to solve the so-called double bunch issue of a neutron beam from the J-PARC spallation neutron source. The spallation neutron source is operated at a repetition rate of 25 Hz. Hence, neutrons are generated every 40 ms. The J-PARC accelerator adopts a special operational pattern called double bunch operation, in which two proton pulses with a separation time of 600 ns are injected into the spallation neutron target for each neutron burst cycle. The purpose of this operation is to increase the thermal neutron intensity, important for most of measurements of the neutron beam lines in

MLF. For thermal neutron experiments, the time structure of the incident proton beam is negligible. The Doppler broadening effect and moderation time in a moderator erase the proton beam time structure in the thermal neutron TOF region around 10-30 ms. However this double bunch mode is very problematic for measurement in higher energy region above 100 eV. The double bunch structure appears in TOF spectra in the high energy region. Neutrons having two different energies originating two incident proton pulses overlap at the same TOF in measurement. The capture yield at each TOF point includes cross section values at two different neutron energies and deconvolution of the results is not easy.

The neutron beam filter system solves this issue. The neutron beam filter method is often used in nuclear reactor experiments [4,5]. A reactor neutron beam which has a continuous energy distribution can be tailored to be mono or quasi-mono energetic through filter materials that have sharp resonance dips of total cross section at certain resonance energies. In this project, the neutron filter technique is combined with the TOF technique to separate out coexisting different energy neutrons at the same TOF. The neutron beam filter system is under development. Filter materials were chosen and tested in a neutron beam facility in Tokyo Tech in 2018. Based on the test results, the system was designed in 2018 and will be installed in the ANNRI beam line of J-PARC MLF in early 2019.

3. Neutron Capture Cross Section Measurement

This project focuses on fast-neutron capture cross section data of MA. This requires a fast detection and data acquisition systems. Fast neutron events appear in fast TOF region close to the gamma flash, an intense γ-ray emission produced at the moment that the incident proton beam pulse reaches the spallation neutron target. The gamma flash overwhelms the detection system and detection signals are distorted for μs (sometimes ms) after the gamma flash. To detect neutron capture events in the fast TOF region, the system needs to recover quickly from the distortion caused by the gamma flash. In addition to the gamma-flash, an intense neutron beam from the J-PARC spallation neutron source increase the detector counting rate, leading to large count loss due to the system dead time.

We plan to measure the neutron capture cross sections of MAs using NaI(Tl) detectors of ANNRI. NaI(Tl) detectors are suitable for the measurement in fast TOF region [6]. Scintillation detectors have faster response than semiconductor detectors, and what's more, an NaI(Tl) detector can measure a γ-ray spectrum. The pulse height weighting technique to derive neutron capture cross sections is well established for a NaI(Tl) detector [7]. However the present data acquisition system for the ANNRI-NaI(Tl) detectors is not fast enough to analyze the pulse height and TOF of signals. In this project, a new data acquisition system and fast signal processing method is under development. The new system is built on a waveform digitizer that can record the waveform of each signal and then the recorded signals

are analyzed offline. The dead time of the waveform digitizer is considerably small and offline sophisticated signal processing is allowed. The data acquisition system was tested in 2017 and 2018. Cross section measurements of MAs using the ANNRI-NaI(Tl) detectors and the new data acquisition system will be conducted in 2019 and 2020.

4. Sample Characteristic Assay

Sample characteristic assay is an important task to improve the accuracy of cross sections. Uncertainties of sample characteristics such as total mass, isotope composition and impurities can be crucial systematic uncertainties. In this project, we plan to analyze the isotope composition and impurities of MA samples by thermal ionization mass spectrometry (TIMS) at the Institute of Integrated Radiation and Nuclear Science of Kyoto University. The target accuracy of analysis is set at less than 1% in this project. The key to achieving such a high accuracy is the stability of ion emission from a filament of the TIMS ion source. To stabilize the ion emission, the monitoring method of the filament temperature, most dominant factor for ion emission, was improved in 2018. A test experiment showed significant improvement of ion emission control. TIMS analysis of MA samples is planned to conduct in 2019 and 2020.

5. Theoretical Reaction Model Study

Theoretical nuclear reaction models can predict neutron capture cross sections. Combined with experimental data, theoretical reaction models become powerful tools in nuclear data evaluation. In this project, neutron capture γ-ray spectra measured with the ANNRI-NaI(Tl) detectors are used to refine theoretical reaction models. Capture γ-ray spectra give more information on reaction mechanism than taking into account only capture cross section. Comparing theoretical calculations with the measured γ-ray spectra, model parameters such as gamma-ray strength function and level density can be determined. However direct output spectra from experiments cannot be compared with theoretical capture γ-ray spectra because measured spectra convolute detector response. Unfolding measured spectra with detector response function is often performed to compare with theoretical spectra [7] but the unfolding process adds uncertainties to experimental data. Instead, we adopted the opposite way for comparison. We fold theoretical spectra with detector response and then compare them to experimental data. Folding process is less ambiguous than unfolding process. We built a geometrical model of the ANNRI-NaI(Tl) detectors for the Monte Carlo simulation code PHITS [8] and calculated the detector response matrix. For a benchmark calculation, the capture γ-ray spectrum of ^{197}Au was calculated with the theoretical reaction model code CCONE [9] and then folded the calculated spectrum with the detector response matrix. Comparison with experimental data is planned to test the present method in early 2019.

6. Summary and Future Prospect

The project entitled *"Study on accuracy improvement of fast-neutron capture reaction data of long-lived MAs for development of nuclear transmutation systems"* started in 2017 as a four-year project. The first two years were spent for development of the neutron beam filter system, fast data acquisition method for the ANNRI-NaI(Tl) detectors and MA sample characteristic assay. Now the project is going into the actual experimental phase to measure the capture cross sections and capture γ-ray spectra of MAs.

Acknowledgements

This work is supported by the Innovative Nuclear Research and Development Program from the Ministry of Education, Culture, Sports, Science and Technology of Japan.

References

[1] M. Salvatores *et al.*, OECD/NEA Report No.6410 (2008).
[2] Hiroki Iwamoto *et al.*, J. Nucl. Sci. Technol., **50**, 856 (2013).
[3] Koichi Kino *et al.*, Nucl. Instr. Meth. A, **736**, 66 (2014).
[4] O. D. Simpson and L. G. Miller, Nucl. Instr. Meth, **61**, 245 (1968).
[5] Tran Tuan Anh *et al.*, Ann. Nucl. En. **113**, 420 (2018).
[6] Tatsuya Katabuchi *et al.*, Nucl. Instr. Meth. A, **764**, 369 (2014).
[7] Satoshi Mizuno *et al.*, J. Nucl. Sci Technol., **36**, 493 (1999).
[8] Tatsuhiko Sato *et al.*, J. Nucl. Sci Technol., **55**, 684 (2018).
[9] Osamu Iwamoto *et al.*, Nucl. Data Sheets, **131**, 259 (2016).

This is a blank page.

36 Fission Yield Calculations with Hauser-Feshbach Statistical Decay Theory and Beta Decay

Shin Okumura[1], Toshihiko Kawano[2], and Satoshi Chiba[3]

[1]International Atomic Energy Agency, 1400 Vienna, Austria
[2]Los Alamos National Laboratory, Los Alamos, NM 87545, USA
[3]Tokyo Institute of Technology, 2-12-1 Ookayama, Meguro-ku, Tokyo 152-8550, Japan
e-mail:s.okumura@iaea.org

Abstract

We performed the fission product yield (FPY), prompt and delayed neutron emission, and decay heat calculations with the Hauser-Feshbach Fission Fragment Decay (HF^{3}D), beta decay, and summation calculation codes for the neutron induced fission of ^{235}U with the incident neutron energy from thermal to 5 MeV. A series of sequential calculations for one particular incident neutron energy starts with a primary fission fragment distribution that is characterized by $Y(Z, A, E_{ex}, J, \pi)$. The HF^{3}D code deterministically generates and numerically integrates such distributions for more than 500 of excited primary fission fragment pairs for each incident neutron energy. A set of calculated independent FPY at each energy is used as an input for the β-decay and summation calculations that tracks the β-decay of all nuclides to obtain the cumulative FPY, the decay heat, and the delayed neutron yield. The calculated fission observables are compared with available experimental data.

1 Introduction

The fission product yield (FPY) is an important ingredient for the safe and efficient operation of nuclear power plant, the reprocessing of the spent nuclear fuel, and various nuclear energy applications. Despite its importance, the FPY data in the current evaluated nuclear data libraries are not sufficient especially for heavier actinides and wide energy range due to scarce experimental data.

Many theoretical efforts have also been made for either understanding the fundamental physics of the nuclear fission or developing models and codes to reproduce fission observables. However, accurate predictions of fission observables by only theoretical calculations in a consistent manner have not reached the stage of real use for the nuclear data evaluation. In the past, England and Rider[1], as well as many evaluators of the nuclear data libraries, have made efforts to establish some empirical models such as Los Alamos Model for prompt neutron fission spectra (PFNS) [2] and Wahl systematics for the independent FPY[3]. Such models aim to reproduce the existing experimental data and to predict data for unknown nuclide. These approaches have still been used for the evaluation today. Generally, these models specialize in certain observables such as PFNS and FPY. Therefore, each model has no consistency with each other. Concerning FPY, up to now, few code can calculate incident energy dependence of the independent or cumulative FPY. FPY's distribution is different by either fissile or incident neutron energy. Therefore, an accurate prediction of FPY data that are consistent with other fission observables in the energy dependent manner is desired.

In this study, we demonstrate the sequential steps of calculation in the energy dependent manner which combines the statistical decay of the fission fragment pairs using the HF^{3}D code with the β decay and the summation calculations. The calculated fission observables, i.e. prompt neutron emission multiplicity and its

spectrum, independent FPY, cumulative FPY, decay heat, and delayed neutron yield are compared with available experimental data.

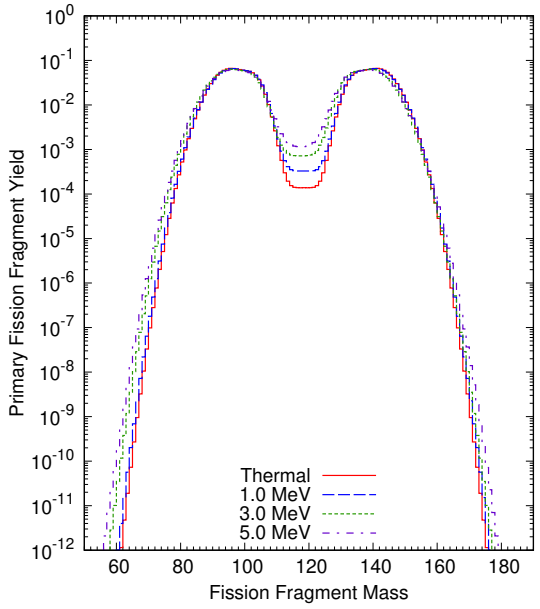

Figure 1: Primary fission fragment distributions $Y_P(A)$ for thermal, 1, 3, and 5 MeV generated using the HF^{3}D code.

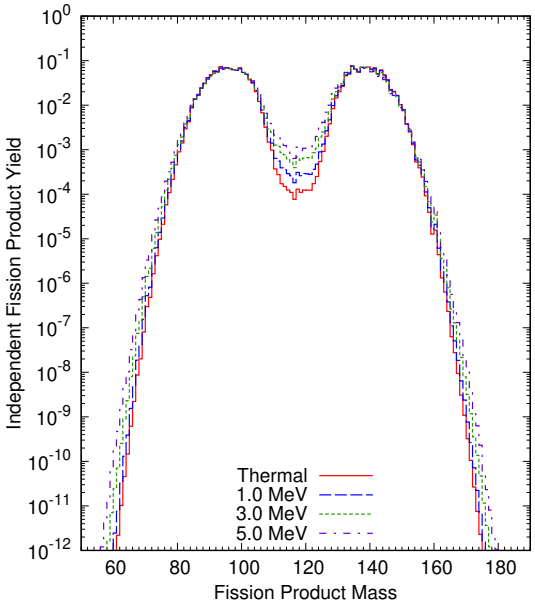

Figure 2: Calculated fission product distributions $Y_I(A)$ for thermal, 1, 3, and 5 MeV.

2 Calculation Method

A general concept of the HF^{3}D code and the generation of fission fragment distributions are discussed in the literature [4]. Initially, primary fission fragment distributions at each incident neutron energy are produced based on available experimental $Y_P(A)$ data as a function of the primary fission fragment mass. We fit $Y_P(A)$ and $TKE(A)$ by simple analytical functions and interpolate them smoothly between energies. The distribution including charge, i.e. $Y_P(A,Z)$, is obtained by using $Y_P(A)$ with Z_P model in the Wahl systematics[3]. The parameters that are defined in Z_P model generate distributions of charge for each mass by Gaussian and incorporate the even-odd proton and neutron effects in it. These parameters are defined in the energy dependent manner. We use these parameters, although the original pourpose of Z_P model is to generate independent FPY.

We use a simple analytical function to fit the experimentally available total kinetic energy $TKE(A)$ and energy dependence of mass averaged TKE $\overline{TKE}$. Using these functions, we generate the incident energy dependence of $Y_P(A,Z,TKE)$. Next, the TKE for a given fission fragment pair is converted into total excitation energy (TXE) and separated into light and heavy fragments by the anisothermal model that is defined as the ratio of effective temperatures of complemental fragments[5, 6]. We have tested various patterns of energy sharing between two primary fragments and found that taking a constant ratio reproduces prompt neutron multiplicity $\overline{\nu}(A)$ well for ^{235}U [7]. The fission fragment mass distribution $Y_P(A)$ at thermal, 1, 3, and 5 MeV generated by the HF^{3}D code and used in this study are shown in Fig. 1. The statistical decay calculations for all set of fission fragment pairs for each energy were performed using the HF^{3}D code [4]. β decay and the summation calculations were performed using the calculated Y_I and ENDF/B-VII decay data library.

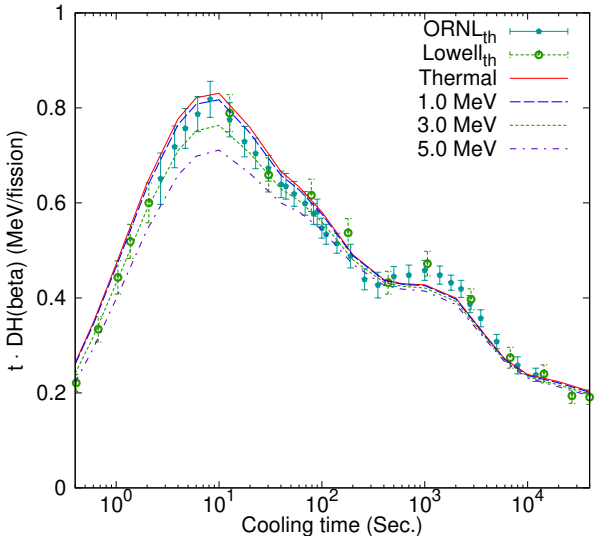

Figure 3: Decay heat from β ray.

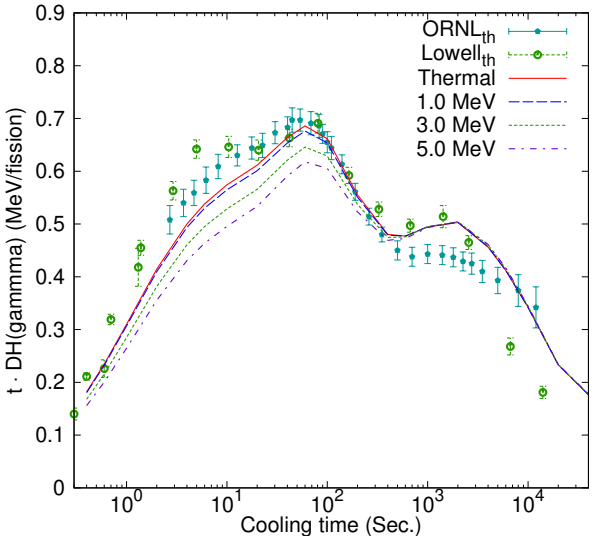

Figure 4: Decay heat from γ ray.

3 Results and Discussion

Figure 2 shows the calculated independent FPY $Y_I(A)$ for thermal, 1, 3, and 5 MeV. The $Y_I(A)$ at the thermal energy showed a good agreement with the evaluated nuclear data [4]. The neutron multiplicity calculated simultaneously with $Y_I(A)$ also showed a good agreement with experimental data [4]. The sets of calculated $Y_I(A)$ for each incident neutron energy are used to calculate $Y_C(A)$, and the resulted $Y_C(A)$ also are in good accordance with experimental data [7, 8].

The calculated decay heats from the β and γ components by the summation calculation are shown in Fig. 3 and Fig. 4, respectively. The experimental data are available for the thermal and fast energies, and only thermal energy data are plotted for the comparisons. The calculations reproduce the experimental data well for the decay heat from the β component in wide range of the cooling period, whilst a slight difference appeared in the early cooling period for the γ component. The decay heat varies as a function of the incident neutron energy. In Fig. 3 and Fig. 4, the calculated decay heats using Y_I at different incident neutron energies, 1.0, 3.0, and 5.0 MeV, are also shown and the results imply that the decay heat from the both components decreases with increasing the incident neutron energy [9]. This implies that FPY of precursors decreases with increasing the incident energy.

The delayed neutron yields ν_d as a function of cooling time for different incident neutron energies are shown in Fig. 5. The result for the thermal energy tends to overestimate for in the cooling period before 10 seconds. By comparison with the calculated results using JENDL/FPY-2011 $Y_I(Z, A)$ data as an input of the summation calculation, our calculation overestimates or underestimates some nuclides which are the main contributors to the delayed neutron emissions with mass number around 90-99. The energy dependence of the five delayed neutron precursors is shown in Fig. 6 together with the experimental ν_d at thermal energy[9]. The ν_d from representative five precursors all decreases with increasing the incident neutron energy. By comparison with the experimental ν_d for five precursors at the thermal energy, the calculated ν_d from some of precursors are not in well accordance with that of experimental data.

The fission observables in the β decay stage are quite sensitive to the FPY data, although the prompt neutron and gamma emission, and the resulting independent FPY obtained from statistical decay calculation do not show noticeable difference compared with experimental data. From this study, it is revealed that the charge distribution generated by the Wahl systematics needs to be revised to improve the accuracy of the prediction. The decay scheme

in the decay data library also plays an important role in these calculations.

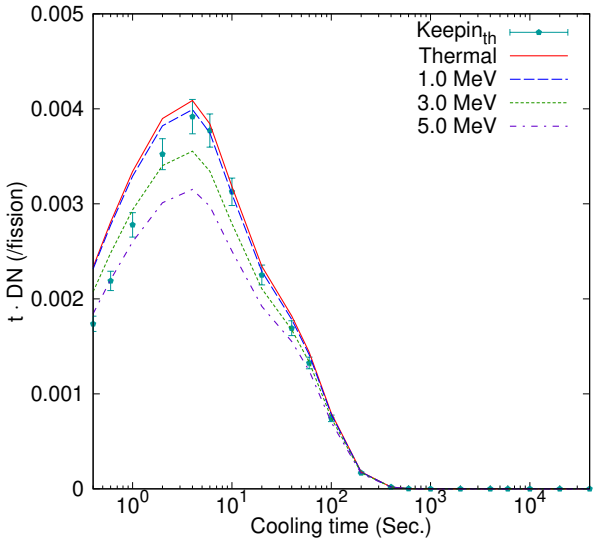

Figure 5: Cooling time dependence of the delayed neutron yield.

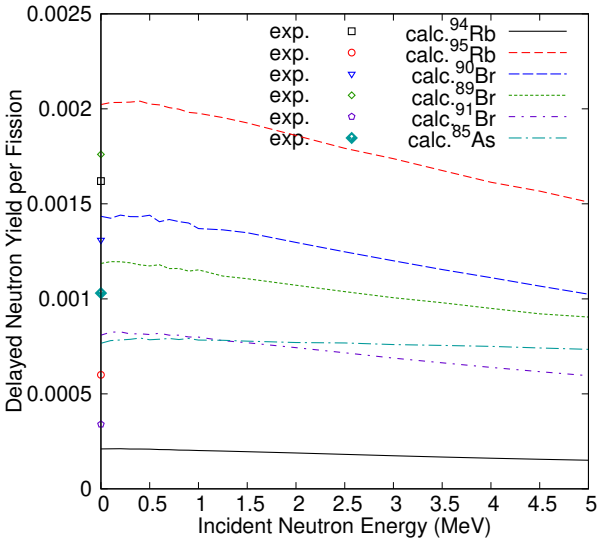

Figure 6: Incident neutron energy dependence of th delayed neutron yield.

4 Conclusion

We performed the fission product yield (FPY), prompt and delayed neutron emission, and decay heat calculations with the Hauser-Feshbach Fission Fragment Decay (HF^{3}D), beta decay, and summation calculations for the fission of ^{235}U. These fission observables are calculated as a function of the incident neutron energy from thermal to 5 MeV. A set of calculated $Y_I(A)$ for each energy is used as an input for the β-decay and the summation calculations. The decay heat of the β component reproduces well the experimental data, while the gamma component are not for early cooling period after the fission burst. The delayed neutron yield tend to be overestimated until 10 seconds from the fission burst. We found that the model needs to modify in terms of the charge distribution of fission fragments to reproduce the β decay observables. However, we showed that the code and such sequential calculations are quite useful for the evaluation of FPY. We anticipate that the future evaluation will use this types of method with experimental data to generate energy dependent yield sets that reproduce other fission or decay observables simultaneously.

Acknowledgements

This work was partially supported by the grant 'Development of prompt-neutron measurement in fission by surrogate reaction method and evaluation of neutron- energy spectra,' en- trusted to JAEA by Ministry of Education, Culture, Sports, Science and Technology. This work was partly carried out under the auspices of the National Nuclear Security Administra- tion of the U.S. Department of Energy at Los Alamos National Laboratory under Contract No. 89233218CNA000001.

References

[1] England TR, Rider BF. Evaluation and compilation of fission product yields. Los Alamos National Laboratory; 1994. ENDF-349, LA-UR-94-3106.

[2] Madland DG. Total prompt energy release in the neutron-induced fission of ^{235}U, ^{238}U, and ^{239}Pu. Nuclear Physics A. 2006;772(3):113 – 137.

[3] Wahl AC. Systematics of Fission-Product Yields. Los Alamos National Laboratory; 2002. LA-13928.

[4] Okumura S, Kawano T, Jaffke P, Talou P, Chiba S. ^{235}U(n, f) Independent fission product yield and isomeric ratio calculated with the statistical Hauser–Feshbach theory. Journal of Nuclear Science and Technology. 2018;55(9):1009–1023.

[5] Kawano T, Talou P, Stetcu I, Chadwick MB. Statistical and evaporation models for the neutron emission energy spectrum in the center-of-mass system from fission fragments. Nuclear Physics A. 2013;913(2):51 – 70.

[6] Ohsawa T, Horiguchi T, Hayashi H. Multimodal analysis of prompt neutron spectra for ^{237}Np(n,f). Nuclear Physics A. 1999;653(1):17 – 26.

[7] Okumura S, Kawano T, Jaffke P, Talou P, Yoshida T, Chiba S. Fission Product Yield Calculation by Hauser-Feshbach Statistical Decay and Beta Decay. CERN Proceedings series. 2018;In preparation.,.

[8] Okumura S, Kawano T, Chiba S. Prompt and Delayed Neutron Emission and Fission Product Yield Calculations with Hauser-Feshbach Theory and Beta Decay. EPJ Web of Conferences, WONDER-2018. 2018;In preparation.,.

[9] Borzakov SB, Panteleev TT, Pavlov SS, Ruskov IN, Zamyatnin YS. Study of delayed neutron decay curves from thermal neutron induced fission of 235U and 239Pu. Progress in Nuclear Energy. 2002;41(1):125 – 133.

This is a blank page.

国際単位系（SI）

表１．SI 基本単位

基本量	SI 基本単位	
	名称	記号
長さ	メートル	m
質量	キログラム	kg
時間	秒	s
電流	アンペア	A
熱力学温度	ケルビン	K
物質量	モル	mol
光度	カンデラ	cd

表２．基本単位を用いて表されるSI組立単位の例

組立量	SI 組立単位	
	名称	記号
面積	平方メートル	m^2
体積	立方メートル	m^3
速さ，速度	メートル毎秒	m/s
加速度	メートル毎秒毎秒	m/s^2
波数	毎メートル	m^{-1}
密度，質量密度	キログラム毎立方メートル	kg/m^3
面積密度	キログラム毎平方メートル	kg/m^2
比体積	立方メートル毎キログラム	m^3/kg
電流密度	アンペア毎平方メートル	A/m^2
磁界の強さ	アンペア毎メートル	A/m
量濃度(a)，濃度	モル毎立方メートル	mol/m^3
質量濃度	キログラム毎立方メートル	kg/m^3
輝度	カンデラ毎平方メートル	cd/m^2
屈折率(b)	（数字の） 1	1
比透磁率(b)	（数字の） 1	1

(a) 量濃度（amount concentration）は臨床化学の分野では物質濃度（substance concentration）ともよばれる。
(b) これらは無次元量あるいは次元１をもつ量であるが、そのことを表す単位記号である数字の１は通常は表記しない。

表３．固有の名称と記号で表されるSI組立単位

組立量	SI 組立単位			
	名称	記号	他のSI単位による表し方	SI基本単位による表し方
平面角	ラジアン(b)	rad	1 (b)	m/m
立体角	ステラジアン(b)	sr(c)	1 (b)	m^2/m^2
周波数	ヘルツ(d)	Hz		s^{-1}
力	ニュートン	N		$m\ kg\ s^{-2}$
圧力，応力	パスカル	Pa	N/m^2	$m^{-1}\ kg\ s^{-2}$
エネルギー，仕事，熱量	ジュール	J	N m	$m^2\ kg\ s^{-2}$
仕事率，工率，放射束	ワット	W	J/s	$m^2\ kg\ s^{-3}$
電荷，電気量	クーロン	C		s A
電位差（電圧），起電力	ボルト	V	W/A	$m^2\ kg\ s^{-3}\ A^{-1}$
静電容量	ファラド	F	C/V	$m^{-2}\ kg^{-1}\ s^4\ A^2$
電気抵抗	オーム	Ω	V/A	$m^2\ kg\ s^{-3}\ A^{-2}$
コンダクタンス	ジーメンス	S	A/V	$m^{-2}\ kg^{-1}\ s^3\ A^2$
磁束	ウエーバ	Wb	Vs	$m^2\ kg\ s^{-2}\ A^{-1}$
磁束密度	テスラ	T	Wb/m^2	$kg\ s^{-2}\ A^{-1}$
インダクタンス	ヘンリー	H	Wb/A	$m^2\ kg\ s^{-2}\ A^{-2}$
セルシウス温度	セルシウス度(e)	℃		K
光束	ルーメン	lm	cd sr(c)	cd
照度	ルクス	lx	lm/m^2	m^{-2} cd
放射性核種の放射能(f)	ベクレル(d)	Bq		s^{-1}
吸収線量，比エネルギー分与，カーマ	グレイ	Gy	J/kg	$m^2\ s^{-2}$
線量当量，周辺線量当量，方向性線量当量，個人線量当量	シーベルト(g)	Sv	J/kg	$m^2\ s^{-2}$
酸素活性	カタール	kat		s^{-1} mol

(a)SI接頭語は固有の名称と記号を持つ組立単位と組み合わせても使用できる。しかし接頭語を付した単位はもはやコヒーレントではない。
(b)ラジアンとステラジアンは数字の１に対する単位の特別な名称で、量についての情報をつたえるために使われる。実際には、使用する時には記号radおよびsrが用いられるが、習慣として組立単位としての記号である数字の１は明示されない。
(c)測光学ではステラジアンという名称と記号srを単位の表し方の中に、そのまま維持している。
(d)ヘルツは周期現象についてのみ、ベクレルは放射性核種の統計的過程についてのみ使用される。
(e)セルシウス度はケルビンの特別な名称で、セルシウス温度を表すために使用される。セルシウス度とケルビンの単位の大きさは同一である。したがって、温度差や温度間隔を表す数値はどちらの単位で表しても同じである。
(f)放射性核種の放射能（activity referred to a radionuclide）は、しばしば誤った用語で"radioactivity"と記される。
(g)単位シーベルト（PV,2002,70,205）についてはCIPM勧告2（CI-2002）を参照。

表４．単位の中に固有の名称と記号を含むSI組立単位の例

組立量	SI 組立単位		
	名称	記号	SI 基本単位による表し方
粘度	パスカル秒	Pa s	$m^{-1}\ kg\ s^{-1}$
力のモーメント	ニュートンメートル	N m	$m^2\ kg\ s^{-2}$
表面張力	ニュートン毎メートル	N/m	$kg\ s^{-2}$
角速度	ラジアン毎秒	rad/s	$m\ m^{-1}\ s^{-1}=s^{-1}$
角加速度	ラジアン毎秒毎秒	rad/s^2	$m\ m^{-1}\ s^{-2}=s^{-2}$
熱流密度，放射照度	ワット毎平方メートル	W/m^2	$kg\ s^{-3}$
熱容量，エントロピー	ジュール毎ケルビン	J/K	$m^2\ kg\ s^{-2}\ K^{-1}$
比熱容量，比エントロピー	ジュール毎キログラム毎ケルビン	J/(kg K)	$m^2\ s^{-2}\ K^{-1}$
比エネルギー	ジュール毎キログラム	J/kg	$m^2\ s^{-2}$
熱伝導率	ワット毎メートル毎ケルビン	W/(m K)	$m\ kg\ s^{-3}\ K^{-1}$
体積エネルギー	ジュール毎立方メートル	J/m^3	$m^{-1}\ kg\ s^{-2}$
電界の強さ	ボルト毎メートル	V/m	$m\ kg\ s^{-3}\ A^{-1}$
電荷密度	クーロン毎立方メートル	C/m^3	m^{-3} s A
表面電荷	クーロン毎平方メートル	C/m^2	m^{-2} s A
電束密度，電気変位	クーロン毎平方メートル	C/m^2	m^{-2} s A
誘電率	ファラド毎メートル	F/m	$m^{-3}\ kg^{-1}\ s^4\ A^2$
透磁率	ヘンリー毎メートル	H/m	$m\ kg\ s^{-2}\ A^{-2}$
モルエネルギー	ジュール毎モル	J/mol	$m^2\ kg\ s^{-2}\ mol^{-1}$
モルエントロピー，モル熱容量	ジュール毎モル毎ケルビン	J/(mol K)	$m^2\ kg\ s^{-2}\ K^{-1}\ mol^{-1}$
照射線量（X線及びγ線）	クーロン毎キログラム	C/kg	kg^{-1} s A
吸収線量率	グレイ毎秒	Gy/s	$m^2\ s^{-3}$
放射強度	ワット毎ステラジアン	W/sr	$m^4\ m^{-2}\ kg\ s^{-3}=m^2\ kg\ s^{-3}$
放射輝度	ワット毎平方メートル毎ステラジアン	$W/(m^2\ sr)$	$m^2\ m^{-2}\ kg\ s^{-3}=kg\ s^{-3}$
酵素活性濃度	カタール毎立方メートル	kat/m^3	$m^{-3}\ s^{-1}$ mol

表５．SI 接頭語

乗数	名称	記号	乗数	名称	記号
10^{24}	ヨタ	Y	10^{-1}	デシ	d
10^{21}	ゼタ	Z	10^{-2}	センチ	c
10^{18}	エクサ	E	10^{-3}	ミリ	m
10^{15}	ペタ	P	10^{-6}	マイクロ	μ
10^{12}	テラ	T	10^{-9}	ナノ	n
10^9	ギガ	G	10^{-12}	ピコ	p
10^6	メガ	M	10^{-15}	フェムト	f
10^3	キロ	k	10^{-18}	アト	a
10^2	ヘクト	h	10^{-21}	ゼプト	z
10^1	デカ	da	10^{-24}	ヨクト	y

表６．SIに属さないが、SIと併用される単位

名称	記号	SI 単位による値
分	min	1 min=60 s
時	h	1 h =60 min=3600 s
日	d	1 d=24 h=86 400 s
度	°	1°=(π/180) rad
分	’	1’=(1/60)°=(π/10 800) rad
秒	”	1”=(1/60)’=(π/648 000) rad
ヘクタール	ha	1 ha=1 $hm^2=10^4m^2$
リットル	L, l	1 L=1 l=1 $dm^3=10^3cm^3=10^{-3}m^3$
トン	t	1 t=10^3 kg

表７．SIに属さないが、SIと併用される単位で、SI単位で表される数値が実験的に得られるもの

名称	記号	SI 単位で表される数値
電子ボルト	eV	1 eV=1.602 176 53(14)×10^{-19}J
ダルトン	Da	1 Da=1.660 538 86(28)×10^{-27}kg
統一原子質量単位	u	1 u=1 Da
天文単位	ua	1 ua=1.495 978 706 91(6)×10^{11}m

表８．SIに属さないが、SIと併用されるその他の単位

名称	記号	SI 単位で表される数値
バール	bar	1 bar=0.1MPa=100 kPa=10^5Pa
水銀柱ミリメートル	mmHg	1 mmHg≈133.322Pa
オングストローム	Å	1 Å=0.1nm=100pm=10^{-10}m
海里	M	1 M=1852m
バーン	b	1 b=100fm^2=$(10^{-12}cm)^2$=$10^{-28}m^2$
ノット	kn	1 kn=(1852/3600)m/s
ネーパ	Np	SI単位との数値的な関係は、対数量の定義に依存。
ベル	B	
デシベル	dB	

表９．固有の名称をもつCGS組立単位

名称	記号	SI 単位で表される数値
エルグ	erg	1 erg=10^{-7} J
ダイン	dyn	1 dyn=10^{-5}N
ポアズ	P	1 P=1 dyn s cm^{-2}=0.1Pa s
ストークス	St	1 St =1$cm^2\ s^{-1}$=$10^{-4}m^2\ s^{-1}$
スチルブ	sb	1 sb =1cd cm^{-2}=10^4cd m^{-2}
フォト	ph	1 ph=1cd sr cm^{-2} =10^4lx
ガル	Gal	1 Gal =1cm s^{-2}=$10^{-2}ms^{-2}$
マクスウエル	Mx	1 Mx = 1G cm^2=10^{-8}Wb
ガウス	G	1 G =1Mx cm^{-2} =10^{-4}T
エルステッド(a)	Oe	1 Oe ≙ $(10^3/4\pi)$A m^{-1}

(a) ３元系のCGS単位系とSIでは直接比較できないため、等号「 ≙ 」は対応関係を示すものである。

表10．SIに属さないその他の単位の例

名称	記号	SI 単位で表される数値
キュリー	Ci	1 Ci=3.7×10^{10}Bq
レントゲン	R	1 R = 2.58×10^{-4}C/kg
ラド	rad	1 rad=1cGy=10^{-2}Gy
レム	rem	1 rem=1 cSv=10^{-2}Sv
ガンマ	γ	1 γ=1 nT=10^{-9}T
フェルミ		1 フェルミ=1 fm=10^{-15}m
メートル系カラット		1 メートル系カラット= 0.2 g = 2×10^{-4}kg
トル	Torr	1 Torr = (101 325/760) Pa
標準大気圧	atm	1 atm = 101 325 Pa
カロリー	cal	1 cal=4.1858J（「15℃」カロリー），4.1868J（「IT」カロリー），4.184J（「熱化学」カロリー）
ミクロン	μ	1 μ =1μm=10^{-6}m

（第8版，2006年）